Archive ouverte UNIGE

https://archive-ouverte.unige.ch

Thèse 2020

Open Access

This version of the publication is provided by the author(s) and made available in accordance with the copyright holder(s).

Characterizing the non-linear evolution of dark energy models

Hassani, Farbod

How to cite

HASSANI, Farbod. Characterizing the non-linear evolution of dark energy models. Doctoral Thesis, 2020. doi: 10.13097/archive-ouverte/unige:143066

This publication URL: https://archive-ouverte.unige.ch/unige:143066
Publication DOI: 10.13097/archive-ouverte/unige:143066

© This document is protected by copyright. Please refer to copyright holder(s) for terms of use.

UNIVERSITÉ DE GENÈVE
Section de Physique
Département de Physique Théorique

FACULTÉ DES SCIENCES
Professeur Martin Kunz

Characterizing the non-linear evolution of dark energy models

THÉSE

présentée à la Faculté des sciences de l'Université de Genève
pour obtenir le grade de
Docteur ès sciences, mention physique

par
Farbod Hassani
de
Téhéran (Iran)

Thése N°0000

GENÈVE
Atelier de reproduction de la Section de Physique
2020

ABSTRACT

In this thesis we mainly focus on characterizing the non-linear evolution of dark energy and modified gravity models with the aim to probe some of these models precisely while treating all cosmological components including the dark energy part accurately. This treatment of dark sector is especially required by the future high precision cosmological surveys.

In Chapter 1 we discuss the standard model of cosmology and some established ideas which are necessary for the rest of this thesis. We will also talk about the importance of the effective field theory description of dark energy models and how one can implement this general description in N-body codes.

We introduce k-evolution a relativistic N-body code, designed to simulate clustering dark energy while keeping all the relevant non-linear terms in Chapter 2. However, in this chapter we show the results for when the clustering dark energy becomes non-linear due to following the dark matter particles. We specifically focus on k-essence with a speed of sound much smaller than unity but we lay down the basis to extend the code to other dark energy and modified gravity models.

Chapter 3 is dedicated to study of cosmological observables on the past light cone of a fixed observer in the context of clustering dark energy. In this chapter we focus on observables that probe the gravitational field directly, namely the integrated Sachs-Wolfe and non-linear Rees-Sciama effect (ISW-RS), weak gravitational lensing, gravitational redshift and Shapiro time delay.

In Chapter 4 based on k-evolution and gevolution codes we quantify the non-linear effects from clustering dark energy through an effective parameter μ that encodes the additional contribution of a dark energy fluid or a modification of gravity to the Poisson equation. We also discuss how the parametric form of μ can be used to improve Fisher forecasts or Newtonian N-body simulations for clustering dark energy models.

In Chapter 5 we discuss non-linear terms in the Effective Field Theory of Dark Energy (EFT of DE) for k-essence model. We study such models in 3+1

dimensions using cosmological N-body simulation k-evolution and we show that several k-essence simulations seem to blow up as a function of parameters. This led us to an interesting question of blow-up in partial differential equations of the hydrodynamic type appearing in cosmological dark energy simulations. We have discovered the non-linear instability and studied it analytically in 1+1 dimensions.

In Chapter 6 we discuss about the possibility of detecting the relativistic corrections in cosmological N-body simulations. We give a recipe for the needed temporal and spatial resolution of an N-body simulation such that one can detect the relativistic corrections in a specific orbit.

In Chapter 7 we introduce `MG-evolution`, an N-body code based on gevolution for parametrised modifications of gravity. This code is built based on the combination of parametrised linear model with a parametrisation of the highly nonlinear regime extrapolated from modified spherical collapse computations. We test `MG-evolution` against linearised and Chameleon $f(R)$ gravity and the normal branch of the Dvali-Gabadadz-Porrati braneworld model with and without Vainshtein type screening mechanism.

Chapter 8 is devoted to the study of the turn-around radius – special radius that the inwards gravitational attraction and the outwards expansion of the Universe cancel each other – as a probe of gravity.

Our conclusions and outlook are summarized in Chapter 9.

This thesis is wholeheartedly dedicated to my beloved family, Mona, Eshrat, Mitra, and Ali, and dear Jean-Pierre.

ACKNOWLEDGEMENTS

First of all, I would like to express my deep gratitude to my supervisor, Martin Kunz for his invaluable supports during my Ph.D, for his motivation, patience, and kindness. I could not have imagined having a better supervisor in my Ph.D.

I am also extremely grateful to Jean-Pierre Eckmann, who supported me in all phases of my Ph.D. Talking to him during the coffee sessions was the most important part of my Ph.D.

I would like to express my special thanks to Julian Adamek, who is my role model in numerical cosmology, and Peter Wittwer, who showed me how to be pedantic.

I am grateful to my collaborators Julian Adamek, Jean-Pierre Eckmann, Martin Kunz, Lucas Lombriser, Steen H. Hansen, Benjamin L'Huillier, Arman Shafieloo, Filippo Vernizzi, Pan Shi, Shant Baghram and Hassan Firouzjahi.

I would like to express my very great appreciation to my friends and colleagues (in alphabetical order):

Mahmoud Reza Amini, Amir Nezam Amiri, Hossein Ayoubi, Mohammad Reza Ayromlou, Reza Babatabar, Shant Baghram, Abdol Ali Banihashemi, Enis Belgacem, Camille Bonvin, Benjamin Bose, Joyce Byun, Giulia Cusin, Charles Dalang, David Daverio, Yves Dirian, Azadeh Moradinezhad Dizgah, Ruth Durrer, Aghile Ebrahimi, Golshan Ejlali, Farida Farsian, Andreas Finke, Pierre Fleury, Jérémie Francfort, Antonia Frassino, Tomohiro Fujita, Basundhara Ghosh, Mina Ghodsi, Reza Golpayegani, Sedighe Hashemi, Soumya Jana, Goran Jelic-Cizmek, Arash Jofrehei, Joe Kennedy, Ali Khadem, Abbas Khanbeigi, Hasti Khorami-Nezhad, Nima Khosravi, Francesca Lepori, Elisabetta Majerotto, Shahram Maleki, Reza Mansouri, William Matthewson, Mani Mohammadi, Milad Moham-

madi, Tahmasb Moshiri, Zahra Nazlabadi, Viraj Nistane, Felipe Oliveira, Sohrab Rahvar, Jacques Rougemont, Alireza Vafaei Sadr, Farshad Seifollahi.

I want to thank my hosts for their hospitality during my visits, especially David Mota, Hans Winther, Arman Shafieloo, Benjamin L'Huillier, Shant Baghram, Nima Khosravi, Sohrab Rahvar and Encieh Erfani.

Finally, I wish to express my very great appreciation to my family members, Mona Jalilvand, Mitra Rabiei, Ali Hassani, Eshrat Sharifi, Andia Hassani, Ashraf Kabiri, Ghasem Jalilvand and Hamed Jalilvand for their support throughout my study.

JURY MEMBERS

- Prof. Jean-Pierre Eckmann
  Département de Physique Théorique & Section de Mathématiques, Université de Genève, Switzerland

- Prof. Lucas Lombriser
  Département de Physique Théorique & Center for Astroparticle Physics, University of Geneva, Switzerland

- Prof. David F. Mota
  Institute of Theoretical Astrophysics, University of Oslo, 0315 Oslo, Norway

- Prof. Romain Teyssier
  Institute for Computational Science, University of Zurich, Winterthurerstrasse 190, 8057 Zurich, Switzerland

- Prof. Martin Kunz
  Département de Physique Théorique & Center for Astroparticle Physics, University of Geneva, Switzerland

I would like to appreciate them all for accepting to be part of the Jury for my Thesis defense.

LIST OF PUBLICATIONS

The following articles have been considered as part of this thesis:

- **Farbod Hassani**, Julian Adamek, Martin Kunz and Filippo Vernizzi,
  k-evolution: a relativistic N-body code for clustering dark energy,
  JCAP **12**, 011 (2019), arXiv:1910.01104.

- **Farbod Hassani**, Julian Adamek and Martin Kunz
  Clustering dark energy imprints on cosmological observables of the gravitational field,
  Submitted to Monthly Notices of the Royal Astronomical Society, arXiv:2007.04968.

- **Farbod Hassani** and Lucas Lombriser
  N-body simulations for parametrised modified gravity ,
  Monthly Notices of the Royal Astronomical Society 2020 497 (2): 1885-1894, arXiv:2003.05927.

- Jean-Pierre Eckmann and **Farbod Hassani**,
  The detection of relativistic corrections in cosmological N-body simulations,
  Celestial Mechanics and Dynamical Astronomy **132**, 2 (2020), arXiv:1909.04652.

- **Farbod Hassani**, Benjamin L'Huillier, Arman Shafieloo, Martin Kunz and Julian Adamek,
  Parametrising non-linear dark energy perturbations,
  JCAP **04**, 039 (2020), arXiv:1910.01105.

- Steen H. Hansen, **Farbod Hassani**, Lucas Lombriser, Martin Kunz,
  Distinguishing cosmologies using the turn-around radius near galaxy clusters,
  JCAP **01**, 048 (2020), arXiv:1906.04748.

- **Farbod Hassani**, Pan Shi, Julian Adamek, Martin Kunz, Peter Wittwer
  A new instability in clustering dark energy,
  in preperation

RÉSUMÉ

Dans cette thèse, nous nous concentrons principalement sur la caractérisation de l'évolution non linéaire des modèles d'énergie noire et de gravité modifiée dans le but de sonder certains de ces modèles avec précision tout en traitant avec précision toutes les composants cosmologiques, y compris la partie d'énergie sombre. Ce traitement du secteur sombre est particulièrement requis par les futurs levés cosmologiques de haute précision.

Dans le chapitre 1, nous discutons du modèle standard de la cosmologie et de quelques idées établies qui sont nécessaires pour la suite de cette thèse. Nous parlerons également de l'importance de la description effectif de la théorie des champs des modèles d'énergie noire et de la manière dont on peut implémenter cette description générale dans les codes à N-corps.

Nous introduisons k-evolution, un code relativiste à N-corps, conçu pour simuler le clustering d'énergie noire tout en conservant tous les termes non linéaires pertinents dans le chapitre 2. Cependant, dans ce chapitre, nous montrons les résultats pour le moment où l'énergie sombre de regroupement devient non linéaire en raison du mouvement des particules de matière noire. Nous nous concentrons spécifiquement sur k-essence avec une vitesse du son beaucoup plus petit que l'unité mais nous posons les bases pour étendre le code à d'autres modèles d'énergie noire et de gravité modifiée.

Le chapitre 3 est dédié à l'étude des observables cosmologiques sur le cône de lumière passéd'un observateur fixe dans le contexte de regroupement de l'énergie noire. Dans ce chapitre, nous nous concentrons sur les observables qui sondent le champ gravitationnel directement, à savoir l'effet Sachs-Wolfe intégré et l'effet Rees-Sciama non linéaire (ISW-RS), lentille gravitationnelle faible, décalage vers le rouge gravitationnel et retard Shapiro.

Dans le chapitre 4 basésur les codes k-evolution et gevolution, nous quantifions les effets non-linéaires du regroupement d'énergie noire via un paramètre effectif μ qui encode la contribution supplémentaire d'un fluide d'énergie sombre ou d'un modification de la gravitéà l'équation de Poisson. Nous discutons également-

ment comment la forme paramétrique de μ peut être utilisée pour améliorer les prévisions de Fisher ou les simulations Newtoniennes à N-corps pour regrouper les modèles d'énergie noire.

Dans le chapitre 5, nous discutons des termes non linéaires dans le description effectif de la théorie des champs des modèles d'énergie noire (EFT de DE) pour le modèle k-essence. Nous étudions ces modèles en 3 + 1 dimensions en utilisant une simulation cosmologique N-corps k-evolution et nous montrons que plusieurs simulations k-essence semblent exploser en fonction des paramètres. Ceci nous a conduit à la question intéressante de la divergence dans les équations aux dérivées partielles de type hydrodynamique apparaissant dans les simulations cosmologiques d'énergie noire. Nous avons découvert l'instabilité non linéaire et l'avons étudiée analytiquement en dimensions 1 + 1.

Dans le chapitre 6 nous discutons de la possibilité de détecter les corrections relativistes dans les simulations cosmologiques N-corps. Nous donnons une recette pour la résolution temporelle et spatiale nécessaire d'une simulation de N-corps telle que l'on puisse détecter les corrections relativistes dans une orbite spécifique.

Dans le chapitre 7 nous introduisons `MG-evolution`, un code N-corps basé sur la gevolution pour les modifications paramétriques es de la gravité. Ce code est basé sur la combinaison du modèle linéaire paramétré avec une paramétrisation du très non linéaire régime extrapolé à partir de calculs d'effondrement sphérique modifiés. Nous testons `MG-evolution` contre la gravité linéarisée et Chameleon $f(R)$ et la normale branche du modèle braneworld Dvali-Gabadadz-Porrati avec et sans mécanisme de criblage de type Vainshtein.

Le chapitre 8 est consacréà l'étude du rayon de retournement - rayon spécial où l'attraction gravitationnelle vers l'intérieur et l'expansion vers l'extérieur de l'Univers s'annulent - en tant que sonde de gravité.

Nos conclusions et perspectives sont résumées dans le chapitre 9.

NOTATIONS

List of symbols used in the thesis

a	scale factor
H	Hubble parameter (H_0 denotes Hubble parameter today)
$\mathcal{H}$	comoving Hubble parameter $\mathcal{H} = aH$
h	reduced Hubble parameter $h = H_0/100$
τ, τ_0	conformal time (today)
t ,t_0	cosmic time (today)
χ	comoving distance $\chi = \eta_0 - \eta$
z	redshift
$\mathbf{n}$, $\hat{n}$	line-of-sight direction
$\mathbf{r}$	relative position of two objects $\mathbf{r} = \mathbf{x}_1 - \mathbf{x}_2$
Φ, Ψ	Bardeen potentials
δ, δ_m	matter density contrast in Poisson gauge
ψ_N	the Newtonian gravitational potential
$\delta_m^{\rm count}$	counting density (rest mass per coordinate volume)
$\mathbf{v}(\mathbf{x})$	velocity perturbation

$v(x)$	velocity potential $\mathbf{v} = -\nabla v$
c_s	speed of sound
θ	$\nabla_i v^i$
Δ	the comoving density contrast (total-matter variable)
χ	defined as $\Phi - \Psi$
$K_{\nu\mu}$	the extrinsic curvature tensor
π	scalar field perturbation
Δ_x	normalized cross power spectrum
$P_m(k)$	matter power spectrum
$\xi(\theta)$	two-point correlation function
C_ℓ	angular power spectrum
ψ	lensing potential
κ	convergence defined as $-\frac{1}{2}\hat{\nabla}^2\psi$
γ_1 and γ_2; γ	shear components; complex shear
ϵ	ellipticity
q_{ab}	second moments of brightness distribution
$\mathcal{P}_\ell(\mathrm{X})$	Legendre polynomials
$Y_{\ell m}(\theta, \phi)$	Spherical harmonics
$J_n(x)$	Bessel functions
$j_\ell(x)$	Spherical Bessel functions
δ_{ij}, δ^D	Kronecker and Dirac delta functions
ϵ_{ijk}	Levi-Civita tensor

ABBREVIATIONS

Abbreviations	
ΛCDM	Cosmological constant Cold dark matter
FLRW	Freidmann-Lemaître-Robertson-Walker
GR	General relativity
CMB	Cosmic microwave background
LSS	Large-scale structures
BAO	Baryon acoustic oscillations
RSD	redshift-space distortion
ISW-RS	Integrated Sachs-Wolfe and Rees-Sciama effect
SPT	Standard perturbation theory
EFT	Effective field theory
EFT of DE	Effective field theory of dark energy
PM	Particle Mesh scheme
P^3M	Particle-Particle-Particle Mesh

LIST OF FIGURES

1.1 A graphical view of the Cosmic Calendar, from the early Universe to today mapped into a year, ... 3

1.2 A Picture that shows the densities and gravitational potentials of some structures in the weak field and strong field regime, including the Sun, the Milky Way, a neutron star and a black hole. We have not depicted larger structures, however the structures with larger sizes (galaxies, clusters, filaments and super-clusters) have less density and less gravitational potential compared to the Sun and Milky way, so they also belong to the weak field regime. The numbers for the neutron star and black hole are computed for a typical kind. 21

1.3 A schematic image showing a constant scalar filed hypersurface and the geometric objects associated with it. 31

1.4 A figure in the original paper of Holmberg showing the interaction of two spiral galaxies 42

1.5 The schematic picture showing the main loop of k-evolution code. 47

2.1 Schematic description of the three different codes used in this work, where the blue arrows show if one component sources the other. On the left, the two blue arrows going from non-linear matter and potentials to δ_{DE}, and *vice-versa*, show that in k-evolution all the components interact and source each other. Although we have used the density of linearized dark energy, its solution becomes non-linear since it is sourced by other species. In *gevolution* the matter and potentials become non-linear and are sourced by linear dark energy density, while δ_{DE} is computed with `CLASS`. In `CLASS` all the components are linear and interact with each other. 60

2.2 The top panel shows the matter power spectra from k-evolution and `CLASS` at different redshifts for $c_s^2 = 10^{-7}$. The bottom panel shows the relative difference between the matter power spectra of `CLASS`-Halofit and those of `CLASS`-k-evolution. The relative difference increases in the quasi-linear regime and for $z = 0$ reaches $\sim -5\%$ at its peak for `CLASS`-k-evolution and $\sim -2\%$ for `CLASS`-Halofit, while at high wavenumbers the non-linearity dominates. Notice that the vertical axis of the bottom panel is logarithmic above 0.05 and linear below. 61

2.3 Comparison of the power spectra of the gravitational potential Φ computed with k-evolution (solid lines) and `CLASS` (dashed lines), for $c_s^2 = 10^{-7}$. At the top, we show the power spectra at different redshifts and at the bottom their relative difference. On intermediate scales, the power spectra computed with k-evolution are suppressed compared to those of `CLASS`, while the situation is reversed in the non-linear regime, for $k > 0.1h/\text{Mps}$. 63

2.4 Comparison of the dark energy density power spectra from k-evolution (solid lines) and from `CLASS` (dashed lines) at different redshifts, for two different speeds of sound, $c_s^2 = 10^{-7}$ (left-panel) and $c_s^2 = 10^{-4}$ (right-panel). The vertical dashed lines show the value of the dark energy sound-horizon at each redshift, using the same color as the corresponding power spectrum. The turn-around in the power spectra takes place inside the sound-horizon. Its exact position is affected by dark matter non-linearities, as one can see comparing the case $c_s^2 = 10^{-4}$, where the turn-around happens on linear scales, and the case $c_s^2 = 10^{-7}$, where the turn-around takes place in the non-linear regime. Notice also that, as for the matter power spectrum, in the linear and quasi-linear regime at $z = 0$, the non-linear dark energy power spectrum is smaller than the linear one. 64

2.5 Comparison of π power spectra at different redshifts from k-evolution (solid lines) and `CLASS` (dashed lines), for $c_s^2 = 10^{-4}$ (right-panel) and $c_s^2 = 10^{-7}$ (left-panel). Δ_π has units of Mpc^2/h^2; multiplying it by k^2 makes it dimensionless. The vertical dashed lines show the value of the dark energy sound-horizon at each redshift. The dark energy velocity divergence power spectrum, $\Delta_{\theta_{\rm DE}}$, is simply given by $k^4\Delta_\pi$. 65

2.6 Comparison of the ratio between dark energy and matter power spectra from `CLASS` and k-evolution for two speeds of sound, $c_s^2 = 10^{-4}$ (right panel) and $c_s^2 = 10^{-7}$ (left panel), at different redshifts. For $c_s^2 = 10^{-4}$, the sound-horizon is at about the scale of matter non-linearity and the result from k-evolution agrees well with the one from `CLASS`. For $c_s^2 = 10^{-7}$, the sound-horizon is smaller than the matter non-linearity scale and we observe significant differences between the k-evolution and `CLASS` results, due to the matter and dark energy clustering, which are absent in the linear theory. The upturn visible in the ratio on large scales for $z = 50$ is a gauge effect on horizon scales. 66

2.7 At the top, comparison of the matter power spectra from k-evolution and *gevolution* at different redshifts, for $c_s^2 = 10^{-7}$. At the bottom, relative difference between the two power spectra at each redshift is shown. The figure shows that the effect of non-linearity of dark energy on the matter power spectrum is negligible. 68

2.8 In the top panel, the potential power spectra from k-evolution and *gevolution* at three different redshifts are shown and in the bottom panel the relative difference between the power spectra at the same redshifts are plotted. The dark energy clustering changes the potential power spectrum by up to $\sim 4\%$ at mildly linear scales at $z = 0$. 69

2.9 Comparison of the power spectra of $\Phi'/\mathcal{H}$ for k-evolution, *gevolution* and `CLASS` at different redshifts, for $c_s^2 = 10^{-4}$ (right panel) and $c_s^2 = 10^{-7}$ (left panel). The onset of non-linear effects in Φ' is on much larger scales than in Φ or δ_m. The results from k-evolution and *gevolution* are more similar, with differences reaching to $\sim$5% between the two codes. 71

2.10 Normalized cross correlation power spectra at different redshifts for speed of sound $c_s^2 = 10^{-4}$ on the right and $c_s^2 = 10^{-7}$ on the left. In *gevolution*, for both speeds of sound the only important scale is the scale of matter non-linearity as in *gevolution* the dark energy does not follow the non-linear matter structures, and we see that after this scale the cross correlation power decays. In k-evolution for $c_s^2 = 10^{-4}$ almost at all scales the dark energy and matter densities are fully correlated, as inside the sound-horizon dark energy does not cluster strongly and closely follows the matter density. In the case with lower speed of sound, where dark energy clusters and has self-dynamics the cross correlation power starts to decay on small scales. 72

2.11 Cross-correlation power spectra between matter and dark energy densities at different redshifts, for $c_s^2 = 10^{-4}$ (right panel) and $c_s^2 = 10^{-7}$ (left panel), computed by k-evolution and *gevolution*. In *gevolution*, the dynamics of dark energy and matter decouple beyond the scale of matter non-linearity, so the dashed lines and solid lines start deviating roughly at the scale of non-linearity. In k-evolution, for $c_s^2 = 10^{-4}$ the dark energy density does not cluster at scales where matter clusters, and the dark energy follows matter. This is why the cross-correlation power between the two densities is large. For $c_s^2 = 10^{-7}$, the dark energy density clusters and the turn-around in the cross-correlation power spectrum takes place at the sound-horizon scale. 73

2.12 Ratio of dark energy and matter densities power spectra in k-evolution (solid lines) and *gevolution* (dashed lines), at different redshifts for $c_s^2 = 10^{-7}$ (left panel) and $c_s^2 = 10^{-4}$ (right panel). The scale at which *gevolution* and k-evolution start disagreeing is giving by a combination of sound-horizon and scale of matter non-linearity. In the low speed of sound case, $c_s^2 = 10^{-7}$, this happens at smaller scales. Also this ratio increases with the redshift, as the matter clustering is much stronger than the dark energy clustering at lower redshifts. 74

2.13 The matter power spectra and the relative difference from two Newtonian simulations, one with the back-scaled initial conditions for $c_s^2 = 10^{-7}$ and one with the correct initial conditions from the linear Boltzmann code `CLASS` and correct evolution for $c_s^2 = 10^{-7}$ including linear dark energy perturbations. The simulation with back-scaled initial condition works well at $z = 0$ especially at linear scales by construction while it reaches 1% error at non-linear scales. At higher redshifts the relative errors are typically larger, but remain below 2% on all scales. 79

2.14 The gravitational potential power spectra and the relative difference from two Newtonian simulations, one with the back-scaled initial conditions for $c_s^2 = 10^{-7}$ and one with the correct initial conditions and correct evolution for $c_s^2 = 10^{-7}$ including linear dark energy perturbations. The simulation with back-scaled initial condition does not give the correct gravitational potential power spectrum at large scales; we find about 7% relative error. 80

2.15 Respectively from the left to the right, the dark energy density computed with *gevolution* (using the `CLASS` interface) and the dark energy and matter density computed with k-evolution, as a function of the redshift (from the bottom to the top), measured in units of the critical density. The dark energy structures form around massive halos. Note that the color scheme for the visualisation of $\rho^{(\mathrm{DE})}$ changes between lower panels and upper panels. . . 81

2.16 A comparison of dark energy clustering in simulations. 82

2.17 Change in the particles positions due to dark energy clustering. The arrows show the difference between the position of each particle in k-evolution and that of the same particle in *gevolution*. The colors show the length of the arrows measured in Mpc/h. Red arrows around the virial radius of the halo point toward the center. 83

2.18 The transformations in `CLASS` to obtain π and π' in a certain gauge from the fluid properties. In the top part, it is assumed that the user runs `CLASS` in Synchronous gauge which θ_{Synch} and δ_{Synch} in Synchronous gauge are the direct output of the code. To obtain π_{Synch} and π'_{Synch} one needs to use the given transformations. In the bottom part, it is assumed that the user runs `CLASS` in Newtonian gauge. Follow the recipe one obtains π_{Newt} and π'_{Newt} . . . 89

2.19 The transformations in `hi_class` to obtain a certain quantity in a specific gauge. In the top, the recipe in synchronous gauge is given. In `hi_class`, π_{Synch} and π'_{Synch} are the direct output of the code. To obtain δ_{Synch} and θ_{Synch} one needs to follow the given transformations. In the bottom part, the recipe for obtaining quantities in Newtonian gauge in both languages are given. 90

3.1 ***Left:*** The conformal Hubble parameter as a function of redshift for ΛCDM and wCDM with $w_0 = -0.9$. In the bottom panel we show the relative difference. As expected, the effect of dark energy goes away at high redshifts. ***Centre:*** The comoving distance as a function of redshift for the two cosmologies is plotted. In the bottom panel again the relative difference is shown. The relative difference asymptotes to a constant at high redshifts because the comoving distance is an integrated quantity. ***Right:*** In the top panel, the logarithmic growth rate f as a function of redshift for a fixed wavenumber is plotted. In the bottom the relative difference between different scenarios is shown with respect to ΛCDM. While in the latter case the growth rate is scale independent (neglecting corrections due to neutrinos), in a clustering dark energy model the behaviour of a mode depends on whether it is inside or outside of the sound horizon. We compare three cases with ΛCDM, namely the mode $k = 0.5$ Mpc^{-1} with $c_s^2 = 10^{-7}$, $k = 10$ Mpc^{-1} with $c_s^2 = 10^{-7}$ and $k = 0.5$ Mpc^{-1} with $c_s^2 = 1$. Only the first case corresponds to a mode outside the sound horizon, while the other two are well inside. Thus we see the same behaviour for $k = 10$ Mpc^{-1} with $c_s^2 = 10^{-7}$ and $k = 0.5$ Mpc^{-1} with $c_s^2 = 1$. 101

3.2 ***Left:*** Full-sky maps of the ISW-RS temperature anisotropy, gravitational redshift, convergence and Shapiro time delay from a ΛCDM simulation using *gevolution*, integrated to $z \sim 0.8$ are shown. ***Right:*** Difference between the maps for k-essence with $c_s^2 = 10^{-7}$ and k-essence with $c_s^2 = 1$, both simulated with k-evolution. All simulations used the same seed to generate the random initial conditions and hence the difference maps indicate the importance of k-essence clustering. . . . 112

3.3 ***Top panel:*** The angular power spectra of the lensing convergence κ at a source distance of $\chi_s = 2000$ Mpc$/h$ for some of our N-body simulations, as well as predictions from `CLASS` with and without the Halofit prescription. Based on the convergence test of App. 3.A we can trust the convergence spectrum here to $\ell \approx 200$, which is roughly where the dots start to deviate from the CLASS-Halofit curve. Relative spectra remain accurate to much higher ℓ. ***Bottom panel:*** Data points show the relative difference between the convergence power spectra from our N-body simulations for different models, whereas dashed lines represent the corresponding predictions from `CLASS` with Halofit, shown in matching colours. The blue points show the impact of k-essence non-linearities by comparing non-linear k-essence from k-evolution with its linear implementation in *gevolution*. 114

3.4 Same as Fig. 3.3, but for a source distance of $\chi_s = 4500$ Mpc/h, corresponding roughly to $z \approx 3.3$, and using N-body simulation data that covers $\sim 5\%$ of the sky. Again based on App. 3.A we can trust the dots in the top panel to $\ell \approx 500$, while the relative spectra shown in the bottom panel are again valid to higher ℓ. . . 115

3.5 ***Top panel:*** The late-ISW-RS angular power spectra for different cosmologies integrating to $\chi_s = 2000$ Mpc/h are shown. Note that `CLASS` only predicts the linear ISW signal without any non-linear correction applied. The convergence study of App. 3.A indicates that these spectra are reliable to $\ell \approx 500$, the relative spectra are again valid to higher ℓ. ***Bottom panel:*** The relative difference between different models in the ISW-RS power spectra are shown. At large scales the result from N-body codes agree with `CLASS`, however, already at $\ell < 100$ the linear and non-linear curves diverge due to the non-linear RS effect. 116

3.6 Same as Fig. 3.5, but for a source distance of $\chi_s = 4500$ Mpc/h, corresponding roughly to $z \approx 3.3$, and using N-body simulation data that covers $\sim 5\%$ of the sky. From the convergence study in the appendix we conclude that these spectra are reliable over the full range of scales shown. 117

3.7 ***Top panel:*** The cross power spectra of lensing convergence κ and ISW-RS integrated to comoving distance $\chi_s = 2000$ Mpc/h from k-evolution with two speeds of sound $c_s^2 = 10^{-7}$ and $c_s^2 = 1$ are shown, together with our ΛCDM reference run. ***Bottom panel:*** The relative difference between the cross power spectra for several models is shown. 120

3.8 Same as Fig. 3.7, but for a source distance of $\chi_s = 4500$ Mpc/h, corresponding roughly to $z \approx 3.3$, and using N-body simulation data that covers $\sim 5\%$ of the sky. 121

3.9 ***Top panel:*** The cross-correlation coefficient of lensing convergence κ and ISW-RS integrated to comoving distance $\chi_s = 2000$ Mpc/h for the results shown in Fig. 3.7. ***Bottom panel:*** Absolute difference in the cross-correlation coefficient for different models. 123

3.10 ***Top panel:*** The gravitational redshift angular power spectra of different cosmologies for a source plane at comoving distance $\chi_s = 2000$ Mpc/h. ***Bottom panel:*** The relative difference between the angular power spectra of the gravitational redshift in different cosmologies. 125

3.11 ***Top panel:*** The angular power spectra of Shapiro time delay integrated to comoving distance $\chi_s = 2000$ Mpc/h for different cosmologies. ***Bottom panel:*** The relative difference between Shapiro delay angular power spectra for different models. 126

3.12 ***Top panel:*** We compare the convergence power spectra from two simulations with different resolutions, $N_{\rm grid} = N_{\rm pcl} = 4608^3$ and $N_{\rm grid} = N_{\rm pcl} = 2304^3$, at two source redshifts $z = 0.85$ and $z = 3.3$. ***Middle panel:*** The relative difference between the convergence power spectra of the same cosmology but different resolutions of the simulations are shown. This gives us an estimation of the finite resolution error on the convergence angular power spectra. The grey areas show 1% and 2% numerical agreement. ***Bottom panel:*** Comparing the relative change in the convergence power spectra between ΛCDM and k-essence cosmology with the speed of sound $c_s^2 = 10^{-7}$ from two simulations with different resolutions, $N_{\rm grid} = N_{\rm pcl} = 4608^3$ and $N_{\rm grid} = N_{\rm pcl} = 2304^3$, at source redshifts $z = 0.85$ and $z = 3.3$. The dashed lines show the linear theory prediction obtained from `CLASS`. The agreement across different resolutions shows that one can trust the relative change of power spectra at much higher multipoles than is the case for the individual power spectra themselves. 130

3.13 ***Top panel:*** We compare the ISW-RS angular power spectra from two simulations with different resolution, $N_{\rm grid} = N_{\rm pcl} = 4608^3$ and $N_{\rm grid} = N_{\rm pcl} = 2304^3$, at two source redshifts $z = 0.85$ and $z = 3.3$. ***Middle panel:*** The relative difference between the ISW-RS angular power spectra of the same cosmology but different resolutions of the simulations are shown. ***Bottom panel:*** The relative difference of ISW-RS angular power spectra between the k-essence cosmology with $c_s^2 = 10^{-7}$ and ΛCDM for two different spatial resolutions $N_{\rm grid} = N_{\rm pcl} = 4608^3$ and $N_{\rm grid} = N_{\rm pcl} = 2304^3$ at two source redshifts $z = 0.85$ and $z = 3.3$. The dashed lines show the linear theory prediction obtained from `CLASS`. Like Fig. 3.12, this figure shows that the finite resolution effect is cancelled significantly in the relative changes of the angular power spectra. 131

3.14 ***Left:*** The ISW-RS angular power spectra for two different cosmologies, ($w_0 = -0.9$, $c_s^2 = 1$) and ΛCDM with standard and low value of A_s, the amplitude of scalar perturbations. ***Right:*** The ratio of the ISW-RS signal from high value of A_s to low value of A_s are compared. The linear result is constant at all scales, and is simply the ratio of the two values of A_s. The fractional contribution of the Rees-Sciama effect depends on w_0 mainly because of suppressed growth and the corresponding shift of the non-linear scale with respect to ΛCDM. 132

4.1 Sources to the Hamiltonian constraint, normalized to $\mathcal{H}^2$, in terms of wavenumber at different redshifts, from k-evolution in solid lines and from `CLASS` in dashed lines, for a k-essence speed of sound of $c_s^2 = 10^{-7}$. For the figures on the right, the y-axis is shown on the right. The x-axis is common between each column of figures. The figure on the left bottom, showing the short-wave corrections, is obtained using a simulation with $N_{\text{grid}} = 3840^3$ and box size $L = 9000\,h^{-1}$Mpc, while in the other three figures the results are obtained combining three simulations with $N_{\text{grid}} = 3840^3$ and box sizes $L = 90000\,h^{-1}$Mpc, $L = 9000\,h^{-1}$Mpc and $L = 1280\,h^{-1}$Mpc. 140

4.2 The quantity $\sqrt{\frac{\mathcal{P}_{\Phi-\Psi}}{\mathcal{P}_{\Phi}}}$ from k-evolution (solid lines) and from `CLASS` (dashed lines) at different redshifts as a function of wavenumber k. In k-evolution this quantity is non-zero due to the non-linearities in matter, k-essence and short-wave corrections, while in `CLASS` it is generated due to the radiation perturbations which oscillate and decay in k. The results are obtained combining three simulations with $N_{\text{grid}} = 3840^3$ and box sizes $L = 90000\,h^{-1}$Mpc, $L = 9000\,h^{-1}$Mpc and $L = 1280\,h^{-1}$Mpc. 142

4.3 $\mu(k, z)$ from four different simulations and for two speeds of sound are compared. The left plots depict the case $c_s^2 = 10^{-4}$: all the curves agree well which shows that for high speeds of sound we can trust even linear codes. On the right we see the situation for k-essence with speed of sound $c_s^2 = 10^{-7}$, where differences are clearly visible. In the top panels k-evolution is compared with `CLASS` at different redshifts, while in the bottom figures we compare $\mu(k, z)$ from *gevolution*, k-evolution and `CLASS` with and without Halofit, at $z = 0$. The results are obtained using two simulations with two different box sizes $L = 9000\,h^{-1}$Mpc and $L = 1280\,h^{-1}$Mpc and $N_{\text{grid}} = 3840^3$. 144

4.4 The fitted parameter values for the μ parametrization (4.19), for the two k-essence models with $c_s^2 = 10^{-4}$ (left) and $c_s^2 = 10^{-7}$ (right), as a function of redshift. Points and dashed lines are respectively the results of k-evolution and `CLASS`. 146

4.5 This picture compares the way that different codes solve the Poisson equation. On the left we have the relativistic N-body code k-evolution which uses the full Poisson equation including non-linear k-essence and matter densities, relativistic terms and short wave corrections (all in green). Standard Newtonian N-body codes (middle) solve the Poisson equation for the correct background expansion rate (term in light yellow), and include non-linear matter densities as well as relativistic terms in N-body gauge (terms in green), but do not take into account k-essence perturbations or shortwave (nonlinear GR) terms (in red). Linear Boltzmann codes like `CLASS` (on the right) are fully relativistic and include linear density perturbations for both matter and k-essence (in yellow), but no non-linear GR and matter contributions (in red). 148

4.6 The relative error for the fits compared to the actual μ obtained from k-evolution, for two different speeds of sound, $c_s^2 = 10^{-7}$ (right) and $c_s^2 = 10^{-4}$ (left). The accuracy of the fit is of the sub-percent level for both speeds of sound at all redshifts and all scales. 153

4.7 The relative error of the fits compared to `CLASS` results for two speeds of sound, $c_s^2 = 10^{-7}$ (right) and $c_s^2 = 10^{-4}$ (left). The results show that the accuracy of the fit is of the sub-percent level for both speeds of sound at all redshifts and all scales. 154

4.8 Evolution of the fit parameters $\log_{10}(1 + \alpha)$, β, and γ for k-evolution and `CLASS` data for two speeds of sound $c_s^2 = 10^{-4}$ (top) and 10^{-7} (bottom) is shown. The arrows show the direction of decreasing redshift (increasing time). For the case of low speed of sound (bottom panel) the parameter values obtained from k-evolution and from the linear code `CLASS` differ, while for large speed of sound (top panel) the parameters almost match, suggesting that one could simply use linear Boltzmann codes for treating high speed of sound k-essence models. 155

5.1 From top to bottom: The evolution in time of the scalar field π evolution in a 2D cross section in $x-y$, $x-z$ and $y-z$ surfaces in a short interval of time around blowup time at the point with the maximum curvature. The instability is formed locally in a point with the maximum curvature which physically corresponds to the center of the dark matter halos. 163

5.2 1D cross section of the scalar field evolution on a line passing through the point with the maximum curvature. These figures show how the instability is formed in the local minima with highest curvature. 164

5.3 The average of ζ as a function of blow-up redshift for different speeds of sound are plotted. As it is clear from the figure, the blow up happens very fast and the average value of the fields go from a very small value to a very large value. This is a simulation for the case when k-essence does not source other components and also the initial condition is set to 0 at $z = 100$. When ζ blows up, the scalar field π and other components, if they are coupled, blow up immediately. Here we only showed the results for the speeds of sound for which the scalar field blows up, so in fact according to our numerical result $c_s^2 \leq 10^{-4.7}$. The PDE blows up in the age of the Universe ($z = 0$). 165

5.4 The speed of sound squared as a function of blow up redshift is shown. There are two limits, namely high speed of sound for which the system does not blow up anymore and very low speed of sound for which the system blows up at the redshift near to the blow up redshift for $c_s^2 \to 0$. This figure is calculated for the case when the scalar field does not source matter and potentials and also, when the initial condition is chosen equal to zero. 166

5.5 Time resolution of the simulation as a function of the blow up time for the case dark energy component, respectively, sources and does not source other components (circles and stars respectively). As we increase the time resolution, i.e. decrease $d\tau$ in the simulation the blow-up time converges. 167

5.6 Number of grids, equal to number of particles, as a function of the blowup redshift for the clustering dark energy with $c_s^2 = 10^{-7}$ and $w = -0.9$, for the two cases where dark energy sources, respectively, does not source other components. The case when dark energy PDE is solved without sourcing dark matter and potentials is shown by stars in the figure and the case when the full equations are solved is shown with circles. As we increase the spatial resolution, the system blows up at higher redshifts or earlier time. 168

5.7 The initial redshift of the simulation versus the blow up redshift is plotted. If we start the simulation at higher redshifts the blowup redshift converges. 169

5.8 ***Top***: The scalar field and its time derivatives on the 1+1 D lattice at different times for a cos function as an initial condition are shown. Analytically the curvature of the scalar field at the minimum blows up at time $\tau_b \approx 76$.
Bottom: The scalar field and its spatial derivative on the lattice for different times are shown. Due to the numerical noises appearing in the second order spatial derivative we only show the results up to $\tau = 62.7$. It is also interesting to see that $\partial_x \pi$ behaves similar to a gradient catastrophe that one would see in some situations in the fluid dynamics. 180

5.9 The evolution of the curvature of the minimum in time according to the Eq. 5.33. According to the figure the solution of the ODE, the analytical solution in (5.46) and the curvature evolution obtained from the solution of the PDE are consistent. 181

5.10 Similar to the Fig. 5.9 but for when the full PDE in 1+1 D for $c_s^2 = 1$ is solved. According to this figure for the large value of c_s^2 the system is stabilized. 182

5.11 The evolution of the curvature at the minimum point according to the numerical solution to the full PDE. The curvature at the minima reach a maximum and then decreases. 183

6.1 Detecting the spurious perihelion change for the Kepler problem for the Mercury-Sun system. For each time step of integration we determine the angle and the distance from the central body (the blue points), using the 2nd order Runge-Kutta method. We then fit a parabola through these points, and the minimum of the distance to the Sun is the red point (perihelion point). Note that the red point is very slightly to the left of 0 and shows the spurious perihelion shift due to the time integration imprecisions. We use this method to find the perihelion shift and to decrease the errors we take average over three revolutions. 192

6.2 Achievable precision for different integrators, as a function of step size h. Shown is the absolute value of the perihelion shift for the Mercury-Sun problem. To make relativistic corrections distinguishable, only points in the green region are good enough. The data points correspond to 1/3 of the advance after 3 rotations. . . 193

6.3 **Left**: The absolute value of the perihelion shift as a function of the normalized relativistic parameter $\beta = \Upsilon/\Upsilon_0$, where Υ_0 is the relativistic parameter for Mercury-Sun. The red region shows where the method will fail to discriminate the relativistic perihelion advance from the integration errors (for the chosen step size of $h = 0.0002$). In the green region one can safely use the method, for that specific orbit. When increasing β, the numerical perihelion shift increases, as according to (6.6) the velocity of the object in the perihelion point scales like $\sqrt{\Upsilon}$, while the perihelion distance scales like $\frac{1}{\Upsilon}$. In all the methods the slope of the curve is higher than the slope of the relativistic advance curve $\Delta\varphi \sim \Upsilon$, which shows that for the orbits with large relativistic parameters, one has to choose the method and the time step very carefully. **Right**: The same representation as a function of eccentricity e. In all the methods, by increasing the eccentricity the numerical perihelion variation increases, as according to the (6.7) the velocity of the object and perihelion distance rescales respectively by $\sqrt{\frac{1+e}{1+e_0}}$ and $\frac{1-e}{1-e_0}$. In order to be able to measure the relativistic perihelion advance at each eccentricity we need to use the method with the appropriate step size, for example Euler and second order Runge-Kutta do not work for any eccentricity, while leapfrog is good for $e \lesssim 0.5$ and fourth order Runge-Kutta works perfectly for all eccentricities. All data points correspond to 1/3 of the advance after 3 rotations 195

6.4 Notation for a plaquette on the unit mesh in ^{2}. 196

6.5 **Left**: Linear interpolation: The advance of the perihelion due to the discretization effect depends on the initial angle of the perihelion. For each value of dx, we show the deviation in radians, divided by dx. The curves clearly coincide. This shows that the deviations scale linearly with dx. **Right**: Bilinear interpolation: We consider the perihelion shifts, divided by $dx^{1.3}$, for 180 equally spaced initial angles of the orbit. The bar graphs show the distribution of these quantities, for various choices of dx. We see that they obey a Gaussian fit (the solid lines). This shows that the shifts are random. 199

6.6 Dependence of the standard deviation of the perihelion shift for the two methods, as a function of dx. For the bilinear method, numerical fluctuations are too large to get reliable results for $dx \lesssim 10^{-3}$. The grey regions around the fitted blue and magenta lines show the 50% deviation from the central fit value. 200

6.7 Comparison of linear vs. bilinear interpolation. **Left**: Behavior as a function of the theoretical relativistic parameter β. The green line shows the relativistic perihelion advance and therefore the green/magenta area determines the regions for β where one can/-cannot detect the perihelion advance. Note that for the parameters e, dx, and N_{grid} used in the figure, no method is able to detect relativistic corrections. **Right:** The same study, now as a function of eccentricity e. According to the green/magenta regions the relativistic effects can not be detected for the choice of β, dx, and N_{grid}. 200

6.8 Some examples of the parameterization of elliptic orbits, which show the role of $\beta = \Upsilon/\Upsilon_0$, e, and θ. The orbits are obtained by solving the differential equations. 205

7.1 Relative difference between the matter power spectra produced by the parametrised (Eq. (7.11)), and exact (Eq. (7.9)) `MG-evolution` implementations of the Yukawa suppression in linearised $f(R)$ gravity for redshifts $z = 0$ (*left panels*) and $z = 1$ (*right panels*) and three different values of the interpolation parameter b. The simulations are run for $\bar{f}_{R0} = -10^{-5}$ (*top panels*) and $\bar{f}_{R0} = -10^{-6}$ (*bottom panels*). The value $b = 3$ provides a good match of the parametrised simulations to the exact implementation. 218

7.2 Same as Fig. 7.1 but for chameleon $f(R)$ gravity with comparison of the parametrised `MG-evolution` simulations against the exact model simulations [Cataneo et al., 2019]. The parametrised simulations were run for four different values each of the interpolation parameter b and the environmental suppression scale k_{env}, where the corresponding comoving top-hat radius was fixed to $r_{\text{th}} =$ 7 Mpc/h. *Top panel*: For the values ($b = 1.1$, $k_{\text{env}} = 0.16$ h/Mpc) at $z = 0$ and ($b = 1.7$, $k_{\text{env}} = 0.2$ h/Mpc) at $z = 1$ we find a $\sim 1\%$ match over all scales to $k = 2.5$ h/Mpc. *Bottom panel*: A match of $\sim 1\%$ is found for ($b = 5.0$, $k_{\text{env}} = 0.1$ h/Mpc) at $z = 0$ and ($b = 6.0$, $k_{\text{env}} = 0.005$ h/Mpc) at $z = 1$. 219

7.3 Same as Fig. 7.2 but for nDGP gravity. *Top panels*: Comparison for the model parameter $H_0 r_c = 0.5$ for four different values of the effective Vainshtein wavenumber k_* at $z = 0$ (*left panel*) and $z = 1$ (*right panel*). The value $k_* = 1.6$ h/Mpc at $z = 0$ and $k_* =$ 2.7 h/Mpc at $z = 1$ recovers the exact simulations at percent level across all scales to $k = 2.5$ h/Mpc. *Bottom panels*: Comparison for $H_0 r_c = 2.0$ for four different values of k_* at $z = 0$ (*left panel*) and $z = 1$ (*right panel*). The values $k_* = 1.1$ h/Mpc at $z = 0$ and $k_* = 2.0$ h/Mpc at $z = 1$ provide sub-percent level matches. . . . 222

8.1 This figure exemplifies that the turn-around radius is hard to identify uniquely. The green dots represent all particles out to 10 virial radii around a large galaxy cluster. The central blue region is one virial radius, and the red circle is a guide-the-eye line. The red, triangular symbols represent galaxies which happen to have zero radial velocity with respect to the central galaxy cluster. The corresponding radius is the turn-around radius. Along directions with massive substructures the potential is highly non-trivial (and non-spherical) and hence the turn-around radius depends on the direction in which it is measured. Left panel: The zero radial velocity galaxies (colour-coded red) are selected from a thin slice perpendicular to the line-of-sight. Right panel: All the (almost spherically distributed) galaxies with zero radial velocity are colour-coded red. 232

8.2 Peculiar velocity as a function of radial distance. The 49 green lines each represent particles in a cone on the sky. The solid red curve is the spherical average. This cluster is particularly well behaved and equilibrated. Within approximately 1 virial radius the average radial velocity is zero, and therefore eq. (3.1) tells us that the peculiar velocity on average exactly cancels the Hubble expansion. Between approximately 1 and 3 virial radii there is infall towards the galaxy cluster (the total radial velocity is negative), and toward larger radii the peculiar velocity transitions slowly to zero. 235

8.3 Peculiar velocity as a function of radial distance. The 49 lines each represent particles in a cone on the sky. Many of the directions are seen to behave similarly at large distances, however, a few directions stand out: A few directions (red) even have positive peculiar velocities, and a few have a clear transition (blue, here transitioning between 6 and 8 virial radii). These non-trivial peculiar velocity profiles arise because of massive sub-structures perturbing the overall potential. 236

8.4 The spatial distribution of the particles belonging to the peculiar velocity profiles of figure 8.3. Some of the particles at 4 o'clock even have positive peculiar velocities. 237

8.5 The measured turn-around radius as a function of virial mass for 100 massive galaxy clusters from a ΛCDM simulation. The data can be approximated with a line of the shape in equation (8.5) using $r_{15} = 5.2 \pm 0.1$ and $\alpha_r = -0.74 \pm 0.4$. 238

8.6 The relative error-bars on the turn-around radius as a function of mass for a ΛCDM simulation. The figure shows the symmetrized error-bars divided by the central value of r_{ta}. 238

8.7 ΛCDM v.s. k-essence with $w = -0.9$ and $c_s^2 = 1$ (corresponding to a quintessence model). The turn-around radius for the quintessence model with $w = -0.9$ (red symbols, red solid line) is seen to have essentially the same dependence on mass as ΛCDM (blue symbols, blue dashed line). These two models cannot be distinguished when measuring the turn-around radius for 100 galaxy clusters. 243
8.8 ΛCDM v.s. scalar dark sector interaction (SDSI). The turn-around radius for the SDSI model (red symbols, red solid line) is seen to have moved to slightly higher turn-around radius for the same mass, when compared to ΛCDM (blue symbols, blue dashed line). The SDSI mass-dependence of the virial mass may be approximated with a straight line of the form in equation (8.5), using $r_{15} = 5.4 \pm 0.08$ and $\alpha_{\mathrm{r}} = -0.7 \pm 0.3$. Measuring the turnaround radius for approximately 100 clusters will allow one to distinguish the two cosmologies. 244

LIST OF TABLES

1.1 A table showing the order of perturbative quantities we consider to obtain the equations in the weak field regime. This table is similar to the table in Adamek et al. [2016a] which is the framework used in the gevolution N-body code. 22

1.2 The dictionary to translate the expressions from one to the other notation. 37

2.1 Values of the cosmological parameters used in this paper. In particular, n_s and A_s are respectively the spectral index and amplitude of the primordial scalar fluctuations; $\Omega_{\rm b}$, $\Omega_{\rm CDM}$ and $\Omega_{\rm DE}$ are the critical densities, respectively of baryons, CDM and dark energy; $h \doteq H_0/(100\,{\rm Km}\,s^{-1}{\rm Mpc}^{-1})$ is the reduced Hubble constant; N_ν is the Standard Model effective number of neutrino species while w is the equation of state of dark energy. We also consider pivot wavenumber $k_p = 0.05$ Mpc^{-1}. 59

4.1 Parameter values fitted to k-evolution results for both speeds of sound at two redshifts, $z = 0$ and $z = 1$. 147

8.1 The table shows the full information of the simulations, the red color shows where the parameters are changed in different simulations. In the absence of baryons the scalar dark sector interaction (SDSI) model matches a linearised Hu-Sawicki ($n = 1$) f(R) gravity model with $\chi_0 = |f_{R0}|$. Note that the imaginary sound speed for k-essence is simply chosen to maximise phenomenological modifications in the simulations. 242

CONTENTS

1 Introduction 1
1.1 The isotropic and homogenous Universe 4
1.1.1 The geometrical properties of the FLRW metric 6
1.2 The cosmological dynamics 8
1.2.1 The stress energy tensor 9
1.2.2 Friedmann Equations 10
1.2.3 The Hubble Law and cosmic redshift 11
1.2.4 Comoving distance 12
1.3 The cosmological perturbation theory 12
1.3.1 Short wave corrections 20
1.4 Measures of inhomogeneity 23
1.5 Dark energy and modified gravity 25
1.6 The Effective Field Theory of Dark Energy 27
1.6.1 Geometrical quantities 28
1.6.2 ADM coordinates 30
1.6.3 General Lagrangian in unitary gauge 32
1.6.4 Cosmology: Background evolution 33
1.6.5 Cosmology: The EFT quadratic action 35
1.6.6 Evolution of the cosmological perturbations 37
1.6.7 Evolution of linear perturbations in Newtonian gauge . . . 38
1.6.8 Short-wave corrections 40
1.7 Cosmological N-body simulations 41
1.7.1 Physical requirements 43
1.7.2 Newtonian N-body codes 45
1.7.3 Relativistic N-body codes 45

2 k-evolution: a relativistic N-body code for clustering dark energy 49
2.1 Introduction 50

2.2 The EFT of k-essence . . . 51
    2.2.1 The action and the homogeneous equations . . . 52
    2.2.2 Stückelberg trick to conformal time . . . 53
    2.2.3 Perturbations . . . 55
    2.2.4 Implementation . . . 58
2.3 Numerical results for power spectra . . . 58
    2.3.1 k-evolution versus `CLASS` . . . 60
    2.3.2 k-evolution versus *gevolution* 1.2 using its `CLASS` interface . 67
    2.3.3 Newtonian simulations with "back-scaled" initial conditions 75
2.4 Snapshot analysis . . . 76
2.5 Conclusions . . . 77
2.A Stress-energy conservation and the π equation of motion . . . 84
2.B Numerical implementation . . . 86
2.C Initial conditions and gauge transformations . . . 87
2.D Limit of small speed of sound c_s^2 . . . 90
2.E Supplementary materials . . . 92

3 Clustering dark energy imprints on cosmological observables of the gravitational field 95
3.1 Introduction . . . 96
3.2 Theory . . . 98
3.3 Observables . . . 103
    3.3.1 Weak gravitational lensing . . . 104
    3.3.2 Integrated Sachs-Wolfe and non-linear Rees-Sciama effect . 107
    3.3.3 Gravitational redshift . . . 108
    3.3.4 Shapiro time delay . . . 109
3.4 Simulations . . . 111
3.5 Numerical results . . . 113
    3.5.1 Weak gravitational lensing . . . 118
    3.5.2 ISW-RS effect . . . 119
    3.5.3 Gravitational redshift . . . 122
    3.5.4 Shapiro time delay . . . 124
3.6 Conclusion . . . 124
3.A Convergence test . . . 129
3.B Non-linear Rees-Sciama effect . . . 129

4 Parametrising non-linear dark energy perturbations 133
4.1 Introduction . . . 134
4.2 The k-essence model . . . 135
4.3 Numerical results . . . 138
    4.3.1 The k-evolution code . . . 138
    4.3.2 Sources to the Hamiltonian constraint . . . 139

4.3.3 Linear versus non-linear $\mu(k,z)$ 143
4.3.4 A fitting function for μ in k-essence 145
4.4 Applications of $\mu(k,z)$ 147
4.4.1 Improving linear Boltzmann codes and Fisher forecasts with a parametrised μ 147
4.4.2 Improving Newtonian simulations 148
4.5 Conclusions 149
4.A Discussion about N-body gauge 150
4.B Details of the fitting function for $\mu(k,z)$ 151
4.C Scalar-vector-tensor decomposition and notation 152

5 A new instability in clustering dark energy 157
5.1 Introduction 158
5.2 Field equations 160
5.3 Simulations 161
5.4 1+1 dimensions 166
5.4.1 Full non-linear PDE in 1+1 D 167
5.4.2 Simplified PDE 169
5.4.3 Simplification 170
5.4.4 Solution to the simplified PDE 172
5.4.5 An example 175
5.4.6 Spherically symmetric case 177
5.4.7 Numerical studies in 1+1 D 177
5.A Linear equation 184

6 The detection of relativistic corrections in cosmological N-body simulations 185
6.1 Introduction 186
6.2 Using standard time integrators 188
6.3 Perihelion variation for time integrators with fixed time step . . . 189
6.3.1 Results for various integration schemes 191
6.4 Force interpolation 194
6.5 Discretization vs relativistic perihelion advance 197
6.6 Conclusions 199
6.A Newtonian and relativistic orbits 202
6.B The parameterization of orbits 203

7 N-body simulations for parametrised modified gravity 207
7.1 Introduction 208
7.2 Parametrising modified gravity for N-body simulations 210
7.2.1 Linear parametrisation 211
7.2.2 Nonlinear parametrisation 212

        7.2.3 Full parametrisation in Fourier space 213
        7.2.4 Implementation in N-body code 215
    7.3 Testing the N-body code 215
        7.3.1 Linearised $f(R)$ gravity 216
        7.3.2 Chameleon $f(R)$ gravity 217
        7.3.3 Normal branch DGP gravity 221
    7.4 Conclusions 224
    7.A Semi-dynamical perturbations 226
    7.B Fourier versus real space simulations 227

8 Distinguishing cosmologies using the turn-around radius near galaxy clusters 229
    8.1 Introduction 230
    8.2 Turn-around radius 231
    8.3 Finding the turn-around radius 233
    8.4 Spatial cones 234
    8.5 Various cosmologies 239
        8.5.1 Quintessence 239
        8.5.2 k-essence 239
        8.5.3 Scalar dark sector interactions 240
    8.6 Numerical simulations 241
        8.6.1 Results 242
    8.7 Conclusions 245

9 Summary and Conclusion 247
    9.1 Summary 247
    9.2 Outlook 249

Chapter 1

INTRODUCTION

The fundamental questions about the origin and evolution of the Universe, the meaning of time and the possible futures for the Universe, have long been major issues of study in the human history. Cosmology is the science[1] to systematically answer these questions through theories being tested by experiments and observations. If we look at the history of the Universe and we map it to a year, only very recently compared to the cosmic time we have been able to know how the Universe evolves and what it is made of, which makes the current millennium very special. The Fig. 1.1 shows the cosmic calendar from when the Universe (according to the currently accepted model) has been started to today approximately when I'm writing this thesis. This timeline shows how little our knowledge is as we only recently (compared to the age of Universe) had the chance to do science, especially doing cosmology and at the same time nonetheless how much we know.

Looking at Fig. 1.1 in this calendar about 0.22 cosmic seconds ago (in 1927 of Georgian calendar) based on the observations of Edwin Hubble we obtained the observational basis for the expansion of the universe. According to the Hubble-Lemaître law, objects (mainly galaxies) are moving away from us at velocities proportional to their distance. The velocity of the galaxies according to this effect has been determined by measuring the redshift, a shift to the red color in the spectrum due to the Doppler shift.

Then, in 1965, (0.12 cosmic seconds) Arno Penzias and Robert Woodrow Wilson, by chance detected the cosmic microwave background (CMB) radiation.[2] Afterward several surveys have been launched, including NASA Cosmic Background Explorer (COBE) satellite that orbited in (1989-1996 /0.07-0.05 cosmic seconds) which detected the large scale anisotropies of the CMB with a low resolution. In 1998 (0.05 cosmic seconds) we have obtained evidence for dark energy Perlmutter et al. [1999], Riess et al. [1998a], an unknown component which is responsible for the accelerated expansion of the Universe. In 2001 (0.04 cosmic second), NASA launched WMAP, to make more precise measurements of the CMB anisotropies over the full sky. Finally, the most precise CMB space mission, Planck was launched in 2009.

---

[1] Science: An attempt to systematically model the structure and evolution of a system. Falsifiability and validity through experiment and observation are the key properties that a model has to possess.

According to all of these observations the standard model of cosmology ΛCDM (or the cosmological constant cold dark matter) with 6 parameters and with an initial conditions of almost Gaussian nature, has by far been the simplest model that successfully predicts and explains the cosmological and astronomical observations. The important properties that either are predicted or explained by the standard model of cosmology are Durrer [2015]

- The observed abundances of elements in the Universe, mainly hydrogen, deuterium, helium, and lithium
- The statistics of the large scale structure of the Universe
- The existence of the CMB and its anisotropies
- The observed late time accelerated expansion of the Universe

In spite of all of its successes there are still challenging questions related to the nature of dark energy of dark matter and physics of the early universe. Among these we can point out some of the most significant ones as follows (see e.g. Bullock & Boylan-Kolchin [2017], Del Popolo & Le Delliou [2017] for a review), which are still unknown.

- The cosmological constant problems, including the fine tuning problem and the cosmic coincidence problem.
- The tensions between low and high redshift observations, e.g. between the 2013 Planck parameters and σ_8 obtained from the large scale structure data, tension in the value of H_0 from Planck with type one Supernovae data, tension between The Planck 2015 data and CFHTLenS weak lensing.
- low-ℓ (large angle) anomalies in the WMAP and Plank CMB data, e.g. a quadrupole-octuple alignment, a power hemispherical asymmetry and a cold spot.

---

[2] photons reaching us from an early stage of the universe.

- The small scales problems like,
    - the core/cusp problem,
    - the missing satellite problem,
    - the angular momentum catastrophe,

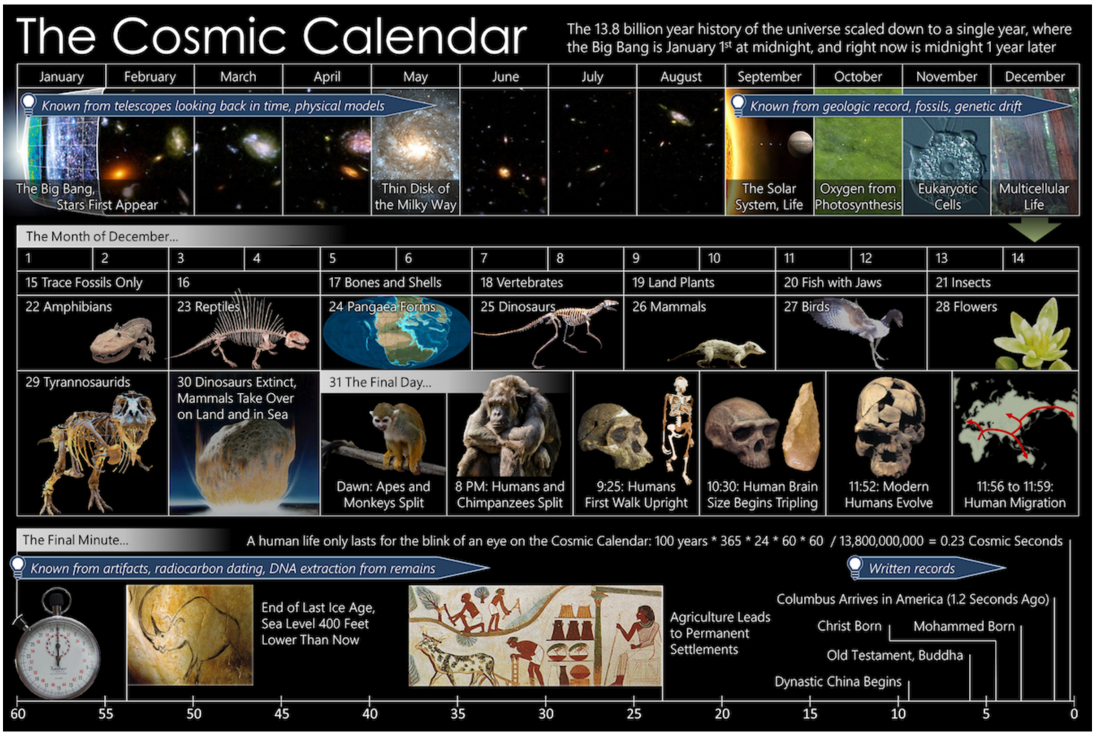
The Cosmic Calendar
The 13.8 billion year history of the universe scaled down to a single year, where the Big Bang is January 1st at midnight, and right now is midnight 1 year later
January
February
March
April
May
June
July
August
September
October
November
December
Known from telescopes looking back in time, physical models
Known from geologic record, fossils, genetic drift
The Big Bang, Stars First Appear
Thin Disk of the Milky Way
The Solar System, Life
Oxygen from Photosynthesis
Eukaryotic Cells
Multicellular Life
The Month of December...
1
2
3
4
5
6
7
8
9
10
11
12
13
14
15 Trace Fossils Only
16
17 Bones and Shells
18 Vertebrates
19 Land Plants
20 Fish with Jaws
21 Insects
22 Amphibians
23 Reptiles
24 Pangaea Forms
25 Dinosaurs
26 Mammals
27 Birds
28 Flowers
29 Tyrannosaurids
30 Dinosaurs Extinct, Mammals Take Over on Land and in Sea
31 The Final Day...
Dawn: Apes and Monkeys Split
8 PM: Humans and Chimpanzees Split
9:25: Humans First Walk Upright
10:30: Human Brain Size Begins Tripling
11:52: Modern Humans Evolve
11:56 to 11:59: Human Migration
The Final Minute...
A human life only lasts for the blink of an eye on the Cosmic Calendar: 100 years * 365 * 24 * 60 * 60 / 13,800,000,000 = 0.23 Cosmic Seconds
Known from artifacts, radiocarbon dating, DNA extraction from remains
Written records
End of Last Ice Age, Sea Level 400 Feet Lower Than Now
Agriculture Leads to Permanent Settlements
Columbus Arrives in America (1.2 Seconds Ago)
Christ Born
Mohammed Born
Old Testament, Buddha
Dynastic China Begins
60
55
50
45
40
35
30
25
20
15
10
5
0

© Eric Fisk Wikipedia contributors [2020a]

Figure 1.1: A graphical view of the Cosmic Calendar, from the early Universe to today mapped into a year,

The reason for the observed accelerating expansion of the Universe are among the most important mysteries in cosmology, and probably in theoretical physics. Although ΛCDM is a successful model which agrees well with the current cosmological observations, Λ (the cosmological constant) is not a well motivated parameter by any fundamental theory and it suffers from severe problems including fine-tuning of the initial conditions of the Universe and the coincidence problem (for a review of the cosmological constant problems see e.g. [Martin, 2012a]). These theoretical issues of Λ and the aforementioned tensions in the ΛCDM model that have emerged over the past years have encouraged cosmologists to propose an abundance of dark energy (in the form of an additional "dark" fluid with negative pressure or a scalar field) and modified gravity models (in the form of a general relativity modification) to explain the late-time accelerating expansion [Clifton et al., 2012a, Joyce et al., 2016a]. Due to the large number of possible modified gravity and dark energy theories, the effective field theory (EFT) approach and the parametrization frameworks have been developed and have become most-liked over the past years.

In this thesis, toward understanding the nature of cosmic acceleration we explore various effects coming from dark energy and modified gravity models well into the nonlinear regime. We use the EFT framework in Chapters 2, 4, 8, 3 and 5 to study the so called k-essence theory in the EFT form. Furthermore, we use the parametrization framework in Chapter 7 and 8 to explore the numerous cosmological implications from the possible modifications of gravity.

In the following subsections we will review the standard materials and techniques that will be useful for the rest of the thesis. In Sections 1.1 and 1.2 we discuss the standard model of cosmology at the background level, i.e. considering a spatially maximally symmetric Universe. In Section 1.3 we study the cosmological perturbation theory around a homogenous and isotropic background. The Section 1.4 is devoted to the practical tools in order to statistically measure the properties of inhomogeneities in the Universe. In Section 1.5 we will have a brief look on the idea of dark energy and modified gravity models and in Section 1.6, in detail, we discuss the effective field theory approach. In Section 1.7 we talk about the cosmological N-body simulations and why they are important to cosmology.

1.1 The isotropic and homogenous Universe

The simplest model that one can consider for the Universe is obtained using the homogeneity and isotropy assumptions of the matter[3] distribution. According to Einstein's field equations the geometric property of the Universe is defined based on the matter distribution. As a result the 3 dimensional space should also be homogenous and isotropic, in other words any geometrical quantity on the constant time manifolds, for example the 3D Ricci scalar and extrinsic curvature should be independent of the position and direction. However, this of course does not necessarily hold for the 4D geometrical objects like the 4D Ricci scalar as they can be time dependent (for a detailed discussion see e.g. Amendola & Tsujikawa [2010], Dodelson [2003], Durrer [2008], Padmanabhan [1996], Padmanabhan [2000], Padmanabhan [2002, 2010], Weinberg [2008])

The assumption of 3D isotropy and homogeneity defines a set of equivalent observers, the special observer who sees the Universe homogenous and isotropic.

---

[3] dark matter, dark energy and radiation.

Other observers that have a relative velocity with respect to these observers or using a peculiar coordinate to do measurements, they see an anisotropic and inhomogeneous Universe. We, for example, are among these "bad" observers that see the Universe anisotropic, because according to our relative velocity we see the cosmic microwave background radiation anisotropic (we see a dipole in the CMB which is detected by Plank, WMAP and COBE satellite).

Considering the coordinate (t, x^α) for the special observers (who sees the Universe isotropic and homogenous) we can write a general space-time interval as following,

$$ds^2 = g_{\mu\nu}dx^\mu dx^\nu = -g_{00}dt^2 - 2g_{0i}dtdx^i + \sigma_{ij}dx^i dx^j, \tag{1.1}$$

where σ_{ij} is the spatial part of the line element. We are going to simplify the line element according to the symmetries we have. The isotropy of the Universe implies that $g_{0i} = 0$ since a non-zero value of these elements means that the measured quantity, and as a result, the geometrical objects depend on the direction of measurement. Moreover if we use the proper time of clocks carried by these observers we have $g_{00} = 1$. The line element then is written as,

$$ds^2 = -dt^2 + \sigma_{ij}dx^i dx^j. \tag{1.2}$$

At any time the three-metric σ_{ij} is homogenous and isotropic. According to the isotropic assumption which is equivalent to the spherical symmetry in the three-metric we can write,

$$\sigma_{ij}dx^i dx^j = a(t)^2\left[\lambda^2(r)dr^2 + r^2\left(d\theta^2 + \sin^2\theta d\phi^2\right)\right]. \tag{1.3}$$

Now we can use the three dimensional Ricci scalar and the symmetries to simplify the previous expression. The 3D Ricci scalar, or the scalar curvature, reads

$$\begin{aligned} {}^3R = \sigma^{ij}R_{ij} =& \sigma^{ij}\left[\frac{\partial\Gamma^l_{ij}}{\partial x^l} - g^{ij}\frac{\partial\Gamma^l_{il}}{\partial x^j} + \sigma^{ij}\Gamma^l_{ij}\Gamma^m_{lm} - \sigma^{ij}\Gamma^m_{il}\Gamma^l_{jm}\right] \\ =& \frac{3}{2a^2r^3}\frac{d}{dr}\left[r^2\left(1 - \frac{1}{\lambda(r)^2}\right)\right], \end{aligned} \tag{1.4}$$

where for $i, j, l = 1, 2, 3$[4] and the Christoffel symbols Γ^i_{jk} on the 3D hypersurfaces are defined as,

$$\Gamma^i_{jk} = \frac{1}{2}g^{il}\left(-\frac{\partial g_{lj}}{\partial x^k} + \frac{\partial g_{kl}}{\partial x^j} + \frac{\partial g_{jk}}{\partial x^l}\right). \tag{1.5}$$

The homogeneity implies that ${}^3R$ as a three dimensional geometrical object should be independent of the position (here r), i. e. ${}^3R$ should be a constant.

$$\frac{3}{2a^2r^3}\frac{d}{dr}\left[r^2\left(1 - \frac{1}{\lambda(r)^2}\right)\right] = \text{const.} \tag{1.6}$$

---

[4] According to our convention the Greek letters indices span the space-time coordinates (0,...,3) and the latin letters indices span the space coordinates (1, . . . , 3)

Integrating over r results in,

$$r^2\left(1-\frac{1}{\lambda(r)^2}\right)=c_1r^4+c_2, \tag{1.7}$$

where c_1 and c_2 are constants. Avoiding a singularity at $r=0$ implies $c_2=0$, and thus we have

$$\lambda^2=\frac{1}{(1-c_1r^2)}\,. \tag{1.8}$$

When $c_1\neq 0$ we can rescale r to have $c_1=+1$ or $c_1=-1$ and the full metric reads,

$$ds^2=-dt^2+a(t)^2\left[\frac{dr^2}{1-kr^2}+r^2\left(d\theta^2+\sin^2\theta d\phi^2\right)\right], \tag{1.9}$$

where $a(t)$ scales the spatial metric and is called the scale factor. The previous metric is called the Friedmann-Lemaitre-Robertson-Walker (FLRW) metric which is an exact solution of Einstein's field equations and it describes a spatially maximally symmetric (isotropic and homogeneous) universe. The spatial hypersurfaces of the FLRW metric have positive, zero and negative curvature for respectively $k=+1$, $k=0$ and $k=-1$.

1.1.1 The geometrical properties of the FLRW metric

In order to have a geometrical intuition of the FLRW metric it is better to use the following coordinate for different values of the spatial curvature k

$$\chi=\int\frac{dr}{\sqrt{1-kr^2}}=\begin{cases}\sin^{-1}(r) & k=1\\ r & k=0\\ \sinh^{-1}(r) & k=-1\end{cases}, \tag{1.10}$$

moreover, we change the time coordinate from the real time to the conformal time defined by $d\tau=dt/a(t)$. Then the metric reads,

$$ds^2=a(\tau)^2\left[-d\tau^2+d\chi^2+f^2(\chi)\left(d\theta^2+\sin^2\theta d\phi^2\right)\right], \tag{1.11}$$

where f is

$$f(\chi)=\begin{cases}\sin(\chi) & k=1\\ \chi & k=0\\ \sinh(\chi) & k=-1\end{cases}. \tag{1.12}$$

The metric in (1.11) is especially useful since the curvature has gone into the angular part of the metric, so we can more easily study the distances. Let us now study the geometrical properties of this metric for different values of k.

For $k = 0$ the spatial part of the metric represents the flat Euclidian three-dimensional space. For $k = 1$, the spatial part of the metric describes a three sphere of radius a embedded in a flat four dimensional Euclidian space. We can show such a 3-Sphere as,

$$x_1^2 + x_2^2 + x_3^2 + x_4^2 = a^2, \tag{1.13}$$

where x_i are the cartesian coordinates of the four dimensional space. The metric on the 3-Sphere embedded in the higher dimension is written as

$$dL^2 = dx_1^2 + dx_2^2 + dx_3^2 + dx_4^2\,. \tag{1.14}$$

We can express the 3-Sphere by three angular coordinates (γ, θ, ϕ) instead, defined by

$$\begin{aligned} x_1 &= a\cos\gamma\sin\theta\sin\phi, \quad x_2 = a\cos\gamma\sin\theta\cos\phi, \\ x_3 &= a\cos\gamma\cos\theta, \quad x_4 = a\sin\gamma. \end{aligned} \tag{1.15}$$

Substituting the new coordinate in the metric (1.14) we obtain

$$dL^2 = a^2\left[d\gamma^2 + \sin^2\gamma\left(d\theta^2 + \sin^2\theta d\phi^2\right)\right], \tag{1.16}$$

which is the same expression as (1.9) for $k = 1$. In fact the whole space of a positive curvature model is covered by the angle ranges $0 \le \gamma \le \pi;\ 0 \le \theta \le \pi;\ 0 \le \phi < 2\pi$ in which results to a finite volume:

$$V = \int_0^{2\pi} d\phi \int_0^{\pi} d\theta \int_0^{\pi} d\gamma\sqrt{\sigma} = a^3 \int_0^{2\pi} d\phi \int_0^{\pi} \sin\theta d\theta \int_0^{\pi} \sin^2\chi d\chi = 2\pi^2 a^3, \tag{1.17}$$

where σ is the determinant of the 3D metric.

In the case of $k = -1$ we have a hyperboloid geometry embedded in a four-dimensional Lorentzian space. The line element in Lorentzian space is

$$dL^2 = dx_1^2 + dx_2^2 + dx_3^2 - dx_4^2\,. \tag{1.18}$$

On the other hand a three-dimensional hyperboloid embedded in a 4D Lorentzian space is represented by the relation

$$x_4^2 - x_1^2 - x_2^2 - x_3^2 = a^2. \tag{1.19}$$

Like the 3-Sphere we can represent this hyperboloid with 3 angles (γ, θ, ϕ) defined by

$$\begin{aligned} x_1 &= a \sinh \chi \sin \theta \sin \phi, \quad x_2 = a \sinh \chi \sin \theta \cos \phi \,, \\ x_3 &= a \sinh \chi \cos \theta, \quad x_4 = a \cosh \chi \,, \end{aligned} \tag{1.20}$$

which by substituting to the line element we can see that this metric corresponds to the FLRW metric with $k = -1$. An important point about this space is that γ is not bounded anymore and the angles ranges are $0 \leq \phi \leq 2\pi$; $0 \leq \theta \leq \pi$; $0 \leq \gamma \leq \infty$. This space, unlike the positive curvature space, has an infinite volume.

From now on during this thesis we alway assume $k = 0$ which is consistent with the cosmological observations.

1.2 The cosmological dynamics

Using the line element written for the maximally symmetric Universe (1.9) we obtain the cosmological dynamics by solving the Einstein equations,

$$G^{\mu}_{v} = 8\pi G T^{\mu}_{v} \,, \tag{1.21}$$

where T^{μ}_{v} is the energy momentum of the components and G^{μ}_{v} is the Einstein tensor and is defined by the Ricci scalar and the Ricci tensor:

$$G_{\mu\nu} \equiv R_{\mu\nu} - \frac{1}{2} g_{\mu\nu} R \,. \tag{1.22}$$

The Christoffel symbols, the Ricci scalar and the the Ricci tensor are defined similar to the their 3D versions in (1.5) and (1.4) while now the indices span the space-time coordinates,

$$\Gamma^{\rho}_{\mu\nu} \equiv \frac{g^{\rho\lambda}}{2} \left(\partial_{\mu} g_{\nu\lambda} + \partial_{\nu} g_{\mu\lambda} - \partial_{\lambda} g_{\mu\nu} \right) \,, \tag{1.23}$$

$$R_{\mu\nu} \equiv \partial_{\alpha} \Gamma^{\alpha}_{\mu\nu} - \partial_{\nu} \Gamma^{\alpha}_{\mu\alpha} + \Gamma^{\alpha}_{\beta\alpha} \Gamma^{\beta}_{\mu\nu} - \Gamma^{\alpha}_{\beta\nu} \Gamma^{\beta}_{\mu\alpha} \,, \tag{1.24}$$

$$R \equiv R^{\mu}_{\mu} = g^{\mu\nu} R_{\mu\nu} \,. \tag{1.25}$$

The left hand side of the Einstein equation (1.22) specifies the geometric properties of the space-time and the right hand side characterizes the energies and momenta of the particles. For the FLRW metric with zero curvature $k = 0$ the

Christoffel symbols $\Gamma^{\rho}_{\mu\nu}$ using the Eq. (1.23) are:

$$\begin{aligned}
&\Gamma^0_{00} = 0, \quad \Gamma^0_{0i} = \Gamma^0_{i0} = 0, \\
&\Gamma^0_{ij} = a\dot{a}\,\delta_{ij}, \quad \Gamma^i_{0j} = \Gamma^i_{j0} = \tfrac{\dot{a}}{a}\delta^i_j, \\
&\Gamma^1_{11} = 0, \quad \Gamma^1_{22} = -r, \quad \Gamma^1_{33} = -r\sin^2\theta, \\
&\Gamma^2_{33} = -\sin\theta\cos\theta, \quad \Gamma^2_{12} = \Gamma^2_{21} = \Gamma^3_{31} = \Gamma^3_{13} = \tfrac{1}{r}, \\
&\Gamma^3_{23} = \Gamma^3_{32} = \cot\theta,
\end{aligned} \tag{1.26}$$

where $\dot{a} \equiv \frac{da}{at}$ and t is the cosmic time. Note that $g_{\alpha\nu}$ satisfies the relation $g^{\mu\rho}g_{\rho\nu} = \delta^{\mu}_{\nu}$, where δ^{ν}_{μ} is Kronecker's delta $\left(\delta^{\nu}_{\mu} = 1 \text{ for } \mu = \nu \text{ and } \delta^{\nu}_{\mu} = 0 \text{ for } \mu \neq \nu\right)$. Unlike the Kronecker's delta $\delta_{\mu\nu}$ is not a tensor [5], however it shares similar properties i. e. ($\delta_{\mu\nu} = 1$ for $\mu = \nu$ and $\delta_{\mu\nu} = 0$ for $\mu \neq \nu$) which is useful to write the results in a compact way. The Ricci tensor and the Ricci scalar are computed by equations (1.24) and (1.25)

$$R_{00} = -3\left(H^2 + \dot{H}\right), \quad R_{0i} = R_{i0} = 0, \quad R_{ij} = a^2\left(3H^2 + \dot{H}\right)\delta_{ij}\,, \tag{1.27}$$

$$R = 6\left(2H^2 + \dot{H}\right)\,, \tag{1.28}$$

where $H \equiv \dot{a}/a$ is the Hubble parameter and represents the expansion rate of the Universe. The Einstein tensor components, using the equation (1.22) reads

$$G^0_0 = -3H^2, \quad G^0_i = G^i_0 = 0, \quad G^i_j = -\left(3H^2 + 2\dot{H}\right)\delta^i_j\,, \tag{1.29}$$

where we have used $G^{\mu}_{\nu} = g^{\mu\alpha}G_{\alpha\nu}$.

1.2.1 The stress energy tensor

The stress energy tensor contains all the information about the energy content of the Universe. This tensor is symmetric as a result of the Einstein equation and the symmetry of the Einstein tensor $G_{\mu\nu}$. The assumption of isotropy and homogeneity implies that T^{μ}_0 must be zero and T^j_i must be diagonal with equal values $T^1_1 = T^2_2 = T^3_3$. Thus, in the FLRW space-time the energy-momentum tensor can only take the perfect fluid form:

$$T^{\mu}_{v} = (\rho + P)u^{\mu}u_{\nu} + P\delta^{\mu}_{v}\,, \tag{1.30}$$

where $u^{\mu} = (-1, 0, 0, 0)$ is the four velocity in the comoving coordinates, ρ and P correspond respectively to the density and the pressure of the perfect fluid.

---

[5] Under coordinate transformation this object does not transform correctly.

1.2.2 Friedmann Equations

From the $(0,0)$ and (i,i) components of the Einstein equations Eq. (1.21) we obtain,

$$H^2 = \frac{8\pi G}{3}\sum_X \rho_X \,, \tag{1.31}$$

$$3H^2 + 2\dot{H} = -8\pi G \sum_X P_X \,, \tag{1.32}$$

where the sums are over all cosmological species. Combining the two equations we can write an equation for $\ddot{a}$,

$$\frac{\ddot{a}}{a} = -\frac{4\pi G}{3}(\rho + 3P)\,, \tag{1.33}$$

which is equivalent to the continuity equation if we multiply by a^2 and take a time derivative,

$$\dot{\rho} + 3H(\rho + P) = 0\,. \tag{1.34}$$

It is worth mentioning that the equivalence of the two equations comes from the fact that the Einstein tensor satisfies the Bianchi identities, *i.e.,* the covariant derivative of the Einstein tensor vanishes, $\nabla_\mu G^\mu_\nu = 0$, and from the Einstein equations the same symmetry should be hold in the stress-energy tensor i.e., $\nabla_\mu T^\mu_\nu = 0$. The conservation of the stress-energy tensor gives the same equation as Eq. (1.34) in the FLRW background. That is why the equation (1.34) is called the conservation or continuity equation.

We can rewrite the first Friedman equation Eq. (1.31) in the following form,

$$\Omega_r + \Omega_m + \Omega_{DE} = 1\,, \tag{1.35}$$

where $\Omega_X \equiv \frac{8\pi G\rho_X}{3H^2}$. The density parameters respectively correspond to the relativistic particles, non-relativistic matter and dark energy. Once we have the equation of the state $P = P(\rho)$ we can solve the aforementioned equations to obtain $a(t)$, $\rho(t)$ and $P(t)$.

For a constant linear equation of state $P = w\rho$ the continuity equation Eq. (1.34) gives , $\rho \propto a^{-3(1+w)}$. As a result for non-relativistic matter $(w \simeq 0)$ $\rho_m \propto a^{-3}$, for relativistic particles $(w = 1/3)$ is $\rho_m \propto a^{-4}$ and for the cosmological constant $(w = -1)$ ρ is a constant. The negative pressure from the cosmological results in the late time cosmic acceleration which has been approved by many cosmological observations. However, the cosmic acceleration could be produced with values of w other than -1 and yet be consistent with the cosmological data. Using the density relation for each component and Eq. (1.35) we can rewrite the equation in the following form,

$$H^2 = H_0^2\left(\Omega^0_\Lambda + \Omega^0_k a^{-2} + \Omega^0_m a^{-3} + \Omega^0_r a^{-4}\right), \tag{1.36}$$

where H_0 is the current value of the Hubble constant.

1.2.3 The Hubble Law and cosmic redshift

The light emitted by a distant observer is stretched while traveling due to the expansion of the Universe. This effect is similar to the Doppler shift in the frequency of a wave in classical physics but this happens because the emitter is receding from us and according to General Relativity the cosmic expansion dilutes the photons' energy. In the 1920s Slipher and Hubble realised that the measured wavelength λ_o of absorption lines of distant astronomical objects is larger than the wavelength λ_e measured in the laboratories. We define the redshift as follows

$$z \equiv \frac{\lambda_o}{\lambda_e} - 1 = \frac{a_o}{a_e} - 1\,, \tag{1.37}$$

where a_0 and a_e are respectively the scale factors at the observation time and at the emission time.

For the small values of recessional velocity v compared to the speed of light, we have $\lambda_0 \simeq (1 + v/c)\lambda_e$ from the Doppler effect which results in,

$$z \simeq v/c\,. \tag{1.38}$$

In an expansing Universe the physical r and comoving χ distances of the objects are related by the scale factor at each time,

$$\vec{r} = a(t)\vec{\chi}\,. \tag{1.39}$$

Taking the time derivative of the previous relation gives,

$$\dot{\vec{r}} = H\vec{r} + a\dot{\vec{\chi}}\,, \tag{1.40}$$

where the first term appears due to the cosmic expansion and the second term is peculiar velocity v_p and is the movement of an object with respect to the Hubble flow. It is obvious that in a maximally symmetric Universe the peculiar velocities should vanish because these velocities are different at different positions which is in contradiction with the homogeneity and isotropy of the Universe.

Slipher in 1912 for the first time measured the spectrum of a galaxy, M31, which for many years was the highest measured velocity for any object which was about -300kms^{-1}. He continued measuring velocities of "nebulas" for several years, his "catalogue" appearing in Eddington's book "The Mathematical Theory of Relativity", published in 1924.

However, only after Robertson's work, Slipher's measurement was interpreted as being due to the cosmic expansion. The main problem at the time was ignorance of the distances to the galaxies and also Robertson's work was largely diregarded.

Hubble, based on previous works, reported an extragalactic distance for 18 galaxies and was able to plot the relationship between distance and recession velocity. Most of Hubble's data for velocity came from Slipher's measurements. Hubble, in fact, wrongly interpreted the velocity-distance relationship to the de-Sitter effect in a static de Sitter Universe [6], not to cosmic expansion - Robertson had already done that. De Sitter in 1933 wrote the linear expansion law taking into account of redshift-distance relation in the de Sitter model. But then the Friedmann-Lemaître model was acknowledged by physicists. That acceptance was mainly due to the later paper of Eddington in 1930 in which he "rediscovers" the papers of Friedmann and Lemaître. This of course was after Robertson had published his paper in 1929 claiming that the redshift was due to cosmic expansion, and also after Hubble's redshift-distance relationship (see Jones [1997] for the history of cosmology).

1.2.4 Comoving distance

The lights we observe from distant objects are traveling on a light cone and satisfy the geodesic equation

$$\mathrm{d}s^2 = -c^2\mathrm{d}t^2 + a^2(t)\mathrm{d}\chi^2 = 0\,. \tag{1.41}$$

Considering the case in which light travels from $t = t_e$ at distance $\chi = \chi_e$ (redshift z) and reaches us at $t = t_o$ at $\chi = 0$ ($z = 0$), and using the line element, gives us a distance which is defined as,

$$d_c \equiv \chi_1 = \int_0^{\chi_1} d\chi = -\int_{t_0}^{t_1} \frac{c}{a(t)}\mathrm{d}t\,, \tag{1.42}$$

where d_c is called the comoving distance.

In this section we have studied a homogenous and isotropic Universe and we derived the FLRW metric and the Friedmann equations. The homogeneity and isotropy are a good approximation of the Universe at large scales. However, we know that these symmetries are not respected at smaller scales anymore and in the next section we will perturb the FLRW metric and we study the evolution of the perturbations in such an Universe.

1.3 The cosmological perturbation theory

The Friedmann model that has been discussed so far describes a maximally symmetric Universe. However we know that the Universe is not homogenous and isotropic at all scales and the presence of the structures including ourselves break the symmetry at small scales. In fact, it is believed that the structures we see in the Universe grew out of small fluctuations which originated from the early universe. In order to study the formation of such structures in the Universe, we need to understand how the small fluctuations around the maximally symmetric Universe evolve and eventually result in the non-linear structures (see Amendola & Tsujikawa [2010], Dodelson [2003], Durrer [2008], Padmanabhan [1996], Padmanabhan [2000], Padmanabhan [2002, 2010], Weinberg [2008] for a detailed discussion about the subject).

---

[6] de Sitter effect: lights emitted from particles at rest in the de Sitter static Universe are redshifted. The situation is, in fact, far more complicated than was thought and was not attributed properly until the mid 1930 's. One difficulty is that particles placed at a point in the de Sitter Universe start to also accelerate away from the reference point. This brings an additional effect to the redshift.

A metric that deviates from a maximally symmetric space can be written as the sum of an FLRW part which respects all the symmetries plus a perturbed metric;

$$g_{\mu\nu} = g^{(0)}_{\mu\nu} + \delta g_{\mu\nu}, \tag{1.43}$$

where the perturbed part is assumed to be small compared to the background metric.

In General Relativity the equations should be invariant under a general coordinate transformation. This implies that the splitting between an unpertubed metric and a perturbed one is not unique. We can of course choose a special coordinate frame and write down the equations, but it would be very confusing if we change the background metric by changing the coordinates. So we intend to keep the FLRW metric as the background whenever we make a general transformation. This procedure suggests a class of infinitesimal transformations that does not change $g^{(0)}_{\mu\nu}$, while the perturbed metric $\delta g_{\mu\nu}$ is subject to change. This class of coordinate transformations are called gauge transformations.

To be specific we consider a general coordinate transformation from the coordinate system x^μ to another $\hat{x}^\mu$ as

$$x^\mu \longrightarrow \hat{x}^\mu = x^\mu + \epsilon^\mu(x)\,. \tag{1.44}$$

The metric tensor as a result is transformed as,

$$\hat{g}_{\mu\nu}(\hat{x}) = \frac{\partial x^\lambda}{\partial \hat{x}^\mu}\frac{\partial x^\rho}{\partial \hat{x}^\nu} g_{\rho\lambda}(x)\,. \tag{1.45}$$

As discussed previously, this transformation is a pure coordinate transformation which in general changes the background and perturbation quantities. As explained above it is more convenient to work with the “gauge transformations” which only transform the perturbations. In fact after the coordinate transformation we relabel the coordinates by dropping the hat on the coordinate argument, which means that we are dealing with two different points on the manifold, since x in two coordinates are assigned with two different but near physical points. So the gauge transformation on the metric tensor results in,

$$\begin{aligned}\Delta h_{\mu\nu}(x) &\equiv \hat{g}_{\mu\nu}(x) - g_{\mu\nu}(x)\\ &= \hat{g}_{\mu\nu}\left(\hat{x}^{\kappa} - \epsilon^{\kappa}\right) - g_{\mu\nu}(x) = \hat{g}_{\mu\nu}(\hat{x}) - \partial_{\rho} g_{\mu\nu}(x)\epsilon^{\rho} - g_{\mu\nu}(x)\\ &= \frac{\partial x^{\lambda}}{\partial\left(x^{\mu}+\epsilon^{\mu}\right)}\frac{\partial x^{\rho}}{\partial\left(x^{\nu}+\epsilon^{\mu}\right)} g_{\rho\lambda}(x) - g_{\mu\nu}(x) - \partial_{\rho} g_{\mu\nu}(x)\epsilon^{\rho} - g_{\mu\nu}(x)\\ &= -\bar{g}_{\lambda\mu}(x)\frac{\partial\epsilon^{\lambda}(x)}{\partial x^{\nu}} - \bar{g}_{\lambda\nu}(x)\frac{\partial\epsilon^{\lambda}(x)}{\partial x^{\mu}} - \frac{\partial\bar{g}_{\mu\nu}(x)}{\partial x^{\lambda}}\epsilon^{\lambda}(x),\end{aligned} \tag{1.46}$$

where we have denoted the gauge transformation with Δ. It is obvious that the background metric under the gauge transformation remains unchanged as we demanded, but it may contribute in first order perturbations.

$$\Delta\bar{g}_{\mu\nu} = \hat{\bar{g}}_{\mu\nu}(t) - \bar{g}_{\mu\nu}(t) = 0 + \mathcal{O}(\epsilon)\,. \tag{1.47}$$

There are often two approaches to deal with the gauge problem in cosmology. The first is to fix a specific gauge, *i.e.,* to choose conditions on the space-time coordinates which completely remove the gauge freedom, the second is to work with a basis of gauge invariant variables, but this approach usually leads to unintuitive variables and complicated equations Brandenberger [2004]. Using the first approach (fixing a specific gauge), we can choose a specific coordinate which is called the Newtonian gauge and the observers in this gauge detect a velocity field and measure a gravitational potential. This gauge is particularly interesting as the metric tensor in this gauge is diagonal which simplifies the calculations and leads to straightforward geodesic equations. Moreover, the metric perturbation in this gauge plays the role of the gravitational potential in the Newtonian limit and as a result has a simple physical explanation. Plus, the two scalar potentials in this gauge are identical to the gauge-invariant Bardeen potentials Φ_A and Φ_H (see Ma & Bertschinger [1995a] for a discussion about the Newtonian and Synchronous gauges).

We start with the most general perturbed metric about the background FLRW written in the form $g_{\mu\nu} = g^{(0)}_{\mu\nu} + \delta g_{\mu\nu}$ as

$$\delta g_{\mu\nu} = a(\tau)^2 \begin{pmatrix} -2\Psi & -B_i \\ -B_i & \left(-2\Phi\delta_{ij} + h_{ij}\right) \end{pmatrix}, \tag{1.48}$$

where Ψ and Φ are respectively the temporal and spatial scalar perturbations, B_i is the vector perturbation and h_{ij} is the tensor perturbation. Using the scalar-vector-tensor (SVT) decomposition we can recover the 4 scalars, 4 vectors, and two tensors degrees of freedom in the metric as we can decompose the vector perturbation part B_i into the curl-free (longitudinal) and divergence-free (transverse) components,

$$B_i = B_i^{\perp} + B_i^{\parallel} \text{ where } \vec{\nabla} \cdot B^{\perp} = \vec{\nabla} \times B^{\parallel} = 0. \tag{1.49}$$

Also we can decompose the tensor perturbations similarly,

$$h_{ij} = h_{ij}^{\parallel} + h_{ij}^{\perp} + h_{ij}^{(S)}. \tag{1.50}$$

Here,

$$h_{ij}^{\parallel} = \left(\nabla_i \nabla_j - \frac{1}{2}\delta_{ij}\nabla^2\right) \Phi^{(h)}\,, \tag{1.51}$$

where Φ_h is a scalar and we have assumed that h_{ij} is traceless a tensor, and

$$h_{ij}^{\perp} = \nabla_i h_j^{\perp} + \nabla_j h_i^{\perp} \tag{1.52}$$

where $h_i^{\perp}$ is a divergenceless vector. The two physical degrees of freedom left in the tensor modes $h_{ij}^{(S)}$ correspond to the two polarisations of gravitational waves. After the SVT decomposition we can rewrite the "scalar" perturbations of the metric in the following form,

$$\delta g_{\mu\nu} = a^2(\tau) \begin{pmatrix} -2\Psi & -B_{,i} \\ -B_{,i} & -2\Phi\delta_{ij} + \Phi^{(h)}_{,ij} \end{pmatrix}. \tag{1.53}$$

Fixing the gauge to the Newtonian gauge will remove two scalar degrees of freedom as we have

$$B = \Phi^{(h)} = 0. \tag{1.54}$$

At the end the line element in the Newtonian gauge is written as,

$$ds^2 = a(\tau)^2 \left[-(1+2\Psi)d\tau^2 + (1-2\Phi)\delta_{ij}dx^i dx^j\right]. \tag{1.55}$$

It is important to note that in first order perturbation theory the equations for the scalars, vectors and tensors decouple and one can study each independently. Moreover, in this section we neglect the vector and tensor perturbations since the tensorial modes are coupled to matter only for anisotropic perturbations and vectorial modes (if present initially) decay in time as $1/a$ (see for detailed discussion Amendola & Tsujikawa [2010], Dodelson [2003], Durrer [2008], Weinberg [2008] and also Chapter 4 where we discuss the generation of vector and tensor perturbations due to the non-linear structure formation).

To obtain the first order Einstein field equations we decompose the Einstein tensor and the stress energy tensor into the background and perturbed part, similar to what we did to the metric;

$$G^{\mu}_{\nu} = G^{\mu(0)}_{\nu} + \delta G^{\mu}_{\nu}\,, \quad T^{\mu}_{\nu} = T^{\mu(0)}_{\nu} + \delta T^{\mu}_{\nu}\,, \tag{1.56}$$

which help us to solve the equations perturbatively, *i.e.,*

$$G^{\mu(0)}_{\nu} = T^{\mu(0)}_{\nu}\,, \tag{1.57}$$

$$\delta G^{\mu}_{\nu} = 8\pi G \delta T^{\mu}_{\nu}\,. \tag{1.58}$$

Eq. (1.57) gives the Friedmann equations we obtained in the previous section, while Eq. (1.58) results in the equations for the evolution of the metric perturbations. To compute δG^{μ}_{ν} we need to calculate the first order geometric quantities, i.e., $\delta\Gamma^{\mu}_{\nu\lambda}$, $\delta R_{\mu\nu}$ and δR.

The perturbed Christoffel symbols $\delta\Gamma^{\mu}_{\upsilon\lambda}$ read,

$$\delta\Gamma^{\mu}_{\nu\lambda} = \frac{1}{2}\delta g^{\mu\alpha}\left(g_{\alpha\nu,\lambda} + g_{\alpha\lambda,\alpha} - g_{\nu\lambda,\alpha}\right) + \frac{1}{2}g^{\mu\alpha}\left(\delta g_{\alpha\nu,\lambda} + \delta g_{\alpha\lambda,\alpha} - \delta g_{\nu\lambda,\alpha}\right)\,. \tag{1.59}$$

Next, we have to calculate perturbations in the Ricci tensor and in the Ricci scalar;

$$\begin{aligned}
&\delta R_{\mu\nu} = \delta\Gamma^{\alpha}_{\mu\nu,\alpha} - \delta\Gamma^{\alpha}_{\mu\alpha,\nu} + \delta\Gamma^{\alpha}_{\mu\nu}\Gamma^{\beta}_{\alpha\beta} + \Gamma^{\alpha}_{\mu\nu}\delta\Gamma^{\beta}_{\alpha\beta} - \delta\Gamma^{\alpha}_{\mu\beta}\Gamma^{\beta}_{\alpha\nu} - \Gamma^{\alpha}_{\mu\beta}\Gamma^{\beta}_{\alpha\nu} \\
&\delta R = \delta g^{\mu\alpha}R_{\alpha\mu} + g^{\mu\nu}\delta R_{\alpha\mu},
\end{aligned} \tag{1.60}$$

and finally the perturbed Einstein tensors are obtained by,

$$\delta G_{\mu\nu} = \delta R_{\mu\nu} - \frac{1}{2}\delta g_{\mu\nu}R - \frac{1}{2}g_{\mu\nu}\delta R\,, \tag{1.61}$$

$$\delta G^{\mu}_{\nu} = \delta g^{\mu\nu}G_{\alpha\nu} + g^{\mu\alpha}G_{\alpha\nu}\,. \tag{1.62}$$

For the metric written in the Newtonian gauge the perturbed Einstein tensors read,

$$\begin{aligned}
\delta G^{0}_{0} =& 2a^{-2}\left[3\mathcal{H}\left(\mathcal{H}\Psi + \Phi'\right) - \nabla^2\Phi\right]\,, \\
\delta G^{0}_{i} =& 2a^{-2}\left(-\Phi' - \mathcal{H}\Psi\right)_{|i}\,, \\
\delta G^{i}_{j} =& 2a^{-2}\left[\left(\mathcal{H}^2 + 2\mathcal{H}'\right)\Psi + \mathcal{H}\Psi' + \Phi'' + 2\mathcal{H}\Phi'\right]\delta^{i}_{j}\,, \\
&+ a^{-2}\left[\nabla^2(\Psi - \Phi)\delta^{i}_{j} - (\Psi - \Phi)^{i}_{|j}\right]\,,
\end{aligned} \tag{1.63}$$

where the subscript "|" shows a 3D covariant derivative and $\nabla^2 f \equiv f^{;\lambda}_{;\lambda}$.

To write down the Einstein's equations we need to also specify the matter source and determine the perturbed energy-momentum tensor δT^{μ}_{v}, which also let us to obtain the first order continuity equation $\delta T^{\mu}_{\nu;\mu} = 0$.

To determine the perturbed stress energy tensor, we need to calculate the perturbed four-velocity $u^{\mu} \equiv \frac{\mathrm{d}x^{\mu}}{\mathrm{d}s}$. Considering only first order perturbations, we have

$$u^{\mu} = \left[\tfrac{1}{a}(1 - \Psi), \tfrac{v^i}{a}\right]\,,$$

$$u_{\mu} = g_{\mu\nu}u^{\nu} = \left[-a(1 + \Psi), av_i\right]\,,.$$

$$u_{\mu}u^{\mu} = -1\,,$$

where $v^i = \frac{\mathrm{d}x^i}{\mathrm{d}\tau} = a\frac{\mathrm{d}x^i}{\mathrm{d}t}$ is the peculiar velocity of matter with respect to the expansion. For a single fluid, the stress-energy tensor in general is given by

$$T_{\mu\nu} = (\rho + P)u_\mu u_\nu + Pg_{\mu\nu} + [q_\mu u_\nu + q_\mu u_\mu + \pi_{\mu\nu}] \,, \tag{1.64}$$

where $\rho, P, u_\mu, q_\mu, \pi_{\mu\nu}$ represents the energy density, pressure, four-velocity vector, heat flux vector and viscous shear tensor respectively. The heat flux vector and viscous shear tensor are important for fluids with sizable internal energy. However, for perfect fluids we have $q_\mu = \pi_{\mu\nu} = 0$.

The perturbed stress-energy tensor using Eq. (1.64) for a perfect fluid is written as

$$\delta T^\mu_v = \rho \left[\delta \left(1 + c_s^2\right) u_\nu u^\mu + (1 + w)\left(\delta u_\nu u^\mu + u_\nu \delta u^\mu\right) + c_s^2 \delta \ \delta^\mu_v\right] \,, \tag{1.65}$$

where $w = P/\rho$ is the equation of state and the speed of sound c_s is defined as

$$c_s^2 \equiv \frac{\delta P}{\delta \rho} = \frac{dP}{d\rho} = \frac{\dot{P}}{\dot{\rho}} \,, \tag{1.66}$$

and also we have used the following definitions for the divergence of velocity θ and the density contrast $\delta\rho/\rho \equiv (\rho(x) - \bar{\rho})/\bar{\rho}$,

$$\delta \equiv \frac{\delta\rho}{\rho}, \quad \theta \equiv \nabla_i v^i \,. \tag{1.67}$$

It is worth mentioning that in general the pressure P can depend on internal properties of the system e.g. the entropy s. Then the speed of sound is not simply $\sqrt{\dot{P}/\dot{\rho}}$ and in general is,

$$c_s^2 = \frac{\delta P(\rho, s)}{\delta\rho} = \frac{\partial P}{\partial \rho} + \frac{\partial P}{\partial s}\frac{\partial s}{\partial \rho} = c^2_{s(a)} + c^2_{s(na)} \,, \tag{1.68}$$

where $c_{s(a)} \equiv \sqrt{\dot{P}/\dot{\rho}}$ is called the adiabatic sound speed and $c_{s(na)}$ is the non-adiabatic sound speed.

The stress-energy tensor components for a perfect fluid which is assumed to remain perfect under perturbation,

$$\begin{aligned} \delta T^0_0 &= -\delta\rho \,, \\ \delta T^0_i &= -\delta T^i_0 = (1 + w)\rho v^i \,, \\ \delta T^1_1 &= \delta T^2_2 = \delta T^3_3 = c_s^2 \delta\rho \,. \end{aligned} \tag{1.69}$$

As a result, the perturbed Einstein equations using the $\delta G^{\mu}_{v} = 8\pi G \delta T^{\mu}_{v}$ are written as,

$$\begin{aligned}
&3\mathcal{H}\left(\mathcal{H}\Psi + \Phi'\right) - \nabla^2\Phi = -4\pi G a^2 \delta\rho\,, \\
&\nabla^2\left(-\Phi' - \mathcal{H}\Psi\right) = 4\pi G a^2 (1+w)\rho\theta\,, \\
&\Psi = \Phi\,, \\
&-\Phi'' - 2\mathcal{H}\Phi' - \mathcal{H}\Psi' - \left(\mathcal{H}^2 + 2\mathcal{H}'\right)\Psi = -4\pi G a^2 c_s^2 \delta\rho\,.
\end{aligned} \tag{1.70}$$

Moreover, according to the definition of covariant derivative of a tensor,

$$T^{\mu}_{\nu;\mu} = T^{\mu}_{\nu,\mu} - \Gamma^{\alpha}_{\nu\beta}T^{\beta}_{\alpha} + \Gamma^{\alpha\beta\alpha}T^{\beta\nu}_{\nu}\,. \tag{1.71}$$

The first order equation for the divergence of the stress-energy tensor for the 0th component is written as,

$$\delta T^{\mu}_{0,\mu} - \delta\Gamma^{\alpha}_{0\beta}T^{\beta}_{\alpha} - \Gamma^{\alpha}_{0\beta}\delta T^{\beta}_{\alpha} + \delta\Gamma^{\alpha}_{0\alpha}T^{0}_{0} + \Gamma^{\alpha}_{\beta\alpha}\delta T^{\beta}_{0} = 0\,, \tag{1.72}$$

which, using the expressions for the first order Christoffel symbols in Eq. (1.59), results in the first order continuity equation,

$$(\delta\rho)' + 3\mathcal{H}(\delta\rho + \delta P) = -(\rho + P)\left(\theta - 3\Phi'\right)\,, \tag{1.73}$$

in which we can write it in terms of the equation of state w, the speed of sound c_s and the density contrast as ,

$$\delta' + 3\mathcal{H}\left(c_s^2 - w\right)\delta = -(1+w)\left(\theta - 3\Phi'\right)\,. \tag{1.74}$$

The Euler equation is obtained by $\delta T^{\mu}_{\nu;\mu} = 0$ for $\nu = i$ and reads as,

$$\delta V' + 3\mathcal{H}\delta V = -a\delta P - (\rho + P)a\Psi\,, \tag{1.75}$$

where $\delta V \equiv a(\rho+P)v$ and v is the velocity potential defined by $v^i = \nabla^i\theta$. Taking the divergence of the previous expression results in the familiar form of the Euler equation,

$$\theta' + \left[\mathcal{H}(1-3w) + \frac{w'}{1+w}\right]\theta = -\nabla^2\left(\frac{c_s^2}{1+w}\delta + \Psi\right)\,. \tag{1.76}$$

The equations we have written up to now are linear partial differential equations. It is most convenient to solve these equations in the Fourier space. The reason is that in the Fourier space the resulting Fourier amplitudes lead to an ordinary differential equations which are much easier to solve than the partial differential equation in the real space for the same dynamics. It is important to note that the maximally symmetric background makes the Fourier transform useful as the background variables are only time dependent and the only $\vec{x}$ dependence is in the perturbation variables themselves. We use the following notation for Fourier transform,

$$\begin{aligned} f_{\mathbf{k}} &= A \int \mathrm{d}^3 x f(\mathbf{x}) \mathbf{e}^{-i\mathbf{k}\cdot\mathbf{x}} \,, \\ f(\mathbf{x}) &= B \int \mathrm{d}^3 k f_{\mathbf{k}} e^{i\mathbf{k}\cdot\mathbf{x}} \,, \end{aligned} \tag{1.77}$$

where we choose the convention $A = 1, B = 1/(2\pi)^3$ which makes the basis function $e^{i\mathbf{kx}}$ orthonormal rather than just orthogonal. In practice we can substitute each quantity and its spatial derivatives using the following expressions,

$$\begin{aligned} & f(x,\eta) \rightarrow f_k(\eta) \,, \\ & \nabla f(x,\eta) \rightarrow i\mathbf{k} f_k(\eta) \,, \\ & \nabla^2 f(x,\eta) \rightarrow -k^2 f_k(\eta) \,. \end{aligned} \tag{1.78}$$

Dropping the subscript "k" from the quantities in the Fourier space, we can write the full evolution equations for each Fourier mode k as following,

$$-k^2\Phi + 3\mathcal{H}\left(-\Phi' - \mathcal{H}\Psi\right) = 4\pi G a^2 \rho \delta \,, \tag{1.79}$$

$$k^2\left(-\Phi' - \mathcal{H}\Psi\right) = -4\pi G a^2 (1+w)\rho\theta \,, \tag{1.80}$$

$$\Psi = \Phi \,, \tag{1.81}$$

$$-\Phi'' - 2\mathcal{H}\Phi' - \mathcal{H}\Psi' - \left(\mathcal{H}^2 + 2\mathcal{H}'\right)\Psi = -4\pi G a^2 c_s^2 \delta\rho \,, \tag{1.82}$$

$$\delta' + 3\mathcal{H}\left(c_s^2 - w\right)\delta = -(1+w)\left(\theta - 3\Phi'\right) \,, \tag{1.83}$$

$$\theta' + \left[\mathcal{H}(1-3w) + \frac{w'}{1+w}\right]\theta = k^2\left(\frac{c_s^2}{1+w}\delta + \Psi\right) \,, \tag{1.84}$$

where $\theta = i\mathbf{k}\cdot\mathbf{v}$. Note that the six equations above are not independent.

By combining the first two equations we obtain the relativistic Poisson equation,

$$-k^2\Phi = 4\pi G a^2 \rho \left[\delta + 3\mathcal{H}(w+1)\theta/k^2\right] = 4\pi G a^2 \rho \, \Delta \,, \tag{1.85}$$

where we define the comoving density contrast (total-matter variable):

$$\Delta \equiv \delta + 3\mathcal{H}(w+1)\theta/k^2 \,. \tag{1.86}$$

Note that in our conventions an overdensity $\Delta > 0$ generates negative gravitational potentials, *i.e.,* $\Phi < 0$ and $\Psi < 0$.

1.3.1 Short wave corrections

In the previous subsection we discussed the equations for the evolution of the first order perturbations. The non-linear structures we observe in the Universe today are the result of the growth of initial small perturbations. This suggests us the perturbative expansion we have considered will be broken at some time and some scale. However the cosmological observations propose that while there are highly dense regions at small scales but there are no strong gravitational fields objects at the scales of interest. Using the observational evidence we can pick the weak field approximation to study the structure formation in the Universe.

The weak-field limit requires that the metric perturbations about the background FLRW metric and consequently the gravitational potentials remain small but the matter perturbations can become large and should not be treated perturbatively. This scheme seems relevant for the cosmological studies since most of the objects of interest are within the weak field regime. In Fig. 1.2 we show the gravitational potentials and the densities of some structures in the Universe. From the figure and the observational fact that by increasing the size of structures their densities and gravitational potentials decrease, one can see that most of the structures important for cosmological studies are in the weak field regime. To explain the objects in the strong field regime (neutron stars, black holes) we cannot use the weak field approximation anymore and we need to pick the appropriate metric according to the symmetries.

To this end, we assume that the potentials remain small, but their variation of fluctuations (like the curvature of the potential wells) at small scales can become large which leads to large density fluctuations, so $\delta\rho/\rho \sim (k/\mathcal{H})^2\Phi$ can become very large in principle. To do the expansion consistently, considering a small parameter ϵ, we assume Φ, Ψ, B_i and h_{ij} are at most of order $\mathcal{O}(\epsilon)$. Also for non-relativistic components, time derivatives are usually of order Hubble thus do not change the order of a term in the expansion. But each spatial derivative decreases the order of a term by one half, for instance $\partial_i\Phi \sim \mathcal{O}(\epsilon^{1/2})$ and $\nabla^2\Phi \sim \mathcal{O}(\epsilon^0)$ (see Adamek et al. [2016a], Adamek et al. [2016b], Fidler et al. [2017], Hassani et al. [2019c] for detailed discussion about the weak field approximation). In Table 1.1 we show the order of quantities in the weak field framework. To summarize, in the equations we keep the terms up to linear order in the metric perturbations, but from the quadratic terms we only keep the ones that have exactly two or more spatial derivatives. For example at the first order in the weak field framework we keep $\Psi\nabla^2\Psi$ or $\delta^{ij}\Phi_{,i}\Phi_{,j}$ while we neglect the terms like $\Phi\Phi', \delta^{ij}B_i\Delta B_j$. The higher order terms in the standard perturbation theory contributing to the equations in the weak field framework are called “short wave corrections” as they become only relevant at small scales.

In the following part, we are going to include the short wave corrections into the Einstein field equations. To do so, we need to consider higher order terms

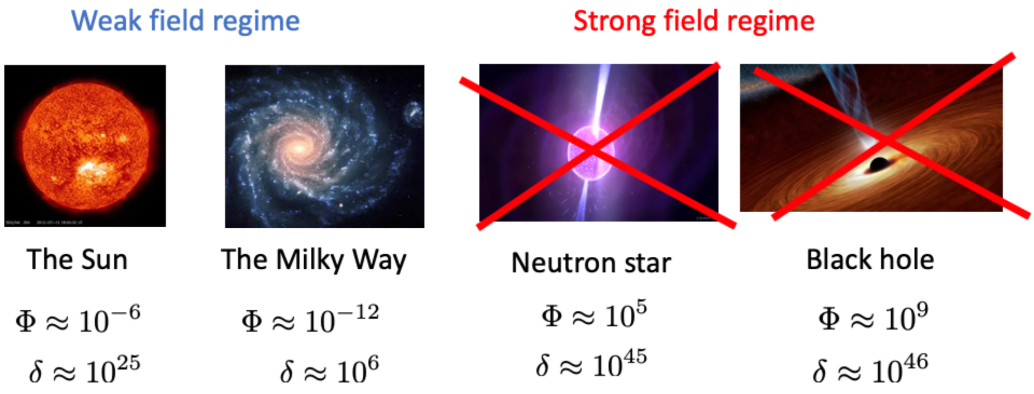
Weak field regime
Strong field regime
The Sun
The Milky Way
Neutron star
Black hole
$\Phi \approx 10^{-6}$
$\delta \approx 10^{25}$
$\Phi \approx 10^{-12}$
$\delta \approx 10^{6}$
$\Phi \approx 10^{5}$
$\delta \approx 10^{45}$
$\Phi \approx 10^{9}$
$\delta \approx 10^{46}$

Figure 1.2: A Picture that shows the densities and gravitational potentials of some structures in the weak field and strong field regime, including the Sun, the Milky Way, a neutron star and a black hole. We have not depicted larger structures, however the structures with larger sizes (galaxies, clusters, filaments and super-clusters) have less density and less gravitational potential compared to the Sun and Milky way, so they also belong to the weak field regime. The numbers for the neutron star and black hole are computed for a typical kind.

in the perturbative expansion and keep track of the number of fields and spatial derivatives in order to use the weak field framework. To be consistent, since for the perturbations of order higher than one, the scalar, vector and tensor modes couple to each other, we need to write the metric in the full form, *i.e.*, , considering the vector and tensor modes in addition to the scalar modes.

We thus start from the general metric in Eq. (1.48),

$$\mathrm{d}s^2 = g_{\mu\nu}\mathrm{d}x^\mu \mathrm{d}x^\nu = a^2(\tau)\left[-(1+2\Psi)\mathrm{d}\tau^2 - 2B_i \mathrm{d}x^i \mathrm{d}\tau + (1-2\Phi)\delta_{ij}\mathrm{d}x^i \mathrm{d}x^j + h_{ij}\mathrm{d}x^i \mathrm{d}x^j\right] . \tag{1.87}$$

We use the Poisson gauge, which implies $\delta^{ij}B_{i,j} = \delta^{ij}h_{ij} = \delta^{jk}h_{ij,k} = 0$ to remove the extra degrees of freedom. Solving the Einstein's equations in the weak field limit $G^\mu_\nu = 8\pi G T^\mu_\nu$ results in the following time-time component (for details see Adamek et al. [2016a, 2017b], Hassani et al. [2020b],

$$(1+4\Phi)\Delta\Phi - 3\mathcal{H}\Phi' + 3\mathcal{H}^2(\chi - \Phi) + \frac{3}{2}\delta^{ij}\Phi_{,i}\Phi_{,j} = -4\pi G a^2 \left(T^0_0 - \bar{T}^0_0\right) , \tag{1.88}$$

where $\chi \doteq \Phi - \Psi$. This equation in the first order limit and neglecting the relativistic corrections reduce to the Newtonian Poisson equation $\Delta\psi_N = 4\pi G a^2 \delta\rho$

variable	order
$\Phi, \Psi, \Phi', \Psi', \Phi'', \Psi''$	ϵ
$\Phi_{,i}, \Psi_{,i}, \Phi'_{,i}, \Psi'_{,i}$	$\epsilon^{1/2}$
$\Phi_{,ij}, \Psi_{,ij}$	1
$\chi, \chi', \chi'', \chi_{,i}, \chi'_{,i}, \chi_{,ij}$	ϵ
$B_i, B'_i, B''_i, B_{i,j} B'_{i,j} B_{i,jk}$	ϵ
$h_{ij}, h'_{ij}, h''_{ij}, h_{ij,k}, h'_{ij,k}, h_{ij,kl}$	ϵ
$\delta T^0_0/\bar{T}^0_0$	1
$T^0_i/\bar{T}^0_0$	$\epsilon^{1/2}$
$\Pi_{ij}/\bar{T}^0_0$	ϵ
v^i, q_i	1

Table 1.1: A table showing the order of perturbative quantities we consider to obtain the equations in the weak field regime. This table is similar to the table in Adamek et al. [2016a] which is the framework used in the gevolution N-body code.

and at the first order is similar to the Eq. (1.85). The other 5 degrees of freedom i.e. χ (one scalar degree of freedom), B_i (two vector degree of freedom) and h_{ij} (two tensor degree of freedom) are determined from the traceless part of space-space Einstein's equations which are fully relativistic without Newtonian analogue. In the weak-field expansion they read;

$$\begin{aligned}\left(\delta^i_k\delta^j_l - \frac{1}{3}\delta^{ij}\delta_{kl}\right)\bigg[\frac{1}{2}h''_{ij} + \mathcal{H}h'_{ij} - \frac{1}{2}\Delta h_{ij} + B'_{(i,j)} + 2\mathcal{H}B_{(i,j)} + \chi_{,ij} \\ - 2\chi\Phi_{,ij} + 2\Phi_{,i}\Phi_{,j} + 4\Phi\Phi_{,ij}\bigg] = 8\pi G a^2\left(\delta_{ik}T^i_l - \frac{1}{3}\delta_{kl}T^i_i\right) \doteq 8\pi G a^2\Pi_{kl}\,.\end{aligned} \tag{1.89}$$

The other four Einstein's equations obtained from the time-space equations and the spatial trace, are not independent and can be obtained from the previous equations, however sometime it is useful some of those equations to do consistency checks of the solutions.

1.4 Measures of inhomogeneity

In the previous section we studied the cosmological perturbations around the homogenous and isotropic FLRW background and later we discussed the idea of weak field framework which led us to take the so called "short wave" corrections into account. Our goal in this section is to introduce the statistical tools to quantify the inhomogeneities in the Universe.

Due to two main reasons the Universe we observe is modeled as a stochastic realization of an ensemble of many possibilities. First, we do not have access to the primordial fluctuations in a deterministic way due to the quantum nature of those fluctuations, *i.e.,* having the definite initial conditions for the evolution equations. Second, we cannot trace the objects in the Universe by observation as we can only observe through our past light cone in which we observe different objects at different times of their evolution, thus testing the evolution of structure must be done statistically.

We consider some physical stochastic quantity $f(\mathbf{x})$ like the density contrast or gravitational potential which charactrises the inhomogeneities in the universe. However, in the real space one can define the two-point correlation function $\xi(r)$ of the field $f(\mathbf{x})$ as

$$\xi(r) = \langle f(\mathbf{x}) f(\mathbf{x}+\mathbf{r}) \rangle_{\text{ensemble}} \,, \tag{1.90}$$

where the averaging, in principle, should be done at two specific points x and y over different ensembles of the universes. But as a single observer we only have access to one of the samples (our Universe). Under the following assumptions one can prove the ergodic theorem, which implies that the averages over a large domain within a single realization can be treated as averages over the probability ensemble.

The assumptions needed to prove the ergodic theorems are (see Watts & Coles [2003], Weinberg [2008] for in-depth discussion);

- First we assume that the distribution function of $f(\mathbf{x})$ is homogeneous, meaning that the average of any product of $f(\mathbf{x})$ with different arguments only depends on the differences of the arguments.

$$\langle f(\mathbf{x_1}) f(\mathbf{x_2}) \cdots f(\mathbf{x_n}) \rangle = \langle f(\mathbf{x_1}+\mathbf{r})) f(\mathbf{x_2}+\mathbf{r})) \cdots f(\mathbf{x_n}+\mathbf{r}) \rangle \,. \tag{1.91}$$

- Second, we assume that the fields at distant space-time positions are uncorrelated, *i.e.,* for $|r| \to \infty$,

$$\begin{aligned}
&\langle f(\mathbf{x_1}+\mathbf{r})) f(\mathbf{x_{21}}+\mathbf{r})) \cdots f(\mathbf{y_1}+\mathbf{r})) f(\mathbf{y_2}+\mathbf{r})) \cdots \rangle \,, \\
&\to \langle f(\mathbf{x_1}+\mathbf{r})) f(\mathbf{x_2}+\mathbf{r}) \cdots \rangle \langle f(\mathbf{y_1}+\mathbf{r}) f(\mathbf{y_2}+\mathbf{r}) \cdots \rangle \,, \\
&= \langle f(\mathbf{x_1}) f(\mathbf{x_2}) \cdots \rangle \langle f(\mathbf{y_1}) f(\mathbf{y_2}) \cdots \rangle \,.
\end{aligned} \tag{1.92}$$

By using the ergodic theorem we can write the Eq. (1.90) as

$$\xi = \langle f(\mathbf{x}) f(\mathbf{x}+\mathbf{r})\rangle_{sky}\,, \tag{1.93}$$

where the subscript “sky” means that we take the average over different points separated with the same distance on the sky instead of over different ensembles of universes. Writing the field f in the Fourier space, results in

$$\xi(\mathbf{r}) = \langle f(\mathbf{x}) f(\mathbf{x}+\mathbf{r})\rangle = \int \frac{d^3\mathbf{k}}{(2\pi)^3}\frac{d^3\mathbf{k}'}{(2\pi)^3} f_{\mathbf{k}} f^*_{\mathbf{k}'} e^{i\mathbf{k}\cdot\mathbf{r}} \left\langle e^{(i(\mathbf{k}-\mathbf{k}')\cdot\mathbf{x})}\right\rangle\,. \tag{1.94}$$

In practice we can evaluate $\langle\cdots\rangle$ by averaging over a cubical box of size $2L$. In any one dimension, so we have,

$$\left\langle e^{i\left(k_l-k_l'\right)x}\right\rangle \equiv \int_{-L}^{L}\frac{dx}{2L}e^{i\left(k_l-k_l'\right)x} = \frac{\sin\left(k_l-k_l'\right)L}{\left(k_l-k_l'\right)L}$$

For large L, we can use the following limit

$$\lim_{L\to\infty}\left\{\frac{\sin kL}{kL}\right\} = \frac{2\pi}{(2L)}\delta_{\rm D}(k)\,,$$

which results in,

$$\begin{aligned}\xi(\mathbf{r}) &= \frac{(2\pi)^3}{V}\int \frac{d^3\mathbf{k}}{(2\pi)^3}\frac{d\mathbf{k}'}{(2\pi)^3} f_{\mathbf{k}} f^*_{\mathbf{k}'} e^{i\mathbf{k}\cdot\mathbf{r}}\delta_{\rm Dirac}\left(\mathbf{k}-\mathbf{k}'\right)\\ &= \int \frac{d^3\mathbf{k}}{(2\pi)^3}\frac{\left|f_{\mathbf{k}}\right|^2}{V}e^{i\mathbf{k}\cdot\mathbf{r}} \equiv \int\frac{d^3\mathbf{k}}{(2\pi)^3}P(\mathbf{k})e^{i\mathbf{k}\cdot\mathbf{r}}\,,\end{aligned}$$

where the volume $V = (2L)^3$ and $P(\mathbf{k}) = \left|f_{\mathbf{k}}\right|^2 V^{-1}$ is the power spectrum of $f(\mathbf{x})$. Similarly we can also calculate the two-point correlation in Fourier space,

$$\begin{aligned}\left\langle\delta\left(\mathbf{k}\right)\delta\left(\mathbf{k}'\right)\right\rangle &= \int\frac{d^3\mathbf{x}}{(2\pi)^3}\frac{d^3\mathbf{r}}{(2\pi)^3}\xi(r)e^{-i(\mathbf{k}+\mathbf{k}')\cdot\mathbf{x}-i\mathbf{k}'\cdot\mathbf{r}}\\ &= \delta_{\rm D}\left(\mathbf{k}+\mathbf{k}'\right)\int\frac{d^3\mathbf{r}}{(2\pi)^3}\xi(r)\exp(i\mathbf{k}\cdot\mathbf{r})\\ &\equiv (2\pi)^3\delta_{\rm D}\left(\mathbf{k}+\mathbf{k}'\right)P(k)\end{aligned} \tag{1.95}$$

As we saw in the previous section at linear order the Fourier modes decouple and they evolve independently. So the easiest way to quantify the variation of a field $f(\mathbf{x})$ is to use the amplitude of the field in the Fourier space $\left|f_{\mathbf{k}}\right|^2$. Moreover, in the linear regime (at large scales) the cosmological fields e.g., the density field are Gaussian. These features make the power spectrum a very powerful tool for the cosmological studies as it is sufficient to entirely describe the fields (see Amendola & Tsujikawa [2010], Dodelson [2003], Durrer [2008], Padmanabhan [1996] for more details)

1.5 Dark energy and modified gravity

In the late 1998's two independent groups of astronomers were searching for supernovae at high redshifts with the hope to measure the deceleration rate of the Universe. Surprisingly, the independent observations were suggesting that the expansion of the Universe was accelerating. Cosmologists and astronomers started to build models to describe the observations: knowing that,

- The component responsible for the cosmic acceleration accounts for about 70% of the cosmic energy density.
- It acts opposite to gravity and is in fact gravitationally repulsive.
- It does not seem to cluster similar to the baryons and dark matter in the non-linear structures like galaxies, clusters and etc.

Due to its mysterious nature cosmologists called it "dark energy", a puzzling component with all aforementioned properties and responsible for the late time accelerating expansion of the Universe (see Caldwell [2004] for a historical discussion about dark energy and modified gravity). Since then thousands of papers have been written on dark energy and accelerating expansion to solve the main puzzle i.e., what is the nature of dark energy?

In fact the main difficulty is that the existence of a gravitationally repulsive component has some unexpected outcomes from the fundamental physics view. The most conservative fundamental physics-friendly suggestions are that there is a uniform fluid of zero point energy (cosmological constant) in the Universe, or some scientists proposed to consider a new fundamental particle with a mass about 10^{-39} times smaller than the electron mass. As a completely different point of view, some researchers have also suggested to change the Einstein's general theory of relativity such that the cosmological evolution changes at large distances. But none of the proposed models have been adequately verified by both theory (fundamentally) and observations yet. However, the cosmological constant Λ as a phenomenological parameter which corresponds to the simplest scenario for dark energy, although not being theoretically well motivated but has been a successful theory by now according to the cosmological observations and thus is favored by some cosmologists.

In the following list we summarize the most important events related to the dark energy in a chronological way including the year 2011 when the Nobel prize was awarded for the discovery of cosmic acceleration (for a detailed list see Li et al. [2011], Straumann [2002], Weinberg [1989])

1917: The idea of the cosmological constant was suggested by Einstein, when he added a constant term in the field equations. He considered the cosmological constant due to two main reasons: first to obtain a static universe;

second, to isolated mass to prevent having a structure on space at infinity in a closed universe.

1920s: Pauli found out that for a radiation field the vacuum energy is too large to gravitate. In fact the vacuum energy density of a radiation field is shown to be proportional to the cutoff of the theory to the fourth power. Pauli, in an unpublished work, showed that using the electron radius as an ultraviolet cutoff, the universe curvature will be so large and the Universe "could not even reach to the moon".

1932: Einstein regretted adding the cosmological constant his field equations because of the discovery of the cosmic expansion. Although in 1923 he already wrote to Weyl : "If there is no quasi-static world, then away with the cosmological term!", apparently until 1932 he did not believe in "no quasi-static world".

1960s: In order to explain why there is significant clustering of quasars around redshift $z \approx 1.95$ some researches proposed to use the Lemaitre model (closed Universe with $\Lambda > 0$and curvature$k = 1$), where at that redshift the universe looks like the Einstein's static universe.

1967: The old cosmological problem was established by Zeldovich when he reexpressed the cosmological constant problem by taking the fluctuations of the vacuum energy into account. Zeldovich also used the phrase of "fine-tuning" for the first time in this field.

1987: Steven Weinberg "predicted" the existence of a small cosmological constant in the Universe.

1998: Riess et al. first discovered the acceleration of expanding universe based on the analysis of 16 distant and 34 nearby supernovae. A bit later, Perlmutter et al. using 18 nearby supernovae and 42 high-redshift supernovae confirmed the discovery of cosmic acceleration.

1998-today: Many dark energy (in the form of a scalar field or fluid) and modified gravity models (in the form of a modification to general relativity) was suggested by cosmologists and particle physicists in order to explain the cosmic acceleration.

2011: For the discovery of late time cosmic acceleration, Adam Riess, Brian Schmidt, and Saul Perlmutter won the Nobel prize in physics in 2011.

Now: Still we don't know the nature of dark energy. This thesis is an attempt toward understanding its nature mainly by focusing on the non-linearities in the cosmological components including the dark energy part and utilizing the future cosmological surveys data. Using the predictions of the current thesis for some dark energy models that go well into the non-linear regime we will hopefully be able to constrain dark energy models tightly and we might find a clear evidence for clustering of dark energy which would rule out the cosmological constant as the reason behind the cosmic acceleration.

1.6 The Effective Field Theory of Dark Energy

The first step toward modification of the ΛCDM theory is adding a single degree of freedom in the form of a scalar field. The scalar field can be interpreted as either in the form of a modification to the GR or as a dark energy fluid, which in either cases it has the role of dark energy to explain the accelerating expansion of the Universe with some additional properties compared to the cosmological constant Λ (for a review of the subject see Clifton et al. [2012a], Gleyzes [2015], Joyce et al. [2015])[7]

The Effective Field Theory of Dark Energy (EFT of DE) on the other hand allows us to study very general dark energy and modified gravity models based on a single scalar degree of freedom, in a relativistic setting and with a minimal set of parameters. So it seems that the appropriate language to deal with the additional scalar field is the EFT of DE and thus we choose this language to write down the equations of motion.

In general the EFT, in physics, is a type of approximation for an underlying fundamental theory. The fundamental theory could be the quantum field theory, statistical physics, quantum gravity and etc. In the EFT approach we use the relevant degrees of freedom at a certain range of energies/distances while neglecting high energy/ short distance behavior of the system. In fact the EFT framework could be seen as such we average over all the high energy/small scale behavior of the system and we associate all the small scale/high energy details as an average to the low energy description. As a result the EFT approach is safe to be used at a range of energies/scales far from the EFT limit. As an important example of the EFT framework we can name the fluid approach in which we express a fluid with a huge number of particles with just couple of low energy/long distance parameters like the speed of sound, pressure, density and etc. However we know that when we look at a fluid at very short distances the fluid description is not anymore valid to explain the behaviour of the system (see Endlich et al. [2013], Hartmann [2001], Pich [1998], Wikipedia contributors [2020b]).

---

[7] One could of course think of adding arbitrary degrees of the freedom, but that is not usually a first step that physicists should start from plus the fact that we do not have any hint of many additional extra degrees of freedom from observations. Moreover, considering the easiest scenario helps us to easily generalize the theory to include more complicated scenarios.

The idea of applying the EFT framework in cosmology was first done for theory of inflation in Cheung et al. [2008], Creminelli et al. [2006] where they have used the EFT framework to express the most general theory for a single scalar field in the inflationary phase to describe the fluctuations around a quasi de Sitter background. Then a similar framework was applied for the dark energy problem with the terminology of the "Effective Field Theory of Dark Energy (EFT of DE)" in Gubitosi et al. [2013a] .

The EFT of DE is especially considered important and worth studying because, although it is not a fundamental theory, it offers several advantages Bellini & Sawicki [2014], Creminelli et al. [2009], Frusciante & Papadomanolakis [2017], Gleyzes [2015], Gleyzes et al. [2013, 2015], Gubitosi et al. [2013a]:

- First, we can express a large class of dark energy and modified gravity (DE/MG) models with a minimal number of parameters in a model-independent approach and using a unified language.

- Second, the phenomenological parameters of the effective theory can be constrained directly by cosmological observations without being specific to any DE/MG models nor to their original motivations.

- Third, the EFT approach allows the theorists to carefully examine the unexplored regions of the space of parameters which could in principle guide towards new viable theories for dark energy.

In the following we will discuss the main ideas of the EFT of DE and we write down the full EFT of DE action,

1.6.1 Geometrical quantities

First, we assume the weak equivalence principle meaning that there is a metric $g_{\mu\nu}$ which is universally coupled to all matter fields. The main idea here would be to use the uniform scalar field hypersurfaces as the time coordinate. In other words, we redefine the time such a way that the scalar becomes a constant without any perturbations on these hypersurfaces while the scalar field perturbations have gone into the time coordinate and geometric objects. Then without having the difficulties of dealing with the scalar field perturbations we write a generic action based on the basic geometric quantities that appear in an ADM[8] decomposition of space-time. This action would describe cosmological perturbations around a FLRW background which is useful to express a theory beyond ΛCDM.

---

[8] ADM named after Richard Arnowitt, Stanley Deser and Charles W. Misner, the three authors of "Dynamical Structure and Definition of Energy in General Relativity" Arnowitt et al. [1959] for the Hamiltonian formulation of general relativity.

We assume the scalar field to be space-like or equivalently characterized by a time-like space-time gradient, *i.e.*, to have a gradient such that $\nabla_\mu\varphi\nabla^\mu\varphi < 0$. In this case, the constant scalar field hypersurfaces define a foliation of time and the uniform scalar field hypersurfaces can be used for 3+1 decomposition of space-time, which separate the quantities into orthogonal and parallel to the hypersurface $\varphi = \text{const}$ based on the ADM formalism. We use the gauge freedom in the theory to choose this specific time foliation which is called the unitary gauge.

In the new time coordinate (unitary gauge) the perturbations in the scalar field φ are hidden, so we have,

$$\varphi(\tilde{t},\vec{x}) = \varphi_0(\tilde{t}) + \delta\varphi(\tilde{t},\vec{x}) = \varphi_0(t) \tag{1.96}$$

where t is chosen such that $\delta\varphi(t,\vec{x}) = 0$. The kinetic term for φ in this gauge reads,

$$X \equiv \nabla_\mu\varphi\nabla^\mu\varphi = g^{00}\dot{\varphi}_0^2 \tag{1.97}$$

where $g^{00} = -1 + \delta g^{00}$ and thus the kinetic term contributes to the perturbative expansion.

This space-time foliation allow us to define various geometric objects. The first associated geometric quantity is defined based on the fact that the hypersurfaces are constant scalar field, so the vectors perpendicular to these hypersurfaces are obtained by $\vec{\nabla}\varphi$. The future-oriented time-like unit vector normal to the hypersurfaces read as,

$$n_\mu = -\frac{1}{\sqrt{-X}}\nabla_\mu\varphi, \quad X \equiv g^{\rho\sigma}\nabla_\rho\varphi\nabla_\sigma\varphi \tag{1.98}$$

where $g_{\mu\nu}n^\mu n^\nu = -1$ and $n_\mu n^\lambda\nabla_\lambda n^\mu = 0$ assuring all the properties of being time-like, unit vector and orthogonal to the constant field hypersurfaces. Using n^μ and the four dimensional metric $g_{\mu\nu}$ we can define the projection tensor $h_{\mu\nu}$ as

$$h_{\mu\nu} \equiv g_{\mu\nu} + n_\mu n_\nu\,. \tag{1.99}$$

Intrinsic curvature of the hypersurfaces is described by the three-dimensional Ricci tensor, in which it has the same degrees of freedom as Riemann tensor in three-dimensional space-time

$$^{(3)}R_{\mu\nu}\,, \tag{1.100}$$

which is defined based on the metric $h_{\mu\nu}$ on the hypersurfaces. The extrinsic curvature tensor is defined as,

$$K^\mu_\nu \equiv h^{\mu\rho}\nabla_\rho n_\nu\,. \tag{1.101}$$

These are the main geometric quantities we can define on these hypersurfaces, while other quantities can be derived by combining the above quantities together with the covariant derivative ∇_μ and the 4D metric $g_{\mu\nu}$. For example the "acceleration" vector field is defined as,

$$a^\mu \equiv n^\lambda \nabla_\lambda n^\mu \,, \tag{1.102}$$

which is tangent to the hypersurfaces and thus orthogonal to n^μ *i.e.,* $n_\mu a^\mu = 0$.

It is useful to write down the aforementioned expressions explicitly based on the scalar field, because some dark energy models are given explicitly in terms of a scalar field. As previously mentioned $n_\mu = -\frac{1}{\sqrt{-X}}\nabla_\mu\varphi$ and the extrinsic curvature reads,

$$K_{\mu\nu} = -\frac{1}{\sqrt{-X}}\nabla_\mu\nabla_\nu\varphi + n_\mu a_\nu + n_\nu a_\mu + \frac{1}{2X} n_\mu n_\nu n^\lambda \nabla_\lambda X \tag{1.103}$$

We can use the Gauss-Codazzi relations to define the other three-dimensional quantities based on the four-dimensional ones and the extrinsic curvature (see Gleyzes et al. [2013] for more details),

$$^{(3)}R_{\mu\nu} = (R_{\mu\nu})_{\|} + (n^\sigma n^\rho R_{\mu\sigma\nu\rho})_{\|} - KK_{\mu\nu} + K_{\mu\sigma}K^\sigma_\nu \,, \tag{1.104}$$

$$^{(3)}R = R + K^2 - K_{\mu\nu}K^{\mu\nu} - 2\nabla_\mu\left(Kn^\mu - \dot{n}^\mu\right) \,, \tag{1.105}$$

where the symbol $\|$ means projection on the 3D-hypersurfaces using the 3D metric $h_{\mu\nu}$, e.g. $(V_\mu)_{\|} \equiv h^\nu_\mu V_\nu$ and $\dot{n}_\mu = n^\nu \nabla_\nu\, n_\mu$. In Fig. 1.3 we have schematically shown a hypersurface and the geometric quantities associated with it.

1.6.2 ADM coordinates

So far all the geometric quantities have been defined intrinsically without assuming any coordinate. However, since we have specified a special time foliation according to the $\varphi = const$ hypersurfaces, it is useful to adopt a coordinate system according to this slicing. So we express the four-dimensional metric in the ADM form in which we choose the constant time hypersurfaces coinciding with the $\varphi = const$ hypersurfaces,

$$ds^2 = -N^2 dt^2 + h_{ij}\left(dx^i + N^i dt\right)\left(dx^j + N^j dt\right) \,, \tag{1.106}$$

where N is the lapse and N^i the shift function. The components of the metric and of its inverse in the matrix form are written respectively as

$$g_{\mu\nu} = \begin{pmatrix} -N^2 + h_{ij}N^iN^j & h_{ij}N^j \\ h_{ij}N^i & h_{ij} \end{pmatrix} , \quad g^{\mu\nu} = \begin{pmatrix} -1/N^2 & N^j/N^2 \\ N^i/N^2 & h^{ij} - N^iN^j/N^2 \,. \end{pmatrix} \tag{1.107}$$

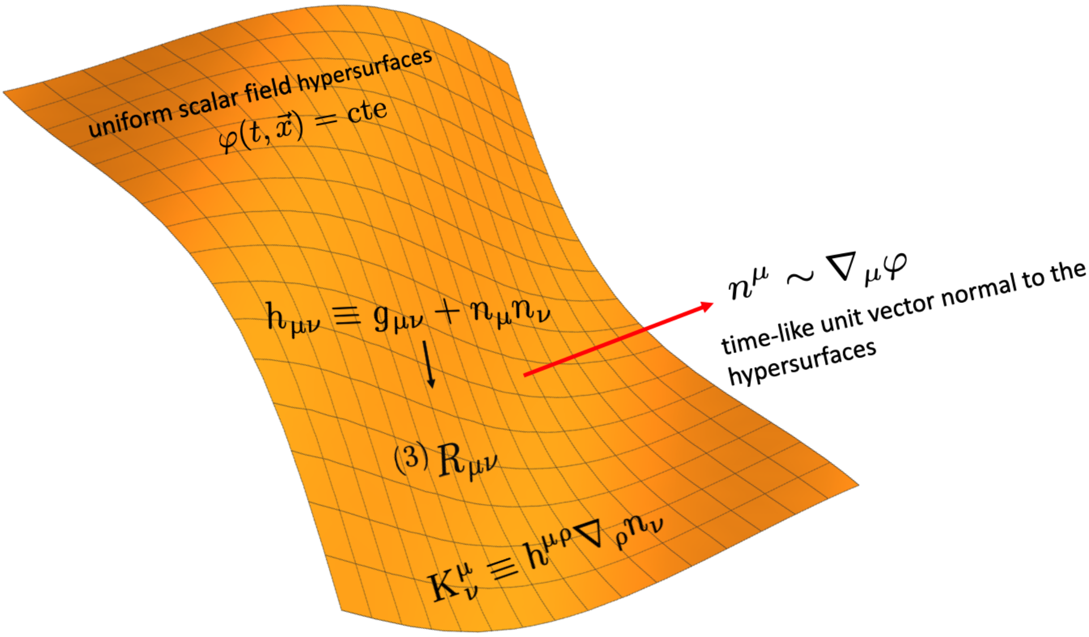
uniform scalar field hypersurfaces
$\varphi(t,\vec{x}) = \mathrm{cte}$
$h_{\mu\nu} \equiv g_{\mu\nu} + n_\mu n_\nu$
${}^{(3)}R_{\mu\nu}$
$K^\mu_\nu \equiv h^{\mu\rho}\nabla_\rho n_\nu$
$n^\mu \sim \nabla_\mu \varphi$
time-like unit vector normal to the hypersurfaces

Figure 1.3: A schematic image showing a constant scalar filed hypersurface and the geometric objects associated with it.

The standard kinetic term in this coordinate reads,

$$X = g^{00}\dot{\varphi}^2(t) = -\frac{\dot{\varphi}^2(t)}{N^2}\,, \tag{1.108}$$

since the scalar field is space independent, the components of the normal vector are;

$$n_0 = -N, \quad n_i = 0\,. \tag{1.109}$$

The components of the extrinsic curvature tensor on the 3D hypersurfaces read;

$$K_{ij} = \frac{1}{2N}\left(\dot{h}_{ij} - D_i N_j - D_j N_i\right)\,, \tag{1.110}$$

where a dot stands for a time derivative with respect to t, and D_i indicates the 3D covariant derivative associated with the 3D spatial metric h_{ij}. The 3D spatial indices are raised and lowered by the spatial metric h_{ij}.

There are two main advantages in using the unitary gauge (see Arkani-Hamed et al. [2004], Cheung et al. [2008], Creminelli et al. [2006], Gleyzes et al. [2013])

- We can write a generic action for cosmological perturbations in a straightforward way using this gauge. The reason is that the dynamics of the scalar field has been put into the metric, the most generic action is written similar to that for the metric perturbations around a FLRW solution.

- The second advantage is the 3 + 1 splitting in unitary gauge allows us to keep the number of time derivatives under control, while we can consider higher space derivatives. As a result using the unitary gauge, we can systematically write the theories with higher spatial derivative.

1.6.3 General Lagrangian in unitary gauge

The most general gravitational actions written in terms of the geometrical quantities and being invariant under spatial diffeomorphism [9] expressed in ADM coordinates,

$$S_g = \int d^4x\sqrt{-g}L\left(N, K_{ij}, R_{ij}, h_{ij}, D_i; t\right) \,, \tag{1.111}$$

where the determinant of the 4D metric is written as $\sqrt{-g} = N\sqrt{h}$, and where h is the determinant of the 3D metric h_{ij}.

In the following we derive the Lagrangian written in the previous form (1.111) for three theories, namely General Relativity, the k-essence and $f(R)$ theories.

General Relativity:

We start from the Einstein-Hilbert action

$$S_{\rm GR} = \int d^4x\sqrt{-g}\frac{M_{\rm Pl}^2}{2}R\,. \tag{1.112}$$

using the Gauss-Codazzi expression in (1.105) we can write the 4D Ricci scalar in terms of the geometrical objects on the 3D hypersurfaces. Therefore we can easily obtain the Lagrangian in the ADM form (1.111) General Relativity (GR),

$$L_{\rm GR} = \frac{M_{\rm Pl}^2}{2}\left[K_{ij}K^{ij} - K^2 + {}^{(3)}R\right] \,. \tag{1.113}$$

Note that, in the case of GR there is no scalar degree of freedom and thus the slicing of space-time is arbitrary. This provides us with an additional symmetry in the GR Lagrangian and leads to full four-dimensional diffeomorphism invariance, which is not immediately clear in the ADM form while it is clear in the 4D version as the 4D Ricci scalar is by definition 4D diffeomorphism invariant.

k-essence:

The simplest way to extend the GR action is to add a scalar field in the form of a potential and a standard kinetic term as following,

$$S_{\rm quinessence} = \int d^4x\sqrt{-g}\left(-\frac{1}{2}\partial_\mu\varphi\partial^\mu\varphi - V(\varphi)\right) \,. \tag{1.114}$$

---

[9] invariant under the change of spatial coordinates

This action corresponds to the quintessence model which is added to the GR action,

$$S = S_{\rm GR} + S_{\rm quintessence} \tag{1.115}$$

The ADM Lagrangian of the $S_{\rm quintessence}$ is simply Creminelli et al. [2009],

$$L_{\rm quintessence}(t,N) = \frac{\dot{\varphi}^2(t)}{2N^2} - V(\varphi(t))\,. \tag{1.116}$$

Similarly, we can describe k-essence theories in the ADM form. The k-essence theories can be expressed as a general form of quintessence models, in which the action is a general function of a potential and a kinetic term Armendariz-Picon et al. [2000, 2001],

$$S_{k\text{-essence}} = \int d^4x\sqrt{-g}P(X,\varphi)\,. \tag{1.117}$$

The k-essence Lagrangian is written in the ADM form as following Bellini & Sawicki [2014], Gleyzes [2015], Gleyzes et al. [2015],

$$L_{k\text{-essence}}\,(t,N) = P\left[-\frac{\dot{\varphi}^2(t)}{2N^2},\varphi(t)\right]\,. \tag{1.118}$$

$f(R)$ theories:

In these theories the Lagrangian is a nonlinear function of the four-dimensional Ricci scalar R. These theories are equivalent to a scalar-tensor theory. It can be shown that the $f(R)$ Lagrangian can be written in the following form Burgess [2004], Gleyzes et al. [2015],

$$L_{f(R)} = f(\varphi) + f_\varphi(\varphi)\,(R-\varphi)\;. \tag{1.119}$$

This is equivalent to the Lagrangian $f\,(R)$, because they lead to the same equations of motion (as long as the second derivative of $f(R)$ with respect to R is non zero i.e., $f_{RR} \neq 0)$. Using the previous Lagrangian one can easily express these theories in the ADM form Bellini & Sawicki [2014], Gleyzes et al. [2015],

$$L_{F(R)} = F_\varphi\left(R + K_{\mu\nu}K^{\mu\nu} - K^2\right) + 2F_{\varphi\varphi}K\sqrt{-X} + F(\varphi) - \varphi F_\varphi\,. \tag{1.120}$$

1.6.4 Cosmology: Background evolution

In this subsection we discuss the cosmological background equations. We consider a spatially flat FLRW metric,

$$ds^2 = -\bar{N}^2(t)dt^2 + a^2(t)\delta_{ij}dx^idx^j\,, \tag{1.121}$$

where previously in Eq. (1.9) we set $\bar{N}(t) = 1$ as we considered an especial time coordinate, but here we let it to be unspecified. In this space-time, the intrinsic curvature tensor of the 3D hypersurfaces vanishes, *i.e.,* $R_{ij} = 0$, and the extrinsic curvature reads,

$$K^i_j = H(t)\delta^i_j, \quad \mathcal{S} \equiv K_{\mu\nu}K^{\mu\nu} = 3H(t)^2/N(t)^2 \,, \tag{1.122}$$

where $H \equiv \frac{\dot{a}}{\bar{N}a}$ is the Hubble parameter. Substituting into the ADM form of the Lagrangian (1.111) we thus find an homogeneous Lagrangian,

$$\bar{L}(a, \dot{a}, \bar{N}) \equiv L\left[K^i_j = \frac{\dot{a}}{\bar{N}a}\delta^i_j, R^i_j = 0, N = \bar{N}(t)\right] . \tag{1.123}$$

The action thus reads as

$$\bar{S}_{\text{background}} = \int dt d^3x\, \bar{N}a^3\bar{L}\left[K^i_j = \frac{\dot{a}}{\bar{N}a}\delta^i_j, R^i_j = 0, N = \bar{N}(t)\right] . \tag{1.124}$$

The variation of this action with respect to the lapse and scale factor leads to,

$$\delta\bar{S}_{\text{background}} = \int dt d^3x \Big\{ a^3\left(\bar{L} + \bar{N}\frac{\partial L}{\partial N} - 3H\mathcal{F}\right)\delta\bar{N} \tag{1.125}$$

$$+ 3a^2\bar{N}\left(\bar{L} - 3H\mathcal{F} - \frac{\dot{\mathcal{F}}}{\bar{N}}\right)\delta a\Big\} , \tag{1.126}$$

where $\mathcal{F}$ is defined from the derivative of the Lagrangian with respect to the extrinsic curvature, evaluated on the background

$$\left(\frac{\partial L}{\partial K_{ij}}\right)_{\text{background}} \equiv \mathcal{F}a^{-2}\delta^{ij} \,, \tag{1.127}$$

where $a^{-2}\delta^{ij}$ corresponds to the spatial components of the inverse background metric $\bar{g}^{ij}$. To obtain the evolution we add matter minimally coupled to the metric $g_{\mu\nu}$, in which the variation of the matter action with respect to the metric defines the energy-momentum tensor,

$$\delta S_{\text{matter}} = \frac{1}{2}\int d^4x\sqrt{-g}T^{\mu\nu}\delta g_{\mu\nu} \,. \tag{1.128}$$

In a FLRW Universe,

$$\delta\bar{S}_{\text{matter}} = \int d^4x\bar{N}a^3\left(-\rho_{\text{m}}\frac{\delta\bar{N}}{\bar{N}} + 3p_{\text{m}}\frac{\delta a}{a}\right) . \tag{1.129}$$

As a result the variation of the total homogeneous action including the matter part and the gravity part $\bar{S}_{\text{total}} = \bar{S}_{\text{background}} + \bar{S}_{\text{matter}}$ with respect to the lapse N and the scale factor a gives the first and second Friedmann equations respectively.

$$\bar{L} + \bar{N}L_N - 3H\mathcal{F} = \rho_{\text{m}} \,, \tag{1.130}$$

$$\bar{L} - 3H\mathcal{F} - \dot{\mathcal{F}}/\bar{N} = -p_{\mathrm{m}} \,. \tag{1.131}$$

Obviously, in order to write these equations in the usual form we need to write down the quantities for the GR case,

$$\frac{\partial L_{\mathrm{GR}}}{\partial K^i_j} = M_{\mathrm{Pl}}^2 \left(K_i^j - K\delta_i^j \right) \,, \tag{1.132}$$

which, having $K^i_j = H\delta^i_j$, gives,

$$\mathcal{F}_{\mathrm{GR}} = -2M_{\mathrm{Pl}}^2 H, \tag{1.133}$$

moreover, $\bar{L}_{\mathrm{GR}} = -3M_{\mathrm{Pl}}^2 H^2$ and $L_N = 0$. Substituting these into the (1.130) and (1.131) yields the known form of the Friedman equations (1.31) and (1.32).

1.6.5 Cosmology: The EFT quadratic action

In this subsection we limit ourselves to the linear perturbations about the FLRW background solution, in which we expand the action written in the ADM form up to quadratic order (see Frusciante & Perenon [2020], Gleyzes et al. [2015], Piazza & Vernizzi [2013], Tsujikawa [2015] for detailed discussion). In general the expansion of the Lagrangian L up to quadratic order gives

$$L\left(N, K^i_j, R^i_j, \dots\right) = \bar{L} + L_N \delta N + \frac{\partial L}{\partial K^i_j}\delta K^i_j + \frac{\partial L}{\partial R^i_j}\delta R^i_j + L^{(2)} + \dots \,, \tag{1.134}$$

where $L^{(2)}$ is the quadratic part given by

$$\begin{aligned} L^{(2)} =& \frac{1}{2} L_{NN}\delta N^2 + \frac{1}{2}\frac{\partial^2 L}{\partial K^i_j \partial K^k_l}\delta K^i_j \delta K^k_l + \frac{1}{2}\frac{\partial^2 L}{\partial R^i_j \partial R^k_l}\delta R^i_j \delta R^k_l + \\ &+ \frac{\partial^2 L}{\partial K^i_j \partial R^k_l}\delta K^i_j \delta R^k_l + \frac{\partial^2 L}{\partial N \partial K^i_j}\delta N \delta K^i_j + \frac{\partial^2 L}{\partial N \partial R^i_j}\delta N \delta R^i_j + \dots \,. \end{aligned} \tag{1.135}$$

The dots in the previous equations correspond to other possible terms which we neglect here. The terms δN and δK_i^j are defined as

$$\delta N \equiv N - \bar{N}, \quad \delta K_i^j \equiv K_i^j - H\delta_i^j \,, \tag{1.136}$$

and all the derivatives are evaluated on the FLRW background. We can simplify the expression (1.135) mainly using integration by parts and employing the background symmetries. For example, according to the definitions we have,

$$\frac{\partial L}{\partial K^i_j}\delta K^i_j = \mathcal{F}\delta K = \mathcal{F}(K - 3H) \,, \tag{1.137}$$

and using the definition of the extrinsic curvature $K = \nabla_\mu n^\mu$ we can simplify the integral using integration by parts,

$$\int d^4x\sqrt{-g}\mathcal{F}K = -\int d^4x\sqrt{-g}n^\mu\nabla_\mu\mathcal{F} = -\int d^4x\sqrt{-g}\frac{\dot{\mathcal{F}}}{N}\,. \tag{1.138}$$

Moreover we can simplify the terms $\frac{\partial^2 L}{\partial X_i^j \partial Y_k^l}$, where X and Y can be K or R, using the fully symmetric FLRW background and write,

$$\begin{aligned}
\frac{\partial^2 L}{\partial K_i^j \partial K_k^l} &= \hat{\mathcal{A}}_K \delta_j^i \delta_l^k + \mathcal{A}_K\left(\delta_l^i\delta_j^k + \delta^{ik}\delta_{jl}\right)\,,\\
\frac{\partial^2 L}{\partial R_i^j \partial R_k^l} &= \hat{\mathcal{A}}_R \delta_j^i \delta_l^k + \mathcal{A}_R\left(\delta_l^i\delta_j^k + \delta^{ik}\delta_{jl}\right)\,,\\
\frac{\partial^2 L}{\partial K_i^j \partial R_k^l} &= \hat{\mathcal{C}} \delta_j^i \delta_l^k + \mathcal{C}\left(\delta_l^i\delta_j^k + \delta^{ik}\delta_{jl}\right)\,,
\end{aligned} \tag{1.139}$$

also with the similar reasoning we have,

$$\frac{\partial^2 L}{\partial N \partial K_j^i} = \mathcal{B}\delta_i^j, \quad \frac{\partial^2 L}{\partial N \partial R_j^i} = \mathcal{B}_R\delta_i^j\,. \tag{1.140}$$

The EFT action

Using the previous expressions and some redefinitions Gleyzes et al. [2013, 2015], we can write the most general EFT Lagrangian, to quadratic order for a single-field dark energy models leading to at most second order equations of motion as;

$$\begin{aligned}
S = \int d^4x\sqrt{-g}\Bigg[&\frac{M_*^2}{2}f(t)^{(4)}R - \Lambda(t) - c(t)g^{00} + \frac{M_2^4(t)}{2}\left(\delta g^{00}\right)^2 - \frac{m_3^3(t)}{2}\delta K \delta g^{00}\\
&-m_4^2(t)\left(\delta K^2 - \delta K_\nu^\mu \delta K_\mu^\nu\right) + \frac{\tilde{m}_4^2(t)}{2}R\delta g^{00}\Bigg]\,.
\end{aligned} \tag{1.141}$$

We can also rewrite the action in another form as following Bellini & Sawicki [2014], Frusciante & Perenon [2020], Gleyzes et al. [2015],

$$\begin{aligned}
S_g = \int d^4x a^3 \frac{M(t)^2}{2}\Big[&\delta K_{\mu\nu}\delta K^{\mu\nu} - \delta K^2 + (1+\alpha_T(t))\left(\delta_2 R + \frac{\delta\sqrt{h}}{a^3}R\right)\\
&+H^2\alpha_K(t)\delta N^2 + 4H\alpha_B(t)\delta N\delta K + (1+\alpha_H(t))\,R\delta N\Big] + \cdots
\end{aligned} \tag{1.142}$$

where the coefficients α_i and M are generally time-dependent. Moreover we can also introduce α_M as,

$$\alpha_M \equiv \frac{2\dot{M}}{HM} \tag{1.143}$$

M^2	α_M	α_K	α_B	α_T	α_H
$M_*^2 f + 2m_4^2$	$\frac{M_*^2 \dot{f} + 2\left(m_4^2\right)}{M^2 H}$	$\frac{2c + 4M_2^4}{M^2 H^2}$	$\frac{M_*^2 \dot{f} - m_3^3}{2M^2 H}$	$-\frac{2m_4^2}{M^2}$	$\frac{2\left(\tilde{m}_4^2 - m_4^2\right)}{M^2}$

Table 1.2: The dictionary to translate the expressions from one to the other notation.

which parameterizes the time evolution of the Planck mass. The advantage of the previous action is that the parameters are defined such a way that ΛCDM+GR is restored by setting all α_i to zero. Moreover, we can interpret these equations physically while it is difficult in the form (1.141). However, one can interchangeably use either definition and simply translate the results using the dictionary in Table. 1.2 (see Bellini & Sawicki [2014], Frusciante & Perenon [2020] for different notations and the complete dictionary).

1.6.6 Evolution of the cosmological perturbations

In this subsection we assume the action (1.141) and we obtain the equations of the motion. First of all, the variation of the action with respect to the lapse function N and the scale factor a gives the background evolution, which will be useful to simplify higher order equations,

$$\begin{aligned} c + \Lambda &= 3M_*^2 \left(f H^2 + \dot{f} H \right) - \rho_{\mathrm{m}} \,, \\ \Lambda - c &= M_*^2 \left(2f \dot{H} + 3f H^2 + 2\dot{f} H + \ddot{f} \right) + p_{\mathrm{m}} \,. \end{aligned} \tag{1.144}$$

We also only focus on the linear scalar perturbations in the Newtonian gauge while neglecting short wave corrections. However, for the case of k-essence scalar field we will discuss the equations considering all the short-wave corrections in detail in Chapter 2.

The action we previously derived was written based on the ADM decomposition and on the constant scalar field hyper surfaces. By definition the action is invariant under the 3D diffeomorphism and does not respect the full diffeomorphism as the time symmetry was broken in the first place. We can restore diffeomorphism invariance of the action (which is required for the theory) by the Stueckelberg trick. By performing a time-diffeomorphism

$$t \to \tilde{t} = t + \xi^0(t, \vec{x}), \quad \vec{x} \to \vec{x} = \vec{x} \,, \tag{1.145}$$

where $\xi^0(t, \vec{x}) = \pi$ describes the fluctuations of the scalar field:

$$\varphi = t + \pi \,. \tag{1.146}$$

Under this diffeomorphism, any function of time f changes up to second order as

$$f \to f + \dot{f}\pi + \frac{1}{2}\ddot{f}\pi^2 + \mathcal{O}\left(\pi^3\right) , \tag{1.147}$$

while the metric component $g^{00} = -1/N^2$ exactly transforms as

$$g^{00} \to g^{00} + 2g^{0\mu}\partial_\mu\pi + g^{\mu\nu}\partial_\mu\pi\partial_\nu\pi . \tag{1.148}$$

For the other first order geometric quantities, we only need their change due to the time-diffeomorphism at linear order in π,

$$\begin{aligned} \delta K_{ij} &\to \delta K_{ij} - \dot{H}\pi h_{ij} - \partial_i\partial_j\pi + \mathcal{O}\left(\pi^2\right) , \\ \delta K &\to \delta K - 3\dot{H}\pi - \tfrac{1}{a^2}\partial^2\pi + \mathcal{O}\left(\pi^2\right) , \\ {}^{(3)}R_{ij} &\to {}^{(3)}R_{ij} + H\left(\partial_i\partial_j\pi + \delta_{ij}\partial^2\pi\right) + \mathcal{O}\left(\pi^2\right) , \\ {}^{(3)}R &\to {}^{(3)}R + \tfrac{4}{a^2}H\partial^2\pi + \mathcal{O}\left(\pi^2\right) . \end{aligned} \tag{1.149}$$

It is important to note that, although we are not in the unitary gauge anymore the above expressions K_{ij} and R_{ij} sill denote the extrinsic and intrinsic curvature on hypersurfaces of constant time.

We then expand the covariant action up to quadratic order in π and variation of the action with respect to the scalar fluctuation π and the four scalar perturbations in the metric yields five equations for the evolution of the scalars. In the next step we are going to discuss these equations written in the Newtonian gauge.

1.6.7 Evolution of linear perturbations in Newtonian gauge

We consider a linearly perturbed FLRW metric with only scalar fluctuations,

$$ds^2 = -(1+2\Psi)dt^2 + 2\partial_i\alpha\, dt dx^i + a^2(t)\left[(1-2\Phi)\delta_{ij} + 2h_{ij}\right] dx^i dx^j , \tag{1.150}$$

where h_{ij} is traceless and given in terms of the scalar perturbation $\beta, h_{ij} \equiv \left(\partial_i\partial_j - \frac{1}{3}\delta_{ij}\partial^2\right)\beta$. Also here we work with the physical time t instead of the conformal time τ in the metric. However, one can easily write the equations in terms of the conformal time using $d\tau = dt/a(t)$ and also redefining π as $\pi(t,\vec{x}) \doteq \xi^0(t,\vec{x})/a(t)$ which is discussed in Chapter 2. The extrinsic curvature and the 3-dimensional Ricci tensor of the new equal-time hypersurfaces thus read,

$$\begin{aligned} K_{ij} &= e^{-\Psi}(H - \dot{\Phi})h_{ij} + \dot{h}_{ij} - \partial_i\partial_j\alpha , \\ {}^{(3)}R_{ij} &= \partial_i\partial_j\Phi + \delta_{ij}\partial^2\Phi + 2\partial_k\partial_{(i}h^k_{j)} - \partial^2 h_{ij} . \end{aligned} \tag{1.151}$$

We also decompose the matter stress-energy tensor at linear order as

$$\begin{aligned}
T^0_0 &\equiv -\left(\rho_m + \delta\rho_m\right) \\
T^0_i &\equiv \left(\rho_m + p_m\right)\partial_i v = -a^2 T^i_0 \\
T^i_j &\equiv \left(p_m + \delta p_m\right)\delta^i_j + \left(\partial^i\partial_j - \frac{1}{3}\delta^i_j\partial^2\right)\sigma
\end{aligned} \tag{1.152}$$

where ρ_m and p_m are respectively the background energy density and pressure and $\delta\rho_m$ and δp_m their perturbations, v is the 3-velocity potential and σ the scalar component of the anisotropic stress.

To this end, we use the previous expressions (1.147), (1.148), (1.149) and (1.151) to rewrite the action for the scalar fluctuations $\Psi, \alpha, \Phi, \beta$ and π. We then expand the action to second order which is enough to obtain the first order field equations. We then fix the gauge to the Newtonian gauge by setting $\alpha = 0 = \beta$ in the final equations. This procedure yields the following five equations in Fourier space (see Creminelli et al. [2009], Frusciante & Papadomanolakis [2017], Gleyzes [2015], Gleyzes et al. [2013, 2015] for detailed discussions):

$$\begin{aligned}
&(\delta S/\delta\Psi = 0): \\
&M_*^2\Big[-2f\left(\tfrac{k^2}{a^2}\Phi + 3H\dot{\Phi} + 3H^2\Psi\right) + \dot{f}\left(\tfrac{k^2}{a^2}\pi + 3H^2\pi - 3H(\Psi - \dot{\pi}) - 3(\dot{\Phi} + H\Psi)\right) \\
&+3H\ddot{f}\pi\Big] - (\dot{c} + \dot{\Lambda})\pi + (2c + 4M_2^4 + 3Hm_3^3)\left(\Psi - \dot{\pi}\right) \\
&+ (m_3^3 - 4Hm_4^2)\left[-\tfrac{k^2}{a^2}\pi + 3(H\Psi + \pi\dot{H} + \dot{\Phi})\right] - 4\tfrac{k^2}{a^2}\tilde{m}_4^2(\Phi + H\pi) = \delta\rho_m
\end{aligned} \tag{1.153}$$

$$\begin{aligned}
&(\delta S/\delta\alpha = 0): \\
&M_*^2[(H\dot{f} - \ddot{f})\pi + \dot{f}(\Psi - \dot{\pi}) + 2f(H\Psi + \dot{\Phi})] - 2c\pi - m_3^3(\Psi - \dot{\pi}) \\
&+ 4m_4^2(H\Psi + \dot{\Phi} + \dot{H}\pi) = -\left(p_m + \rho_m\right)v
\end{aligned} \tag{1.154}$$

$$
\begin{aligned}
&(\delta S/\delta\alpha = 0): \\
&M_*^2\left\{2f\left[-\frac{1}{3}\frac{k^2}{a^2}(\Psi-\Phi)+\left(3H^2+2\dot{H}\right)\Psi+H(\dot{\Psi}+3\dot{\Phi})+\ddot{\Phi}\right]\right. \\
&+\dot{f}\left[-\frac{2}{3}\frac{k^2}{a^2}\pi+2H\Psi+2H(\Psi-\dot{\pi})-\left(3H^2+2\dot{H}\right)\pi+2\dot{\Phi}+\dot{\Psi}-\ddot{\pi}\right] \\
&\left.+\ddot{f}[-2H\pi+2(\Psi-\dot{\pi})]-f^{(3)}\pi\right\}+(\dot{\Lambda}-\dot{c})\pi+2c(\Psi-\dot{\pi}) \\
&-\tfrac{4}{3}\tfrac{k^2}{a^2}\left[\tilde{m}_4^2(\Psi-\dot{\pi})+\left(Hm_4^2+(m_4^2)^{\cdot}\right)\pi+m_4^2\dot{\pi}\right] \\
&+4\left(\dot{H}m_4^2\right)^{\cdot}\pi+4m_4^2\dot{H}\dot{\pi}-\left[(m_3^3)^{\cdot}+3Hm_3^3\right](\Psi-\dot{\pi})-m_3^3(\dot{\Psi}-\ddot{\pi}) \\
&+4\left[H\left(m_4^2\right)^{\cdot}+3H^2m_4^2+\dot{H}m_4^2\right]\Psi \\
&+4\left(m_4^2\right)\dot{\Phi}+4m_4^2H(3\dot{H}\pi+\dot{\Psi}+3\dot{\Phi})+4m_4^2\ddot{\Phi}=\delta p_m
\end{aligned}
\tag{1.155}
$$

$$
\begin{aligned}
&(\delta S/\delta\Phi = 0): \\
&M_*^2\left\{2f\left[-\tfrac{1}{3}\tfrac{k^2}{a^2}(\Psi-\Phi)+\left(3H^2+2\dot{H}\right)\Psi+H(\dot{\Psi}+3\dot{\Phi})+\ddot{\Phi}\right]\right. \\
&+\dot{f}\left[-\tfrac{2}{3}\tfrac{k^2}{a^2}\pi+2H\Psi+2H(\Psi-\dot{\pi})-\left(3H^2+2\dot{H}\right)\pi+2\dot{\Phi}+\dot{\Psi}-\ddot{\pi}\right] \\
&\left.+\ddot{f}[-2H\pi+2(\Psi-\dot{\pi})]-f^{(3)}\pi\right\}+(\dot{\Lambda}-\dot{c})\pi+2c(\Psi-\dot{\pi}) \\
&-\tfrac{4}{3}\tfrac{k^2}{a^2}\left[\tilde{m}_4^2(\Psi-\dot{\pi})+\left(Hm_4^2+(\dot{m}_4^2)\right)\pi+m_4^2\dot{\pi}\right] \\
&+4\left(\dot{H}m_4^2\right)^{\cdot}\pi+4m_4^2\dot{H}\dot{\pi}-\left[(m_3^3)^{\cdot}+3Hm_3^3\right](\Psi-\dot{\pi})-m_3^3(\dot{\Psi}-\ddot{\pi}) \\
&+4\left[H\,(m_4^2)^{\cdot}+3H^2m_4^2+\dot{H}m_4^2\right]\Psi+4\,(m_4^2)\,\dot{\Phi} \\
&+4m_4^2H(3\dot{H}\pi+\dot{\Psi}+3\dot{\Phi})+4m_4^2\ddot{\Phi}=\delta p_m
\end{aligned}
\tag{1.156}
$$

$$
\begin{aligned}
&(\delta S/\delta\beta = 0): \\
&M_*^2[f(\Psi-\Phi)+\dot{f}\pi]+2\left[m_4^2\dot{\pi}+m_4^2H\pi+(m_4^2)^{\cdot}\,\pi\right]+2\tilde{m}_4^2(\Psi-\dot{\pi})=\sigma
\end{aligned}
\tag{1.157}
$$

1.6.8 Short-wave corrections

In order to include the higher order short-wave corrections to the EFT of DE we need to be careful. In fact, it is as simple as assuming the second order action (1.141) and going to the higher order in Stueckelberg trick Stueckelberg [1938] and considering higher order in π terms. Instead, we also need to write down the appropriate EFT action from the scratch to consider higher order contributions. The main difficulty usually is that for some theories the corresponding action including all the short wave corrections is not truncated automatically at some order and we need to truncate the expansion by considering further assumptions, like considering a cut off energy scale in the theory.

However, as it is discussed in detail in Chapter 2 for the k-essence theory in the EFT framework, we can prove that we do not need to construct the higher order action as the action (1.141) is enough to obtain the field equations consistently while considering all the relevant short-wave corrections.

1.7 Cosmological N-body simulations

According to the cosmological observations at small scales the Universe occupied by non-linear, many-body and difficult to deal structures, like galaxies, clusters of galaxies and others. These complex structures are formed as a result of non-linear collapse of small initial perturbations in the early Universe. The main difficulty to deal with these structures is that the perturbation theory breaks down at these scales[10] and we can not use our developed tools to describe these structures anymore. In the absence of analytical approaches, numerical N-body simulations are the only option to deal with non-linear regime and model the Universe at these scales.

The first numerical N-body simulation starts with Holmberg in 1941 Holmberg [1941], where he tried to solve the evolution of a 37 particle system (shown in Fig. 1.4), and he took the advantage of similar r^{-2} scaling of electromagnetic and gravitational interactions to compute the force using lightbulbs and galvanometers. Computer N-body simulations started in the early 1960's simulating up to 100 particles (von Hoerner [1960] and Aarseth [1963]) and then the golden age of N-body simulations started in the 1980's with the development of fast and efficient algorithms such as the particle-mesh technique (see Hockney & Eastwood [1988]) and the tree method Barnes & Hut [1986] as well as the progresses in the computer hardwares (for a historical review see Hockney & Eastwood [1988], Trenti & Hut [2008]). Today (2020) thanks to technology and advanced algorithms, N-body simulations can be performed with beyond $N \approx 10^{13}$ particles.

Apart from helping us to explore the non-linear regime, the are several other applications in using the cosmological N-body simulations Bagla [2005], Bagla & Padmanabhan [1997], Bertschinger [1998], Hockney & Eastwood [1988], Stadel [2001]:

---

[10] the density of these structures is about 1000 times larger than the average density of the Universe

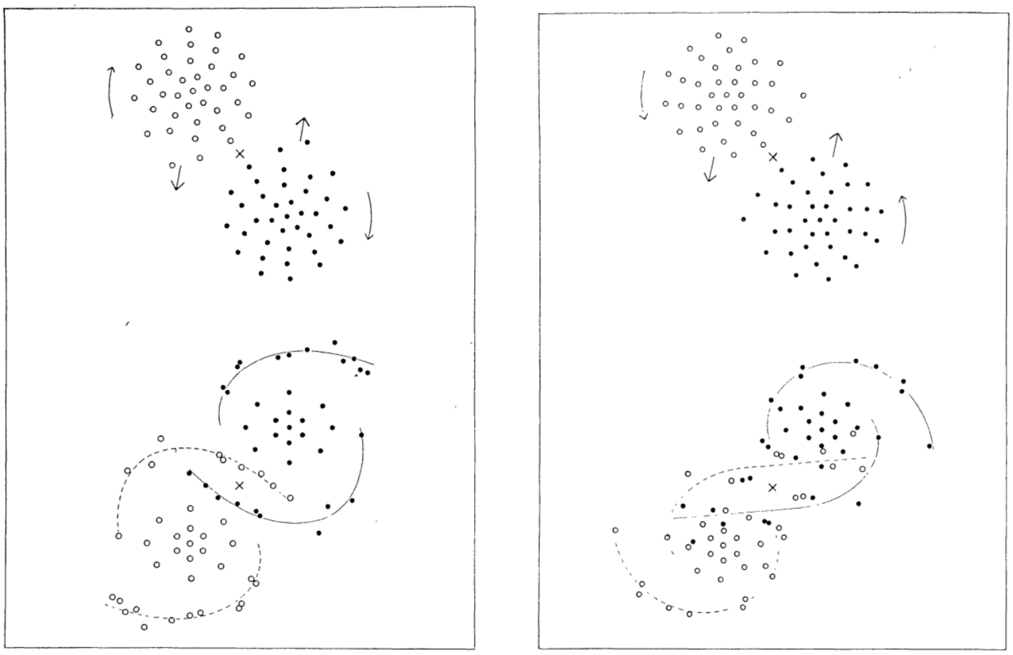

FIG. 4*a*

FIG. 4*b*

FIG. 4*a*.—Tidal deformations corresponding to parabolic motions, clockwise rotations, and a distance of closest approach equal to the diameters of the nebulae. The spiral arms point in the direction of the rotation.

FIG. 4*b*.—Same as above, with the exception of counterclockwise rotations. The spiral arms point in the direction opposite to the rotation.

Figure 1.4: A figure in the original paper of Holmberg showing the interaction of two spiral galaxies

- First, we can make predictions for non-standard cosmologies such as different dark matter and dark energy scenarios.

- Second, N-body simulations give us the chance to compare the results with observations.

- Third, the simulations are helpful for testing approximate solutions and perturbation theory at intermediate scales. Comparing the approximative results with the true solution from the N-body simulations help us to validate the approximations and to understand the range of validity of these approximations.

- Last but not least, we can calibrate our methods for observation on mock catalogues made using N-body simulations. For example we can test if a method works, as in an N-body code we can extract all the details whereas is not the case in the observation.

1.7.1 Physical requirements

When writing an N-body code the following criteria need to be taken into account Adamek et al. [2016a], Bagla [2005], Bagla & Padmanabhan [1997], Hockney & Eastwood [1988], Padmanabhan [1996], Stadel [2001];

- In an N-Body simulation, the Universe should be filled with cosmological components over large scales (much larger than the scales we want to probe). The simulation volume should not be isolated and we need to have access to the outside region of the volume using a method. The best solution to this problem is to assume the periodic boundary conditions. In fact, using other boundary conditions than periodic, the structure in the simulation box will have a tendency to cluster towards the centre of the simulation box, which results into a fake large growth rate for cosmological perturbations.

- The best option for distributing the masses N objects is to consider equal mass. Because having a volume dominated by one object produces a fake dynamics as a result of the tidal force due to dominated object's periodic copies.

- The average density in the box should be equal to the average density of the Universe. This means that the perturbations averaged at the scale of the N-body box must vanish at all times. For example, in case of ΛCDM we would require that the box to be large than 100 h^{-1}Mpc in which is the scale we have a maximally symmetric Universe.

- There is a required minimum number of particles in order to satisfy the previous argument as well as the fact that in an N-body code we want to probe scales that are sufficiently non-linear. For example if we want to compare the galaxies in cosmological context, we need to have the resolution such that the individual masses are less than the mass of the smallest object of interest. As a result the minimum number of particles we require to have to study galaxy clustering should be Bagla & Padmanabhan [1997]:

$$N \geq \frac{M\,(100h^{-1}\mathrm{Mpc})}{M_{\mathrm{galaxy}}} \simeq \frac{5\times 10^{18} M_\odot}{10^{11} M_\odot} \simeq 5\times 10^{7}\,. \tag{1.158}$$

- Due to the limited computational power, we effectively replace a collection of a very large number of particles in the universe by one particle in an N-body simulation . Thus the N-body particles must interact in a collisionless way.

In order to integrate the equations of motion in an N-body code we need to perform of order $\mathcal{O}\left(N_p\right)$ operations. While to compute the force exerted on all N_p particles (summing the force over all pairs) would require of order $\mathcal{O}\left(N_p^2\right)$ operations. For large number of particles it can be shown that direct computation of forces takes a long time and very fast reaches to our available computational resources. In order to overcome the force computation problem, three different schemes have been proposed Bagla & Padmanabhan [1997], Hockney & Eastwood [1988], Stadel [2001];

- Particle Mesh (PM) scheme : The Poisson equation (Hamiltonian constraint) is solved in Fourier space using an appropriate numerical technique and the potential/force is computed on a fixed grid on the lattice. To update the particles positions and velocities, the force and potentials are interpolated to particle positions on the lattice. Then the density and velocity fields (the source for Poisson equation) are also computed on the same mesh(grid) by using an interpolating function from the particle positions. It is worth mentioning that the smoothing of particles over the grid size restricts the resolution of such simulations but guarantees collisionless evolution of N-body particles (see Bouchet & Kandrup [1985], Bouchet et al. [1985]).

- Particle-Particle-Particle Mesh ($\mathrm{P}^3\mathrm{M}$) : This scheme introduced in Efstathiou et al. [1985] is similar to the PM scheme but it improves the PM method by considering a correction to the force for pairs with separation equal or smaller than the grid length. The number of operations needed for this correction is proportional to $N_p\bar{n}$ where $\bar{n}$ is the average number of particles within cell. In this scheme for large number of particles, the number of operations in the dense regions could become very large.

- Tree : In this scheme, the force on a particle is computed according to a hierarchical tree, where in each level of the tree the total mass and the position of the centre of mass is described. The force from distant particles in the box of the simulation is approximated by the force from the centre of mass of particles in that region. This approximation reduces the number of operations for calculating force significantly (see Barnes & Hut [1986], Bouchet & Hernquist [1988])

  Among the previous methods the Particle-Mesh scheme has two major advantages over the other schemes. First, It is the only method for which a collisionless dynamics is guaranteed. Second, it has the simplest algorithm, the fastest method and naturally appropriate for developing "relativistic" N-body codes as one works with the fields in this scheme rather than forces.

1.7.2 Newtonian N-body codes

In these codes the evolution of perturbations are studied in a non-relativistic medium in an expanding background. The Newtonian N-body codes are expected to work in the Newtonian limit at scales that are much smaller than the Hubble horizon (see Fidler et al. [2016] for the relativistic Interpretation of Newtonian simulations). The equations for a set of particles interacting only through the gravitational force can be written as

$$\begin{aligned} &\ddot{\mathbf{x}} + 2\tfrac{\dot{a}}{a}\dot{\mathbf{x}} = -\tfrac{1}{a(\tau)^2}\nabla_x \varphi_N, \\ &\nabla_x^2 \varphi_N = 4\pi G a^2 \bar{\rho}\delta = \tfrac{3}{2}H_0^2\Omega_0\tfrac{\delta}{a}, \end{aligned} \tag{1.159}$$

where φ_N is the Newtonian gravitational potential, which is made using the Newtonian limit of the relativistic Poisson equation (1.88). Three well known Newtonian N-body codes are:

RAMSES is an N-body particle mesh code that works with adaptive mesh refinements (AMR) technique Teyssier [2002a]. In this code particles are evolved on Newtonian orbits using a leapfrog method and also includes a solver to study the evolution of baryons. The Cloud-In-Cell (CIC) scheme is used to perform the particle-to-mesh projection and force interpolation.

GADGET In the GADGET code the gravitational forces are computed with a hierarchical tree algorithm, also a particle-mesh scheme for long-range gravitational forces is available. Both the force and the time stepping in GADGET code are adaptive Springel [2005].

PKDGRAV PKDGRAV Stadel [2001] is a tree based simulation code that constructs a k -d tree. In PKDGRAV3 the Fast Multipole Method in conjunction with individual and adaptive particle time steps are used on supercomputers with GPU-accelerated nodes Potter et al. [2016].

1.7.3 Relativistic N-body codes

The N-body simulations we mentioned in the previous subsection use Newton's law of gravitation to evolve the particles. An important question that arises about these simulations is that whether and how much the Newtonian approximation is valid considering the high precision we need in current era of cosmology. It turn out that the Newtonian limit works comparatively well in the ΛCDM model if we neglect radiation in the late time Universe and assume that there is only non-relativistic matter as the source of perturbations. However, a Newtonian scheme is not appropriate for considering the relativistic sources especially at scales near the Hubble horizon and also is not compatible with the presence of radiation which might have a small effect on the evolution of cosmic structure (see Adamek et al. [2016a], Adamek et al. [2016c], Adamek et al. [2017b] for detailed discussion).

In addition, the Newtonian N-body simulations are not naturally appropriate for considering non-standard dark energy/modified gravity scenarios, as a result some approximations has to be made in the Newtonian schemes in order to implement non-standard scenarios mainly because of the fact that dark energy opposed to dark matter and baryons is not dominated completely by its rest-mass density and thus requires a relativistic treatment.

gevolution is a relativistic N-body code was developed based on the Particle-Mesh scheme. In this code, the continuous fields e.g., the metric perturbations or the stress-energy tensor components are discretized on the lattice grids. The relativistic partial differential equations are solved numerically on the lattice grids using the finite-difference method. While the fields are defined on the lattice grids the positions and momenta of N-body particles can have arbitrary values. The values of the fields and the distribution of the particles should be consistent as they depend on each other according to the projection and interpolation procedures (see Adamek et al. [2020a] for a discussion about comparison between different relativistic N-body codes and their numerical solution to the fields equations).

k-evolution As a first step toward the goal of implementing the full EFT of DE in gevolution we have developed the k-evolution code Hassani et al. [2019c] which is represented completely in Chapter 2. In k-evolution we have added a k-essence scalar field expressed in the EFT framework. In the Fig. 1.5 the main loop of k-evolution is illustrated.

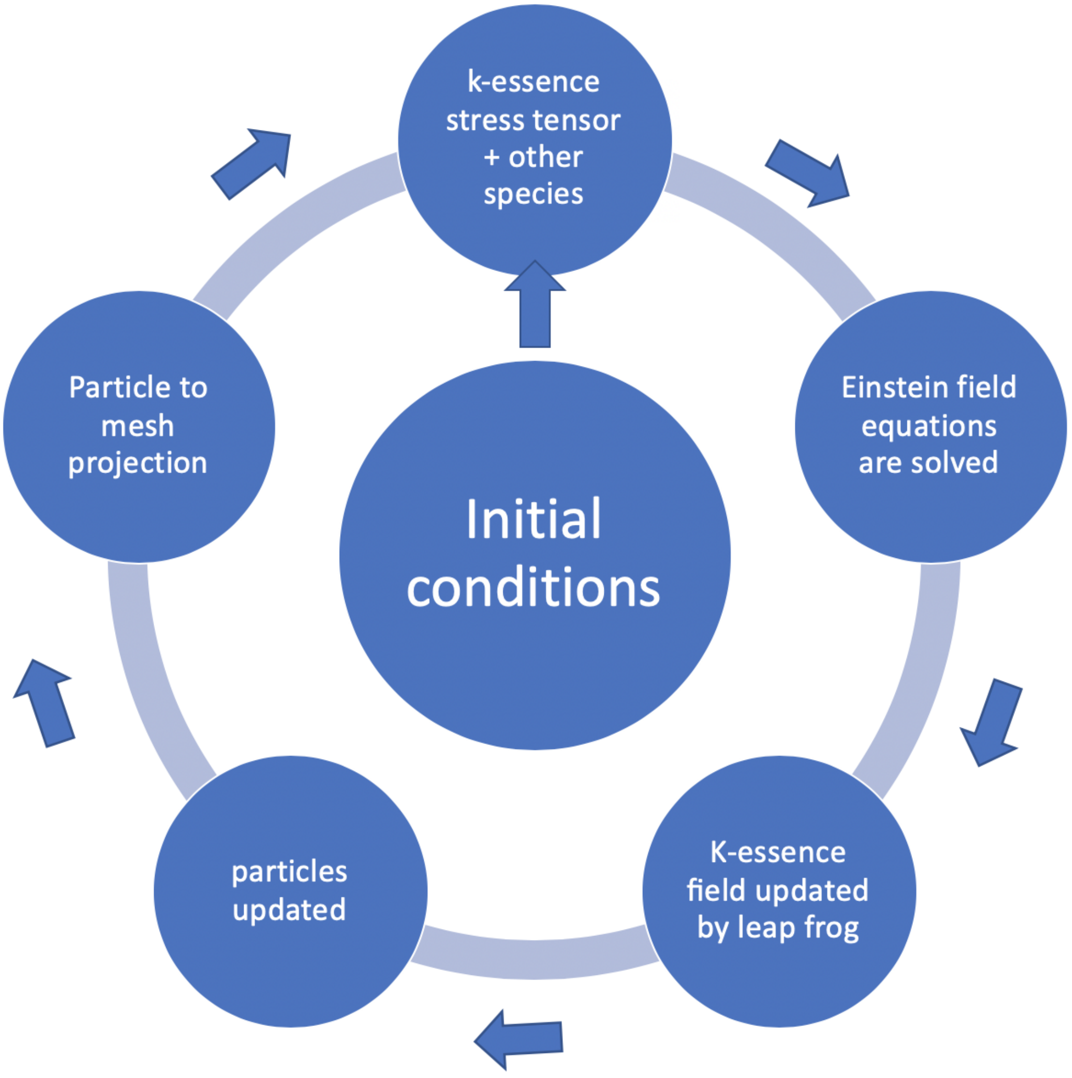
k-essence stress tensor + other species
Einstein field equations are solved
K-essence field updated by leap frog
particles updated
Particle to mesh projection
Initial conditions

Figure 1.5: The schematic picture showing the main loop of k-evolution code.

Chapter 2

K-EVOLUTION: A RELATIVISTIC N-BODY CODE FOR CLUSTERING DARK ENERGY

Based on:

Hassani et al. [2019a] Farbod Hassani(Geneva U., Dept. Theor. Phys.), Julian Adamek (Queen Mary, U. of London), Martin Kunz (Geneva U., Dept. Theor. Phys.), Filippo Vernizzi (IPhT, Saclay)
k-evolution: a relativistic N-body code for clustering dark energy, JCAP 12 (2019) 011, [arXiv: 1910.01104]

Abstract: We introduce k-evolution, a relativistic N-body code based on *gevolution*, which includes clustering dark energy among its cosmological components. To describe dark energy, we use the effective field theory approach. In particular, we focus on k-essence with a speed of sound much smaller than unity but we lay down the basis to extend the code to other dark energy and modified gravity models. We develop the formalism including dark energy non-linearities but, as a first step, we implement the equations in the code after dropping non-linear self-coupling in the k-essence field. In this simplified setup, we compare k-evolution simulations with those of `CLASS` and *gevolution* 1.2, showing the effect of dark matter and gravitational non-linearities on the power spectrum of dark matter, of dark energy and of the gravitational potential. Moreover, we compare k-evolution to Newtonian N-body simulations with back-scaled initial conditions and study how dark energy clustering affects massive halos.

2.1 Introduction

The physical reason for the observed acceleration of the Universe Riess et al. [1998a] is one of the most important mysteries in cosmology, and arguably generally in fundamental physics. Although cosmology has been revolutionised by the arrival of high quality observations that have allowed to pin down many parameters of the standard model Planck Collaboration et al. [2018], the dark sector is still compatible with a cosmological constant and collisionless cold dark matter. This is one motivation for the next generation of large galaxy surveys like Amendola et al. [2016], Santos et al. [2015b] that will observe billions of galaxies to provide galaxy number counts and weak lensing measurements.

But much of this data will probe scales that are mildly or strongly non-linear, a regime that is not well modelled even for the Lambda-cold-dark matter (ΛCDM) standard model Jalilvand et al. [2020]. In this paper we start a systematic study of the effects of dark energy on cosmological structure formation in the non-linear regime. We will do so by implementing dark energy in the relativistic N-body simulation code *gevolution* Adamek et al. [2016a], Adamek et al. [2016b]. The *gevolution* code works in the weak field limit of General Relativity (GR), which makes it easy to include additional relativistic fields. To model dark energy theories, we will use the Effective Field Theory of dark energy (EFT of DE) approach (see e.g. Gubitosi et al. [2013a] and references below; see also Cusin et al. [2018b], Frusciante & Papadomanolakis [2017] for studies of the non-linear action in the EFT of DE approach and Cusin et al. [2018a] for an application to perturbation theory beyond linear order). The EFT of DE allows one to describe, in a relativistic setting and with a minimal set of parameters, very general dark energy and modified gravity models based on a single scalar degree of freedom. The use of *gevolution* allows to combine both the EFT of DE and the weak field expansion systematically, paving the way for N-body simulations of a wide class of dark energy and modified gravity models.

In this first paper we illustrate the approach specifically with the example of k-essence Armendariz-Picon et al. [2000, 2001]. After a brief reminder of the basics of the EFT of DE framework in Sec. 2.2, we derive the relevant equations (with more details given in App. 2.A) and briefly discuss their practical implementation in our new code, k-evolution. We refer the reader to App. 2.B for more details on the numerical implementation of the dark energy equations and to App. 2.C for a discussion on gauge issues when comparing with linear codes and setting the initial conditions.

Then, in Sec. 2.3 we present a detailed analysis of the power spectra computed with k-evolution and compare the spectra to those obtained with other numerical codes. In Sec. 2.4 we examine snapshots of the dark energy simulations computed with k-evolution with particular attention to the environment of massive clusters. Finally, we conclude in Sec. 2.5.

Due to its complexity, the full non-linear treatment of the dark energy perturbation equations requires a dedicated study that will be addressed in a separate publication. (See however App. 2.D where we study the evolution of non-linear perturbations in the limit of small speed of sound and in matter domination.) In this paper we limit the simulations to the linear k-essence equations, although these equations are coupled to the non-linear clustering of the dark matter, which can in turn lead to non-linear clustering of the dark energy. This approach will be called k-evolution in the following. We compare it to the fully linear treatment implemented in version 1.2 of *gevolution*[1] that uses a realisation of the linear fluid transfer functions from `CLASS` Blas et al. [2011a] in the w-c_s^2-parametrisation and is presented here for the first time, as well as to a standard N-body simulation where only the background evolution is changed according to the equation of state w, without allowing for perturbations in the dark energy.

2.2 The EFT of k-essence

In this section we introduce the effective field theory description of dark energy and we derive the relevant equations for its implementation in *gevolution*. We assume that matter – the dark matter and the Standard Model particles – is minimally coupled to the gravitational metric $g_{\mu\nu}$. Moreover, as explained in the introduction, we consider theories with a preferred time-slicing induced by the evolution of a scalar field and we focus on operators describing general scalar-field Lagrangians that can be constructed out of the field value ϕ and its first derivatives contracted with $g_{\mu\nu}$, i.e., $X \doteq g^{\mu\nu}\partial_\mu\phi\partial_\nu\phi$. In the covariant language, the action describing this class of theories is

---

[1] `https://github.com/gevolution-code/gevolution-1.2.git`

$$S_{\rm DE} = \int d^4x\sqrt{-g}P(X,\phi)\ , \tag{2.1}$$

which is also known as k-essence Armendariz-Picon et al. [2000, 2001].

2.2.1 The action and the homogeneous equations

To describe the dark energy fluctuations we adopt the EFT of DE description Bloomfield [2013], Bloomfield et al. [2013], Creminelli et al. [2009], Gleyzes et al. [2013], Gubitosi et al. [2013a] (see also Frusciante & Perenon [2020], Gleyzes et al. [2015], Piazza & Vernizzi [2013], Tsujikawa [2015] for reviews; for other effective relativistic approaches, see for instance Baker et al. [2011, 2013], Battye & Pearson [2012], Bellini & Sawicki [2014], Lagos et al. [2016]), which is particularly convenient for studying fluctuations around cosmological FRW solutions with a preferred slicing induced by the time-dependent background scalar field. In the unitary gauge, where the time coincides with uniform-field hypersurfaces, the EFT action expanded around a spatially flat background reads Cheung et al. [2008], Creminelli et al. [2009]

$$S = \int d^4x\sqrt{-g}\left[\frac{M_{\rm Pl}^2}{2}R - \Lambda(t) - c(t)g^{00} + \frac{M_2^4(t)}{2}\left(\delta g^{00}\right)^2 + \dots\right]\ , \tag{2.2}$$

where R is the four-dimensional Ricci scalar, $\Lambda(t)$, $c(t)$, and $M_2^4(t)$ are time-dependent functions and δg^{00} is the perturbation of g^{00} around its homogeneous value. The ellipsis stands for terms that are of higher order in the fluctuations δg^{00}. These terms can be ignored because they are negligible in the weak-field expansion adopted by *gevolution* (see e.g. Refs. Cusin et al. [2018b] for details). We will come back to this point at the beginning of Sec. 2.2.3.

The functions $\Lambda(t)$ and $c(t)$ are not independent; they can be expressed in terms of the background expansion and matter quantities through the homogenous Friedmann equations. Varying the action with respect to the homogenous lapse $N(t)$ and the scale factor $a(t)$, appearing in the homogenous metric as $ds^2 = -N^2(t)dt^2 + a^2(t)d\vec{x}^2$, we obtain

$$\frac{\dot{a}^2}{a^2} \doteq H^2 = \frac{1}{3M_{\rm Pl}^2}\left(\rho_{\rm m} + c + \Lambda\right)\ , \tag{2.3}$$

$$\frac{\ddot{a}}{a} = \dot{H} + H^2 = -\frac{1}{6M_{\rm Pl}^2}\left(\rho_{\rm m} + 3p_{\rm m} + 4c - 2\Lambda\right)\ , \tag{2.4}$$

where $\rho_{\rm m}$ and $p_{\rm m}$ are respectively the homogeneous matter energy density and pressure.

The stress-energy tensor of dark energy can be computed from the above action as

$$T_{\mu\nu} = -\frac{2}{\sqrt{-g}} \frac{\delta S_{\rm DE}}{\delta g^{\mu\nu}} \ , \tag{2.5}$$

where $S_{\rm DE}$ is the action without the Einstein-Hilbert term. In unitary gauge one finds

$$T_{\mu\nu} = -\left[\Lambda + c g^{00} - \frac{M_2^4}{2} (\delta g^{00})^2 \right] g_{\mu\nu} + 2(c - M_2^4 \delta g^{00}) \delta_\mu^0 \delta_\nu^0 \ . \tag{2.6}$$

The homogeneous part of the stress-energy tensor is obtained by taking $g^{00} = -1$ and $\delta g^{00} = 0$ in the above expression. Rewriting its components in terms of the homogeneous energy density $\rho_{\rm DE}(t)$ and pressure $p_{\rm DE}(t)$ of the dark energy, using $T_{00} = \rho_{\rm DE}(t)$ and $T_{ij} = \delta_{ij} p_{\rm DE}(t)$, we obtain

$$c(t) = \frac{1}{2} \left[\rho_{\rm DE}(t) + p_{\rm DE}(t) \right] \ , \qquad \Lambda(t) = \frac{1}{2} \left[\rho_{\rm DE}(t) - p_{\rm DE}(t) \right] \ , \tag{2.7}$$

which is consistent with the Friedmann equations above. Moreover, using these expressions, taking the derivative with respect to time of Eq. (2.3) and using Eq. (2.4) we can also check that the Friedmann equations are consistent with the homogeneous continuity equation for dark energy, i.e.,

$$\dot\rho_{\rm DE} + 3H(\rho_{\rm DE} + p_{\rm DE}) = 0 \ , \tag{2.8}$$

as expected. From Eq. (2.7), this implies that c and Λ satisfy $\dot c + \dot\Lambda + 6Hc = 0$.

2.2.2 Stückelberg trick to conformal time

To study the cosmological perturbations in this setup, it is convenient to adopt a gauge where the perturbations of the scalar field are explicit. We can restore diffeomorphism invariance of the action by the Stückelberg trick Cheung et al. [2008], Gleyzes et al. [2013], i.e., by performing a time-diffeomorphism

$$t \to \tilde t = t + \xi^0(t, \vec x) \ , \qquad \vec x \to \tilde{\vec x} = \vec x \ , \tag{2.9}$$

and promoting the parameter ξ^0 to a field. In the following, however, instead of using cosmic time t we will present the evolution equations with the conformal time η, which is related to t by $\eta \doteq \int dt/a(t)$. For this reason, instead of defining the Goldstone boson of broken time diffeomorphisms π as the parameter of the time diffeomorphism ξ^0 Cheung et al. [2008], we will adopt a definition adapted to the conformal time η. In particular, we will define π as ξ^0 divided by the scale factor, i.e.,

$$\pi(t, \vec x) \doteq \xi^0(t, \vec x)/a(t) \ . \tag{2.10}$$

We can now compute how the quantities in the action (2.2) change under the time-transformation above, paying attention to expressing the cosmic time quantities in terms of conformal time. The Ricci scalar does not change under the transformation (2.9), while g^{00} transforms as

$$\begin{aligned} g^{00}(t,\vec{x}) \to \tilde{g}^{00}(\tilde{t}(\eta,\vec{x}),\vec{x}) &= \frac{\partial\tilde{t}(\eta,\vec{x})}{\partial x^{\mu}}\frac{\partial\tilde{t}(\eta,\vec{x})}{\partial x^{\nu}}g^{\mu\nu}(t(\eta),\vec{x}) \\ &= \frac{\partial\left[t(\eta)+a(\eta)\pi(\eta,\vec{x})\right]}{\partial x^{\mu}}\frac{\partial\left[t(\eta)+a(\eta)\pi(\eta,\vec{x})\right]}{\partial x^{\nu}}g^{\mu\nu}(\eta,\vec{x})\ , \end{aligned} \tag{2.11}$$

which gives

$$g^{00}(t,\vec{x}) \to \tilde{g}^{00}(t,\vec{x}) = a^{2}\Big[(1+\mathcal{H}\pi)^{2}g^{00}+2(1+\mathcal{H}\pi)g^{0\mu}\partial_{\mu}\pi+g^{\mu\nu}\partial_{\mu}\pi\partial_{\nu}\pi\Big]\ , \tag{2.12}$$

where the untilded metric on the right-hand side is the one in conformal time.

Any function of time, instead, transforms as

$$\begin{aligned} f(t) \to \tilde{f}\left(\tilde{t}(\eta,\vec{x})\right) &= f\left(t(\eta)+a(\eta)\pi(\eta,\vec{x})\right) \\ &= f(\eta)+f'(\eta)\pi(\eta,\vec{x})+\frac{1}{2}\left[f''(\eta)-\mathcal{H}(\eta)f'(\eta)\right]\left[\pi(\eta,\vec{x})\right]^{2}+\dots\ , \end{aligned} \tag{2.13}$$

where $\mathcal{H} \doteq a'/a$ is the conformal Hubble rate. Applying these transformations to the action (2.2), we can derive the fully covariant action,

$$\begin{aligned} S = \int d^{4}x\sqrt{-g}\Bigg\{&\frac{M_{\rm Pl}^{2}}{2}R-\Lambda\left[t(\eta)+a(\eta)\pi\right]-c\left[t(\eta)+a(\eta)\pi\right]a^{2}(\eta)\Big[(1+\mathcal{H}\pi)^{2}g^{00} \\ &+2(1+\mathcal{H}\pi)g^{0\mu}\partial_{\mu}\pi+g^{\mu\nu}\partial_{\mu}\pi\partial_{\nu}\pi\Big]+\frac{M_{2}^{4}\left[t(\eta)+a(\eta)\pi\right]}{2} \\ &\times a^{4}(\eta)\Big[(1+\mathcal{H}\pi)^{2}g^{00}+2(1+\mathcal{H}\pi)g^{0\mu}\partial_{\mu}\pi+g^{\mu\nu}\partial_{\mu}\pi\partial_{\nu}\pi-\bar{g}^{00}\Big]^{2}\Bigg\}\ , \end{aligned} \tag{2.14}$$

where we have used that the Ricci scalar R does not transform, and in the last term we have introduced $\bar{g}^{00}$, the background value of g^{00}, i.e., $\bar{g}^{00} = -1/a^{2}$.

Finally, using the definition (2.5), we can write the expression of the stress-energy tensor, which reads

$$\begin{aligned} T_{\mu\nu} = &-\Big\{\Lambda\left(t+a\pi\right)+c\left(t+a\pi\right)a^{2}\Big[(1+\mathcal{H}\pi)^{2}g^{00}+2(1+\mathcal{H}\pi)g^{0\rho}\partial_{\rho}\pi+g^{\rho\sigma}\partial_{\rho}\pi\partial_{\sigma}\pi\Big] \\ &-\frac{M_{2}^{4}\left(t+a\pi\right)}{2}a^{4}\Big[(1+\mathcal{H}\pi)^{2}g^{00}+2(1+\mathcal{H}\pi)g^{0\rho}\partial_{\rho}\pi+g^{\rho\sigma}\partial_{\rho}\pi\partial_{\sigma}\pi-\bar{g}^{00}\Big]^{2}\Big\}g_{\mu\nu} \\ &+2\Big[(1+\mathcal{H}\pi)^{2}\delta^{0}_{\mu}\delta^{0}_{\nu}+2(1+\mathcal{H}\pi)\delta^{0}_{(\mu}\partial_{\nu)}\pi+\partial_{\mu}\pi\partial_{\nu}\pi\Big]\Big\{c\left(t+a\pi\right)a^{2} \\ &-M_{2}^{4}\left(t+a\pi\right)a^{4}\Big[(1+\mathcal{H}\pi)^{2}g^{00}+2(1+\mathcal{H}\pi)g^{0\rho}\partial_{\rho}\pi+g^{\rho\sigma}\partial_{\rho}\pi\partial_{\sigma}\pi-\bar{g}^{00}\Big]\Big\}\ . \end{aligned} \tag{2.15}$$

This expression is fully nonlinear and can be expanded at any given order in perturbations. In deriving it, we only assumed that higher powers of δg^{00} in the action (2.2) are negligible in the weak field limit, which we justify below.

2.2.3 Perturbations

To study the perturbations, we will use the Poisson gauge, where the metric reads

$$ds^2 = a^2(\eta)\left[-e^{2\Psi}d\eta^2 - 2B_i dx^i dt + (e^{-2\Phi}\delta_{ij} + h_{ij})dx^i dx^j\right] \,, \tag{2.16}$$

where $\delta^{ij}\partial_j B_i = 0$ and $\delta^{ij}h_{ij} = 0 = \delta^{ij}\partial_i h_{jk}$.

In *gevolution* it is assumed that the metric perturbations remain small at the scales of interest. This is implemented by defining a small parameter ϵ, such that Φ, Ψ, B_i and h_{ij} are at most of order $\mathcal{O}(\epsilon)$. For non-relativistic sources, time derivatives are of order Hubble and do not change the order of a term in the expansion. Instead, each spatial derivative lowers the order of a given term by one half, so that for instance $\partial_i\Phi \sim \mathcal{O}(\epsilon^{1/2})$ and $\nabla^2\Phi \sim \mathcal{O}(\epsilon^0)$, where $\nabla^2 \doteq \delta^{ij}\partial_i\partial_j$ defines the Laplacian. We refer the reader to Refs. Adamek et al. [2016a, 2017b] for details.

The Einstein-Hilbert term in the action (2.2) contains at least two spatial derivatives of the metric so that the order of this term is $n-1$, where n is the order of the expansion in metric perturbations. For instance, in *gevolution* one expands the Einstein tensor up to second order in the metric perturbations, which for the terms containing two spatial derivatives corresponds to going at most at order $\mathcal{O}(\epsilon)$ in the equations of motion. The Einstein tensor up to this order can be obtained by varying the Einstein-Hilbert term expanded up to order $\mathcal{O}(\epsilon^2)$. To be coherent with this scheme, we have to keep all the terms in the action that contribute at most to $\mathcal{O}(\epsilon^2)$.

To evaluate the order of an operator in the EFT of DE action, we need to look at the scalar field perturbation π. On large scales, linear cosmological perturbation theory is recovered. In this case π is of the same order as the metric perturbations. In particular, using the scaling above we have

$$\pi \sim \mathcal{O}(\epsilon) \,, \qquad \partial_i\pi \sim \mathcal{O}(\epsilon^{1/2}) \,, \qquad \nabla^2\pi \sim \mathcal{O}(\epsilon^0) \,. \tag{2.17}$$

For instance, this means that we need to expand the operator Λ up to second order in π using Eq. (2.13). Moreover, by Eq. (2.12) δg^{00} is at least of order $\mathcal{O}(\epsilon)$, which implies that any operators of order higher that $(\delta g^{00})^2$ can be neglected, which justifies truncating the action (2.2) at this order.

We can now discuss the field equations. Variation of the action with respect to π gives the evolution equation for the perturbation of the scalar field. For later purposes, it is convenient to introduce the variable

$$\zeta \doteq \pi' + \mathcal{H}\pi - \Psi \ , \tag{2.18}$$

and express the first and second time-derivative of π in terms of ζ and ζ'. Using the conservation equation (2.8), which in terms of the conformal time reads

$$\rho' = -3\mathcal{H}(\rho + p) \ , \tag{2.19}$$

by varying the action we obtain the following system of coupled equations:

$$\begin{aligned}
\pi' &= \zeta - \mathcal{H}\pi + \Psi \ , && (2.20)\\
\zeta' &= (3c_a^2 + s)\mathcal{H}\zeta - 3c_s^2\left(\mathcal{H}^2\pi - \mathcal{H}\Psi - \mathcal{H}'\pi - \Phi'\right) + c_s^2\nabla^2\pi \\
&\quad - \vec{\nabla}\left[2(c_s^2 - 1)\zeta + c_s^2\Phi - \Psi\right]\cdot\vec{\nabla}\pi - \left[(c_s^2 - 1)\zeta + c_s^2\Phi - c_s^2\Psi\right]\nabla^2\pi \\
&\quad - \frac{\mathcal{H}}{2}\left[(2 + 3c_a^2 + c_s^2 + s)(\vec{\nabla}\pi)^2 + 6c_s^2(1 + c_a^2)\pi\nabla^2\pi\right] + \frac{c_s^2 - 1}{2}\partial_i\left(\partial_i\pi(\vec{\nabla}\pi)^2\right) \ , && (2.21)
\end{aligned}$$

where we have introduced the speed of propagation squared of dark energy fluctuations, c_s^2, its rate of change, s, and the adiabatic speed of sound squared (which generally differs from the speed of propagation) c_a^2. These are respectively defined as[2]

$$c_s^2 \doteq \frac{c}{c + 2M_2^4} \ , \qquad s \doteq \frac{(c_s^2)'}{c_s^2\mathcal{H}} \ , \qquad c_a^2 \doteq \frac{p'}{\rho'} = \frac{\Lambda' - c'}{c' + \Lambda'} \ , \tag{2.22}$$

where for the last equality we have used Eq. (2.7). Notice that c_a^2 can be related to the time derivative of the equation of state $w \doteq p/\rho$ by $w' = -3\mathcal{H}(1+w)(c_a^2 - w)$ so that w and c_s^2 completely characterize the model.

Let us pause to comment on these equations. First, all the terms are of order $\mathcal{O}(\epsilon)$, with the exception of $\nabla^2\pi$. This term is $\mathcal{O}(1)$ in our perturbative scheme. But this term generates the pressure support within the sound-horizon of the scalar field, and leads to wave-like behaviour, not a growth of perturbations. For this reason it does not change the order of π which is an $\mathcal{O}(\epsilon)$ quantity. The other terms are all small; as an example we can consider the last term. It involves three fields π (so it is of order 3 in the standard perturbation-theory expansion), and since it contains four spatial derivatives its order is $3 - 4/2 = 1$. Second, the equations are at most of order three in the perturbations, which is a consequence of the fact that we are considering only theories with at most one derivative per field in the action so that one pays at least an $\mathcal{O}(\epsilon^{1/2})$ for each new order in the perturbations. Third, the limit of $c_s^2 \to 1$, obtained by sending $M_2^4 \to 0$, is well defined. In this case the last cubic term vanishes but this is to be expected because it can only come from the operator M_2^4 in the action (2.2). Also the limit $c_s^2 \to 0$ (obtained for $M_2^4 \gg c$) is well defined; we will come back to it at the end of the section.

---

[2] The covariant k-essence action, Eq. (2.1), implies that Bonvin et al. [2006] $w = \frac{P}{2XP_{,X} - P}$ and $c_s^2 = \frac{P_{,X}}{2XP_{,XX} + P_{,X}}$, where we have denoted the symbol of partial derivation by a comma.

Let us turn now to the stress-energy tensor of dark energy. Expanding Eq. (2.15) using the Poisson metric (2.16) one obtains

$$\begin{aligned}
T_0^0 &= -\rho + \frac{\rho+p}{c_s^2}\left[3c_s^2\mathcal{H}\pi - \zeta - \frac{2c_s^2-1}{2}(\vec{\nabla}\pi)^2\right] , \\
T_i^0 &= -(\rho+p)\left[1 - \frac{1}{c_s^2}\left(3c_s^2(1+w)\mathcal{H}\pi - \zeta + c_s^2\Psi\right) + \frac{c_s^2-1}{2c_s^2}(\vec{\nabla}\pi)^2\right]\partial_i\pi , \qquad (2.23) \\
T_j^i &= p\delta_j^i - (\rho+p)\left[3c_a^2\mathcal{H}\pi - \zeta + \frac{1}{2}(\vec{\nabla}\pi)^2\right]\delta_j^i + (\rho+p)\delta^{ik}\partial_k\pi\partial_j\pi ,
\end{aligned}$$

where we have used the homogeneous continuity equation and we have expanded T_0^0 and T_i^j up to order $\mathcal{O}(\epsilon)$ and T_0^i up to order $\mathcal{O}(\epsilon^{3/2})$.

The latter is expanded to higher order than T_0^0 and T_i^j because its divergence, which is $\mathcal{O}(\epsilon)$, appears as the source in the continuity equation. As shown in Appendix 2.A, Eqs. (5.1) and (5.2) are equivalent to the conservation equation $\nabla_\mu T^\mu_\nu = 0$ of the stress-energy tensor above. Note that in the limit $c_s^2 \to 0$ the components T_0^0 and T_i^0 seem to blow up due to the $1/c_s^2$ term. However, one can show that the brackets on the right-hand side of these expressions vanish at leading order in c_s^2, so that the stress-energy tensor remains finite. We discuss this in more detail in the case of matter domination in App. 2.D.

We also note that when linearized, the stress-energy tensor is purely scalar. The higher-order terms do not preserve this property, but the resulting vector and tensor type contributions will be small. For this reason we do not expect scalar dark energy to lead to significantly larger vector and tensor perturbations than ΛCDM. The dark energy stress-energy tensor must be inserted in the Einstein equations (obtained from the variation of Eq. (2.2) with respect to the metric), together with the stress-energy tensors of the other species. The Einstein equations in the weak field approximation are

$$(1+2\Phi)\nabla^2\Phi - 3\mathcal{H}\Phi' - 3\mathcal{H}^2(\Phi-\chi) - \frac{1}{2}\delta^{ij}\partial_i\Phi\partial_j\Phi = -4\pi G a^2 \delta T_0^0 , \qquad (2.24)$$

$$\nabla^4\chi - \left(3\delta^{ik}\delta^{jl}\frac{\partial^2}{\partial x^k\partial x^l} - \delta^{ij}\nabla^2\right)\Phi_{,i}\Phi_{,j} = 4\pi G a^2\left(3\delta^{ik}\frac{\partial^2}{\partial x^j\partial x^k} - \delta^i_j\nabla^2\right)T_i^j , \qquad (2.25)$$

where $\nabla^4 \doteq \delta^{ij}\delta^{kl}\partial_i\partial_j\partial_k\partial_l$ and the stress tensor T^ν_μ includes the relevant species including matter and dark energy, $\chi \doteq \Phi - \Psi$, and the transverse projection tensor is defined as,

$$P_{ij} \doteq \frac{\partial^2}{\partial x^i\partial x^j} - \delta_{ij}\nabla^2 . \qquad (2.26)$$

Here we do not discuss the equations for vector and tensor perturbations, as we are not going to study them in this paper.

2.2.4 Implementation

In this work, we remove the non-linear terms in the π evolution equations and stress-energy tensor. Due to their complexity, we are going to study the non-linear self-interaction of dark energy in detail in a separate work. It is interesting to note that although we have removed the π non-linear self-interaction, the energy density of the scalar field nonetheless becomes non-linear as it is sourced by matter going non-linear. For the sake of simplicity, we also assume that both w and c_s^2 are constant, which implies

$$s = 0 \, , \qquad c_a^2 = w \, . \tag{2.27}$$

Theoretically, this is not well motivated but it would not be difficult to include the time-evolution of w and c_s^2. However, since there are no especially well-motivated models in any case, we prefer to consider here only the simplest scenario.

When we neglect the non-linear terms, the π evolution equations (5.1) and (5.2) read

$$\pi' = \zeta - \mathcal{H}\pi + \Psi \, , \tag{2.28}$$

$$\zeta' = 3w\mathcal{H}\zeta - 3c_s^2\left(\mathcal{H}^2\pi - \mathcal{H}\Psi - \mathcal{H}'\pi - \Phi'\right) + c_s^2\nabla^2\pi \, , \tag{2.29}$$

and the linear stress tensor becomes

$$\begin{aligned} T^0_0 &= -\rho + \frac{\rho + p}{c_s^2}\left(3c_s^2\mathcal{H}\pi - \zeta\right) \, , \\ T^0_i &= -(\rho + p)\partial_i\pi \, , \\ T^i_j &= p\delta^i_j - (\rho + p)\left(3c_a^2\mathcal{H}\pi - \zeta\right)\delta^i_j \, . \end{aligned} \tag{2.30}$$

A detailed description of the numerical implementation can be found in Appendix 2.B.

2.3 Numerical results for power spectra

In this section we compare the power spectra from k-evolution with the linear perturbation solutions from `CLASS` Lesgourgues [2011] and with the power spectra computed with *gevolution* 1.2 using the `CLASS` interface to include dark energy. For both cases we consider two different speeds of sound: $c_s^2 = 10^{-7}$ and $c_s^2 = 10^{-4}$. We also test the effects that arise when trying to simulate a different

h	n_s	A_s	$\Omega_\mathrm{b}h^2$	$\Omega_\mathrm{CDM}h^2$	Ω_DE	$\mathrm{T_{CMB}}[K]$	N_ν	w
0.67556	0.9619	2.215×10^{-9}	0.02203	0.12038	0.68786	2.7255	3.046	-0.9

Table 2.1: Values of the cosmological parameters used in this paper. In particular, n_s and A_s are respectively the spectral index and amplitude of the primordial scalar fluctuations; Ω_b, Ω_CDM and Ω_DE are the critical densities, respectively of baryons, CDM and dark energy; $h \doteq H_0/(100\,\mathrm{Km}\,s^{-1}\mathrm{Mpc}^{-1})$ is the reduced Hubble constant; N_ν is the Standard Model effective number of neutrino species while w is the equation of state of dark energy. We also consider pivot wavenumber $k_p = 0.05$ Mpc^{-1}.

expansion history in a Newtonian simulation without including a dark energy fluid at all.

We always combine two simulations with sizes $L = 9000$ Mpc/h and $L = 1280$ Mpc/h, both with a grid of size $N_\mathrm{grid} = 3840^3$. All the results in this section have been obtained using the cosmological parameters shown in Tab. 8.1.

In Fig. 2.1 we illustrate the conceptual difference between the three codes we use in this section: In k-evolution matter and gravitational potentials are treated non-linearly[3] and act as a source for the linearized dark energy equations so that the dark energy contains non-linear contributions as well. This is consistently taken into account when dark energy density sources the gravitational potential. In *gevolution* the dark energy density is approximated by its linear solution computed with `CLASS` and is therefore not sourced by the non-linearities of matter. However, the gravitational potentials are sourced by this linear dark energy density, and matter evolves accordingly. Finally, in `CLASS` all the fields are linearized and all species source each other.

---

[3] With non-linear gravitational potentials we do not mean that they become large, but that they are different from the linear predictions especially for large wave numbers. However, they still remain small and respect the weak-field approximation.

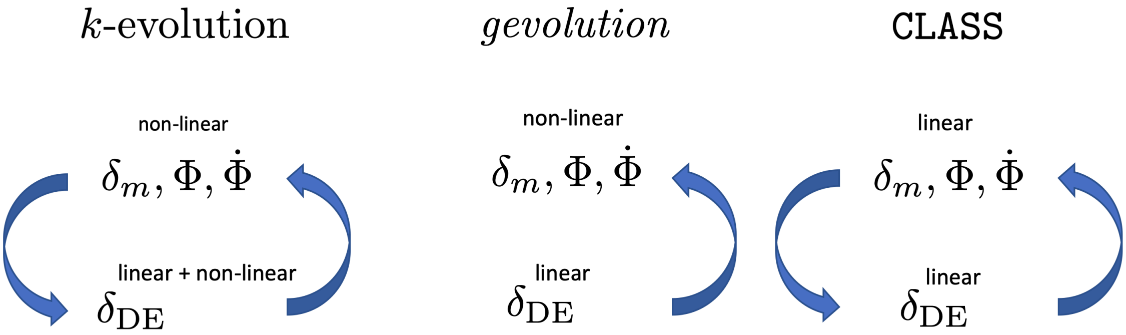

Figure 2.1: Schematic description of the three different codes used in this work, where the blue arrows show if one component sources the other. On the left, the two blue arrows going from non-linear matter and potentials to $\delta_{\rm DE}$, and *vice-versa*, show that in k-evolution all the components interact and source each other. Although we have used the density of linearized dark energy, its solution becomes non-linear since it is sourced by other species. In *gevolution* the matter and potentials become non-linear and are sourced by linear dark energy density, while $\delta_{\rm DE}$ is computed with `CLASS`. In `CLASS` all the components are linear and interact with each other.

2.3.1 k-evolution versus `CLASS`

We start by comparing k-evolution with the linear Boltzmann code `CLASS`. In `CLASS` code, one can extend the matter power spectrum beyond the linear regime by the use of Halofit Takahashi et al. [2012]. However, one should remember that Halofit is calibrated to simulations without clustering dark energy. In the following we will use `CLASS` both with and without the use of Halofit. The power spectrum of a given quantity X is defined by

$$\langle \hat{X}(\vec{k})\hat{X}(\vec{k}')\rangle = (2\pi)^3\delta(\vec{k}+\vec{k}')P_X(k) \ , \tag{2.31}$$

where $\hat{X}(k)$ is the Fourier transform of X. The dimensionless power spectrum is defined by

$$\Delta_X(k) \doteq \frac{k^3}{2\pi^2}P_X(k) \ . \tag{2.32}$$

In Fig. 2.2 we show the matter power spectrum. The onset of non-linear structure formation is clearly visible on scales $k > 0.1h/\mathrm{Mpc}$, where the relative difference between the linear and non-linear power spectra changes sign. On very large scales, k-evolution agrees with `CLASS` at the percent-level for all redshifts, but at intermediate scales and at low redshifts the difference increases to about 5%. We will see in Sec. 2.3.2, where we compare our results from k-evolution with *gevolution*, that the agreement there at low redshifts is much better, which

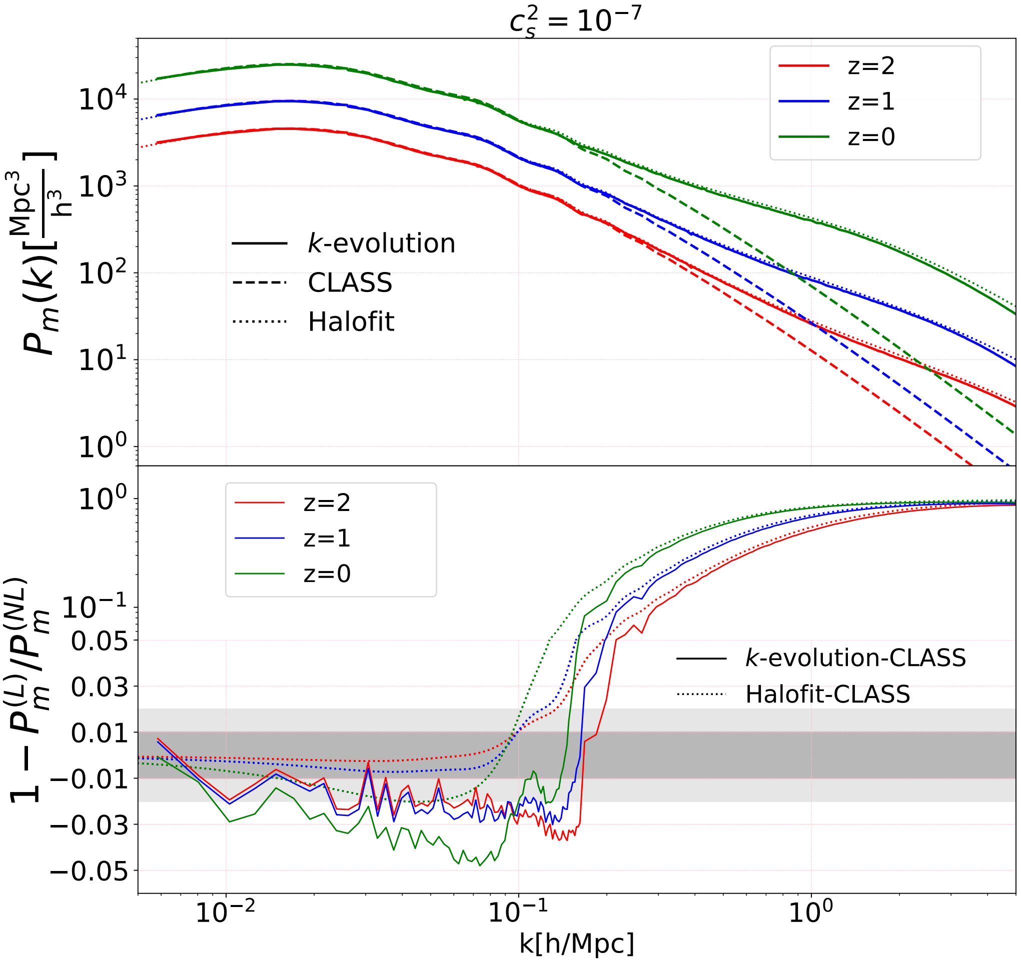

Figure 2.2: The top panel shows the matter power spectra from k-evolution and `CLASS` at different redshifts for $c_s^2 = 10^{-7}$. The bottom panel shows the relative difference between the matter power spectra of `CLASS`-Halofit and those of `CLASS`-k-evolution. The relative difference increases in the quasi-linear regime and for $z = 0$ reaches $\sim -5\%$ at its peak for `CLASS`-k-evolution and $\sim -2\%$ for `CLASS`-Halofit, while at high wavenumbers the non-linearity dominates. Notice that the vertical axis of the bottom panel is logarithmic above 0.05 and linear below.

means that the relative difference here comes from the effect of non-linearities at quasi-linear scales. Here we only plot the results for $c_s^2 = 10^{-7}$ as we will show in Sec. 2.3.2 that the effect of dark energy clustering on the matter power spectrum is negligible so that this plot would look the same for other values of c_s^2.

The power spectrum from `CLASS` extended beyond the linear regime using Halofit exhibits similar features as the one from k-evolution, particularly in the quasi-linear regime: the spectra of both k-evolution and Halofit are slightly suppressed relative to the linear power spectrum due to non-linearities[4]. For Halofit the differences reach $\sim -2\%$, not quite in agreement with the k-evolution result, which may be due to the fact that Halofit is not calibrated for such models.

The situation is similar for the gravitational potential shown in Fig. 2.3, where again we observe the onset of non-linearity at $k > 0.1h/\text{Mpc}$, as well as a scale dependent difference at intermediate scales where the linear power spectrum is larger than the non-linear one. Again, the Φ power spectra for the two speeds of sound are only slightly different, so that we only show the results for $c_s^2 = 10^{-7}$ and we will study the effect of the dark energy speed of sound on the gravitational potential in detail by comparing the potential power spectrum from k-evolution with *gevolution* in Sec. 2.3.2 .

The dark energy density power spectra at different redshifts, for $c_s^2 = 10^{-4}$ and $c_s^2 = 10^{-7}$, are shown in Fig. 2.4. The vertical lines indicate the sound-horizon of dark energy, which roughly corresponds to the peak of the linear dark energy density power spectrum, since on scales smaller than the sound-horizon the perturbations decay while on scales larger than the sound-horizon the perturbations grow. As a result, the density power spectrum of dark energy for $c_s^2 = 10^{-7}$ is much higher than the same quantity for $c_s^2 = 10^{-4}$: the sound-horizon for $c_s^2 = 10^{-7}$ corresponds to much smaller scales and we have an enhancement of perturbations on scales larger than the sound-horizon. For this reason, the non-linear dark energy clustering is much clearer for the simulation with smaller speed of sound. But the enhancement is also present for $c_s^2 = 10^{-4}$. The peak of the dark energy power spectrum is also affected by non-linearities: for example, in the case $c_s^2 = 10^{-7}$ the peak of the dark energy density power spectrum at redshift $z = 0$ is shifted to smaller scales.

In Fig. 2.5, the π power spectra at different redshifts from k-evolution and `CLASS` for the two speeds of sound are compared. Δ_π has units of $[\text{Mpc}^2/\text{h}^2]$, multiplying by k^2 makes it dimensionless. It is important to note that one can obtain the θ_{DE} spectrum from the π spectrum by using $\pi(k, z) = \theta(k, z)/k^2$ according to Eq. (2.21). For both speeds of sound, the dark energy scalar field fluctuations π or equivalently the dark energy velocity divergence θ_{DE} becomes

---

[4] This comes from the fact that in the one-loop contribution to the matter power spectrum in standard perturbation theory, i.e., $P_{22}^{\text{SPT}} + P_{13}^{\text{SPT}}$, the term P_{13}^{SPT} is always negative and is the dominant term at large and quasi-linear scales, up to $\sim 0.1h/\text{Mpc}$, while at smaller scales P_{22}^{SPT} becomes the dominant term Jalilvand et al. [2020].

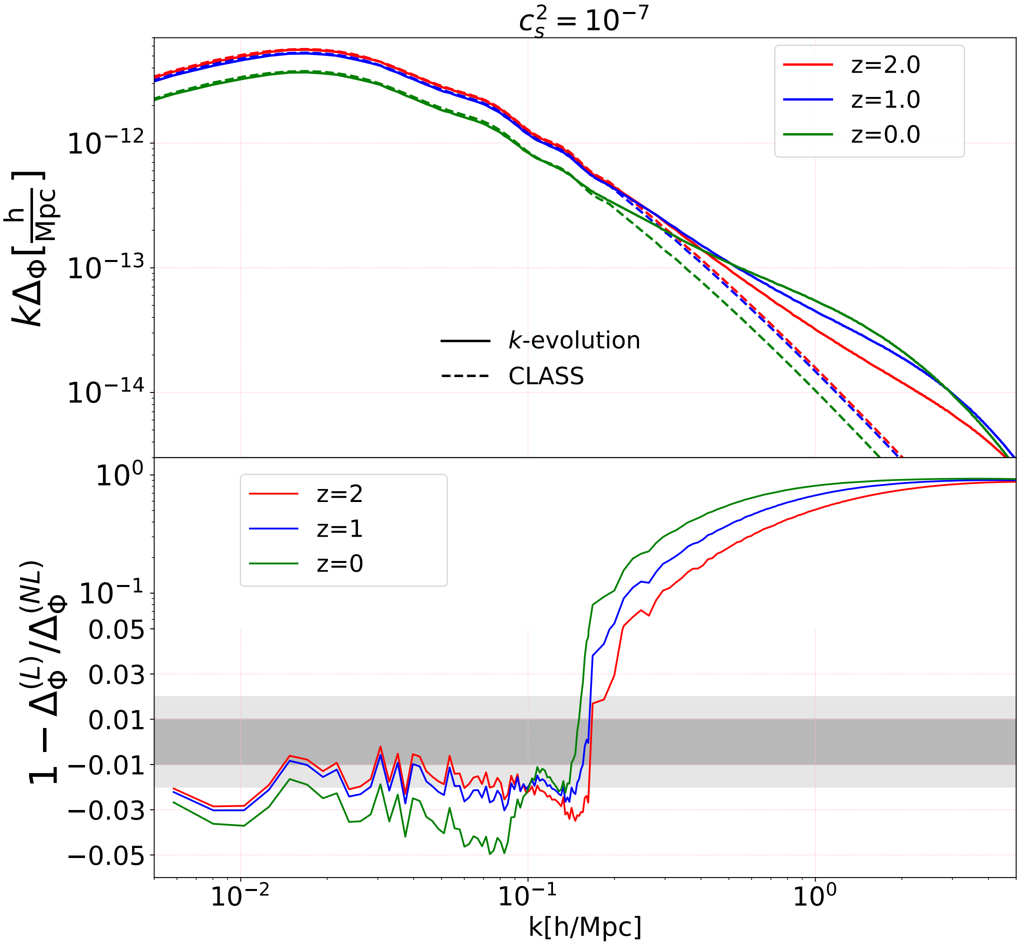

Figure 2.3: Comparison of the power spectra of the gravitational potential Φ computed with k-evolution (solid lines) and `CLASS` (dashed lines), for $c_s^2 = 10^{-7}$. At the top, we show the power spectra at different redshifts and at the bottom their relative difference. On intermediate scales, the power spectra computed with k-evolution are suppressed compared to those of `CLASS`, while the situation is reversed in the non-linear regime, for $k > 0.1h/\text{Mps}$.

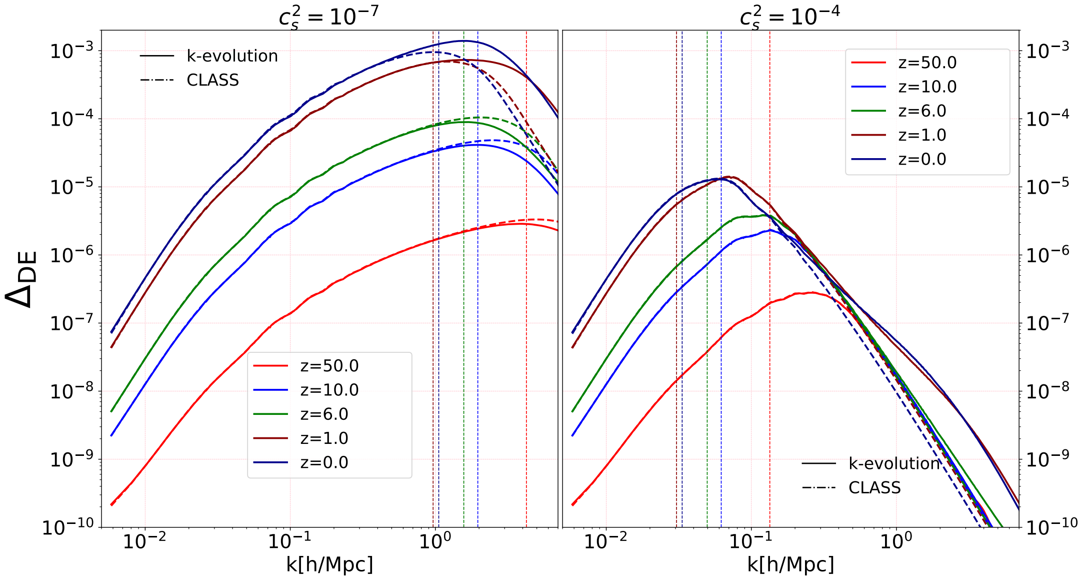

Figure 2.4: Comparison of the dark energy density power spectra from k-evolution (solid lines) and from `CLASS` (dashed lines) at different redshifts, for two different speeds of sound, $c_s^2 = 10^{-7}$ (left-panel) and $c_s^2 = 10^{-4}$ (right-panel). The vertical dashed lines show the value of the dark energy sound-horizon at each redshift, using the same color as the corresponding power spectrum. The turn-around in the power spectra takes place inside the sound-horizon. Its exact position is affected by dark matter non-linearities, as one can see comparing the case $c_s^2 = 10^{-4}$, where the turn-around happens on linear scales, and the case $c_s^2 = 10^{-7}$, where the turn-around takes place in the non-linear regime. Notice also that, as for the matter power spectrum, in the linear and quasi-linear regime at $z = 0$, the non-linear dark energy power spectrum is smaller than the linear one.

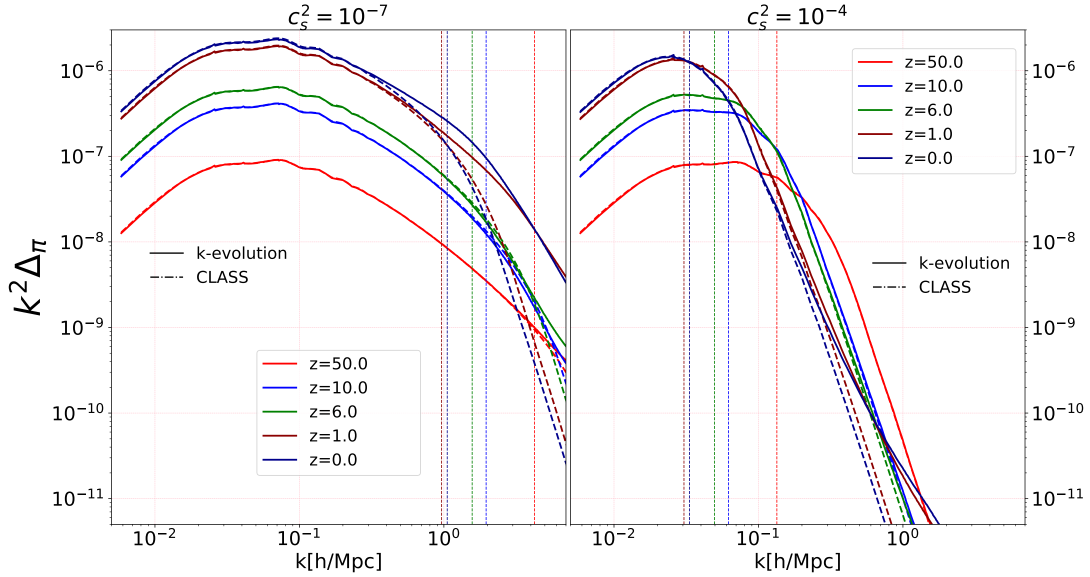

Figure 2.5: Comparison of π power spectra at different redshifts from k-evolution (solid lines) and `CLASS` (dashed lines), for $c_s^2 = 10^{-4}$ (right-panel) and $c_s^2 = 10^{-7}$ (left-panel). Δ_π has units of Mpc^2/h^2; multiplying it by k^2 makes it dimensionless. The vertical dashed lines show the value of the dark energy sound-horizon at each redshift. The dark energy velocity divergence power spectrum, $\Delta_{\theta_{\rm DE}}$, is simply given by $k^4\Delta_\pi$.

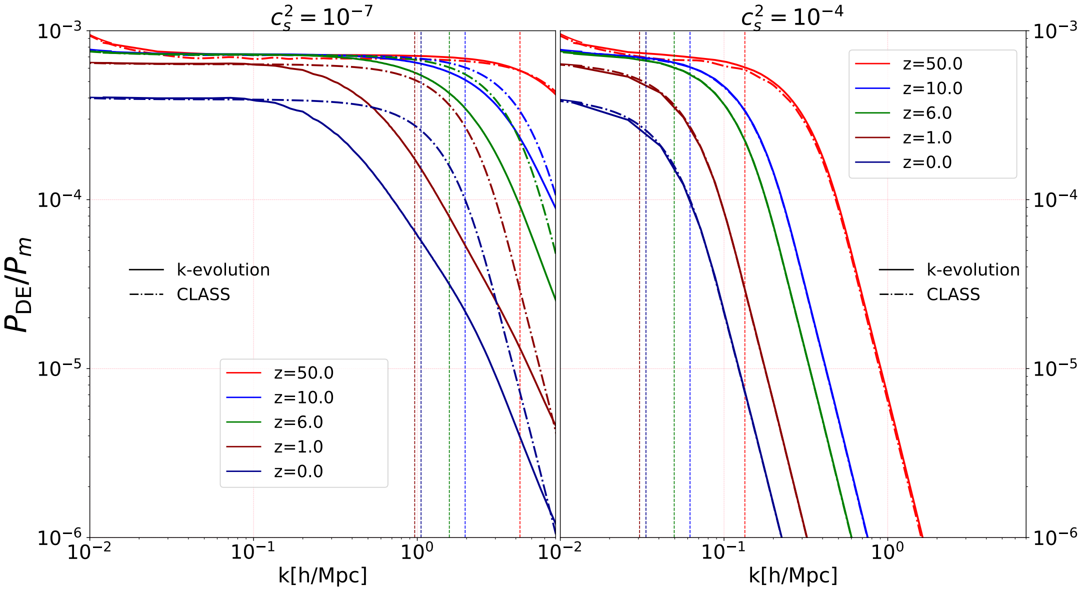

Figure 2.6: Comparison of the ratio between dark energy and matter power spectra from `CLASS` and k-evolution for two speeds of sound, $c_s^2 = 10^{-4}$ (right panel) and $c_s^2 = 10^{-7}$ (left panel), at different redshifts. For $c_s^2 = 10^{-4}$, the sound-horizon is at about the scale of matter non-linearity and the result from k-evolution agrees well with the one from `CLASS`. For $c_s^2 = 10^{-7}$, the sound-horizon is smaller than the matter non-linearity scale and we observe significant differences between the k-evolution and `CLASS` results, due to the matter and dark energy clustering, which are absent in the linear theory. The upturn visible in the ratio on large scales for $z = 50$ is a gauge effect on horizon scales.

non-linear due to the matter non-linearities and decays inside the sound-horizon scale.

Figure 2.6 shows the ratio between the dark energy and matter power spectra at different redshifts, for both speeds of sound $c_s^2 = 10^{-4}$ and $c_s^2 = 10^{-7}$. In the case $c_s^2 = 10^{-4}$, k-evolution and `CLASS` agree well, which shows that the non-linearity in dark energy and matter are roughly proportional. On the other hand, in the case $c_s^2 = 10^{-7}$ we see a large difference between `CLASS` and k-evolution because the dark energy sound-horizon lies inside the scale of matter non-linearity. Here, the ratio $P_{\mathrm{DE}}/P_{\mathrm{m}}$ is more suppressed in k-evolution than in `CLASS`, as the matter non-linearity is more effective than dark energy non-linearity, while inside the sound-horizon (on the very right of the left-hand panel, for redshifts, $z = 0$ and $z = 1$) we see the k-evolution result becoming larger than the one of `CLASS`, due to the effective clustering of dark energy at those scales. A more detailed study of the power ratio can be found in a companion paper Hassani et al. [2020c].

2.3.2 k-evolution versus *gevolution* 1.2 using its `CLASS` interface

Relativistic components that only couple gravitationally to dark matter cluster weakly. It is then a good approximation to describe them using their linear solution. For instance, in N-body simulations one can simply include a realisation of the linear density field of such components in the computation of the gravitational potentials. To this end, one first computes the respective linear transfer functions using an Einstein-Boltzmann solver, and then lays down perturbations matching to the random amplitudes and phases that where used as initial data for the simulation. The correct coupled evolution of dark matter and the additional components is recovered at linear order by construction, and whenever the non-linear growth in the dark matter is completely dominated by its self-gravity one can obtain very accurate results even deep in the non-linear regime. This method has been successfully employed for treating the effect of neutrinos Adamek et al. [2017b], Brandbyge & Hannestad [2009] or radiation Adamek et al. [2017a], Brandbyge et al. [2017] on dark matter clustering, and has been extended to dark energy fluids in the current version 1.2 of *gevolution*. A conceptually similar implementation has been recently presented in Dakin et al. [2019].

As opposed to k-evolution, this method does not allow to track the response of dark energy to the gravitational potentials of non-linear matter structures, as illustrated in Fig. 2.1. This effect is expected to be relevant in particular for low effective speed of sound of the fluid, i.e., when the clustering of the dark energy is not strongly suppressed. In this section we study the non-linear matter power spectrum obtained with both methods, which allows us to quantify the accuracy of the simplified linear treatment as implemented in *gevolution*. We demonstrate that the matter power spectra agree extremely well on all scales and at all times, but find some noticeable corrections to the gravitational potential at baryon acoustic oscillations (BAO) scales once dark energy dominates.

The matter power spectrum from k-evolution and *gevolution* at different redshifts are compared in Fig. 2.7 for $c_s^2 = 10^{-7}$, where we find a sub-percent agreement on all scales and at all redshifts between the two matter power spectra. For the higher value $c_s^2 = 10^{-4}$ (not plotted in this figure) the agreement is even better. We conclude that there is no significant impact of non-linear dark energy fluctuations on the matter spectrum, once non-linear matter clustering is correctly taken into account.

In Fig. 2.8 the gravitational potential power spectra from k-evolution and *gevolution* at different redshifts for the speed of sound $c_s^2 = 10^{-7}$ are compared. Interestingly, the dark energy clustering affects the gravitational potential power spectrum in the mildly non-linear regime, with up to $\sim 4\%$ differences appearing at $z = 0$. This effect could potentially change the lensing signal if the universe

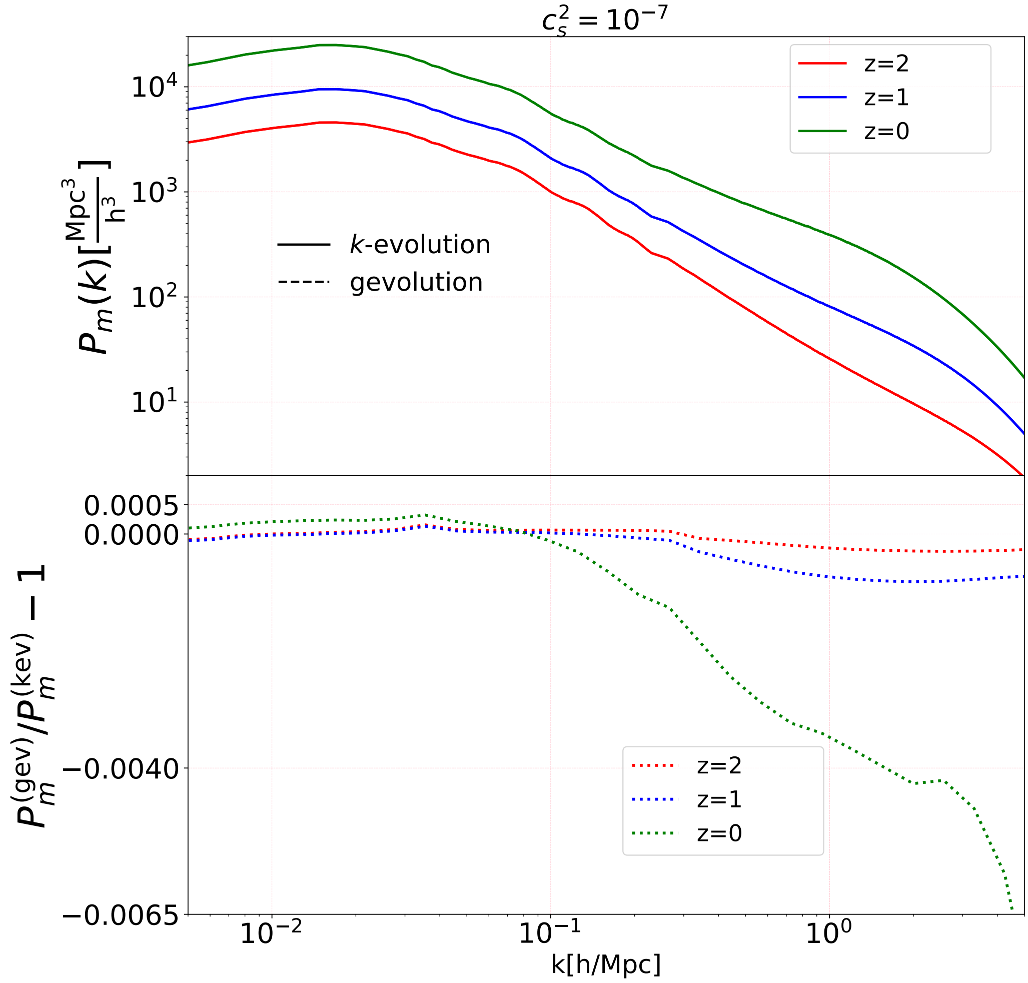

Figure 2.7: At the top, comparison of the matter power spectra from k-evolution and *gevolution* at different redshifts, for $c_s^2 = 10^{-7}$. At the bottom, relative difference between the two power spectra at each redshift is shown. The figure shows that the effect of non-linearity of dark energy on the matter power spectrum is negligible.

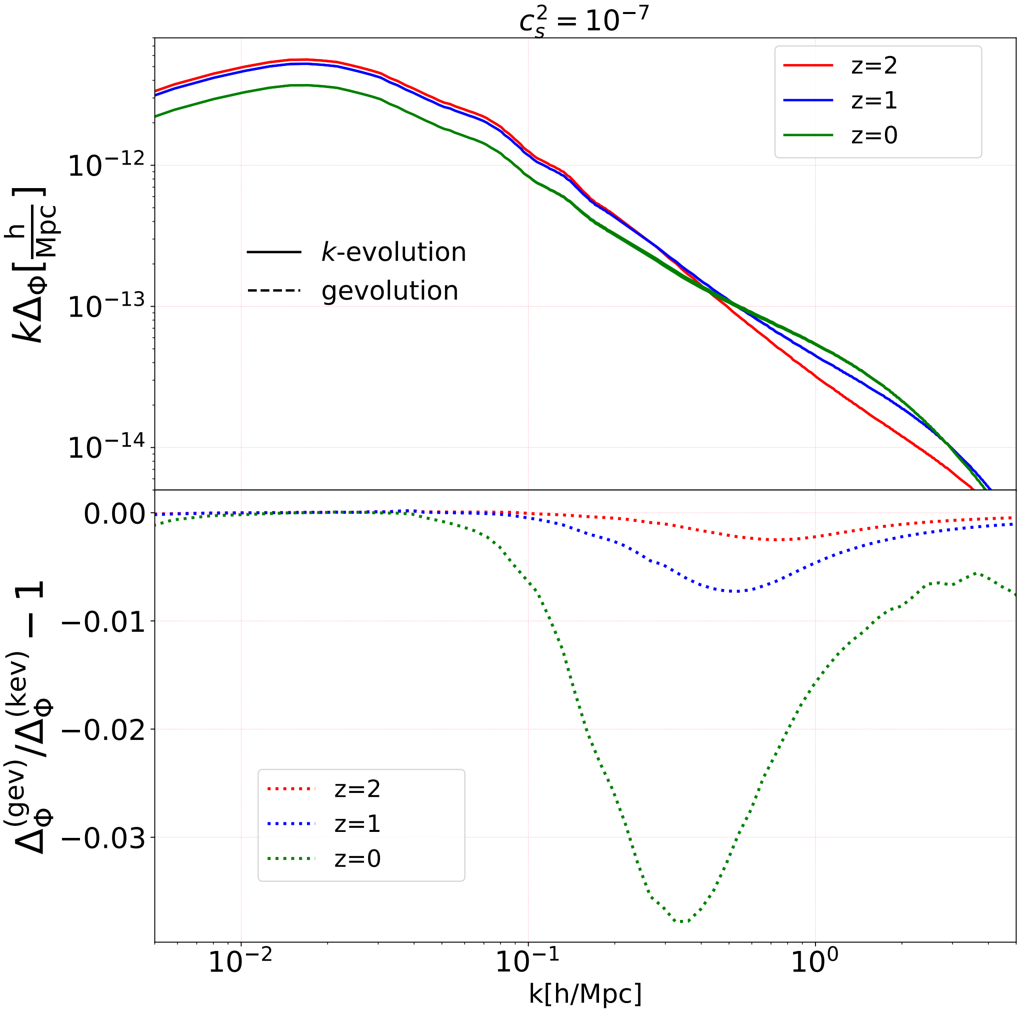

Figure 2.8: In the top panel, the potential power spectra from k-evolution and *gevolution* at three different redshifts are shown and in the bottom panel the relative difference between the power spectra at the same redshifts are plotted. The dark energy clustering changes the potential power spectrum by up to $\sim 4\%$ at mildly linear scales at $z = 0$.

contains k-essence as a dark energy fluid.

The power spectra of the dimensionless quantity $\Phi'/\mathcal{H}$ from k-evolution and *gevolution*, compared to the linear prediction from `CLASS` are shown in the top panel of Fig. 2.9. This is an interesting quantity as it is a direct source of dark energy already at linear order, as can be seen in Eq. (5.2). According to Fig. 2.9, the scale of non-linearity in the Φ' power spectrum starts at $\sim 0.005\, h/\mathrm{Mpc}$, much earlier than the scale of non-linearity in the matter and potential power spectra, which at $z = 0$ is $\sim 0.1\, h/\mathrm{Mpc}$. This effect is not specific to k-essence models, it has also been observed for ΛCDM in Cai et al. [2009a], where it was studied as non-linear integrated Sachs–Wolfe (ISW) effect. Interestingly, this effect adds a new scale into the dynamics of π, in addition to the sound-horizon scale and the scale of matter non-linearity. Comparing k-evolution and *gevolution*, there is a $\sim 3\%$ effect due to the clustering of dark energy at large and quasi-linear scales for both values of c_s^2. Moreover, there is $\sim$ 5% bump due to the dark energy clustering at quasi-linear scales for the case $c_s^2 = 10^{-7}$, which peaks around $k = 0.4\, h/\mathrm{Mpc}$. These changes in Φ', and especially the large difference relative to the linear predictions, even at low k, could potentially affect the ISW effect.

We define the normalized cross power spectrum between matter and dark energy as

$$\Delta_\times = \frac{\Delta_{\mathrm{DE}\times\mathrm{m}}}{\sqrt{\Delta_{\mathrm{DE}}\Delta_{\mathrm{m}}}}, \tag{2.33}$$

where Δ_{DE} and Δ_{m} are respectively the dark energy and the matter power spectrum while $\Delta_{\mathrm{DE}\times\mathrm{m}}$ is their cross spectrum. This quantifies the correlation between the clustering of matter and dark energy. Figure 2.10 compares this quantity computed with k-evolution and *gevolution*. In particular, it shows the cross-spectra at different redshifts, for $c_s^2 = 10^{-4}$ (right panel) and $c_s^2 = 10^{-7}$ (left panel).

According to the Cauchy-Schwarz inequality, this quantity must be in the range $[-1, 1]$. A value of 1 indicates that the two fields are fully correlated, 0 means that they are not correlated, and -1 that they are fully anticorrelated. In linear perturbation theory and for adiabatic initial conditions (assumed here), all quantities are related via a deterministic transfer function to the same initial curvature perturbation, so that all the fields are fully correlated, $\Delta_\times = 1$.

We see that on large scales, where the evolution is effectively linear, the dark energy and matter fluctuations are indeed fully correlated in all cases. In *gevolution*, the matter evolves non-linearly under its own gravity, while dark energy is computed at the linear level. For this reason the two fields start to lose their correlation when the matter perturbations become non-linear.

In k-evolution on the other hand, where dark energy is able to follow the dominant non-linear matter perturbations, the correlations are essentially main-

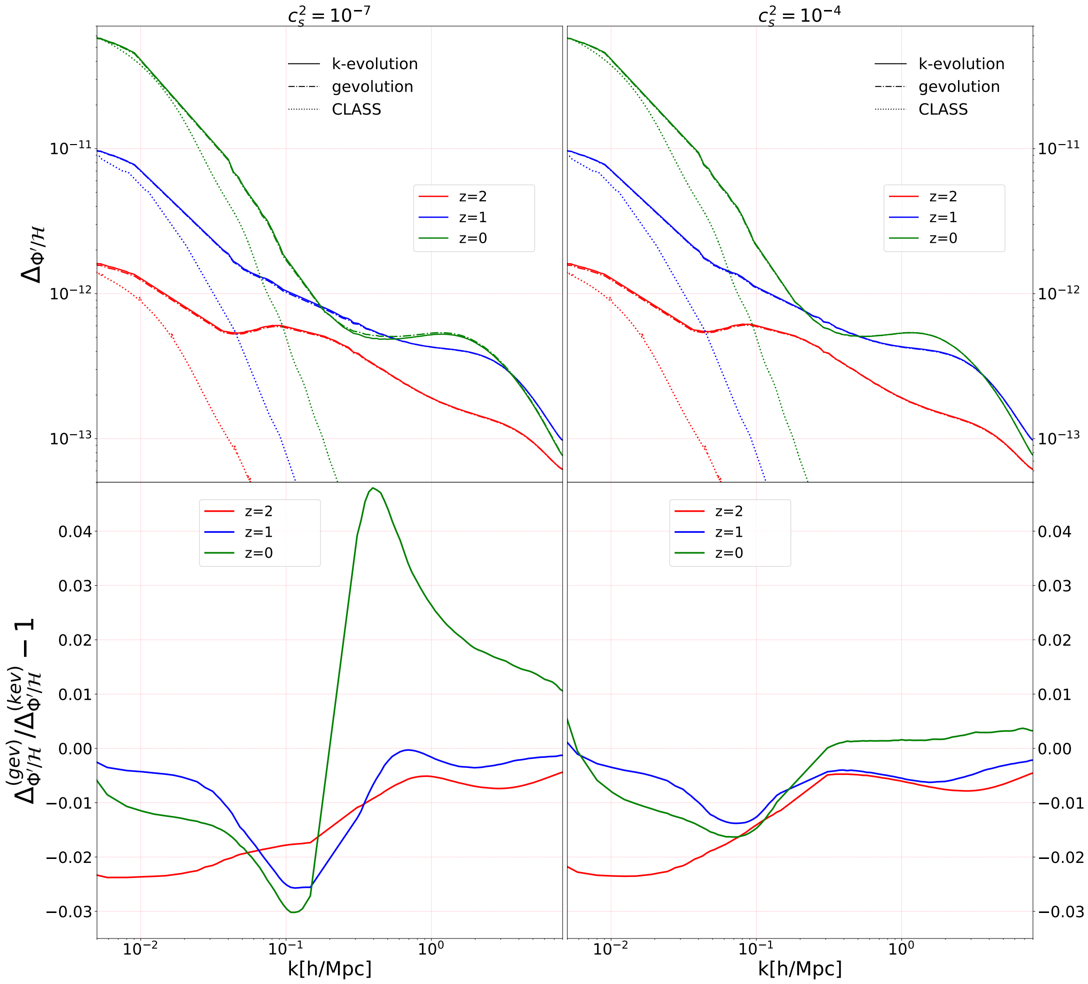

Figure 2.9: Comparison of the power spectra of $\Phi'/\mathcal{H}$ for k-evolution, *gevolution* and `CLASS` at different redshifts, for $c_s^2 = 10^{-4}$ (right panel) and $c_s^2 = 10^{-7}$ (left panel). The onset of non-linear effects in Φ' is on much larger scales than in Φ or δ_m. The results from k-evolution and *gevolution* are more similar, with differences reaching to ∼5% between the two codes.

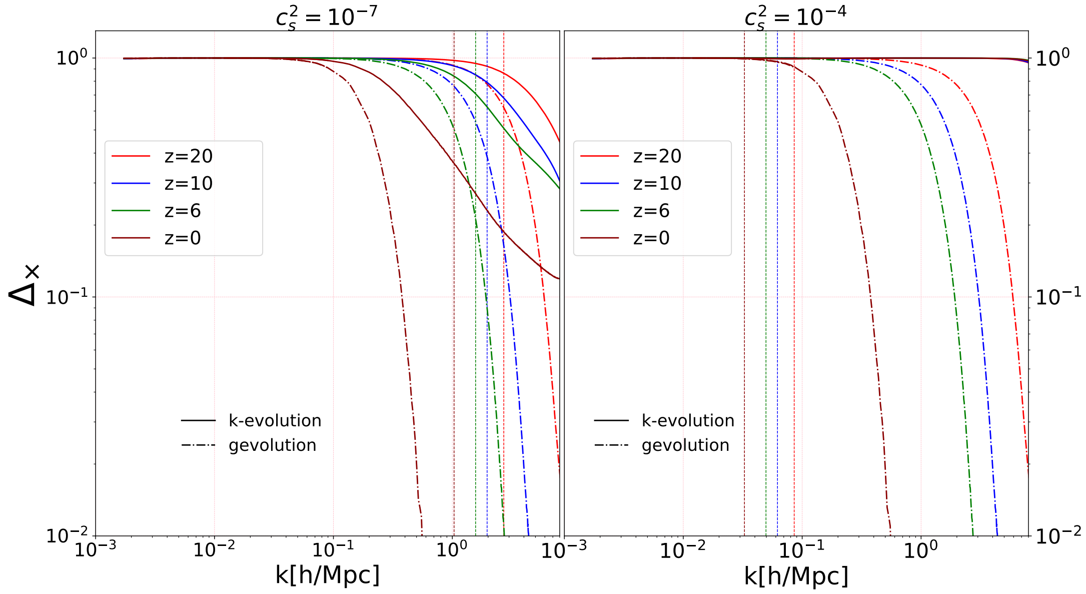

Figure 2.10: Normalized cross correlation power spectra at different redshifts for speed of sound $c_s^2 = 10^{-4}$ on the right and $c_s^2 = 10^{-7}$ on the left. In *gevolution*, for both speeds of sound the only important scale is the scale of matter non-linearity as in *gevolution* the dark energy does not follow the non-linear matter structures, and we see that after this scale the cross correlation power decays. In k-evolution for $c_s^2 = 10^{-4}$ almost at all scales the dark energy and matter densities are fully correlated, as inside the sound-horizon dark energy does not cluster strongly and closely follows the matter density. In the case with lower speed of sound, where dark energy clusters and has self-dynamics the cross correlation power starts to decay on small scales.

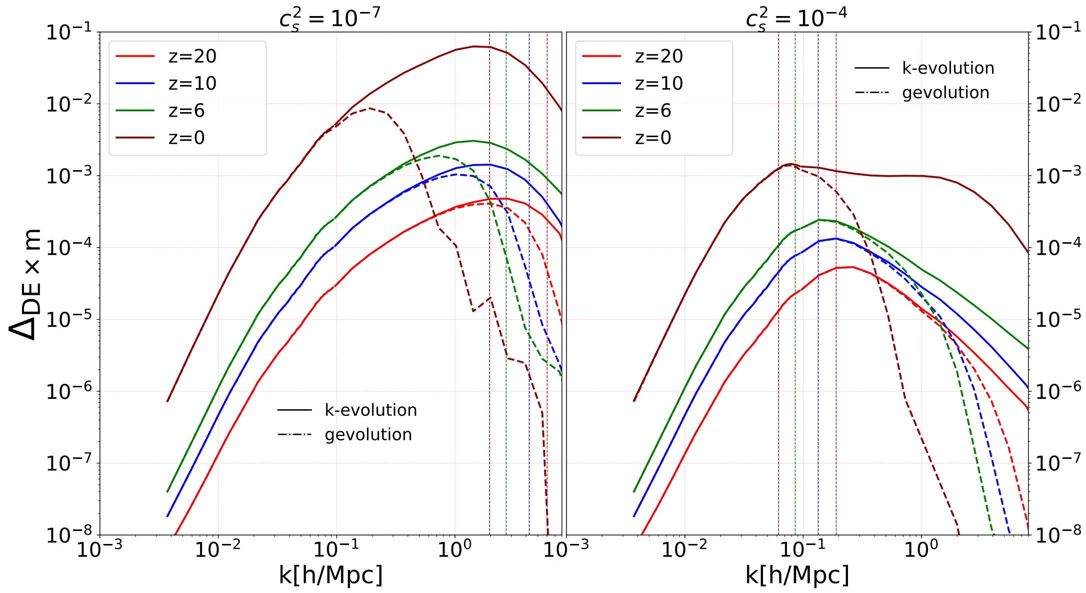

Figure 2.11: Cross-correlation power spectra between matter and dark energy densities at different redshifts, for $c_s^2 = 10^{-4}$ (right panel) and $c_s^2 = 10^{-7}$ (left panel), computed by k-evolution and *gevolution*. In *gevolution*, the dynamics of dark energy and matter decouple beyond the scale of matter non-linearity, so the dashed lines and solid lines start deviating roughly at the scale of non-linearity. In k-evolution, for $c_s^2 = 10^{-4}$ the dark energy density does not cluster at scales where matter clusters, and the dark energy follows matter. This is why the cross-correlation power between the two densities is large. For $c_s^2 = 10^{-7}$, the dark energy density clusters and the turn-around in the cross-correlation power spectrum takes place at the sound-horizon scale.

tained for large speeds of sound such as $c_s^2 = 10^{-4}$. In this case, dark energy crosses its sound-horizon before the scale of matter non-linearity and it is not able to develop an independent dynamics; its clustering simply follows that of the dark matter.

The situation is different for low speeds of sound, such as $c_s^2 = 10^{-7}$, where dark energy becomes non-linear outside the sound-horizon. In that case the correlations start to decay, but more slowly than in *gevolution*, as the matter clustering is still dominant and “drags” the dark energy perturbations at least partially with it. This behaviour is clearly visible also in the field snapshots that we study in Sec. 2.4.

For completeness we also show the raw cross-spectrum between matter and dark energy densities at different redshifts for both speeds of sound in Fig. 2.11. The main feature is the enhanced cross-power on small scales in k-evolution due to the non-linear clustering of dark energy, mostly following the non-linear

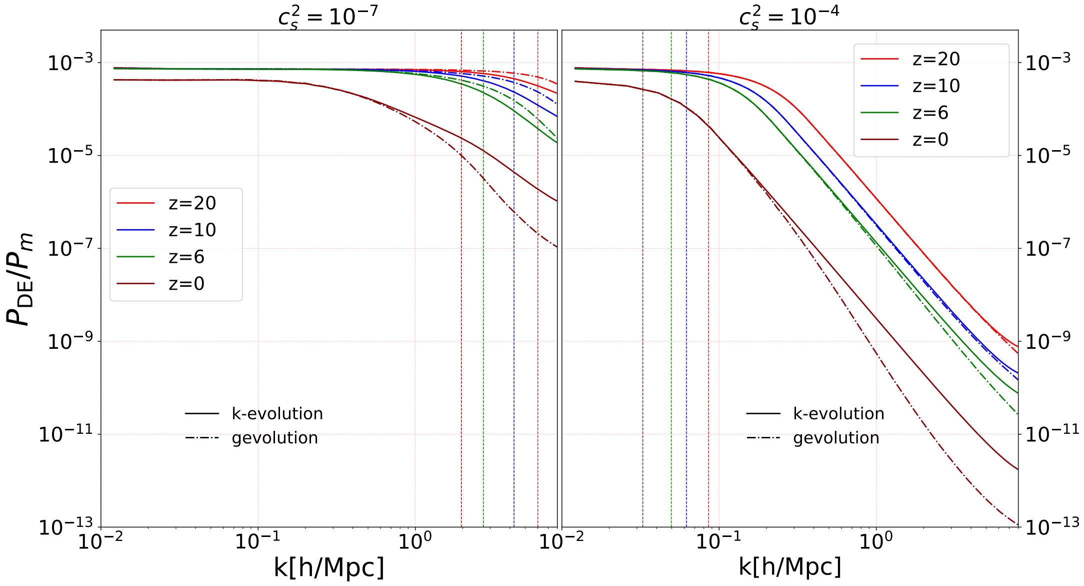

Figure 2.12: Ratio of dark energy and matter densities power spectra in k-evolution (solid lines) and *gevolution* (dashed lines), at different redshifts for $c_s^2 = 10^{-7}$ (left panel) and $c_s^2 = 10^{-4}$ (right panel). The scale at which *gevolution* and k-evolution start disagreeing is giving by a combination of sound-horizon and scale of matter non-linearity. In the low speed of sound case, $c_s^2 = 10^{-7}$, this happens at smaller scales. Also this ratio increases with the redshift, as the matter clustering is much stronger than the dark energy clustering at lower redshifts.

dark matter clustering. In Fig. 2.12 the ratio of dark energy and matter power spectra at different redshifts are compared. On scales above the sound-horizon we expect during matter domination a ratio of Creminelli et al. [2009], Sapone & Kunz [2009]

$$\frac{P_{\rm DE}}{P_m} \simeq \left(\frac{1+w}{1-3w}\right)^2 = \frac{1}{1369}\,, \tag{2.34}$$

for $w = -0.9$, which is verified by the simulations. Dark energy perturbations inside the sound-horizon stop growing, so that the ratio relative to the dark matter perturbations decreases. At lower redshifts, the decrease in k-evolution tends to be slower than in *gevolution*, since in the latter only the dark matter perturbations become non-linear on small scales, while dark energy is always linear. In k-evolution both dark matter and dark energy perturbations become non-linear on small scales.

2.3.3 Newtonian simulations with "back-scaled" initial conditions

Dark energy is a key target for large future surveys like the ESA Euclid satellite Laureijs et al. [2011], and to exploit such data fully it is necessary to have reliable results also on small scales where the matter perturbations are non-linear. To find these results, it is common to use Newtonian N-body simulations where only the expansion rate is changed, and where no dark energy is included Jennings et al. [2010]. However, although the dark energy perturbations are small, it is not clear whether this is really a good approximation as we know that the CMB temperature anisotropies on large scales are very sensitive to the perturbations Weller & Lewis [2003]. In order to study this question, we compare this standard approach with our method that includes the linear dark energy perturbations, as implemented in *gevolution* 1.2.

At the linear level, the presence of dark energy perturbations induces a scale dependence in the growth of matter perturbations. This means that simulations where only the background evolution is adjusted do not even reproduce the linear results correctly. In order to deal with this issue, the common practice is to first choose a redshift at which the accuracy of the N-body simulation should be maximal (e.g., redshift zero) and to compute a linear matter power spectrum for that redshift, including the effects of dark energy perturbations. In a second step, the matter power spectrum is then "scaled back" to the initial redshift of the simulation with the scale-independent growth function obtained by neglecting the dark energy perturbations, based only on the modified expansion rate. While this procedure provides initial data that do not correspond to the true matter configuration at the initial time, the error is deliberately introduced in order to precisely cancel the error in the linear evolution once the simulation reaches the final redshift.

In our comparison we consider a case with a low speed of sound, $c_s^2 = 10^{-7}$. In principle such a choice may pose a challenge to the standard approach, as a scale dependence is introduced close to the non-linear scale where the procedure outlined above becomes less reliable. We run one simulation with *gevolution* using the `CLASS` interface to provide our baseline, and then compare our results with two simulations where the `CLASS` interface is not used and only the background evolution tracks the dark energy equation of state. We provide "back-scaled" initial conditions for the latter two simulations, in one case based on the correct linear matter power at redshift $z = 0$, while in the other case we match to the linear matter power when additionally $c_s^2 = 1$ is assumed for the dark energy, as is done in most numerical studies. All simulations are run in the Newtonian mode, which means that for the baseline simulation the fluid perturbations are taken in the N-body gauge Fidler et al. [2016].

In Fig. 2.13 we compare the matter power spectra of a simulation that used the "back-scaling" approach with the baseline simulation. As expected, Fig. 2.13 shows that the linear scales agree to high accuracy at $z = 0$ when the initial conditions are constructed appropriately. However, the effect of scalar field clustering on the matter power spectrum reaches ∼1% at small scales at $z = 0$, if the initial conditions are prepared for $c_s^2 = 10^{-7}$. As back-scaled Newtonian simulations are often performed with a quintessence-motivated spectrum where $c_s^2 = 1$, we also performed a back-scaled simulation with this wrong speed of sound. We found that this choice does not have a large impact on the results; the errors on small scales are even reduced relative to correct back-scaled case. This might be induced because the large-scale and small-scale errors have opposite sign at earlier redshifts.

The gravitational potential comes with much larger deviations, as is shown in Fig. 2.14. The relative difference in the respective power spectra reaches 7% and could affect the lensing signal. The reason for this large deviation is that back-scaled initial conditions are constructed to produce an accurate matter density but not gravitational potential. The latter is additionally sourced by the perturbations in the dark energy which, however, are only important at late times. It would be possible instead to use initial conditions that improve the agreement for the gravitational potential, but then the matter power spectrum would be off. Using the back-scaling approach it is not possible to obtain good results for both the matter density and the gravitational potential simultaneously. In a related paper Hassani et al. [2020c] we present a possible approach to include a correction for the gravitational potential that addresses this problem.

2.4 Snapshot analysis

In this section we look at the matter and dark energy density from the k-evolution and *gevolution* simulations (where the latter uses the `CLASS` interface), to study how the dark energy field configuration traces the matter structures. First, we compare the results obtained from k-evolution and *gevolution* for a relatively small simulation (128^3 grid points) with a small box (50 Mpc/h), which corresponds to a spatial resolution of 0.39 Mpc/h and a mass resolution of $5 \times 10^9\ \mathrm{M}_\odot/h$. In Fig. 2.15, we show a 2D slice of the box, which passes through the most massive halo found by the ROCKSTAR halo finder Behroozi et al. [2013]. Comparing the left and middle panels of Fig. 2.15 we see that at high redshift, $z = 10$, they are virtually indistinguishable, which is still nearly true at $z = 6$. At low redshifts, $z = 1$ and $z = 0$, the k-evolution results are clearly more clustered than the linear dark energy realisation of *gevolution*. The dark energy clustering is most pronounced in regions of strong dark matter clustering, i.e. dark energy structures are formed around massive dark matter halos, something that is not the case in the linear realisation. This agrees with the relatively high correlation between dark matter and dark energy perturbations visible in Fig. 2.10.

For a more quantitative study we use higher-resolution simulations with 1024^3 grid points and 100 Mpc/h box size which corresponds to 0.097 Mpc/h spatial resolution and a mass resolution of $8 \times 10^8\,\mathrm{M}_\odot/h$, for $c_s^2 = 10^{-7}$ and $w = -0.9$. We pick the most massive halo in the simulation and analyse the particles and the k-essence scalar field inside five virial radii of the halo. Fig. 2.16a shows, respectively from left to right, dark energy density in *gevolution* and k-evolution and matter density in k-evolution at $z = 0$. In each snapshot the position of the halo with 5 virial radii is shown as a shaded region. Figure 2.16b provides a closer look at the halo where the dashed circle is the virial radius of the halo. In k-evolution, dense dark energy structures are formed around the centre of the massive dark matter halo. In Fig. 2.16c the relative difference of dark energy density, matter density and potential between k-evolution and *gevolution* is shown respectively on the left, middle and right, at $z = 0$ and in the same region as Fig. 2.16b. Due to the dark energy clustering that is absent in the linear realisation, we find a large change in the dark energy density distribution. Moreover, in contrast to matter power spectrum there are relatively large changes visible also in the matter density due to the dark energy non-linearity. The dipole visible in the distribution of the gravitational potential comes probably from a small shift of the halo center due to the dark energy non-linearity.

In Fig. 2.17 the change in the position of particles in k-evolution with respect to the same particles in *gevolution* inside three virial radii of the halo is shown. Each arrow represents the displacement of the corresponding particle due to the dark energy non-linearities, i.e., $\Delta\vec{r}^{(i)} = \vec{r}^{(i)}_{\text{kevolution}} - \vec{r}^{(i)}_{\text{gevolution}}$, where $\vec{r}^{(i)}_{\text{kevolution}}$ is the position of particle i in k-evolution and $\vec{r}^{(i)}_{\text{gevolution}}$ is the position of the same particle in *gevolution*. The colors show the length of the arrow measured in Mpc/h. Most changes in particles positions due to the dark energy non-linearities are seen to be around the center of the halo (for a study of the effect of dark energy clustering on the turn-around radius near galaxy clusters see Hansen et al. [2020]).

2.5 Conclusions

We develop k-evolution, an N-body code to compute cosmological observables including the effect of dark energy clustering. The code is based on *gevolution* while dark energy is modelled using the EFT of DE. For simplicity we focus on k-essence but we pave the way to more general cases. We develop the equations to describe the gravitational and dark energy sector in the weak-field expansion but fully non-linearly. As a first initial step, however, we implement in the code only the linear parts of the evolution equation and stress-energy tensor of dark energy.

We compare the power spectra computed with k-evolution with those computed with codes that treat the evolution of the dark energy linearly, in particular with *gevolution* 1.2 (where the dark energy stress-energy tensor is computed using `CLASS`) and with `CLASS`. We find relatively small differences between the matter power spectra computed with k-evolution and *gevolution*. However, the clustering of dark energy uniquely captured by k-evolution affects non-negligibly the power spectra of other quantities, such as the gravitational potential and its time evolution. This is especially the case for low speeds of sound such as the one considered here, i.e. $c_s^2 = 10^{-7}$.

Moreover, we compare k-evolution with simulations that take into account the dark energy component by changing the background evolution and back-scaling the initial conditions. We show that this back-scaling approach cannot compute, with sufficient accuracy, simultaneously the power spectrum of matter and of the gravitational potential. We also analyse snapshots from k-evolution. We find that in dense regions the matter density, the k-essence density and the positions of particles are affected by dark energy clustering.

This paper is the first step of a more general program of developing simulations including the effect of dark energy and modified gravity.

Acknowledgements

FH thanks Jean-Pierre Eckmann for helpful comments about manuscript and useful discussions. FH also would like to thank Benjamin L'Huillier, Arman Shafieloo, Pan Shi, Peter Wittwer, Mona Jalilvand, Hans Winther, Ruth Durrer, Lucas Lombriser, Miguel Zumalacárregui, Eiichiro Komatsu, David Daverio, Joyce Byun, Yan-Chuan Cai and Matteo Cataneo for helping at different stages of the project and useful discussions.
This work was supported by a grant from the Swiss National Supercomputing Centre (CSCS) under project ID s710. We acknowledge financial support from the Swiss National Science Foundation. JA also acknowledges funding by STFC Consolidated Grant ST/P000592/1. Symbolic and numerical computations have been performed with MapleTM 16 and Wolfram Mathematica 9. F.V. acknowledges the Munich Institute for Astro- and Particle Physics (MIAPP) of the DFG cluster of excellence "Origin and Structure of the Universe”, where part of this work was done.

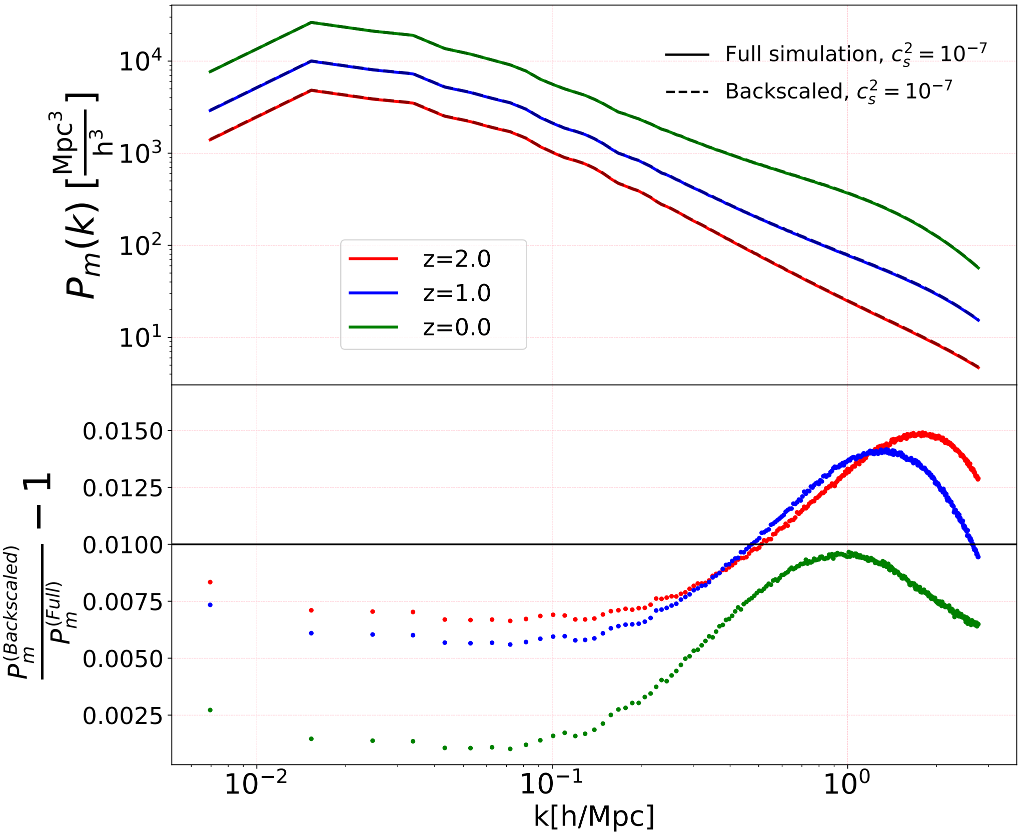

Figure 2.13: The matter power spectra and the relative difference from two Newtonian simulations, one with the back-scaled initial conditions for $c_s^2 = 10^{-7}$ and one with the correct initial conditions from the linear Boltzmann code `CLASS` and correct evolution for $c_s^2 = 10^{-7}$ including linear dark energy perturbations. The simulation with back-scaled initial condition works well at $z = 0$ especially at linear scales by construction while it reaches 1% error at non-linear scales. At higher redshifts the relative errors are typically larger, but remain below 2% on all scales.

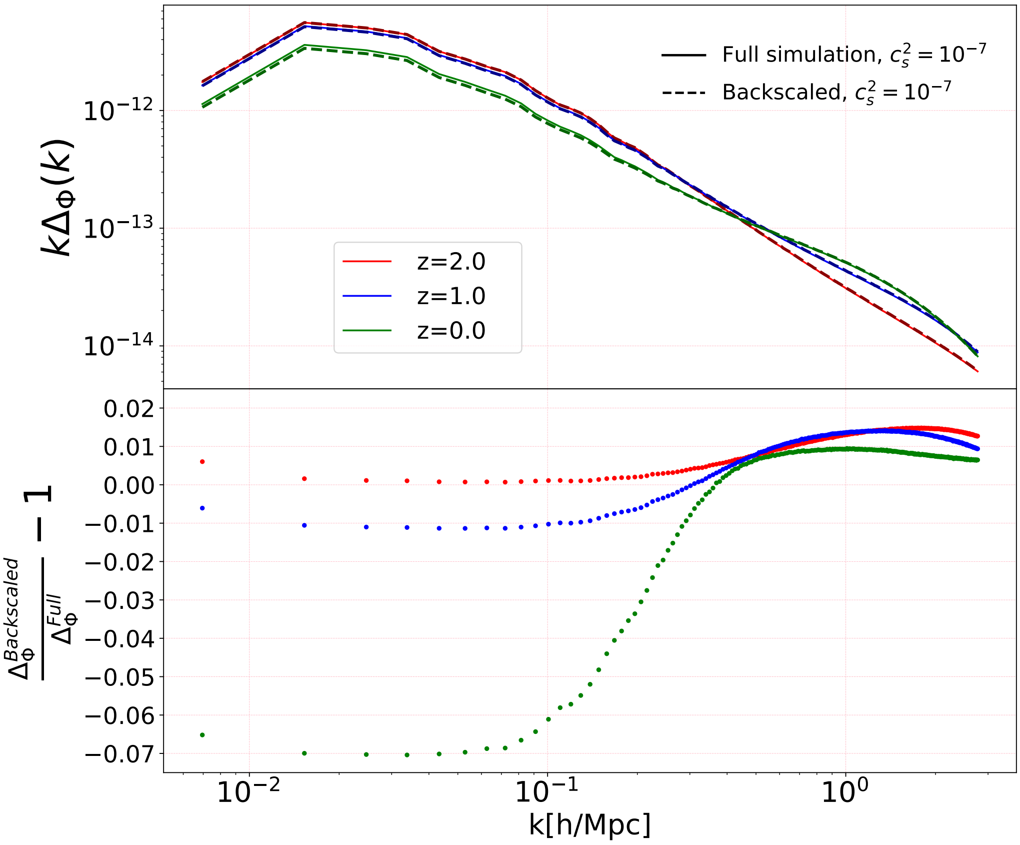

Figure 2.14: The gravitational potential power spectra and the relative difference from two Newtonian simulations, one with the back-scaled initial conditions for $c_s^2 = 10^{-7}$ and one with the correct initial conditions and correct evolution for $c_s^2 = 10^{-7}$ including linear dark energy perturbations. The simulation with back-scaled initial condition does not give the correct gravitational potential power spectrum at large scales; we find about 7% relative error.

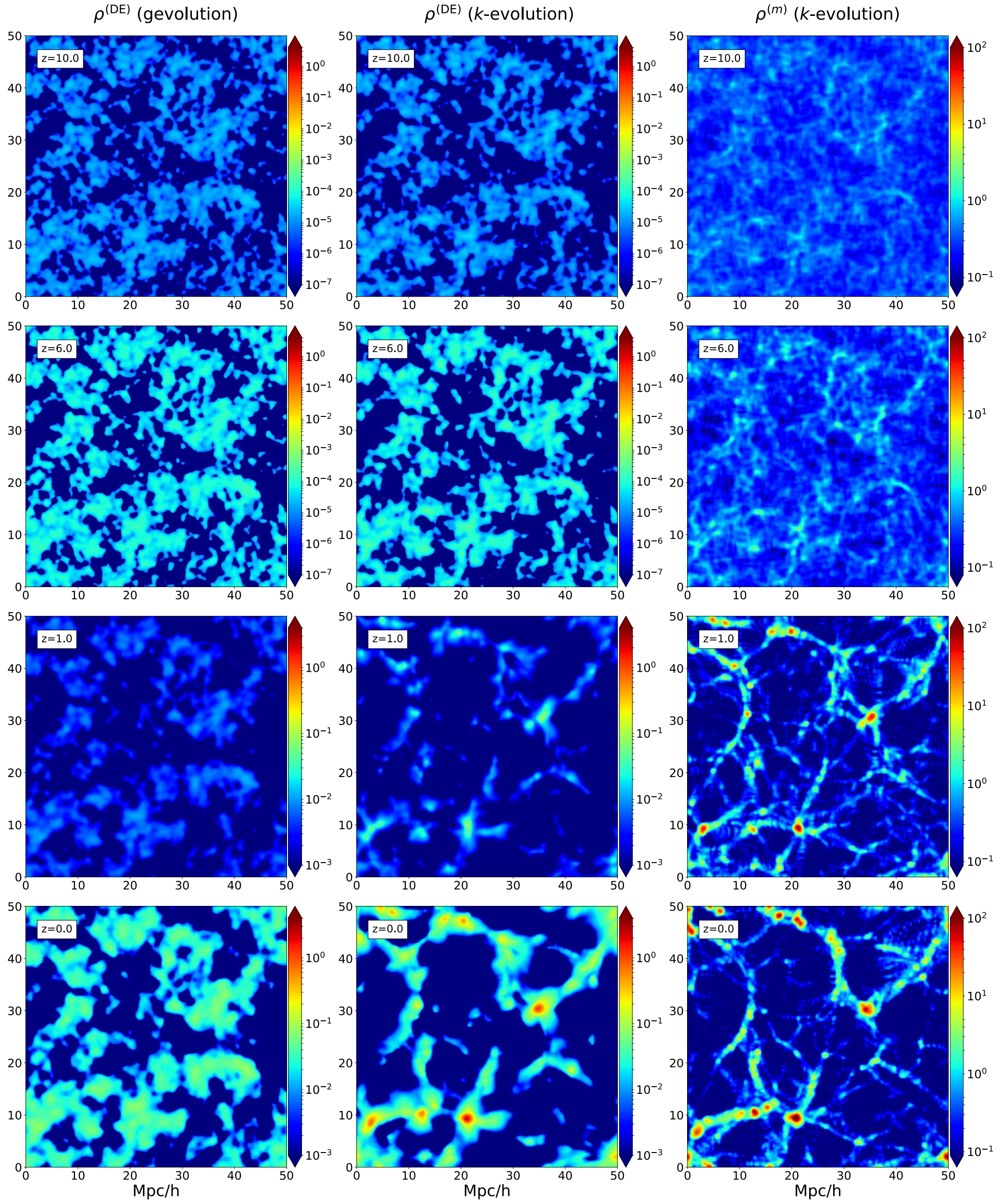

Figure 2.15: Respectively from the left to the right, the dark energy density computed with *gevolution* (using the `CLASS` interface) and the dark energy and matter density computed with k-evolution, as a function of the redshift (from the bottom to the top), measured in units of the critical density. The dark energy structures form around massive halos. Note that the color scheme for the visualisation of $\rho^{(\mathrm{DE})}$ changes between lower panels and upper panels.

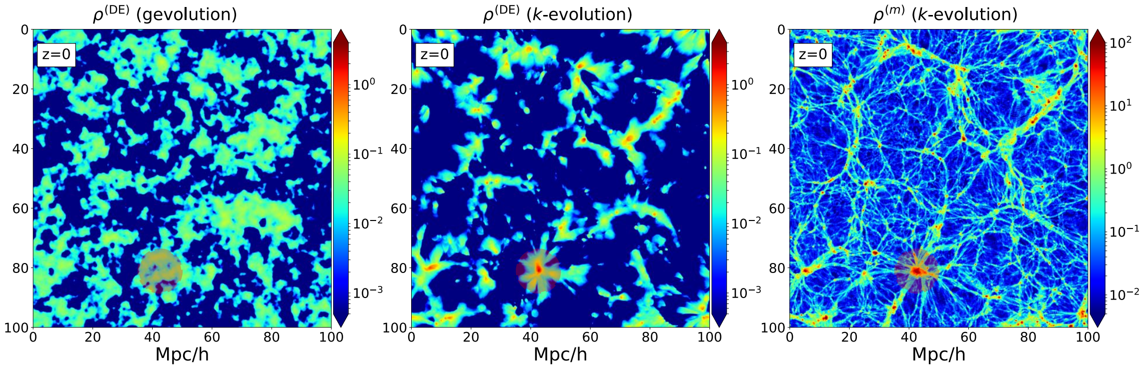

(a) Snapshot for dark energy density from *gevolution* (left panel), k-evolution (middle panel) and matter density from k-evolution (right panel) measured in the critical density unit at $z = 0$ from a high resolution simulation is shown. The shaded region shows the most massive halo in the simulation which is going to be studied in detail in the next figures.

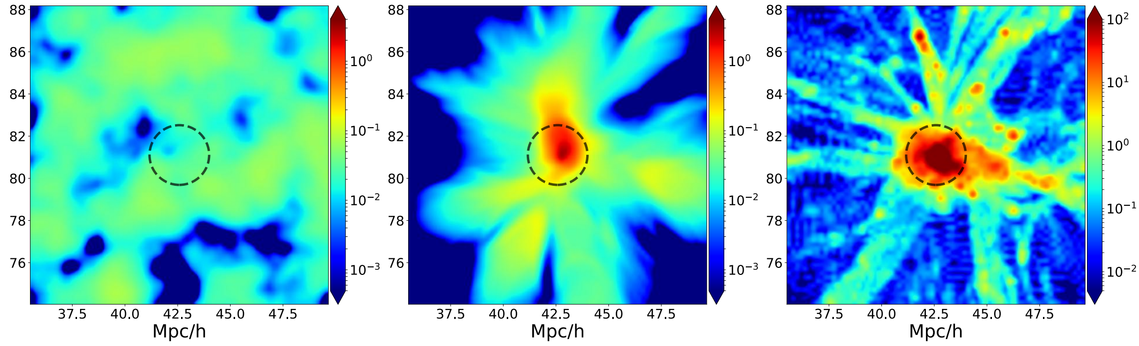

(b) A close look at the most massive halo (shaded region in the previous snapshot). The color bar range for dark energy density is different with matter density, as dark matter clusters more efficiently than dark energy.

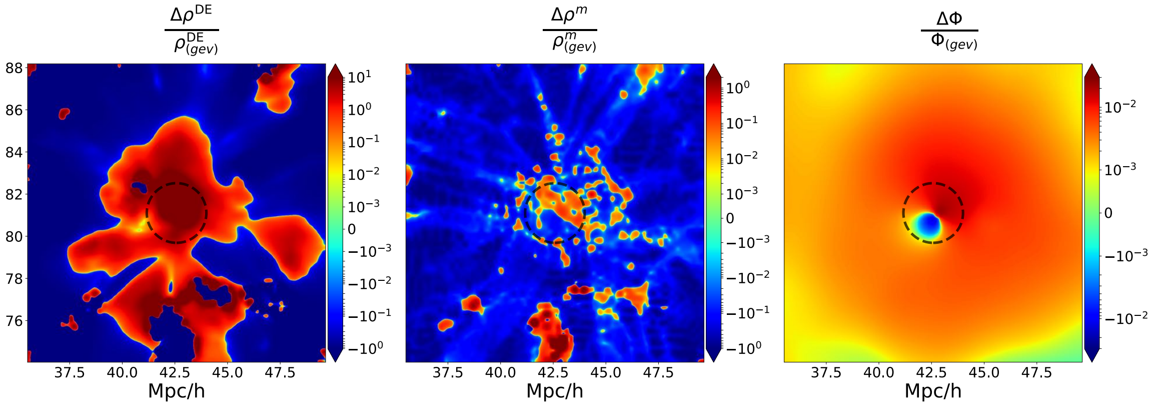

(c) The relative difference of dark energy density (left), matter density (middle) and gravitational potential (right) between the results from k-evolution and *gevolution* at $z = 0$.

Figure 2.16: A comparison of dark energy clustering in simulations.

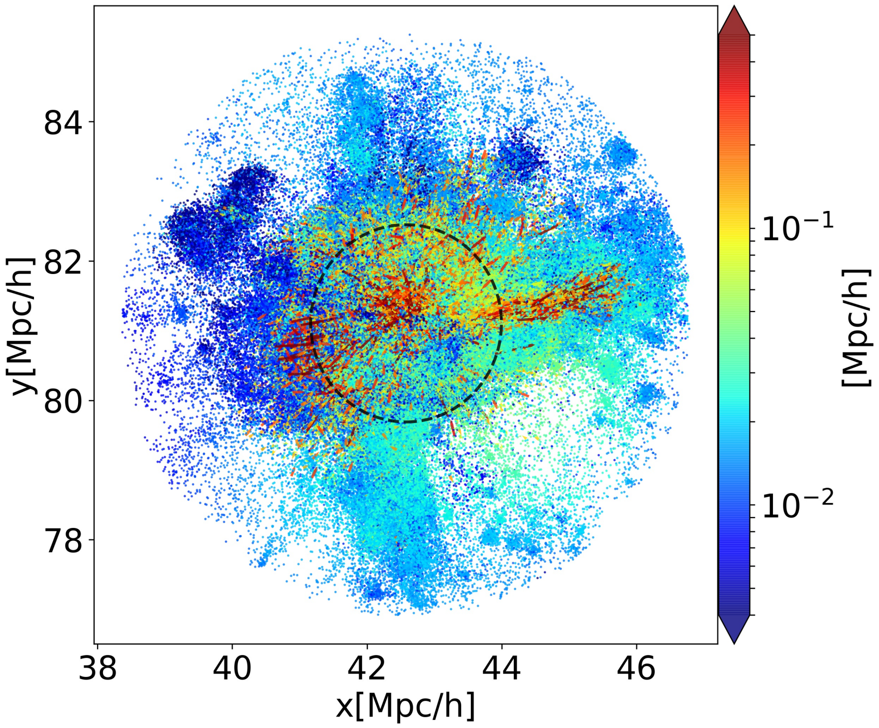

Figure 2.17: Change in the particles positions due to dark energy clustering. The arrows show the difference between the position of each particle in k-evolution and that of the same particle in *gevolution*. The colors show the length of the arrows measured in Mpc/h. Red arrows around the virial radius of the halo point toward the center.

APPENDIX

2.A Stress-energy conservation and the π equation of motion

The stress-energy tensor for a perfect fluid reads,

$$T^{\mu}_{\nu} = (\rho + p)u^{\mu}u_{\nu} + p\delta^{\mu}_{\nu} \, , \tag{2.1}$$

where u^{μ} is the fluid four-velocity normalized to unity, $u^{\mu}u_{\mu} = -1$. This can be decomposed as

$$u^{\mu} = \frac{dx^{\mu}}{ds} = \frac{e^{-\Psi}}{a}(1, v^i) \, , \tag{2.2}$$

so that the fluid components read

$$\begin{aligned} T^0_0 &= -\rho - \delta\rho \, , \\ T^i_0 &= -(\rho + p)v^i = -e^{2(\Phi+\Psi)}T^0_i \, , \\ T^j_i &= (p + \delta p)\delta^j_i + \Sigma^j_i \, , \end{aligned} \tag{2.3}$$

where $\Sigma^j_i \doteq T^j_i - \delta^j_i T^k_k/3$ denote the anisotropic stress, which is traceless $\Sigma^i_i = 0$.

The stress-energy tensor of a k-essence dark energy has the same form as the one of a perfect fluid. In particular, its components in (2.23) can be written as those of (2.3) with

$$\begin{aligned} \delta\rho &= -\frac{\rho + p}{c_s^2}\left[3c_s^2\mathcal{H}\pi - \zeta - \frac{2c_s^2 - 1}{2}(\vec{\nabla}\pi)^2\right] \, , \\ \delta p &= -(\rho + p)\left[3w\mathcal{H}\pi - \zeta + \frac{1}{6}(\vec{\nabla}\pi)^2\right] \, , \\ v^i &= -e^{2(\Phi+\Psi)}\left[1 - \frac{1}{c_s^2}\left(3c_s^2(1+w)\mathcal{H}\pi - \zeta + c_s^2\Psi\right) + \frac{c_s^2 - 1}{2c_s^2}(\vec{\nabla}\pi)^2\right]\partial_i\pi \, , \\ \Sigma_{ij} &= (\rho + p)\left[\partial_i\pi\partial_j\pi - \frac{1}{3}(\partial_k\pi)^2\delta_{ij}\right] \, . \end{aligned} \tag{2.4}$$

For completeness, we use the covariant conservation of the stress-energy tensor of k-essence to derive the continuity and Euler equation of the dark energy fluid. Then we show that the continuity equation is equivalent to the equations of motion for π, Eqs. (5.1) and (5.2). For convenience we define the following notation,

$$w \doteq \frac{p}{\rho} \, , \qquad \delta \doteq \frac{\delta\rho}{\rho} \, , \qquad \theta \doteq e^{-2(\Phi+\Psi)}\partial_i v^i \, , \qquad \sigma \doteq \frac{\partial^{-2}\delta^{ik}\partial_k\partial_j\Sigma^j_i}{\rho + p} \, , \tag{2.5}$$

where w is the equation of state parameter, δ is the density contrast and θ is the velocity divergence. Note that for k-essence v^i is irrotational, so that θ is enough to describe the full vector v^i.

If matter and dark energy are minimally coupled, as in the case of k-essence, the stress-energy tensor satifies the covariant conservation equation

$$\nabla_\mu T^\mu_\nu = 0 \ . \tag{2.6}$$

The continuity equation follows from taking this equation with $\nu = 0$, which gives

$$\delta' = -(1+w)\Big(\partial_i v^i - 3\Phi'\Big) - 3\mathcal{H}\left(\frac{\delta p}{\delta\rho} - w\right)\delta + 3\Phi'\left(1 + \frac{\delta p}{\delta\rho}\right)\delta + \frac{1+w}{\rho} v^i \partial_i\Big(3\Phi - \Psi\Big) \ . \tag{2.7}$$

With the above notation and keeping terms up to order $\mathcal{O}(\epsilon)$ in the weak-field expansion, one finds

$$\delta' = -(1+w)\Big(\theta - 3\Phi'\Big) - 3\mathcal{H}\left(\frac{\delta p}{\delta\rho} - w\right)\delta + 3\Phi'\left(1 + \frac{\delta p}{\delta\rho}\right)\delta + \frac{1+w}{\rho} v^i \partial_i\Big(3\Phi - \Psi\Big) \ . \tag{2.8}$$

The Euler equation follows from $\nu = i$, which gives

$$\begin{aligned}&\rho\, e^{-2(\Phi+\Psi)}(v^i)'(1+w) + e^{-2(\Phi+\Psi)}(1+w)(3w-1)\mathcal{H}\rho\, v^i + \Sigma_i^j\, \partial_j(\Psi - 3\Phi) \\ &+ \partial_i \delta p + \delta p\, \partial_i\Psi - e^{-2(\Phi+\Psi)}\rho v^i(1+w)\,(5\Phi' + \Psi') + \rho\, \partial_i\Psi(1+w) + \partial_i\Psi\, \rho\, \delta + \partial_j\Sigma_i^j = 0 \ .\end{aligned} \tag{2.9}$$

Dividing this equation by $(1+w)\rho$, taking its divergence of and replacing $\partial_i v^i$ using the definition of θ in Eq. (5.5), one finds

$$\begin{aligned}&\theta' + (3w-1)\mathcal{H}\,\theta + \nabla^2(\Psi + \sigma) + \frac{\nabla^2\delta P}{\rho(1+w)} - (5\Phi' + \Psi')\theta + \frac{\nabla^2\Psi}{1+w}\left(1 + \frac{\delta P}{\delta\rho}\right)\delta \\ &- \frac{\partial_i\Sigma_i^j}{\rho(1+w)}\partial_j(3\Phi - \Psi) = 0 \ .\end{aligned} \tag{2.10}$$

One can verify that the continuity equation for the k-essence fluid is equivalent to field equations for π. We do it explicitly in the limit of small speed of sound, where

$$\begin{aligned}\delta &= \frac{1+w}{2c_s^2}\Big[2\zeta - (\vec{\nabla}\pi)^2\Big] \ , \\ v^i &= -\frac{e^{2(\Phi+\Psi)}}{2c_s^2}\Big[2\zeta - (\vec{\nabla}\pi)^2\Big]\partial_i\pi \ , \\ \delta p &= -\rho\,(1+w)\left[3w\mathcal{H}\pi - \zeta + \frac{1}{6}(\vec{\nabla}\pi)^2\right] \ .\end{aligned} \tag{2.11}$$

From the expression for v^i and upon use of Eq. (5.1), the velocity divergence reads

$$\theta = \frac{1}{2c_s^2}\Big[-2\partial_i\zeta\partial_i\pi - 2\zeta\nabla^2\pi + \partial_i\left(\partial_i\pi(\vec{\nabla}\pi)^2\right)\Big] \, . \tag{2.12}$$

Putting the above expressions in the continuity equation (5.3) and multiplying by c_s^2, gives,

$$\zeta' - 3w\mathcal{H}\zeta - \vec{\nabla}\left(2\zeta+\Psi\right)\cdot\vec{\nabla}\pi - \zeta\nabla^2\pi + \frac{\mathcal{H}(2+3w)}{2}(\vec{\nabla}\pi)^2 + \frac{1}{2}\partial_i\left(\partial_i\pi(\vec{\nabla}\pi)^2\right) = 0 \, , \tag{2.13}$$

which is Eq. (5.2) in the small c_s^2 limit.

2.B Numerical implementation

We use the Newton-Stormer-Verlet-leapfrog method Ernst Hairer [0035] to solve the two first order partial differential equations for the linear k-essence scalar field on the lattice,

$$\zeta_{\mathrm{i,j,k}}^{\mathrm{n}+\frac{1}{2}} = \zeta_{\mathrm{i,j,k}}^{\mathrm{n}-\frac{1}{2}} + \zeta'^{\,\mathrm{n}}_{\mathrm{i,j,k}}\,\Delta\tau \tag{2.14}$$

where the superscript n and subscript $\mathrm{i,j,k}$ shows respectively the time step and the position on the lattice, i.e $\zeta_{\mathrm{i,j,k}}^{\mathrm{n}+\frac{1}{2}}$ is the field ζ at discrete time step $(\mathrm{n}+\frac{1}{2})$ and point $(\mathrm{i,j,k})$ on the lattice. To find $\zeta'^{\,\mathrm{n}}_{\mathrm{i,j,k}}$ we discretize Eq.(5.2) as

$$\begin{aligned}\zeta'^{\,\mathrm{n}}_{\mathrm{i,j,k}} =& 3w\mathcal{H}^{\mathrm{n}}\zeta^{\mathrm{n}}_{\mathrm{i,j,k}} - 3c_s^2\mathcal{H}^{\mathrm{n}}\left(\mathcal{H}^{\mathrm{n}}\pi^{\mathrm{n}}_{\mathrm{i,j,k}} - \Psi^{\mathrm{n}}_{\mathrm{i,j,k}} - \frac{\mathcal{H}'^{\mathrm{n}}}{\mathcal{H}^{\mathrm{n}}}\pi^{\mathrm{n}}_{\mathrm{i,j,k}} - \frac{\Phi'^{\,\mathrm{n}}_{\mathrm{i,j,k}}}{\mathcal{H}^{\mathrm{n}}}\right)\\ &+ c_s^2\frac{\Phi^{\mathrm{n}}_{\mathrm{i-1,j,k}} + \Phi^{\mathrm{n}}_{\mathrm{i+j,k}} + \Phi^{\mathrm{n}}_{\mathrm{i,j-1,k}} + \Phi^{\mathrm{n}}_{\mathrm{i,j+1,k}} + \Phi^{\mathrm{n}}_{\mathrm{i,j,k-1}} + \Phi^{\mathrm{n}}_{\mathrm{i,j,k+1}} - 6\Phi^{\mathrm{n}}_{\mathrm{i,j,k}}}{\Delta\mathrm{x}^2}\end{aligned}$$

To update the scalar field fluctuation $\pi^{\mathrm{n}}_{\mathrm{i,j,k}}$ we use,

$$\pi^{\mathrm{n}+1}_{\mathrm{i,j,k}} = \pi^{\mathrm{n}}_{\mathrm{i,j,k}} + \pi'^{\,\mathrm{n}+\frac{1}{2}}_{\mathrm{i,j,k}}\Delta\tau \tag{2.15}$$

while $\pi'^{\,\mathrm{n}+\frac{1}{2}}_{\mathrm{i,j,k}}$ is obtained by,

$$\pi'^{\,\mathrm{n}+\frac{1}{2}}_{\mathrm{i,j,k}} = \zeta^{\mathrm{n}+\frac{1}{2}}_{\mathrm{i,j,k}} - \mathcal{H}^{\mathrm{n}+\frac{1}{2}}_{\mathrm{i,j,k}}\pi^{\mathrm{n}+\frac{1}{2}}_{\mathrm{i,j,k}} + \Psi^{\mathrm{n}+\frac{1}{2}}_{\mathrm{i,j,k}} \tag{2.16}$$

It is important to note that in our scheme we have split the background from perturbations, as a result we have access to the $\mathcal{H}^{\mathrm{n}+\frac{1}{2}}$ independently of the value of the fields. Moreover we compute $\pi^{\mathrm{n}+\frac{1}{2}}_{\mathrm{i,j,k}}$ as following,

$$\pi^{\mathrm{n}+\frac{1}{2}}_{\mathrm{i,j,k}} = \frac{\pi^{\mathrm{n}+1}_{\mathrm{i,j,k}} + \pi^{\mathrm{n}}_{\mathrm{i,j,k}}}{2} \tag{2.17}$$

Putting (2.17) and (2.16) into the (2.15) results in,

$$\pi^{\mathrm{n+1}}_{\mathrm{i,j,k}} = \frac{1}{1+\mathcal{H}^{\mathrm{n}+\frac{1}{2}}\Delta\tau/2}\left[\pi^{\mathrm{n}}_{\mathrm{i,j,k}} + \Delta\tau\left[\zeta^{\mathrm{n}+\frac{1}{2}}_{\mathrm{i,j,k}} - \mathcal{H}^{\mathrm{n}+\frac{1}{2}}_{\mathrm{i,j,k}}\frac{\pi^{\mathrm{n}}_{\mathrm{i,j,k}}}{2} + \Psi^{\mathrm{n}+\frac{1}{2}}\right]\right] \tag{2.18}$$

where,

$$\Psi^{\mathrm{n}+\frac{1}{2}}_{\mathrm{i,j,k}} = \Psi^{\mathrm{n}}_{\mathrm{i,j,k}} + \Psi'^{\,\mathrm{n}}_{\mathrm{i,j,k}}\frac{\Delta\tau}{2} \tag{2.19}$$

Depending on the speed of sound of k-essence field c_s^2, we choose the appropriate Courant factor. Usually the k-essence Courant factor is different from the dark matter Courant factor and shows how many times the k-essence field is updated for one dark matter update. The reason is that for large speed of sound we need to decrease the time step of k-essence field updates to resolve the perturbations well.

2.C Initial conditions and gauge transformations

In this appendix we discuss the initial conditions for the scalar fluctuations π and ζ in k-evolution, provided by the Boltzmann codes at high redshifts, where the linear theory is a good approximation.

In the linear Boltzmann code `CLASS`, dark energy is implemented as a fluid in both Newtonian and Synchronous gauge. In `hi_class`, k-essence is implemented in the field language in Synchronous gauge only. To extract π and ζ from these codes, we need to gauge transform the perturbations to the Poisson gauge used in this article.

Let us first connect the field quantities to the fluid ones, in Newtonian gauge. To do that, we use the density contrast and velocity divergence of dark energy, respectively δ and θ, at linear order given in Eq. (5.6). Using these expression we find

$$\pi_{\mathrm{Newt}}(k,z) = \frac{\theta_{\mathrm{Newt}}(k,z)}{k^2}\,, \tag{2.20}$$

$$\pi'_{\mathrm{Newt}}(k,z) = \frac{c_s^2}{1+w}\delta_{\mathrm{Newt}}(k,z) + c_s^2\mathcal{H}\frac{\theta_{\mathrm{Newt}}(k,z)}{k^2} + \Psi_{\mathrm{Newt}}(k,z)\,, \tag{2.21}$$

where the subscript “Newt” denotes conformal Newtonian gauge.

Thus, using Eq. (2.18) we then obtain, for ζ,

$$\zeta_{\mathrm{Newt}} = \frac{c_s^2}{1+w}\delta_{\mathrm{Newt}}(k,z) + \mathcal{H}\frac{\theta_{\mathrm{Newt}}(k,z)}{k^2}(1+c_s^2)\,. \tag{2.22}$$

Following the discussion in Sec. 3 of Ma & Bertschinger [1995b] on the gauge transformations and employing the same notation, we consider the following coordinate transformation:

$$\begin{aligned} \hat{x}^0 &= x^0 + \alpha, \\ \hat{\vec{x}} &= \vec{x} + \vec{\nabla}\beta(\tau, x) + \vec{\epsilon}(\tau, x), \qquad \vec{\nabla}.\vec{\epsilon} = 0 \end{aligned} \tag{2.23}$$

where α and β are respectively the temporal and spatial part of the infinitesimal coordinate transformation. The metric components transform as,

$$\hat{g}_{\mu\nu}(x) = g_{\mu\nu}(x) - g_{\mu\beta}(x)\partial_\nu \epsilon^\beta - g_{\alpha\nu}(x)\partial_\mu \epsilon^\alpha - \epsilon^\alpha \partial_\alpha g_{\mu\nu}(x) \, . \tag{2.24}$$

As a result the transformed metric perturbations after coordinate transformation read,

$$\begin{aligned} \hat{\Psi}(\tau, \vec{x}) &= \Psi(\tau, \vec{x}) - \alpha'(\tau, \vec{x}) - \mathcal{H}\alpha(\tau, \vec{x}) \, , \\ \hat{\Phi}(\tau, \vec{x}) &= \Phi(\tau, \vec{x}) + \frac{1}{3}\nabla^2\beta(\tau, \vec{x}) + \mathcal{H}\alpha(\tau, \vec{x}) \, , \end{aligned} \tag{2.25}$$

where we have assumed that the coordinate transformation is of the same order as the metric perturbations. We can use these transformations to write down the scalar metric perturbations in Newtonian gauge (Φ, Ψ) in terms of (h, η) in Synchronous gauge. The result is that in Fourier space we can set

$$\alpha(\tau, k) = (h' + 6\eta')/2k^2, \qquad \beta(\tau, k) = (h + 6\eta)/2k^2 \, , \tag{2.26}$$

where (h, η) are the scalar modes of h_{ij} and are defined as,

$$h^{\parallel}_{ij}(\vec{x}, \tau) = \int d^3k e^{i\vec{k}\cdot\vec{x}} \left(\hat{k}_i\hat{k}_j - \frac{1}{3}\delta_{ij}\right) \{h(\vec{k}, \tau) + 6\eta(\vec{k}, \tau)\}, \qquad \vec{k} = k\hat{k} \, . \tag{2.27}$$

To find the gauge transformation for the fluid quantities we use

$$T^\mu_\nu(\text{Synch}) = \frac{\partial \hat{x}^\mu}{\partial x^\sigma}\frac{\partial x^\rho}{\partial \hat{x}^\nu} T^\rho_\sigma(\text{Newt}) \tag{2.28}$$

where $\hat{x}^\mu$ and x^μ denote the Synchronous and Newtonian coordinates respectively. It follows, to linear order, that

$$\begin{aligned} T^0_0(\text{Synch}) &= T^0_0(\text{Newt}) \, , \\ T^j_0(\text{Synch}) &= T^j_0(\text{Newt}) + ik_j\alpha(\bar{\rho} + \bar{P}) \, , \\ T^j_i(\text{Synch}) &= T^j_i(\text{Newt}) \, . \end{aligned} \tag{2.29}$$

From the definitions of the density contrast $\delta = \delta\rho/\bar{\rho} = -\delta T^0_0/\bar{\rho}$, θ, δP and σ in Eq. (5.6) we have,

$$\begin{aligned} \delta(\text{Synch}) &= \delta(\text{Newt}) - \alpha\frac{\dot{\rho}}{\rho}\,, \\ \theta(\text{Synch}) &= \theta(\text{Newt}) - \alpha k^2\,, \\ \delta P(\text{Synch}) &= \delta P(\text{Newt}) - \alpha\dot{P}\,, \\ \sigma(\text{Synch}) &= \sigma(\text{Newt})\,. \end{aligned} \tag{2.30}$$

To obtain the gauge transformation for π we use the fact that $\varphi(x^\mu) = x^0 + \pi(x^\mu)$ is a scalar, i.e., $\hat{\varphi}(\hat{x}^\mu) = \varphi(x^\mu)$. Thus, we find

$$\Delta\varphi(x) \doteq \hat{\varphi}(x) - \varphi(x) = -\partial_\mu\varphi\,\epsilon^\mu = \epsilon^0 = -\alpha\,, \tag{2.31}$$

which can be written as

$$\pi_{\text{Synch}} = \pi_{\text{Newt}} - \alpha\,. \tag{2.32}$$

For practical applications we provide a list of transformations in Fig. 2.18 and Fig. 2.19 for the output of `CLASS` and `hi_class` to obtain the result in a certain language with a certain gauge. In `CLASS`, we assume that the user sets the correct gauge, for example to have the quantities in Synchronous gauge one uses `CLASS` with the gauge is set to “Synchronous”. Then δ and θ in that gauge are the output of the code and one has to use the transformations in Fig. 2.18 to find π, π' in the corresponding gauge.

CLASS

$\pi_{\text{Synch}} = \theta_{\text{Synch}}/k^2$
$\pi'_{\text{Synch}} = \frac{c_s^2}{1+w}\delta_{\text{Synch}} + \left(3c_s^2 - 1\right)\mathcal{H}\theta_{\text{Synch}}/k^2$
θ_{Synch} = direct output
δ_{Synch} = direct output

$\pi_{\text{Newt}} = \theta_{\text{Newt}}/k^2$
$\pi'_{\text{Newt}} = \frac{c_s^2}{1+w}\delta_{\text{Newt}} + \left(3c_s^2 - 1\right)\mathcal{H}\theta_{\text{Newt}}/k^2 + \Psi_{\text{Newt}}$
θ_{Newt} = direct output
δ_{Newt} = direct output

Figure 2.18: The transformations in `CLASS` to obtain π and π' in a certain gauge from the fluid properties. In the top part, it is assumed that the user runs `CLASS` in Synchronous gauge which θ_{Synch} and δ_{Synch} in Synchronous gauge are the direct output of the code. To obtain π_{Synch} and π'_{Synch} one needs to use the given transformations. In the bottom part, it is assumed that the user runs `CLASS` in Newtonian gauge. Follow the recipe one obtains π_{Newt} and π'_{Newt}

.

In `hi_class` the quantities are written in Synchronous gauge only, in the field language. In this case $\pi_{\rm Synch}$ and $\pi'_{\rm Synch}$ are the outputs of the code, while $\delta_{\rm Synch}$, $\theta_{\rm Synch}$, $\pi_{\rm Newt}$ and $\pi'_{\rm Newt}$ are computed according to the formulas given in Fig. 2.19.

hi_class

$$
\begin{aligned}
\pi_{\rm Synch} &= \text{direct output}\\
\pi'_{\rm Synch} &= \text{direct output}\\
\theta_{\rm Synch} &= \pi_{\rm Synch}\, k^2\\
\delta_{\rm Synch} &= \tfrac{1+w}{c_s^2}\left(-\left(3c_s^2-1\right)\mathcal{H}\pi_{\rm Synch} + \pi'_{\rm Synch}\right)
\end{aligned}
$$

$$
\begin{aligned}
\pi_{\rm Newt} &= \pi_{\rm Synch} + \alpha\\
\pi'_{\rm Newt} &= \pi'_{\rm Synch} + \alpha'\\
\theta_{\rm Newt} &= \pi_{\rm Synch} k^2 + \alpha k^2\\
\delta_{\rm Newt} &= \tfrac{1+w}{c_s^2}\left(-\left(3c_s^2-1\right)\mathcal{H}\pi_{\rm Synch} + \pi'_{\rm Synch}\right) - 3(1+w)\mathcal{H}\alpha
\end{aligned}
$$

Figure 2.19: The transformations in `hi_class` to obtain a certain quantity in a specific gauge. In the top, the recipe in synchronous gauge is given. In `hi_class`, $\pi_{\rm Synch}$ and $\pi'_{\rm Synch}$ are the direct output of the code. To obtain $\delta_{\rm Synch}$ and $\theta_{\rm Synch}$ one needs to follow the given transformations. In the bottom part, the recipe for obtaining quantities in Newtonian gauge in both languages are given.

2.D Limit of small speed of sound c_s^2

In this appendix we are going to study the evolution of perturbations in the limit of small speed of sound, in order to show that this limit is well defined. In particular, we are going to show that δ and v^i remain finite in this limit, despite the appearance of a c_s^2 in the denominator of their expressions, see Eq. (2.11). To be able to solve this case analytically, we will assume matter dominance, i.e., $a \propto \tau^2$ (i.e., $\mathcal{H} = 2/\tau$) and $\Psi = \text{const}$. Moreover, we expand ζ and π in perturbations,

$$
\zeta = \zeta^{(1)} + \zeta^{(2)} + \dots\,, \qquad \pi = \pi^{(1)} + \pi^{(2)} + \dots\,, \tag{2.33}
$$

and we start by discussing linear perturbations.

At first order the evolution equations for π read

$$
\begin{aligned}
&\zeta - \pi' - \mathcal{H}\pi + \Psi = 0\,,\\
&\zeta' - 3w\mathcal{H}\zeta + 3c_s^2\left(\mathcal{H}^2\pi - \mathcal{H}\Psi - \mathcal{H}'\pi - \Phi'\right) - c_s^2\nabla^2\pi = 0\,,
\end{aligned} \tag{2.34}
$$

where we initially omit the upper index (1) to avoid cluttering. We can solve these equations for ζ and π perturbatively in c_s^2, i.e., using the expansions

$$\zeta = \zeta_0 + \zeta_1 c_s^2 + \dots \, , \qquad \pi = \pi_0 + \pi_1 c_s^2 + \dots \, . \tag{2.35}$$

At lowest order in c_s^2, the second equation becomes

$$\zeta_0' - 3w\mathcal{H}\zeta_0 = 0 \, . \tag{2.36}$$

Assuming w constant, its solution reads $\zeta_0 = C\, a^{-3w}$, where C is an arbitrary constant. However, in order to prevent the stress-energy tensor of dark energy from blowing up for $c_s^2 \to 0$ (see Eq. (2.11)), we fix it to zero, $C = 0$, so that ζ starts at linear order in c_s^2,

$$\zeta_0^{(1)} = 0 \, . \tag{2.37}$$

Notice that this coincides with assuming adiabatic initial conditions, i.e., $\Phi = \dot{\xi}^0 = \pi' + \mathcal{H}\pi$ Gleyzes et al. [2015]. Plugging $\zeta_0 = 0$ in the first equation of Eq. (2.34) we can solve for π,

$$\pi_0^{(1)} = \frac{\Psi}{3}\tau \, . \tag{2.38}$$

Since ζ vanishes at leading order in c_s^2, let us go to the next order. At first order in c_s^2, the second equation in Eq. (2.34) reads

$$\zeta_1' - 3w\mathcal{H}\zeta_1 + 3\left(\mathcal{H}^2\pi_0 - \mathcal{H}\Psi - \mathcal{H}'\pi_0 - \Phi'\right) - \nabla^2\pi_0 = 0 \, . \tag{2.39}$$

Using the solution for π and taking $\Phi' = 0$, we can solve for ζ_1, which gives

$$\zeta_1^{(1)} = \frac{\tau^2}{6(1-3w)}\nabla^2\Psi \, . \tag{2.40}$$

Since at leading order in c_s^2 we have $\delta = (1+w)\zeta/c_s^2$, see Eq. (2.11), and in matter domination the gravitational potential is given by the matter density contrast δ_m by the usual Poisson equation, $\nabla^2\Psi = (3/2)\mathcal{H}^2\delta_\mathrm{m}$, the above solution for $\zeta^{(1)} = \zeta_1^{(1)} c_s^2$ gives

$$\delta^{(1)} = \frac{1+w}{1-3w}\,\delta_\mathrm{m}^{(1)} \, , \tag{2.41}$$

as expected Creminelli et al. [2009].

At second order in perturbations we have

$$\zeta_0^{(2)\prime} - 3w\mathcal{H}\zeta_0^{(2)} - \vec{\nabla}\Psi \cdot \vec{\nabla}\pi_0^{(1)} + \frac{\mathcal{H}}{2}(2+3w)\left(\vec{\nabla}\pi_0^{(1)}\right)^2 = 0 \, , \tag{2.42}$$

where in the second equation we have assumed $c_s^2 = 0$ and have taken only the leading order in the expansions $\zeta = \zeta_0 + \zeta_1 c_s^2 + \dots$ and $\pi = \pi_0 + \pi_1 c_s^2 + \dots$. Using the linear solution for π, this equation can be solved,

$$\zeta_0^{(2)} = \frac{\tau^2}{18}(\vec{\nabla}\Psi)^2 \, , \tag{2.43}$$

which is exactly what needed to cancel the right-hand side of the first two equations in Eq. (2.11). To solve for $\pi_0^{(2)}$ we use that $\Psi^{(2)} = 0$ in Eq. (5.1), which gives

$$\pi_0^{(2)} = \frac{\tau^3}{90}(\vec{\nabla}\Psi)^2 \ . \tag{2.44}$$

In this case we do not need to go one order higher in c_s^2 to find ζ, because the leading order does not vanish. Using Eq. (2.11), the above solutions show that $\delta^{(2)}$ and $v_i^{(2)}$ vanish at this order in c_s^2. To find these quantities at leading order in c_s^2 we need to solve for $\zeta_1^{(2)}$ and $\pi^{(2)}$ (which requires $\pi_1^{(2)}$) and replace these quantities in Eq. (5.6). Since the solution obtained by this straightforward procedure is not very illuminating, we refrain from giving it here.

Going one order higher in perturbations, at third order the evolution equation of ζ_0 reads

$$\begin{aligned}&\zeta_0^{(3)\prime} - 3w\mathcal{H}\zeta_0^{(3)} - 2\vec{\nabla}\zeta_0^{(2)}\cdot\vec{\nabla}\pi_0^{(1)} - \vec{\nabla}\Psi\cdot\vec{\nabla}\pi_0^{(2)} - \zeta_0^{(2)}\nabla^2\pi_0^{(1)} + \mathcal{H}(2+3w)\vec{\nabla}\pi_0^{(2)}\cdot\vec{\nabla}\pi_0^{(1)}\\&+\frac{1}{2}\nabla_i\left[\nabla_i\pi_0^{(1)}\left(\vec{\nabla}\pi_0^{(1)}\cdot\vec{\nabla}\pi_0^{(1)}\right)\right] = 0 \ .\end{aligned} \tag{2.45}$$

Using the first and second-order solutions for π written above, this equation can be solved giving

$$\zeta_0^{(3)} = \frac{\tau^4}{270}\vec{\nabla}\Psi\cdot\vec{\nabla}(\vec{\nabla}\Psi)^2 \ . \tag{2.46}$$

Replacing this solution in Eq. (2.11) with the lowest order solutions for π shows again that δ remains finite in the $c_s^2 \to 0$ limit. This procedure can be straightforwardly extended to higher orders.

The solution for $\pi_0^{(3)}$ can be found by solving $\zeta_0^{(3)} - \pi_0^{(3)\prime} - \mathcal{H}\pi_0^{(3)} = 0$, giving

$$\pi_0^{(3)} = \frac{\tau^5}{1890}\vec{\nabla}\Psi\cdot\vec{\nabla}(\vec{\nabla}\Psi)^2 \ . \tag{2.47}$$

In summary, at leading order in c_s^2 and up to third order in perturbations we have

$$\begin{aligned}\zeta &= \frac{\tau^2 c_s^2}{6(1-3w)}\nabla^2\Psi + \frac{\tau^2}{18}(\vec{\nabla}\Psi)^2 + \frac{\tau^4}{270}\vec{\nabla}\Psi\cdot\vec{\nabla}(\vec{\nabla}\Psi)^2 \ ,\\ \pi &= \frac{\tau\Psi}{3} + \frac{\tau^3}{90}(\vec{\nabla}\Psi)^2 + \frac{\tau^5}{1890}\vec{\nabla}\Psi\cdot\vec{\nabla}(\vec{\nabla}\Psi)^2 \ .\end{aligned} \tag{2.48}$$

2.E Supplementary materials

This appendix is not part of the submitted paper and we plan to elaborate the details in the original paper.

It is always important to make sure that the computations are performed correctly, thus it would be helpful if we could find an intelligent way to cross check our results using a computer programming. It turns out that the symbolic computation in Mathematica is useful for our purposes. Using this feature of Mathematica we can obtain the Einstein fields equations from the FLRW metric as follows,

```
In[1]:= n=4;
        coord = {t,r,θ,ϕ};
        metric=Array[g,{4,4}];
        1,1]=-1;
        g[2,2]=a[t]^2;
        g[3,3]=a[t]^2r^2;
        g[4,4]=a[t]^2r^2Sin[θ]^2;
        r[l=2,l<5,l++,
        For[i=2,i<5,i++,
        If[i≠l, g[i,l]=0;]
        ]
        ]
        For[i=2,i<5,i++,
        g[1,i]=0 ;
        g[i,1]=0 ;
        ]
```

According the definitions introduced previously in Chapter. 1, we can define the Christoffel symbols, the Ricci tensor and scalar, the Einstein tensor as,

```
In[2]:= affine=Table[1/2*Sum[(inversemetric[[i,s]])*
        (D[metric[[s,j]],coord[[k]] ]+
        D[metric[[s,k]],coord[[j]] ]-D[metric[[j,k]],coord[[s]] ]),{s,1,n}],
        {i,1,n},{j,1,n},{k,1,n}];

        riemann:=riemann=Table[
        D[affine[[i,j,l]],coord[[k]] ]-D[affine[[i,j,k]],coord[[l]] ]+
        Sum[affine[[s,j,l]] affine[[i,k,s]]-affine[[s,j,k]]  affine[[i,l,s]],
        {s,1,n}],
        {i,1,n},{j,1,n},{k,1,n},{l,1,n}] ;

        ricci=Table[Sum[riemann[[i,j,i,l]],{i,1,n}],{j,1,n},{l,1,n}]

        scalaricci=Sum[inversemetric[[i,j]]ricci[[i,j]],{i,1,n},{j,1,n}]
```

```
                          1
einstein:=einstein=ricci- -scalaricci*metric;
                          2

SEHMetric=√-Det[metric]scalaricci ;
```

Now we can compare some elements with our calculated results. In the below we print Γ^1_{10}, the Einstein tensor $G_{\mu\nu}$ in the matrix form and the Ricci scalar R,

```
In[3]:= affine[[2,2,1]]//MatrixForm

Out[3]//MatrixForm=
        a′[t]
        -----
        a[t]

In[4]:= einstein//Simplify//MatrixForm

Out[4]//MatrixForm=
        3  a′[t]²
        ---------       0         0         0
         a[t]²
        0        -a′[t]²-2 a[t] a′′[t]         0         0
        0        0        -r² (a′[t]²+2 a[t]  a″[t])      0
        0        0        0        -r² Sin[θ]²  (a′[t]²+2 a[t]  a″[t] )

In[5]:= scalaricci//Simplify

        6 (a′[t]²+a[t] a″[t])
Out[5]= ---------------------
               a[t]²
```

Chapter 3

CLUSTERING DARK ENERGY IMPRINTS ON COSMOLOGICAL OBSERVABLES OF THE GRAVITATIONAL FIELD

Based on:
Hassani et al. [2020a] Farbod Hassani (Geneva U., Dept. Theor. Phys.), Julian Adamek (Queen Mary, U. of London), Martin Kunz (Geneva U., Dept. Theor. Phys.)
Clustering dark energy imprints on cosmological observables of the gravitational field, Submitted to Monthly Notices of the Royal Astronomical Society, [arXiv: 2007.04968].

Abstract: We study cosmological observables on the past light cone of a fixed observer in the context of clustering dark energy. We focus on observables that probe the gravitational field directly, namely the integrated Sachs-Wolfe and non-linear Rees-Sciama effect (ISW-RS), weak gravitational lensing, gravitational redshift and Shapiro time delay. With our purpose-built N-body code "k-evolution" that tracks the coupled evolution of dark matter particles and the dark energy field, we are able to study the regime of low speed of sound c_s where dark energy perturbations can become quite large. Using ray tracing we produce two-dimensional sky maps for each effect and we compute their angular power spectra. It turns out that the ISW-RS signal is the most promising probe to constrain clustering dark energy properties coded in $w-c_s^2$, as the *linear* clustering of dark energy would change the angular power spectrum by $\sim 30\%$ at low ℓ when comparing two different speeds of sound for dark energy. Weak gravitational lensing, Shapiro time-delay and gravitational redshift are less sensitive probes of clustering dark energy, showing variations of a few percent only. The effect of dark energy *non-linearities* in all the power spectra is negligible at low ℓ, but reaches about 2% and 3%, respectively, in the convergence and ISW-RS angular power spectra at multipoles of a few hundred when observed at redshift ~ 0.85. Future cosmological surveys achieving percent precision measurements will allow to probe the clustering of dark energy to a high degree of confidence. Clear evidence for clustering dark energy at any scale would rule out a cosmological constant as the leading contender for dark energy, and may help to distinguish between different dark energy models.

3.1 Introduction

The accelerated expansion of the Universe which has been attributed to the so called "dark energy" component was first discovered using supernova Ia observations over two decades ago independently by Perlmutter et al. [1999] and Riess et al. [1998b]. Since then the late-time accelerating expansion has been confirmed by several independent measurements, including the cosmic microwave background (CMB) [Ade et al., 2015a, Planck Collaboration et al., 2016, Spergel et al., 2003], large scale structure [Tegmark et al., 2004, 2006] and baryon acoustic oscillations [Aubourg et al., 2015, Percival et al., 2007].

In the ΛCDM standard model of cosmology the cosmological constant Λ is responsible for the late-time acceleration. Although ΛCDM is a successful model that fits the current data well, Λ is a phenomenological parameter which is not theoretically well motivated and suffers from severe fundamental issues including fine-tuning of the initial energy density and the coincidence problem [see Martin [2012b] for a review of the cosmological constant problem]. The theoretical issues of the cosmological constant and tensions between some parameters in various cosmological data sets [Handley & Lemos, 2019, Verde et al., 2019] that have emerged over the past years have motivated cosmologists to propose a plethora of dark energy (in the form of an additional scalar field or “dark” fluid) and modified gravity models (in the form of a modification of general relativity) to explain the late-time cosmic acceleration [Clifton et al., 2012b, Joyce et al., 2016b, Koyama, 2018]. Since the number of viable dark energy and modified gravity models is substantial, the effective field theory (EFT) approach has been developed and has become popular. It describes the theory economically in the low energy limit using symmetries and can connect the specific theory to the observation in a straightforward way.

In the near future with high precision cosmological surveys such as Euclid [Laureijs et al., 2011], the Dark Energy Spectroscopic Instrument (DESI) [Aghamousa et al., 2016a], the Legacy Survey of Space and Time (LSST) [Abate et al., 2012] and the Square Kilometre Array (SKA) [Santos et al., 2015a] we will be able to probe the cosmological models with percent precision into the highly nonlinear regime. One of the main goals of these surveys is to understand the reason behind the cosmic acceleration and to probe the nature of gravity. In the case where the data prefers an alternative dark energy scenario, accurate modeling of the cosmological observables for non-standard models up to highly nonlinear scales is required. A very accurate method to model the cosmological predictions of these theories on such scales is obtained using cosmological N-body simulations.

Until now several N-body codes have been developed for a range of alternative gravity models [Baldi, 2012, Barreira et al., 2013, Brax et al., 2012b, Li et al., 2012a, Li et al., 2013, Llinares et al., 2014, Mead et al., 2015, Oyaizu et al., 2008, Puchwein et al., 2013, Schmidt et al., 2009a, Valogiannis & Bean, 2017, Wyman et al., 2013, Zhao et al., 2011]. These codes are based on Newtonian gravity which is not naturally suited for considering the non-standard dark energy models, therefore requiring a number of approximations. While these may be justified for a crude analysis, the fact that dark energy (as opposed to dark matter) is not dominated by rest-mass density appeals more to a relativistic treatment.

With such applications in mind, some of us have developed *gevolution* [Adamek et al., 2016a], an N-body code entirely based on General Relativity (GR). One of the main advantages of the *gevolution* scheme is that it could be extended naturally to include dark energy or modified gravity models without requiring any approximations in the dark energy sector such as the quasi-static approximation as is done in the Newtonian approaches. A full implementation of the EFT of dark energy encompassing many dark energy and modified gravity models is still a formidable task. As a first step toward this goal we have recently developed the k-evolution code in Hassani et al. [2019a] in which we have added a k-essence scalar field using the EFT language. Based on *gevolution* some of us have recently also developed N-body simulations for parametrised modified gravity in **?**, and Reverberi & Daverio [2019] have implemented $f(R)$ models in *gevolution*.

In this article, we study the effect of k-essence dark energy on the cosmological observables of the gravitational field using our N-body codes *gevolution* and k-evolution. In particular, weak gravitational lensing and the ISW-RS effect probe the gravitational potential and its time derivative directly, and they can be constrained with multiple probes independently. We additionally discuss gravitational redshift and the Shapiro time delay, even though their cosmological detection will be more challenging. We study and quantify the signatures that the k-essence model would imprint on each observable.

In Section 3.2 we discuss the theoretical background, focusing on k-essence in the EFT framework of dark energy, and we present the relevant equations that are solved in k-evolution to evolve the k-essence field. Section 3.3 is devoted to the general discussion about the cosmological observables and how non-standard dark energy or modified gravity models would affect each observable. The cosmological parameters of our simulations and the way we construct the past light cone for a fixed observer in our N-body codes to make the synthetic sky maps of our observables are explained in Section 7.2.4. In Section 3.5 we show the numerical results from k-evolution and *gevolution* and we compare the results with the linear theory prediction obtained from the Boltzmann code `CLASS`. Our conclusions and main take-home points are summarised in Section 3.6.

3.2 Theory

In this section we briefly review the essentials of the k-essence model especially with the focus on its effective field theory description and the k-evolution code, an N-body code recently developed to study the evolution of large scale structure in the presence of a non-linear k-essence scalar field, see Hassani et al. [2019a] for a description.

To study the evolution of the perturbations around a homogenous flat Friedmann Universe, we consider the Friedmann-Lemaître-Robertson-Walker (FLRW) metric written in the conformal Poisson gauge,

$$ds^2 = a^2(\tau)\Big[-e^{2\Psi}d\tau^2 - 2B_i dx^i d\tau + \Big(e^{-2\Phi}\delta_{ij} + h_{ij}\Big)dx^i dx^j\Big], \tag{3.1}$$

where Ψ and Φ are the Bardeen potentials carrying the scalar perturbations of the metric, B_i is the gravitomagnetic vector perturbation with two degrees of freedom as we have $\delta^{ij}\partial_j B_i = 0$, and h_{ij} is the tensor perturbation with the gauge condition $\delta^{ij}h_{ij} = 0 = \delta^{ij}\partial_i h_{jk}$ which results in two remaining degrees of freedom.

The k-essence model was originally introduced to naturally explain the recent accelerated expansion of the Universe through the idea of a dynamical attractor solution in which this model acts as a cosmological constant at the beginning of the matter dominated era without any fine tuning of the parameters [Armendariz-Picon et al., 2000, 2001]. This model is particularly interesting as it does not rely on coincidence or anthropic reasoning, unlike the cosmological constant and quintessence models[1] in which the energy density today is set by tuning the model parameters.

The k-essence action, an action containing at most one single derivative acting on the field, reads

$$S_{\mathrm{DE}} = \int \sqrt{-g}P(X,\varphi)d^4x \ , \tag{3.2}$$

where φ is the scalar field and $X = -\frac{1}{2}g^{\mu\nu}\partial_\mu\varphi\partial_\nu\varphi$ is the kinetic term of the k-essence field. In general we need to choose a specific form for the function $P(X,\varphi)$ to solve the equations of motion for the k-essence scalar field. Since there are many possible choices, one can instead employ the EFT approach to model the dynamics of dark energy. EFT, although not a fundamental theory, offers several advantages: First, we can express a large class of dark energy and modified gravity (DE/MG) models with a minimal number of parameters in a model-independent approach and using a unified language. Second, the phenomenological parameters of the effective theory can be constrained directly by cosmological observations without being specific to any DE/MG models nor to their original motivations. Third, the effective approach allows the theorists to carefully examine the unexplored regions of the space of parameters which could in principle guide towards new viable models [Creminelli et al., 2009, Gubitosi et al., 2013a].

In k-evolution [Hassani et al., 2019a], which is an extension of *gevolution* [Adamek et al., 2016a, Adamek et al., 2016b] in which we have implemented the k-essence model as a dark energy sector, we use the EFT approach to write down the equations of motion parametrised with the equation of state w and the squared speed of sound c_s^2. The scalar field evolution, keeping only linear terms of the scalar field and its time derivative, is given by

$$\pi' = \zeta - \mathcal{H}\pi + \Psi \ , \tag{3.3}$$

$$\zeta' = 3w\mathcal{H}\zeta - 3c_s^2\left(\mathcal{H}^2\pi - \mathcal{H}\Psi - \mathcal{H}'\pi - \Phi'\right) + c_s^2\nabla^2\pi \ , \tag{3.4}$$

where π is the scalar field perturbation around its background value, ζ is written in terms of π and π', $\nabla^2 = \delta^{ij}\partial_i\partial_j$, a prime $'$ denotes the time derivative with respect to the conformal time, and $\mathcal{H}$ is the conformal Hubble function. The linear stress energy tensor reads

---

[1] The quintessence model is a canonical scalar field model, corresponding to the special case of the k-essence model where the kinetic term is canonical.

$$\begin{aligned}
T^0_0 &= -\rho + \frac{\rho + p}{c_s^2}\Big(3c_s^2\mathcal{H}\pi - \zeta\Big) \ , \\
T^0_i &= -(\rho + p)\partial_i\pi \ , \\
T^i_j &= p\delta^i_j - (\rho + p)\Big(3w\mathcal{H}\pi - \zeta\Big)\delta^i_j \ .
\end{aligned} \tag{3.5}$$

It is worth noting that in connection with the EFT language, with the notation used in Gleyzes et al. [2013], apart from the background parameters $\Lambda(t)$ and $c(t)$ the only remaining parameter in EFT for k-essence theory is $M_2^4(t)$. In the alternative EFT notation using $\alpha_i(t)$ explained in Bellini & Sawicki [2014], α_K is the only non-zero parameter.

As discussed in Hassani et al. [2019a], although we keep only linear terms in the scalar field dynamics and we drop higher order self-interactions of π, the scalar field does cluster and form non-linear scalar field structures in k-evolution because it is sourced by non-linearities in matter through gravitational coupling. This is the crucial improvement over the treatment of dark energy in *gevolution*, which uses the transfer functions from linear theory to keep track of perturbations in the dark energy fluid similar to how it is done in Dakin et al. [2019] [see also **?** for a more comprehensive extension of this framework to EFT].

Einstein's equations for the evolution of the scalar perturbations in the weak field regime [Adamek et al., 2017b] read

$$(1 + 2\Phi)\nabla^2\Phi - 3\mathcal{H}\Phi' - 3\mathcal{H}^2\Psi - \frac{1}{2}\delta^{ij}\partial_i\Phi\partial_j\Phi = -4\pi G a^2 \delta T^0_0 \ , \tag{3.6}$$

$$\nabla^4(\Phi - \Psi) - \left(3\delta^{ik}\delta^{jl}\frac{\partial^2}{\partial x^k \partial x^l} - \delta^{ij}\nabla^2\right)\partial_i\Phi\partial_j\Phi = 4\pi G a^2\left(3\delta^{ik}\frac{\partial^2}{\partial x^j \partial x^k} - \delta^i_j\nabla^2\right)T^j_i \ , \tag{3.7}$$

where the stress tensor T^ν_μ includes all the relevant species, i.e. matter, dark energy and radiation.

In Hassani et al. [2019a], we introduce k-evolution and the full non-linear equations for the k-essence model written using the EFT action. We study the dark energy clustering and its impact on the large scale structure of the Universe. Moreover, we discuss that the scalar dark energy does not lead to significantly larger vector and tensor perturbations than ΛCDM. Thus one can safely neglect the vector and tensor perturbation in this theory. In Hassani et al. [2019b] we quantify the non-linear effects from k-essence dark energy through

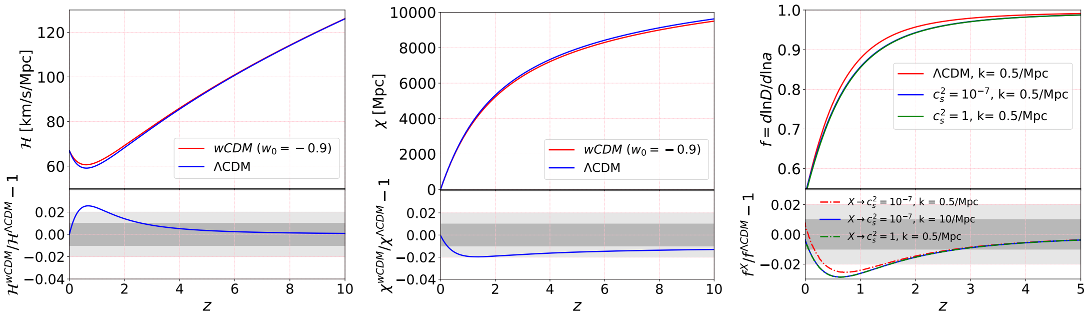

Figure 3.1: ***Left:*** The conformal Hubble parameter as a function of redshift for ΛCDM and wCDM with $w_0 = -0.9$. In the bottom panel we show the relative difference. As expected, the effect of dark energy goes away at high redshifts. ***Centre:*** The comoving distance as a function of redshift for the two cosmologies is plotted. In the bottom panel again the relative difference is shown. The relative difference asymptotes to a constant at high redshifts because the comoving distance is an integrated quantity. ***Right:*** In the top panel, the logarithmic growth rate f as a function of redshift for a fixed wavenumber is plotted. In the bottom the relative difference between different scenarios is shown with respect to ΛCDM. While in the latter case the growth rate is scale independent (neglecting corrections due to neutrinos), in a clustering dark energy model the behaviour of a mode depends on whether it is inside or outside of the sound horizon. We compare three cases with ΛCDM, namely the mode $k = 0.5$ Mpc^{-1} with $c_s^2 = 10^{-7}$, $k = 10$ Mpc^{-1} with $c_s^2 = 10^{-7}$ and $k = 0.5$ Mpc^{-1} with $c_s^2 = 1$. Only the first case corresponds to a mode outside the sound horizon, while the other two are well inside. Thus we see the same behaviour for $k = 10$ Mpc^{-1} with $c_s^2 = 10^{-7}$ and $k = 0.5$ Mpc^{-1} with $c_s^2 = 1$.

the effective parameter $\mu(k, z)$ that encodes the contribution of a dark energy sector to the Poisson equation (see below). We also show that for the k-essence model the difference between the two potentials $\Phi - \Psi$ and short-wave corrections appearing as higher order terms in the Poisson equation can be safely neglected. Moreover, in Hansen et al. [2020], we study the effect of k-essence dark energy as well as some other modified gravity theories on the turn-around radius — the radius at which the inward velocity due to the gravitational attraction and outward velocity due to the expansion of the Universe cancel each other — in galaxy clusters.

It is sometimes useful to parametrise the effect that clustering dark energy has on the gravitational potential phenomenologically through a modified Poisson equation,

$$-k^2\Phi = 4\pi G_N a^2 \mu(k, z) \sum_X \bar{\rho}_X \Delta_X \ , \tag{3.8}$$

where Δ is the comoving density contrast and the species X do not include the dark energy field. Denoting in addition the ratio between the two Bardeen potentials as

$$\eta(k,z) = \frac{\Psi(k,z)}{\Phi(k,z)} \,, \tag{3.9}$$

one obtains a phenomenological classification of DE/MG models through two generic functions of time and scale, with ΛCDM predicting $\eta = \mu = 1$ everywhere [e.g. Ade et al., 2015a, Blanchard et al., 2019]. As discussed in Hassani et al. [2019b], for the case where k-essence plays the role of dark energy, $\eta(k,z) \approx 1$ and $\mu(k,z)$ is fitted well with a tanh function where the amplitude and shape of the function depends on the speed of sound and equation of state.

For the sake of completeness, we show the effect of k-essence, expressed in the form of $w - c_s^2$ in the parameter space, on the background evolution and the growth of matter density perturbation. The effect of k-essence appears on the background evolution via the equation of state but independent of the speed of sound of dark energy. We show the conformal Hubble parameter $\mathcal{H}$ as well as the redshift-distance relation in Fig. 3.1 in the left and middle panel for wCDM with $w = -0.9$ and ΛCDM, which are the cases we consider in this article. We also compare the logarithmic growth rate $f = d\ln\Delta_m/d\ln a$ in the right panel of Fig. 3.1 for different scenarios to see the impact of different choices of w and c_s^2 on the growth of structures. The logarithmic growth rate provides a useful way to distinguish between DE/MG gravity and ΛCDM [Amendola et al., 2016, Blanchard et al., 2019, Dossett & Ishak, 2013, Kunz & Sapone, 2007].

Since the logarithmic growth rate is in general scale dependent, we compute it for different scales by studying the evolution of the comoving matter density contrast Δ_m, which we define for this purpose through $\Omega_m\Delta_m = \Omega_b\Delta_b + \Omega_{\mathrm{cdm}}\Delta_{\mathrm{cdm}}$. We compute Δ_m with the linear Boltzmann code `CLASS` and look at the evolution for wavenumbers $k = 0.5$ Mpc^{-1} and $k = 10$ Mpc^{-1} for the model with $c_s^2 = 10^{-7}$ which corresponds respectively to a mode well outside and a mode well inside the sound horizon. We compare the logarithmic growth rate from the two modes for $c_s^2 = 10^{-7}$, and in addition $k = 0.5$ Mpc^{-1} for $c_s^2 = 1$, with ΛCDM in the bottom right panel of Fig. 3.1. As expected, for the mode $k = 0.5$ Mpc^{-1} in the case where $c_s^2 = 1$, as it is well inside the sound horizon, the result matches with the mode evolution of $k = 10$ Mpc^{-1} in the case where $c_s^2 = 10^{-7}$. The mode $k = 0.5$ Mpc^{-1} has a different evolution in the case where $c_s^2 = 10^{-7}$ because it is outside the sound horizon and the perturbations in the dark energy field are therefore not suppressed.

3.3 Observables

Solving the null geodesic equation ($k^\mu \nabla_\mu k_\nu = 0$) for a light ray with wavevector k^μ in a perturbed FLRW universe results in a change in position and energy of the light beam emitted from the source. The apparent comoving 3D position of the source reads [Adamek et al., 2020b, Bonvin & Durrer, 2011, Breton et al., 2019, Challinor & Lewis, 2011, Yoo et al., 2009]

$$\boldsymbol{s} = \chi_s \boldsymbol{n} + \underbrace{\frac{1}{H_s(\bar{z})}\delta z\, \boldsymbol{n}}_{\text{redshift perturbation}} - \underbrace{\int_0^{\chi_s} (\chi_s - \chi)\, \nabla_\perp (\Phi + \Psi) \mathrm{d}\chi}_{\text{weak gravitational lensing}} \\ \underbrace{- \boldsymbol{n} \int_0^{\chi_s} (\Phi + \Psi) \mathrm{d}\chi}_{\text{Shapiro time delay}}\,, \quad (3.10)$$

where $\boldsymbol{s}$ is the observed position in redshift space, and $\boldsymbol{n}$ and χ_s are respectively the unperturbed direction vector and unperturbed comoving distance to the source. Furthermore, $\nabla_\perp \equiv (\mathbb{1} - \boldsymbol{n} \otimes \boldsymbol{n})\nabla$ is the projected gradient perpendicular to the line of sight, χ is the comoving distance and $H_s(\bar{z})$ is the Hubble rate at the unperturbed redshift $\bar{z}$ of the source. The first term in Eq. (3.10) corresponds to the unperturbed position, the second term corresponds to the redshift perturbation which is computed in Eq. (3.11), the third term (weak gravitational lensing) yields an angular deflection of the source position on the 2D sphere, and the last term changes the radial position due to the Shapiro time delay.

Using the time component of geodesic equation one obtains the redshift perturbation $\delta z = z - \bar{z}$ as

$$\delta z = (1 + \bar{z}) \left[\underbrace{\boldsymbol{n} \cdot (\boldsymbol{v}_s - \boldsymbol{v}_o)}_{\text{Doppler}} + \underbrace{\Psi_o - \Psi_s}_{\substack{\text{gravitational} \\ \text{redshift}}} - \underbrace{\int_0^{\chi_s} \frac{\partial (\Psi + \Phi)}{\partial \tau} d\chi}_{\text{ISW-RS effect}} \right] . \quad (3.11)$$

As a result of Eq. (3.10) and Eq. (3.11), the light ray along its path is deflected, redshifted and delayed due to the different physical phenomena, namely weak gravitational lensing, integrated Sachs-Wolfe and Rees-Sciama (ISW-RS) effect and Shapiro time delay. In addition, there are two local (non-integrated) contributions to the redshift: the relativistic Doppler effect (due to the peculiar velocities $\boldsymbol{v}_s$ and $\boldsymbol{v}_o$ of the source and observer, respectively) and the gravitational redshift (ordinary Sachs-Wolfe effect). Among these, the weak gravitation lensing, ISW-RS, Shapiro time delay and gravitational redshift all depend directly on the configuration of the gravitational field. If they can be observed independently they can be used as a probe of DE/MG. In the current work we are going to look at each individual aforementioned effect to study the impact of

k-essence clustering dark energy. It is important to point out that the Doppler term is also expected to be a powerful probe of dark energy and is worth to be studied in detail. However, in this paper we only focus on the physical effects coming from the metric perturbations Ψ and Φ. These have the advantage that they can be observed (as integrated effects) even in places where there are no visible sources, like e.g. in voids which are naturally expected to be dominated by dark energy.

In the following subsections we shall introduce and derive the relevant expressions for each effect separately and we will discuss why each of these observables could be potentially used to put constraint on DE/MG models, especially clustering dark energy.

3.3.1 Weak gravitational lensing

The light from distant objects is deflected due to inhomogeneities as it travels through the intervening large scale structure in the Universe. The deflection angles are usually small at cosmological scales and this phenomenon is called weak gravitational lensing. As mentioned already, weak gravitational lensing directly probes the distribution of matter and energy, including dark matter and dark energy, which makes it a unique tool to constrain the cosmological parameters [Ade et al., 2014a, Bartelmann & Schneider, 2001, Hassani et al., 2016, Hikage et al., 2019, Lewis & Challinor, 2006, Refregier, 2003]. Weak gravitational lensing can be observed through the statistics of cosmic shear and cosmic convergence, as we will summarise briefly in the following.

Cosmic shear refers to the change of the ellipticities of galaxies observed on the far side of the gravitational lens. The cosmic convergence, on the other hand, magnifies/demagnifies the sizes and magnitudes of the same galaxies [Alsing et al., 2015, Mandelbaum, 2018]. The first detection of cosmic shear have been done about 20 years ago [Bacon et al., 2000, Van Waerbeke et al., 2000], while cosmic convergence was measured for the first time in 2011 [Schmidt et al., 2011]. Since then the precision in cosmic shear and cosmic convergence measurements has been improved and these two have become some of the most promising probes of dark energy and modified gravity [Amendola et al., 2008, Hannestad et al., 2006, Jain & Taylor, 2003, Spurio Mancini et al., 2018].

In Adamek et al. [2019], some of us have implemented a ray-tracing method to analyse relativistic N-body simulations performed with the code *gevolution*. In this method one solves the optical equations in the scalar sector of gravity without any approximation and additionally keeps track of the frame dragging to first order. Weak-lensing convergence and shear obtained with this numerical method were studied in more detail in Lepori et al. [2020]. While other approaches often try to reconstruct the signal from the mass distribution, our method works with the metric perturbations directly and is therefore more robust once we consider

DE/MG like in the present work. To this end we have recently implemented the same light-cone analysis and ray-tracing method in k-evolution. Here, however, we compute each effect only to first order in Φ and Ψ, and we neglect the frame dragging. For the purpose of discussing angular power spectra this is sufficient, as nonperturbative effects (in the ray tracing[2]) would only enter at a detectable level for very high multipoles that are not resolved in our maps.

In the first order weak gravitational lensing formalism one introduces the lensing potential $\psi(\boldsymbol{n}, z)$ defined as

$$\psi(\boldsymbol{n}, z) \equiv -\int_0^{\chi_s} d\chi \frac{\chi_s - \chi}{\chi_s \chi}(\Phi + \Psi) \,, \tag{3.12}$$

where the redshift z and the source distance χ_s are related through the background distance-redshift relation, and the integration is carried out in direction $\boldsymbol{n}$ using the Born approximation.

Using the gradient $\hat{\nabla}^a$ on the 2D sphere we can calculate the deflection angle as $\alpha^a = \theta_o^a - \theta_s^a = \hat{\nabla}^a \psi$, which results in the lensing term in Eq. (3.10). The Jacobi map, which is a map between the unperturbed source angular positions θ_s and the observed angular positions θ_o, i.e. $\mathcal{A}_{ab} = \partial\theta_o^a/\partial\theta_s^b$, contains the full information for weak gravitational lensing and reads

$$\mathcal{A} = \begin{pmatrix} 1 - \kappa - \gamma_1 & \omega - \gamma_2 \\ -\omega - \gamma_2 & 1 - \kappa + \gamma_1 \end{pmatrix} \,, \tag{3.13}$$

which at leading order is rewritten in terms of the gradients of the lensing potential,

$$\mathcal{A} = \mathbb{1} + \left(\hat{\nabla}_a \hat{\nabla}_b \psi\right) \,. \tag{3.14}$$

Note that this also implies $\omega = 0$ at leading order. We can extract the convergence κ and the complex shear from the lensing potential as

$$\kappa = -\frac{1}{2}\hat{\nabla}^2\psi \,, \tag{3.15}$$

$$\gamma \equiv \gamma_1 + i\gamma_2 = -\frac{1}{2}\left(\hat{\nabla}_1^2 - \hat{\nabla}_2^2\right)\psi - \mathrm{i}\hat{\nabla}_1\hat{\nabla}_2\psi \tag{3.16}$$

The relation between a non-perturbative geometrical description and these first-order quantities is discussed in detail in Lepori et al. [2020].

The lensing potential, convergence and complex shear as scalar functions on the 2D sphere may be expanded in the basis of spherical harmonics $Y_{\ell m}(\boldsymbol{n})$,

$$X(\boldsymbol{n}) = \sum_{\ell m} X_{\ell m} Y_{\ell m}(\boldsymbol{n}) \,. \tag{3.17}$$

---

[2] We remind the reader that Φ and Ψ themselves represent nonperturbative solutions obtained with full simulations.

Assuming that these functions obey statistical isotropy, the two-point function of the expansion coefficients $X_{\ell m}$ is diagonal in ℓ and m and we can define the angular power spectrum C_ℓ as,

$$\langle X_{\ell m} X_{\ell' m'} \rangle \equiv \delta_{\ell\ell'} \delta_{mm'} C_\ell^X \,. \tag{3.18}$$

Our code uses directly Eq. (3.12) to construct the lensing map and then computes the angular power spectrum from the map. We can however also compute an expression for the weak-lensing C_ℓ^κ by considering the two-point function of the integrand of Eq. (3.12) and using Eq. (3.15) in harmonic space,

$$\begin{aligned} C_\ell^\kappa = 4\pi^2 \ell^2 \left(\ell+1\right)^2 \int_0^\infty k^2 dk \int_0^{\chi_s} d\chi \frac{\chi_s - \chi}{\chi_s \chi} \int_0^{\chi_s} d\chi' \frac{\chi_s - \chi'}{\chi_s \chi'} \\ \times \left[1 + \eta(k,\chi)\right] \left[1 + \eta(k,\chi')\right] j_\ell(k\chi) j_\ell(k\chi') P_\Phi(k,\chi,\chi') \,, \end{aligned} \tag{3.19}$$

where $P_\Phi(k,\chi,\chi')$ is the unequal-time correlator of the gravitational potential in Fourier space defined by

$$\langle \Phi(\boldsymbol{k},\chi) \Phi^* \left(\boldsymbol{k}',\chi'\right) \rangle = (2\pi)^3 \delta_{\rm D} \left(\boldsymbol{k} - \boldsymbol{k}'\right) P_\Phi\left(k,\chi,\chi'\right) \,. \tag{3.20}$$

Moreover, according to Eq. (3.8) the gravitational potential unequal-time correlator may be written based on the one of matter as follows,

$$\begin{aligned} P_\Phi\left(k,\chi,\chi'\right) = k^{-4} \left(4\pi G_N \bar{\rho}_m^0\right)^2 \mu(k,\chi)\mu(k,\chi') \\ \times \left[1 + \bar{z}(\chi)\right] \left[1 + \bar{z}(\chi')\right] P_{\Delta_m}(k,\chi,\chi') \,. \end{aligned} \tag{3.21}$$

In the last few equations, we use the shorthand $\mu(k,\chi)$ for $\mu\left(k, z(\chi)\right)$ and similar for η, P_Φ and so on.

The lensing signal, as a result, responds to the DE/MG models in multiple ways: at the background level through a change in the distance-redshift relation, and at the level of perturbations through a modified growth and through the modifications encoded in the $\mu(k,z)$ and $\eta(k,z)$ parameters [Spurio Mancini et al., 2018, Takahashi et al., 2017], specifically through the combination $\Sigma = \mu(1+\eta)/2$ that describes the modification of the lensing potential [Amendola et al., 2008]. In Sec. 3.5 we will compute the lensing signal for two fixed source redshifts, namely $z = 0.85$ and $z = 3.3$, in N-body simulations to study the effects of dark energy clustering and of the expansion history on the lensing.

It is also worth mentioning that at leading order in the absence of systematics and shape noise [Kohlinger et al., 2017] the convergence angular power spectrum contains the full lensing information. Decomposing the shear into rotationally-invariant E and B components one can show from Eq. (3.14) that [Becker, 2013]

$$\begin{aligned} C_\ell^{\gamma{\rm E}} &= \frac{1}{\ell^2(\ell+1)^2} \frac{(\ell+2)!}{(\ell-2)!} C_\ell^\kappa \,, \\ C_\ell^{\gamma{\rm B}} &= \frac{1}{\ell^2(\ell+1)^2} \frac{(\ell+2)!}{(\ell-2)!} C_\ell^\omega = 0 \,. \end{aligned} \tag{3.22}$$

In the following sections we therefore only discuss the convergence power spectra.

3.3.2 Integrated Sachs-Wolfe and non-linear Rees-Sciama effect

If the light rays from source galaxies traverse a time-dependent gravitational potential then in general their energy will change [Sachs & Wolfe, 1967]. Specifically, the light is redshifted for rays passing through a growing potential well, and blueshifted if the potential well is decaying. This effect is known as late integrated Sachs-Wolfe effect (late ISW) and is a powerful probe of dark energy at low multipoles.

During matter domination and in linear perturbation theory the gravitational potential wells remain constant in time and as a result the photons do not gain or lose energy along their trajectories after accounting for the expansion of the background. But when dark energy becomes important and the expansion rate of the Universe deviates from the matter-dominated behaviour, the gravitational potential decays at linear scales. As a result, photons gain energy and are blueshifted as they travel through over-dense regions while they lose energy and are redshifted as they travel through voids [Ade et al., 2015a, Carbone et al., 2016]. In this way, the late ISW effect induces additional anisotropies in the power spectrum of the cosmic microwave background (CMB) radiation, primarily at large scales. These anisotropies are correlated with the large-scale structure as they are due to evolving gravitational potential wells.

In addition to this effect in linear perturbation theory, the perturbations on small scales and at late times evolve non-linearly. The non-linear large scale structure of the Universe induces additional energy changes in the light rays as they pass through these structures. This so-called Rees-Sciama effect [Rees & Sciama, 1968] enhances the ISW effect in under-dense regions and decreases it in the over-dense regions as the non-linear growth of structure acts opposed to dark energy [Cai et al., 2010].

The linear late ISW and non-linear Rees-Sciama effects (abbreviated as ISW-RS when combined) are sensitive to the background evolution and growth of structures at late times, when the dark energy dominates over other components [Adamek et al., 2020b, Beck et al., 2018, Cabass et al., 2015, Khosravi et al., 2016].

Direct measurements of the ISW-RS signal from CMB data is demanding, and as a result it is detected indirectly, either by cross-correlating large scale structure data and CMB maps [Ade et al., 2016, Francis & Peacock, 2010, Peiris & Spergel, 2000, Scranton et al., 2003, Seljak, 1996] or by stacking clusters and voids to enhance the signal [Ade et al., 2016, Cai et al., 2014, 2017, Granett et al., 2008]. The effect is also detected through the ISW-lensing bispectrum using Planck data [Ade et al., 2014b].

According to Eq. (3.11), the term responsible for the ISW-RS effect yields a change in CMB temperature,

$$\Theta(\boldsymbol{n}, z) \equiv \frac{\Delta T}{\bar{T}} = -\frac{\delta z}{1+\bar{z}} = \int_0^{\chi_s} \frac{\partial(\Psi + \Phi)}{\partial \tau}\, d\chi\,, \tag{3.23}$$

where χ_s is the distance to the last-scattering surface for the CMB. In the presence of DE/MG the gravitational potentials Φ and Ψ are modified as a result of Eq. (3.8) and Eq. (3.9) for the gravitational slip and clustering parameters $\eta(k,z)$, $\mu(k,z)$. It is also interesting to note that these modifications are projected in a different way for the ISW-RS signal and the lensing signal, and thus these two could probe DE/MG in independent ways. Following the discussion in the previous subsection, $\Theta(\boldsymbol{n}, z)$ may be expanded in terms of spherical harmonics and one can compute the ISW-RS angular power spectrum. Taking the time derivative of the Hamiltonian constraint (the modified Poisson equation) (3.8), and replacing Ψ through (3.9), results in a constraint equation for $\partial\left(\Phi+\Psi\right)/\partial\tau$ which in general is a function of $\mu(k,z)$, $\eta(k,z)$ and their time derivatives:

$$\begin{aligned}\frac{\partial(\Phi+\Psi)}{\partial\tau} &= 4\pi G_N a^2 \bar{\rho}_m \Delta_m \frac{H(z)}{k^2}\Bigg[\mu(k,z)\frac{\partial\eta(k,z)}{\partial z} \\ &\qquad - \left(1+\eta(k,z)\right)\left(\mu(k,z)\frac{f(k,z)-1}{1+z} - \frac{\partial\mu(k,z)}{\partial z}\right)\Bigg] \end{aligned} \tag{3.24}$$

Writing this as $\partial\left(\Phi+\Psi\right)/\partial\tau = g(k,z)\Delta_m$ we find

$$\begin{aligned} C_\ell^\Theta = 16\pi^2 \int_0^\infty k^2 dk \int_0^{\chi_s} d\chi \int_0^{\chi_s} d\chi' j_\ell(k\chi) j_\ell(k\chi') \\ \times\, g(k,\chi) g(k,\chi') P_{\Delta_m}(k,\chi,\chi')\,. \end{aligned} \tag{3.25}$$

In this article we use ray tracing to compute the ISW-RS signal according to Eq. (3.23) by integrating along the past light cone to the source redshifts $z = 0.85$ and $z = 3.3$ as in the previous section. This can be seen either as a direct contribution to the observed redshift of the sources, or as a fractional contribution to the CMB temperature anisotropy that captures the part of the signal that is generated by the structure out to that distance and that could therefore be constrained through a cross-correlation of the CMB with large-scale structure. We use the ISW-RS angular power spectra in Sec. 3.5 to measure the response of this signal to different k-essence scalar field scenarios.

3.3.3 Gravitational redshift

The light rays emitted from source galaxies in the potential well of galaxy clusters and dark matter halos are expected to be redshifted/blueshifted due to the difference in gravitational potential between the source galaxy and the observer. This effect is known as gravitational redshift [Cappi, 1995], or as ordinary Sachs-Wolfe effect in the context of CMB physics [Durrer, 2001], and is the second term in the full expression written in Eq. (3.11),

$$\delta z_{\mathrm{grav}} = (1+\bar{z})\,(\Psi_o - \Psi_s)\ . \tag{3.26}$$

For typical cluster masses (of order $\sim 10^{14} M_{\odot}$) the gravitational redshift is estimated to be two orders of magnitude smaller than the Doppler shift [the first term in Eq. (3.11)] coming from the random motion of source galaxies [Cappi, 1995]. The technique to extract the gravitational redshift signal from other dominant signals depends on the fact that the Doppler shift results in a symmetric dispersion in the redshift-space distribution, while the gravitational redshift changes the mean of the distribution [Broadhurst & Scannapieco, 2000, Kim & Croft, 2004]. In Wojtak et al. [2011] the first measurement of gravitational redshift of light coming from galaxies in clusters was carried out by stacking 7800 clusters from the SDSS survey in redshift space. The signal detection was used to rule out models avoiding the presence of dark matter and also to show the consistency of the results with the predictions of general relativity. The gravitational redshift signal was detected [e.g. in Jimeno et al. [2015], Sadeh et al. [2015]] on scales of a few Mpc around galaxy clusters and recently in elliptical galaxies [Zhu et al., 2019] using spectra from the Mapping Nearby Galaxies at Apache Point Observatory (MaNGA) experiment.

The gravitational redshift as an observable is a prominent and direct probe of gravity at cosmological scales [Alam et al., 2017b, Wojtak et al., 2011]. We expect to see the effect of dark energy perturbations directly in the gravitational redshift signal since $\Psi \propto \mu(k,z)\eta(k,z)\Delta_m$, see Eqs. (3.8) and (3.9). Hence,

$$\begin{aligned} C_\ell^{\delta z_{\mathrm{grav}}} &= 36\pi^2 H_0^4 \Omega_m^2 \left[1+\bar{z}(\chi_s)\right]^4 \\ &\qquad \times \int_0^\infty \frac{dk}{k^2} j_\ell^2(k\chi_s)\mu^2(k,\chi_s)\eta^2(k,\chi_s)P_{\Delta_m}(k,\chi_s)\,. \end{aligned} \tag{3.27}$$

In Sec. 3.5 we study the effect of k-essence dark energy on the gravitational redshift signal.

3.3.4 Shapiro time delay

In addition to all the effects discussed in the previous sections, the gravitational potential of large-scale structure perturbs the interval of cosmic time while a photon traverses a given coordinate distance. This effect is known as Shapiro time delay and is first discussed and introduced in Shapiro [1964] as a fourth test of general relativity.

While the gravitational lensing is due to the gradient of the projected potentials along the photon trajectories and is weighted by the lensing kernel, the Shapiro time delay is proportional to the projected potential itself. As a result we expect much more signal at high multipoles from the lensing convergence compared to the Shapiro time delay, due to the additional factor of $\sim \ell^2$.

Due to Shapiro time delay the last scattering surface is a deformed sphere as different light rays travel through different gravitational potentials to reach us. All the photons we receive from the last scattering surface were released almost at the same time, so the time delay means that the photons reaching us from different directions have started at different distances from us. The modulation of the spherical surface due to Shapiro time delay is ~ 1 Mpc [Hu & Cooray, 2001]. The effect of Shapiro time delay on the CMB temperature and polarisation anisotropies is studied in Hu & Cooray [2001]. They show that, while it is difficult to extract the Shapiro time delay signal from the data, neglecting it would introduce a systematic error. They argue that the Shapiro time delay should be considered in order to reduce the systematics in the analysis, especially for future high precision experiments.

In Li et al. [2019] an estimator quadratic in the temperature and polarization fields is introduced to provide a map of the Shapiro time delays as a function of position on the sky. They show that the signal to noise ratio of this map could exceed unity for the dipole, so the signal could be used to provide an understanding of the Universe on the largest observable scales.

As discussed in Nusser [2016], for tests of the equivalence principle at high redshift that rely on the Shapiro time delay effect, potential fluctuations from the large scale structure of the Universe are at least two orders of magnitude larger than the gravitational potential of the Milky Way. This suggests that the effect of dark energy on these potentials needs to be considered in order to model the Shapiro time delay accurately. From the last term in Eq. (3.10) we get

$$\Delta\tau = (1+\bar{z})\,\Delta t = -\int_0^{\chi_s} (\Phi+\Psi)\mathrm{d}\chi\,, \tag{3.28}$$

and hence

$$\begin{aligned} C_\ell^{\Delta\tau} = 16\pi^2 \int_0^\infty k^2 dk \int_0^{\chi_s} d\chi \int_0^{\chi_s} d\chi' j_\ell(k\chi) j_\ell(k\chi') \\ \times \left[1+\eta(k,\chi)\right]\left[1+\eta(k,\chi')\right] P_\Phi(k,\chi,\chi')\,. \end{aligned} \tag{3.29}$$

The dependence on $\mu(k,z)$ is evident from Eq. (3.21). This expression can be compared to Eq. (3.19) where dark energy enters identically in the integrand, but the effect is weighted differently along the line of sight due to the lensing kernels. In our numerical analysis we obtain sky maps of the Shapiro time delay by directly solving Eq. (3.28).

3.4 Simulations

The results presented in this paper are based on simulations performed with the relativistic N-body codes k-evolution [Hassani et al., 2019a], which includes non-linearly clustering dark energy in the form of a k-essence scalar field, and *gevolution* [Adamek et al., 2016a] for ΛCDM and cases where linear dark energy perturbations are sufficient [see Fig. 1 in Hassani et al. [2019a]]. We also compare our results from these two N-body codes with the linear Boltzmann code `CLASS` [Blas et al., 2011c].

In *gevolution* and k-evolution, for a fixed observer, a "thick" approximate past light cone is constructed that encompasses a region sufficiently large to permit the reconstruction of the true light cone following the deformed photon trajectories in post-processing [Adamek et al., 2019]. The metric information for this thick light cone is saved in spherical coordinates pixelised using HEALPix [Gorski et al., 2005]. This lets us compute light-cone observables including weak gravitational lensing, ISW-RS, Shapiro time delay and gravitational redshift in post-processing. In the present work we use a fast pixel-based method to solve the integrals of Eqs. (3.12), (3.23) and (3.28) in the Born approximation, given that post-Born corrections typically affect the angular power spectra only at very high multipoles. A comparison of this approach with "exact" ray tracing of the deformed geodesics is presented in Lepori et al. [2020] for the case of the weak lensing convergence [see also Pratten & Lewis [2016]] and justifies the use of the Born approximation for the multipoles discussed here. Note, however, that post-Born corrections can play an important role in higher-order correlation functions like the angular bispectrum.

For illustration, in Fig. 3.2 the maps of each physical effect from a ΛCDM simulation are shown in the left panels. In the right panels the difference between the maps from k-essence with $w_0 = -0.9$ and $c_s^2 = 10^{-7}$ and k-essence with $w_0 = -0.9$ and $c_s^2 = 1$ are shown. Since the seed number of the simulations are identical, this shows the effect of k-essence clustering on each map, because k-essence does not cluster significantly for the case with high speed of sound squared, $c_s^2 = 1$.

In our simulations we place the observer in the corner of the box at position (0,0,0) in Cartesian coordinates. We store data on the past light cone of the observer on the full sky out to a comoving distance of $\chi_s = 2015\,\mathrm{Mpc}/h$, which corresponds approximately to $z = 0.8$, and out to a comoving distance of $\chi_s = 4690\,\mathrm{Mpc}/h$ or a corresponding approximate redshift of $z = 3.3$ for a pencil beam covering a sky area of 1932 sq. deg. in the direction of the diagonal of the simulation box.

The simulation boxes have a comoving size of $L = 4032\,\mathrm{Mpc}/h$. The fields evolve on a grid with $N_{\mathrm{grid}} = 4608^3$ grid points, and the matter phase space is

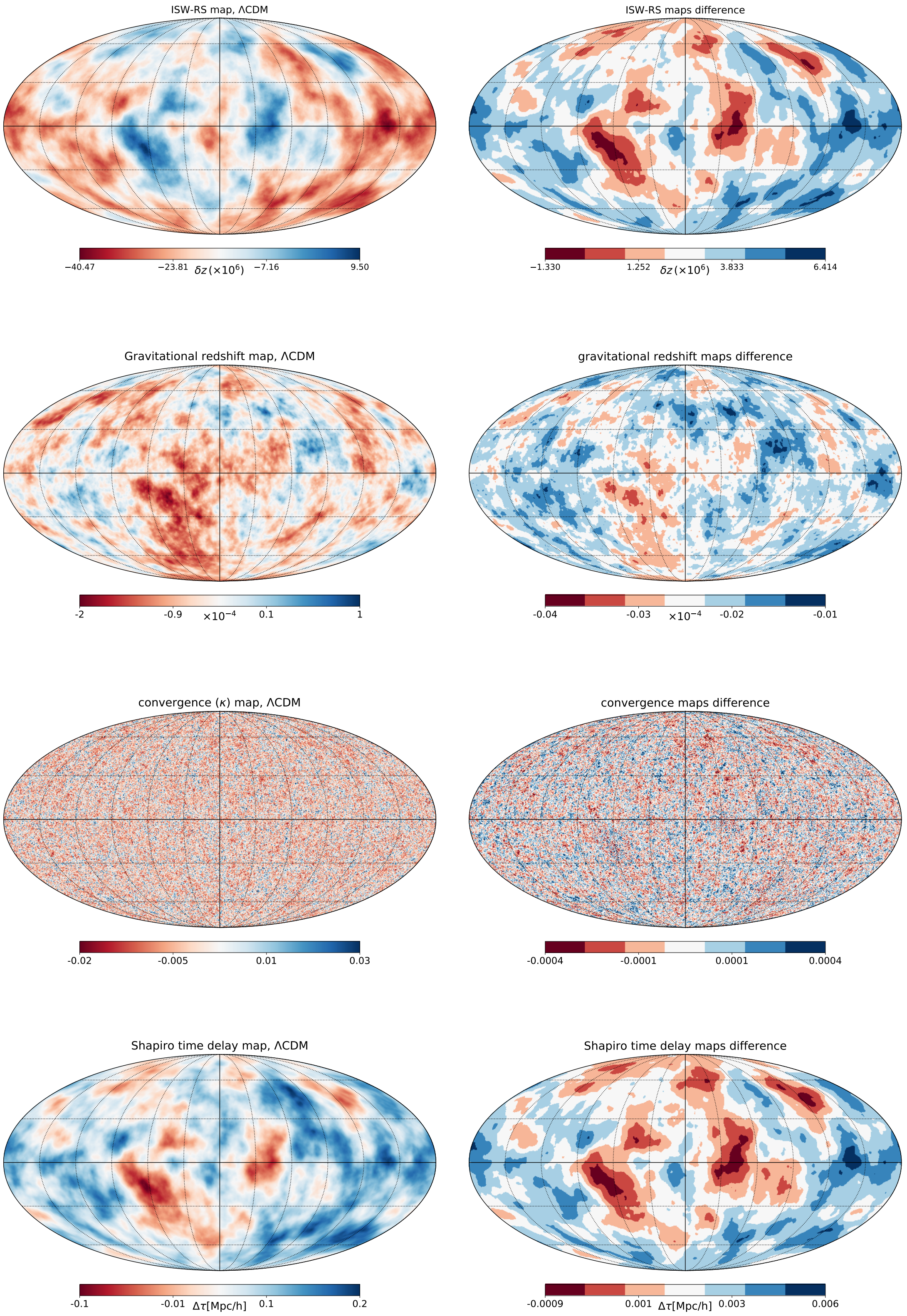
ISW-RS map, ΛCDM
−40.47
−23.81
δz (×10⁶)
−7.16
9.50
ISW-RS maps difference
−1.330
1.252
δz (×10⁶)
3.833
6.414
Gravitational redshift map, ΛCDM
-2
-0.9
×10⁻⁴
0.1
1
gravitational redshift maps difference
-0.04
-0.03
×10⁻⁴
-0.02
-0.01
convergence (κ) map, ΛCDM
-0.02
-0.005
0.01
0.03
convergence maps difference
-0.0004
-0.0001
0.0001
0.0004
Shapiro time delay map, ΛCDM
-0.1
-0.01
Δτ[Mpc/h]
0.1
0.2
Shapiro time delay maps difference
-0.0009
0.001
Δτ[Mpc/h]
0.003
0.006

Figure 3.2: ***Left:*** Full-sky maps of the ISW-RS temperature anisotropy, gravitational redshift, convergence and Shapiro time delay from a ΛCDM simulation using *gevolution*, integrated to $z \sim 0.8$ are shown. ***Right:*** Difference between the maps for k-essence with $c_s^2 = 10^{-7}$ and k-essence with $c_s^2 = 1$, both simulated with k-evolution. All simulations used the same seed to generate the random initial conditions and hence the difference maps indicate the importance of k-essence clustering.

sampled by $N_{\mathrm{pcl}} = 4608^3$ (i.e. about 100 billion) particles. We use the following cosmological parameters for all runs: the amplitude of scalar perturbations is set to $A_s = 2.1 \times 10^{-9}$ at the pivot scale $k_p = 0.05$ Mpc^{-1}, the scalar spectral index is $n_s = 0.96$, the Hubble parameter $h = 0.67$, cold dark matter and baryon densities are, respectively, $\omega_{\mathrm{cdm}} = \Omega_{\mathrm{cdm}} h^2 = 0.121203$ and $\omega_{\mathrm{b}} = \Omega_{\mathrm{b}} h^2 = 0.021996$, and the CMB temperature $T_{\mathrm{CMB}} = 2.7255$ K. We also include two massive neutrino species with masses $m_1 = 0.00868907$ eV and $m_2 = 0.05$ eV with temperature parameter $T_{\mathrm{C}\nu\mathrm{B}} = 1.95176$ K, as well as $N_{ur} = 1.0196$ massless neutrinos [Adamek et al., 2017b]. The effect of neutrino and radiation perturbations is approximated using the linear transfer functions from `CLASS` as described in Brandbyge & Hannestad [2009] and Adamek et al. [2017a], respectively. We only consider spatially flat universes, $\Omega_k = 0$, so that the dark energy density parameter is given by $\Omega_{\mathrm{DE}} = 1 - \sum_X \Omega_X$ where the sum goes over all species except dark energy. For the simulations where the dark energy is not a cosmological constant, we use a constant equation of state relation given by $w_0 = -0.9$ and $w_a = 0$.

The initial conditions for the simulations are set using the linear transfer functions from `CLASS` at $z = 100$ and all the simulations are run with the same seed number which helps us to compare the results.

For our k-essence cosmology we consider three different choices for the speed of sound: $c_s^2 = 1$, $c_s^2 = 10^{-4}$ and $c_s^2 = 10^{-7}$. Strong non-linear clustering of the dark energy field is only expected in the last case, and to study this specific aspect, we run two separate simulations for this case. In one simulation we use the code *gevolution* which approximates the dark energy perturbations by their solution from linear theory, see Hassani et al. [2019a] for more details. In the other simulation we use the code k-evolution in order to keep track of the dark energy field's response to the non-linear clustering of matter. For the higher values of the speed of sound we only run k-evolution. We also do a reference run for the ΛCDM model with *gevolution* – here there is no difference between the two codes because dark energy perturbations are absent.

3.5 Numerical results

In this section we show the results of our numerical simulations. Once we have generated the maps with our pixel-based numerical integrator we use ANAFAST from the PYTHON package of HEALPix to compute the angular power spectra and cross power spectra. However, for the pencil beam maps that cover only about 5% of the sky we instead use the pseudo-C_ℓ estimator of Szapudi et al. [2000], Wandelt et al. [2001] to obtain the power spectra in an unbiased way. To do so we use the PolSpice package to compute the angular power spectra and cross power spectra of the masked maps.

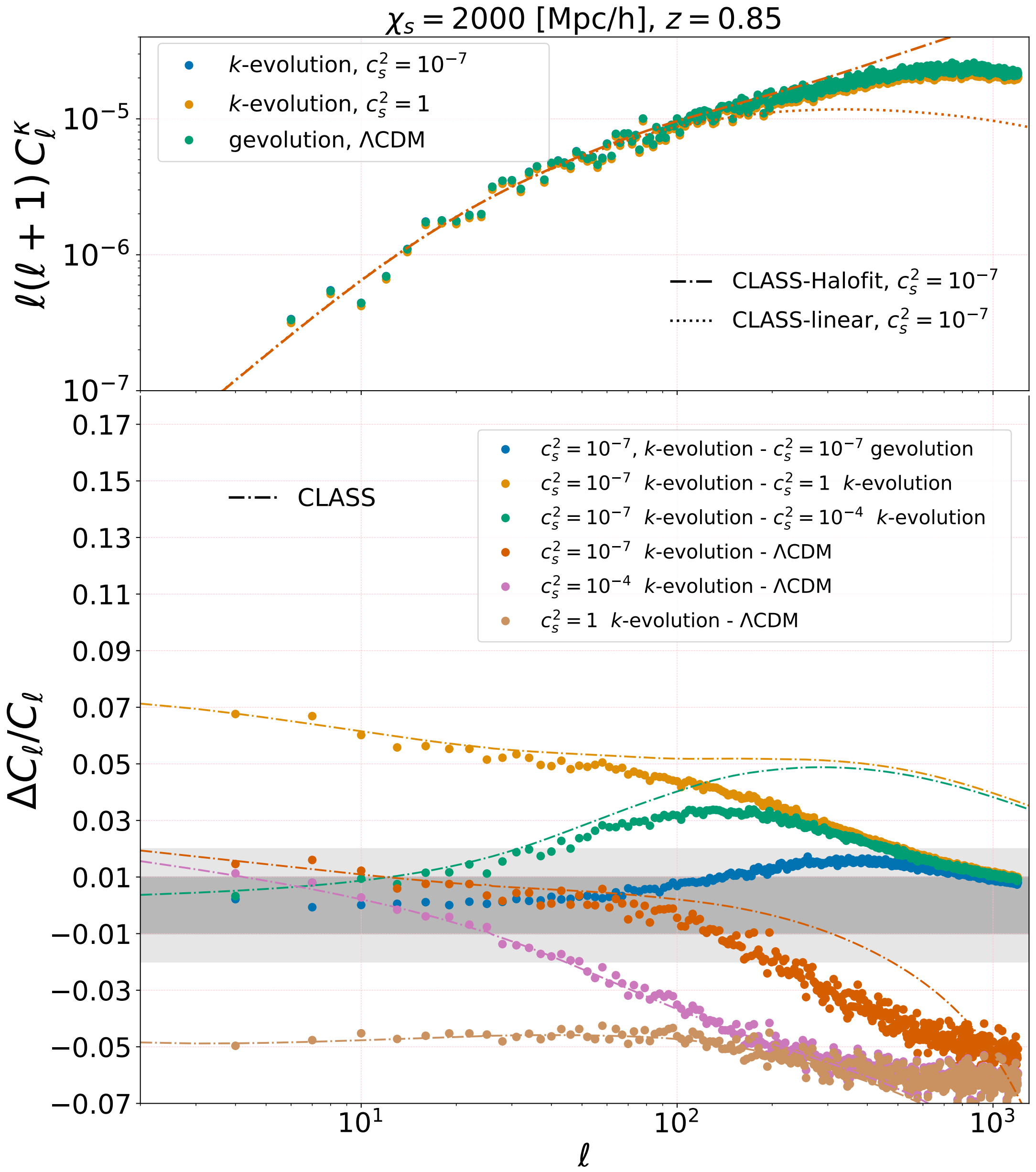

Figure 3.3: ***Top panel:*** The angular power spectra of the lensing convergence κ at a source distance of $\chi_s = 2000$ Mpc$/h$ for some of our N-body simulations, as well as predictions from `CLASS` with and without the Halofit prescription. Based on the convergence test of App. 3.A we can trust the convergence spectrum here to $\ell \approx 200$, which is roughly where the dots start to deviate from the CLASS-Halofit curve. Relative spectra remain accurate to much higher ℓ. ***Bottom panel:*** Data points show the relative difference between the convergence power spectra from our N-body simulations for different models, whereas dashed lines represent the corresponding predictions from `CLASS` with Halofit, shown in matching colours. The blue points show the impact of k-essence non-linearities by comparing non-linear k-essence from k-evolution with its linear implementation in *gevolution*.

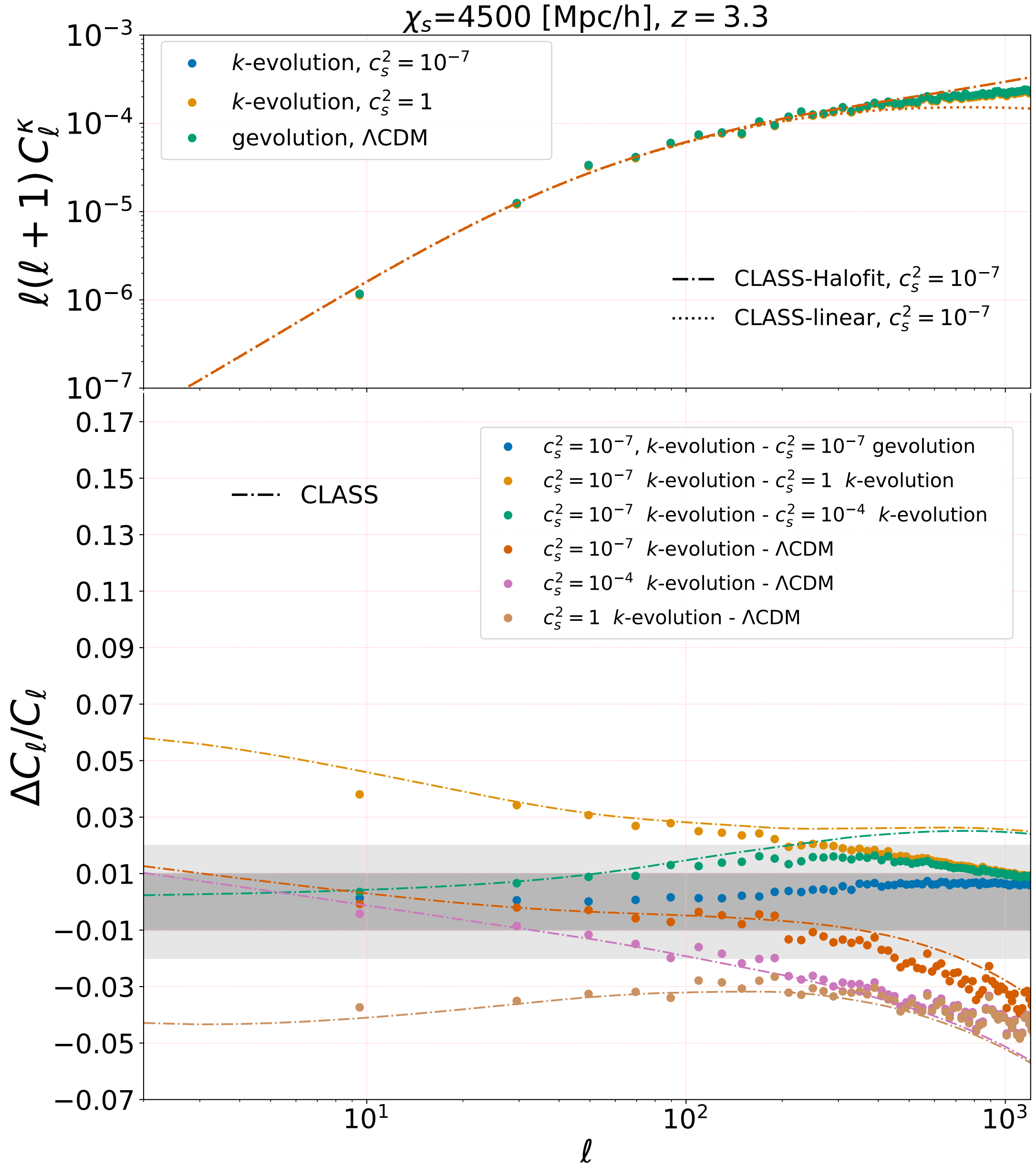

Figure 3.4: Same as Fig. 3.3, but for a source distance of $\chi_s = 4500$ Mpc/h, corresponding roughly to $z \approx 3.3$, and using N-body simulation data that covers $\sim 5\%$ of the sky. Again based on App. 3.A we can trust the dots in the top panel to $\ell \approx 500$, while the relative spectra shown in the bottom panel are again valid to higher ℓ.

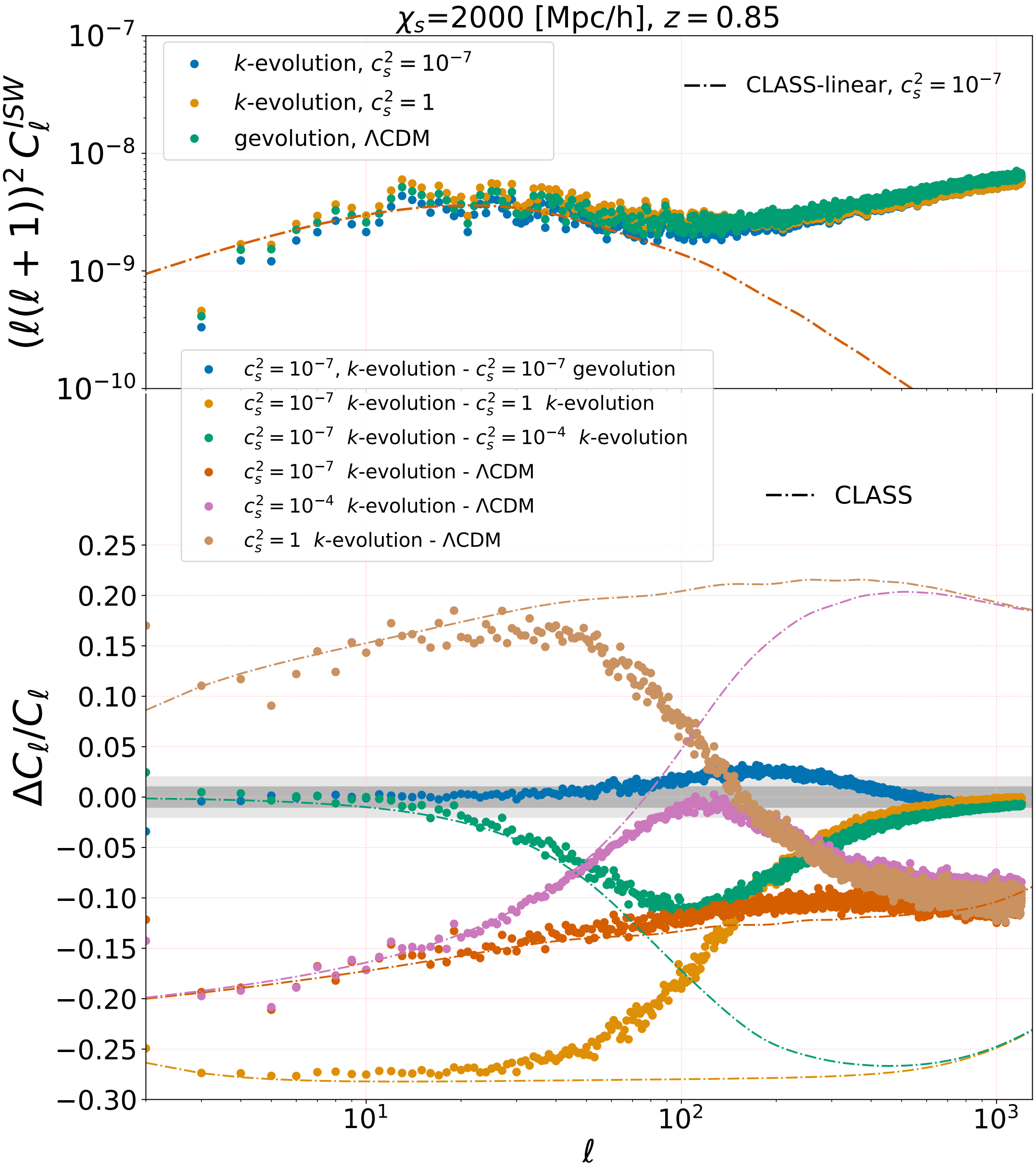

Figure 3.5: ***Top panel:*** The late-ISW-RS angular power spectra for different cosmologies integrating to $\chi_s = 2000$ Mpc/h are shown. Note that `CLASS` only predicts the linear ISW signal without any non-linear correction applied. The convergence study of App. 3.A indicates that these spectra are reliable to $\ell \approx 500$, the relative spectra are again valid to higher ℓ. ***Bottom panel:*** The relative difference between different models in the ISW-RS power spectra are shown. At large scales the result from N-body codes agree with `CLASS`, however, already at $\ell < 100$ the linear and non-linear curves diverge due to the non-linear RS effect.

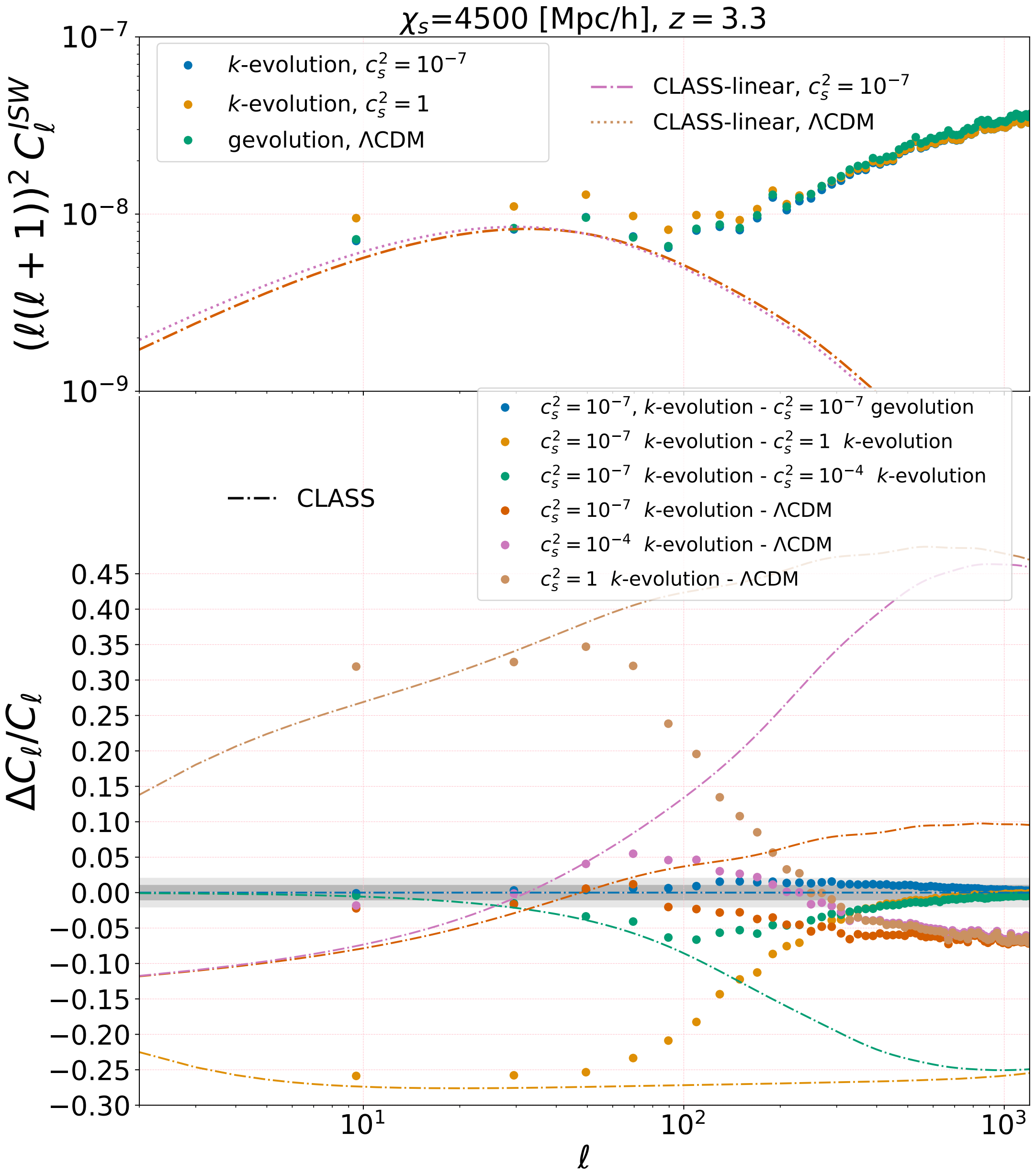

Figure 3.6: Same as Fig. 3.5, but for a source distance of $\chi_s = 4500$ Mpc/h, corresponding roughly to $z \approx 3.3$, and using N-body simulation data that covers $\sim 5\%$ of the sky. From the convergence study in the appendix we conclude that these spectra are reliable over the full range of scales shown.

3.5.1 Weak gravitational lensing

In the top panel of Fig. 3.3 the angular power spectra for the lensing convergence from k-evolution, *gevolution* and `CLASS` integrating up to $\chi_s = 2000$ Mpc/h are shown, which corresponds to a source redshift of approximately $z = 0.85$. On the top the data points show the results for $\ell(\ell+1)C_\ell^\kappa$ of two simulations with $c_s^2 = 10^{-7}$ and $c_s^2 = 1$, as well as for ΛCDM. In addition, results for `CLASS` are shown for the case $c_s^2 = 10^{-7}$ as dash-dotted and dotted lines, respectively using linear theory alone or Halofit [Takahashi et al., 2012] to model the non-linear matter power spectrum.

The effect of matter non-linearities appears in the convergence power spectrum at $\ell \sim 100$ where both Halofit and N-body simulation data start to diverge from the linear prediction. In the bottom panel of Fig. 3.3 the relative difference between the convergence power spectra of different models are shown (we always keep χ_s fixed which means that the source redshift can vary by a small amount depending on the background cosmology). This quantifies the effect of dark energy at different levels and can be compared to the prediction from `CLASS`. The data points show again the numerical results from our N-body simulations, whereas the `CLASS`/Halofit results for the same model comparisons are plotted as dashed lines using the same colours. Note that the comparison between k-evolution and *gevolution* for the case $c_s^2 = 10^{-7}$ has no corresponding prediction from `CLASS`, and quantifies the importance of the nonlinear modelling of k-essence within the N-body simulations. To be specific, our convention is $\Delta C_\ell / C_\ell = (C_\ell^{(\text{dataset 1})} - C_\ell^{(\text{dataset 2})})/C_\ell^{(\text{dataset 2})}$, where "dataset 1" and "dataset 2" are indicated in the legend of each figure.

At large scales, as expected, the results from `CLASS` and N-body simulations agree very well, while at smaller scales some deviations are seen. The deviation of the N-body results from the `CLASS`/Halofit prediction occurs mainly when there is dark energy clustering which is more pronounced for the cases with low speed of sound. Indeed, comparing the case $c_s^2 = 1$ with ΛCDM we find that the `CLASS`/Halofit prediction is accurate at least up to $\ell \sim 1000$, whereas for the lowest speed of sound, $c_s^2 = 10^{-7}$, significant disagreement between `CLASS`/Halofit and N-body simulations appears already for multipoles $\ell \gtrsim 100$. This is in complete agreement with our results in Hassani et al. [2019b] where we show that `CLASS`/Halofit gives the right clustering function $\mu(k, z)$ for high speed of sound.

Our comparison between the two simulation methods (k-evolution and *gevolution*) for the case $c_s^2 = 10^{-7}$ shows that the non-linear response of k-essence to matter clustering produces an effect of $\sim 2\%$ in the convergence power spectrum at multipoles in the range of a few hundred.

According to Fig. 3.3 the effect of dark energy clustering can cancel the effect of the background evolution with $w_0 = -0.9$ on the weak-lensing signal at large angular scales: the $\sim 5\%$ suppression when going from ΛCDM to wCDM with $c_s^2 = 1$ is compensated by an amplification of similar size when going from $c_s^2 = 1$ to low speed of sound. The scale up to which this cancellation works is set by the sound horizon, and at very non-linear scales there is always some residual suppression. In our scenario the cancellation happens only for the case $w_0 > -1$ when the linear growth rate is suppressed (see Fig 3.1), while for the case with $w_0 < -1$, where the growth rate is enhanced compared to ΛCDM, the background evolution and the dark energy clustering effects would act in a similar way.

Fig. 3.4 is similar to Fig. 3.3 but shows results from the pencil beam map integrating to a higher source distance of $\chi_s = 4500$ Mpc/h, corresponding approximately to redshift $z = 3.3$. As we have access to only $\sim 5\%$ of the sky in this case, we have no information about the angular power spectra at low ℓ. The `CLASS`/Halofit and N-body simulation data agree better compared to the lower redshift results, as the scale where the finite resolution of the simulation affects the result is shifted to higher multipoles, see Appendix 3.A [cf. also Appendix C of Lepori et al. [2020]]. Moreover, the relative difference between the angular power spectra is less substantial compared to lower redshift result which comes from the fact that dark energy starts to dominate at lower redshift and integrating to higher redshifts therefore effectively dilutes the signal.

The overall signal amplitude for lensing is larger at higher redshift owing to the fact that it is an integrated effect. Thus, although the relative effect of dark energy clustering is lower at higher redshifts, the detectability of the signal is larger, and combining high and low redshift lensing data still significantly increases the signal to noise ratio.

3.5.2 ISW-RS effect

In Figs. 3.5 and 3.6, the ISW-RS angular power spectra from our N-body simulations and `CLASS` are shown and the different dark energy models are compared in the bottom panel of each figure. The ISW-RS signal is very sensitive to the clustering of dark energy and also its background evolution. Comparing dark energy with low and high speeds of sound with ΛCDM, one finds a huge impact $\sim 35\%$ at $z = 3.3$ and $\sim 30\%$ at $z = 0.85$ from dark energy clustering which makes the ISW-RS signal an excellent probe of this model.

It is also interesting to see that the non-linear RS effect starts to have impact at larger scales than the scale of non-linearity in the lensing signal in Fig. 3.4 which is also observed and discussed in [Adamek et al., 2020b, Cai et al., 2009b]. To verify that the non-linear RS indeed appears in lower moments we design a numerical experiment to decrease the non-linear RS signal by decreasing A_s, the amplitude of scalar perturbations. This shifts the non-linear scale and allows us to separate the linear ISW effect from higher-order corrections. Our numerical results, shown in Appendix 3.B, verify that the non-linear RS effect is responsible

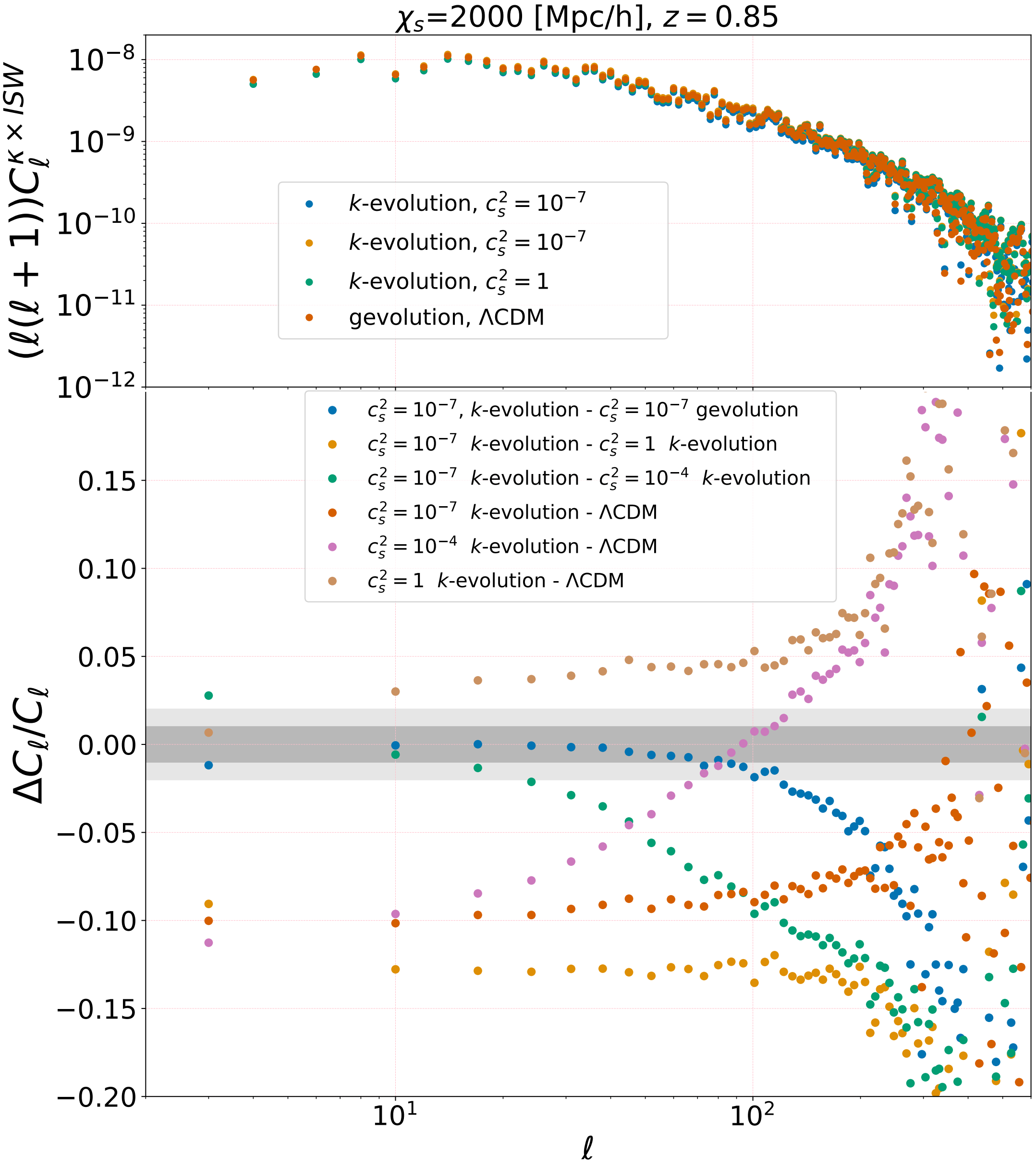

Figure 3.7: ***Top panel:*** The cross power spectra of lensing convergence κ and ISW-RS integrated to comoving distance $\chi_s = 2000$ Mpc/h from k-evolution with two speeds of sound $c_s^2 = 10^{-7}$ and $c_s^2 = 1$ are shown, together with our ΛCDM reference run. ***Bottom panel:*** The relative difference between the cross power spectra for several models is shown.

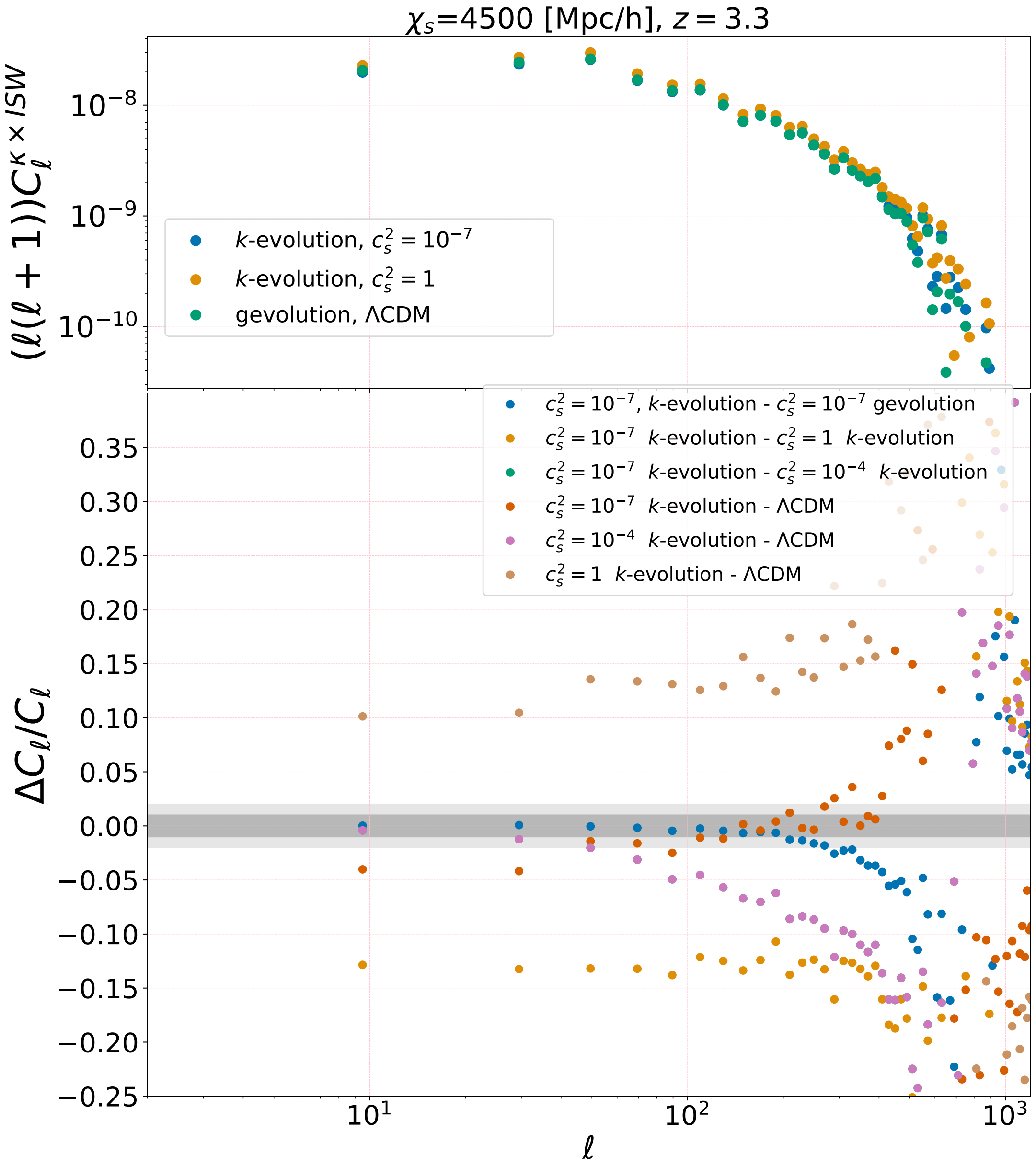

Figure 3.8: Same as Fig. 3.7, but for a source distance of $\chi_s = 4500$ Mpc/h, corresponding roughly to $z \approx 3.3$, and using N-body simulation data that covers $\sim 5\%$ of the sky.

for the deviation at lower ℓ compared to lensing. This is maybe not too surprising given that the lensing kernel suppresses contributions from the vicinity of the observer which would be projected dominantly to low multipoles.

The non-linear RS effect is not implemented in `CLASS` and as a result we a see power drop at $\ell \sim 100$ in the linear power spectra (top panels). Moreover, it is interesting to see that unlike the lensing power spectra, the effect of clustering dark energy and background evolution do not cancel each other in the ISW-RS power spectra and we obtain $\sim -20\%$ relative difference between $c_s^2 = 10^{-7}$ and ΛCDM.

As seen in Fig. 3.6 the signal itself is stronger at higher redshift as it is an integrated signal. However, depending on the parameters the relative difference can change positively or negatively compared to the lower redshift comparison. This is because more linear ISW and less non-linear effect is accumulated at high redshift.

As explained in Sec. 3.3.2 the direct detection of ISW-RS signal is difficult and it is therefore usually detected indirectly, e.g. via cross correlation with other quantities. As an example, we report the convergence-ISW-RS cross power spectra in Fig. 3.7 and Fig. 3.8. Fig. 3.9 shows the cross-correlation coefficient, i.e. the cross power normalised to the r.m.s. of each individual signal. The effects of dark energy clustering and expansion history in the cross power spectra follows similar trends as seen for the individual probes. Interestingly, the cross-correlation coefficient saturates to ~ 0.8 at low ℓ almost independently of the dark energy model. This is because virtually all the effect is taken up by the normalisation. However, the non-linear evolution is different in different models, which leads to an absolute change, ΔC_ℓ, in the cross-correlation coefficient of a few percentage points at high multipoles.

3.5.3 Gravitational redshift

In Fig. 3.10 the gravitational redshift angular power spectra for different scenarios are compared. The top panel shows $\ell(\ell+1)C_\ell^{\delta z_{\rm grav}}$ for three cases, and the bottom panel the relative difference between different angular power spectra. Like for the lensing signal, the effect of clustering and background almost cancel at large scales by coincidence: Comparing power spectra from dark energy with two different speeds of sound ($c_s^2 = 1$ and $c_s^2 = 10^{-7}$) we find a difference of $\sim 2\%$ due to the clustering of dark energy. The relative difference between ΛCDM with wCDM with $c_s^2 = 1$ reaches $\sim -3\%$ due to different background evolution. But the difference between ΛCDM and k-essence with a low sound speed is only about 1%. Fig. 3.10 also shows that the effect of non-linear dark energy clustering becomes visible once again for $\ell \gtrsim 100$, and is generally rather small, of the order of 1%.

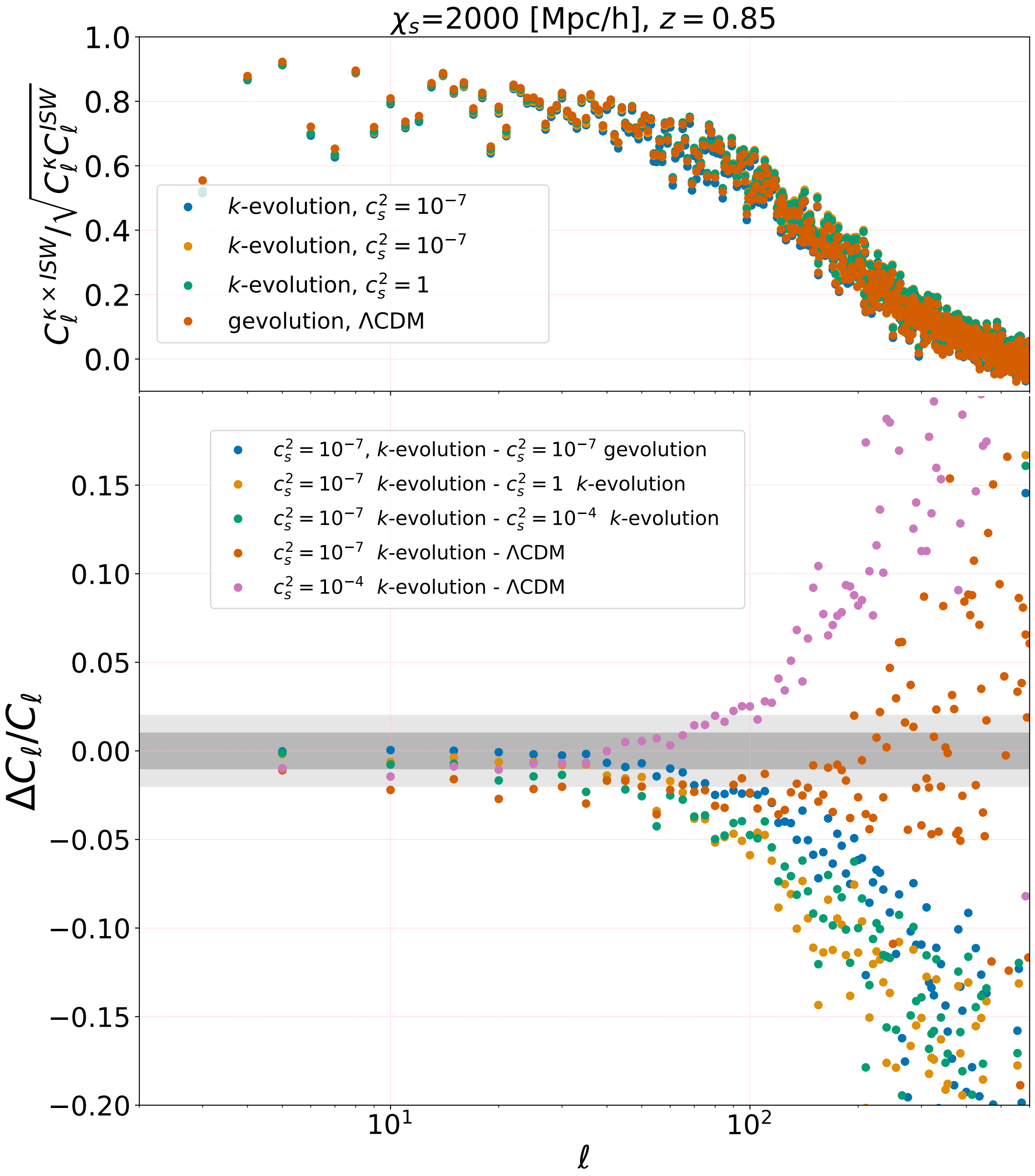

Figure 3.9: ***Top panel:*** The cross-correlation coefficient of lensing convergence κ and ISW-RS integrated to comoving distance $\chi_s = 2000$ Mpc/h for the results shown in Fig. 3.7. ***Bottom panel:*** Absolute difference in the cross-correlation coefficient for different models.

It should be noted that the angular correlation of the gravitational redshift will be very difficult to measure from large-scale structure observations. However, the line-of-sight correlations produce interesting signatures in redshift space, in particular a dipole in the correlation function of different matter tracers [Breton et al., 2019, Wojtak et al., 2011].

3.5.4 Shapiro time delay

In the Fig. 3.11 the angular power spectra for the Shapiro delay signal is plotted. Our result for the relative spectra show a similar pattern as for the gravitational redshift. The effect of dark energy clustering and dark energy background evolution have a $\sim 3\%$ effect on the Shapiro delay power spectrum that again cancel to a significant degree when combined. The non-linear dark energy clustering contributes again about a 1% effect for $\ell \gtrsim 100$. We only report the Shapiro delay integrating to $\chi_s = 2000$ Mpc/h. The cosmological Shapiro time delay will be extremely challenging to measure. It contributes only to subdominant relativistic corrections in the redshift-space clustering, and we are not aware of a probe that easily isolates this effect.

3.6 Conclusion

We are, observationally speaking, in the golden era of cosmology and in the near future we will be able to put stringent constraints on dark energy and modified gravity models. However, to be able to unlock the full power of future observations we need to have a precise understanding of the non-standard scenarios well into the nonlinear regime. The precise modeling of structure formation and cosmological observables covering linear to nonlinear scales can be directly achieved using full N-body simulations.

In this work we have presented the numerical results for the effect of clustering dark energy (specifically the k-essence model) on the observables extracted from the gravitational potential, namely the weak gravitational lensing, ISW-RS, Shapiro time delay and gravitational redshift. The observables discussed in this paper are calculated via a ray-tracing method integrating to the source redshifts $z \approx 0.85$ and $z \approx 3.3$ covering respectively a full sky map and a pencil beam in our simulations. Comparing results from the two N-body codes *gevolution* and k-evolution with the linear Boltzmann code `CLASS` we are able to assess the different effects coming from the dark energy, specifically the effect from a different background evolution, from linear dark energy perturbations and from the non-linear evolution of dark energy itself.

In summary, our numerical analysis of the angular power spectra of each observable shows that:

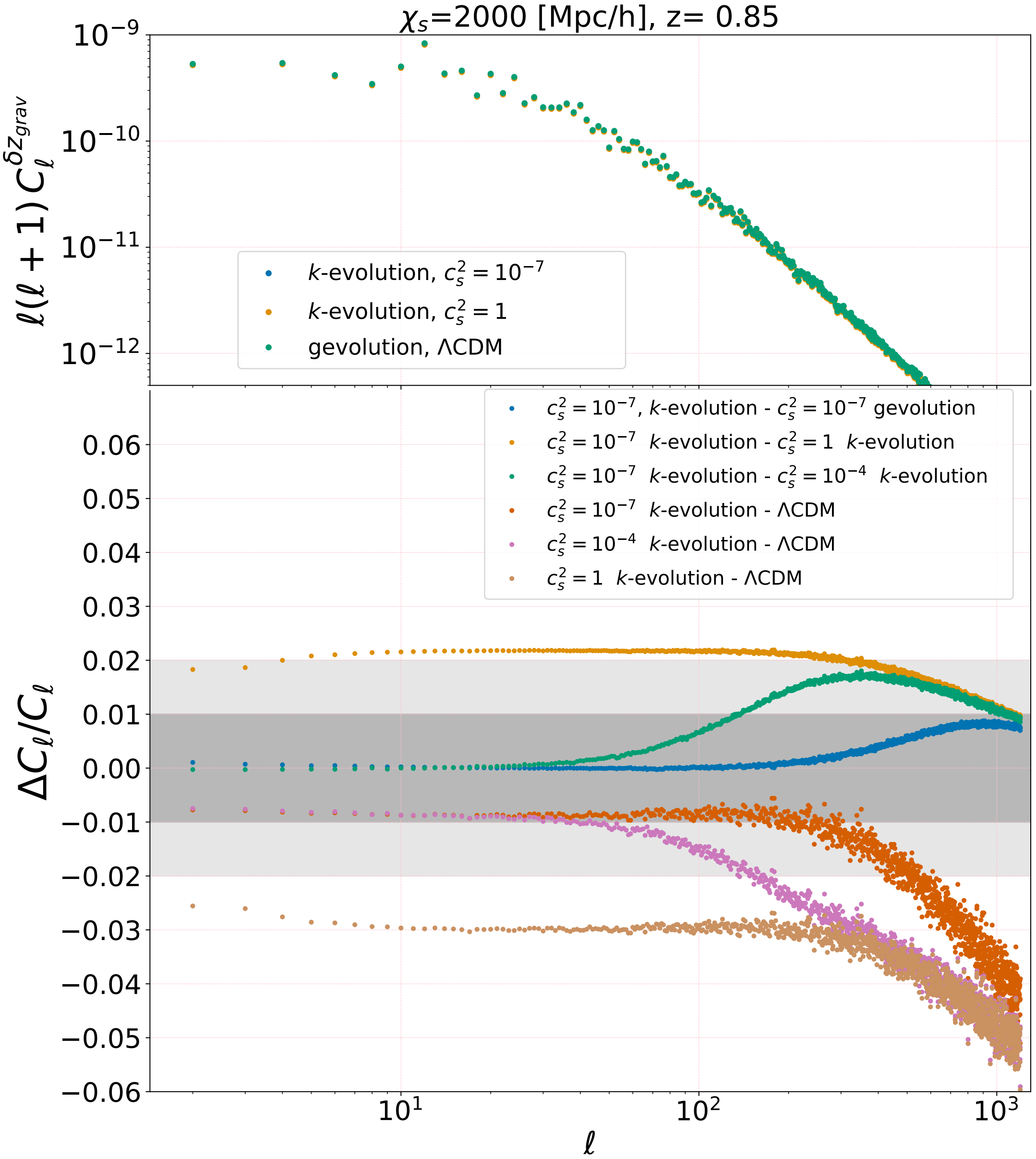

Figure 3.10: ***Top panel:*** The gravitational redshift angular power spectra of different cosmologies for a source plane at comoving distance $\chi_s = 2000$ Mpc$/h$. ***Bottom panel:*** The relative difference between the angular power spectra of the gravitational redshift in different cosmologies.

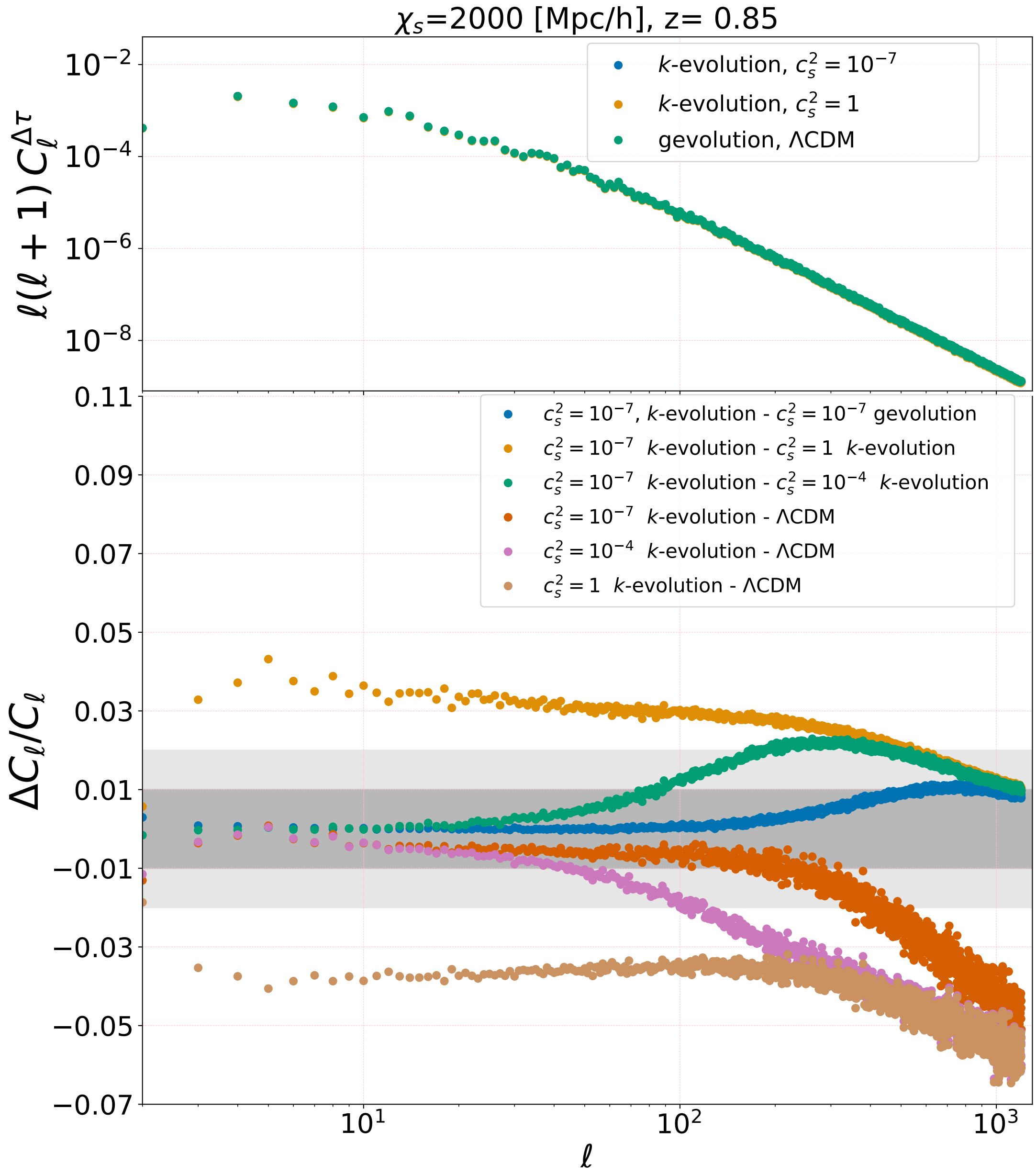

Figure 3.11: ***Top panel:*** The angular power spectra of Shapiro time delay integrated to comoving distance $\chi_s = 2000$ Mpc$/h$ for different cosmologies. ***Bottom panel:*** The relative difference between Shapiro delay angular power spectra for different models.

- The ISW-RS signal is the most powerful probe of different background evolution and the clustering of dark energy. Comparing dark energy with various speeds of sound ($c_s^2 = 10^{-7}$, $c_s^2 = 10^{-4}$ and $c_s^2 = 1$) with ΛCDM one finds a significant impact of clustering dark energy on the ISW-RS angular power spectra reaching $\sim 35\%$ at $z = 3.3$ and $\sim 30\%$ at $z = 0.85$. Moreover, by comparing the linear ISW signal from `CLASS` with the non-linear signal from our N-body codes we are able to determine the scale and amplitude of the nonlinear Rees-Sciama effect in the k-essence scenario.

- The effect of dark energy on the weak gravitational lensing signal could reach $\sim 5\%$. Interestingly, our numerical study shows that the effect of clustering of dark energy and background evolution can partially cancel each other.

- The gravitational redshift and Shapiro time delay signals are less sensitive to the dark energy clustering and background evolution, as dark energy would change these signals at most by $\sim 3\%$ and $\sim 4\%$, respectively, due to the different background evolution. An additional change by $\sim 2\%$ and $\sim 3\%$ can occur due to the clustering of dark energy.

Our numerical study shows how direct probes of the gravitational field, in particular weak lensing and the ISW-RS effect, can be used to constrain the nature of dark energy. It also highlights the relevance of including non-linear effects and provides a framework to model these effects in full N-body simulations. With this we deliver some valuable guidance for the implementation of analysis pipelines that will be used to process the vast amount of upcoming observational data, with the aim to derive robust constraints on dark energy parameters.

Acknowledgements

FH would like to thank Francesca Lepori for helping in the maps analysis, Mona Jalilvand for helping in making linear angular power spectra and Shant Baghram for his comments about cross-correlating LSS data with ISW-RS signal. FH also would like to appreciate invaluable support from Jean-Pierre Eckmann during COVID-19 outbreak and his comments about our manuscript. FH and MK acknowledge funding from the Swiss National Science Foundation, and JA acknowledges funding by STFC Consolidated Grant ST/P000592/1. This work was supported by a grant from the Swiss National Supercomputing Centre (CSCS) under project ID s969. Part of the computations were performed at University of Geneva on the Baobab cluster.

Carbon footprint: Our simulations consumed about 9800 kWh of electrical energy, which is equivalent to 1960 kg CO_2 with a conversion factor of 0.2 kg CO_2 kWh^{-1} from Vuarnoz & Jusselme [2018], table 2, assuming Swiss mix.

Data availability

The N-body codes used for the simulations and data of this paper will be provided upon request to the corresponding author. The version of *gevolution* used in this work, together with the map-making tools, is available on this public repository: `https://github.com/gevolution-code/gevolution-1.2`

APPENDIX

3.A Convergence test

In this appendix we compare the results from our high-resolution simulations ($N_{\mathrm{grid}} = N_{\mathrm{pcl}} = 4608^3$) with some lower-resolution ones ($N_{\mathrm{grid}} = N_{\mathrm{pcl}} = 2304^3$) for ISW-RS and convergence maps at both redshifts $z = 0.85$ and $z = 3.3$. This shows us at which scales the low-resolution simulations have converged to a certain numerical precision, and we can make a reasonable guess on how well we should be able to trust our final results from the high-resolution simulations.

According to Fig. 3.12 the convergence angular power spectrum is converged to within 5% up to $\ell \sim 100$ and $\ell \sim 250$, respectively for a source redshift of $z = 0.85$ and $z = 3.3$. Assuming that a factor of 2 in spatial resolution translates to a similar improvement in the angular resolution, we may want to trust our final results up to $\ell \sim 200$ and $\ell \sim 500$, respectively, maintaining a $\sim 5\%$ absolute convergence threshold. However, the leading-order error due to finite resolution is usually almost independent of cosmology, which means that it cancels out to high accuracy when taking ratios. Whenever we show relative changes, we therefore expect much better numerical convergence. In the bottom panel of the Fig. 3.12 we show the relative change between ΛCDM and wCDM convergence power spectra for two different spatial resolutions. In these relative spectra the curves with different resolutions agree at all ℓ shown, explicitly demonstrating the cancellation of the finite resolution error in the relative power spectra.

Considering Fig. 3.13 we can draw similar conclusions for the numerical convergence of the ISW-RS signal. The 5% error is reached at somewhat higher ℓ, which means we may be able to trust our final results up to $\ell \sim 400$ and $\ell \sim 800$ for the two redshift values if we apply the same requirement on absolute numerical convergence. Also according to the bottom panel of the figure the relative spectra from the two different resolutions are consistent so that we can trust the ISW-RS relative difference power spectra at all scales of interest. We emphasise again that the results shown in this paper were obtained using the higher-resolution simulations.

3.B Non-linear Rees-Sciama effect

In this appendix we quantify in more detail the contribution of the non-linear Rees-Sciama effect to the ISW-RS signal at low multipoles $\ell \lesssim 100$. To this end, we run additional simulations for the wCDM cosmology with $c_s^2 = 1$ and for ΛCDM, but with the power of primordial perturbations, A_s, reduced by

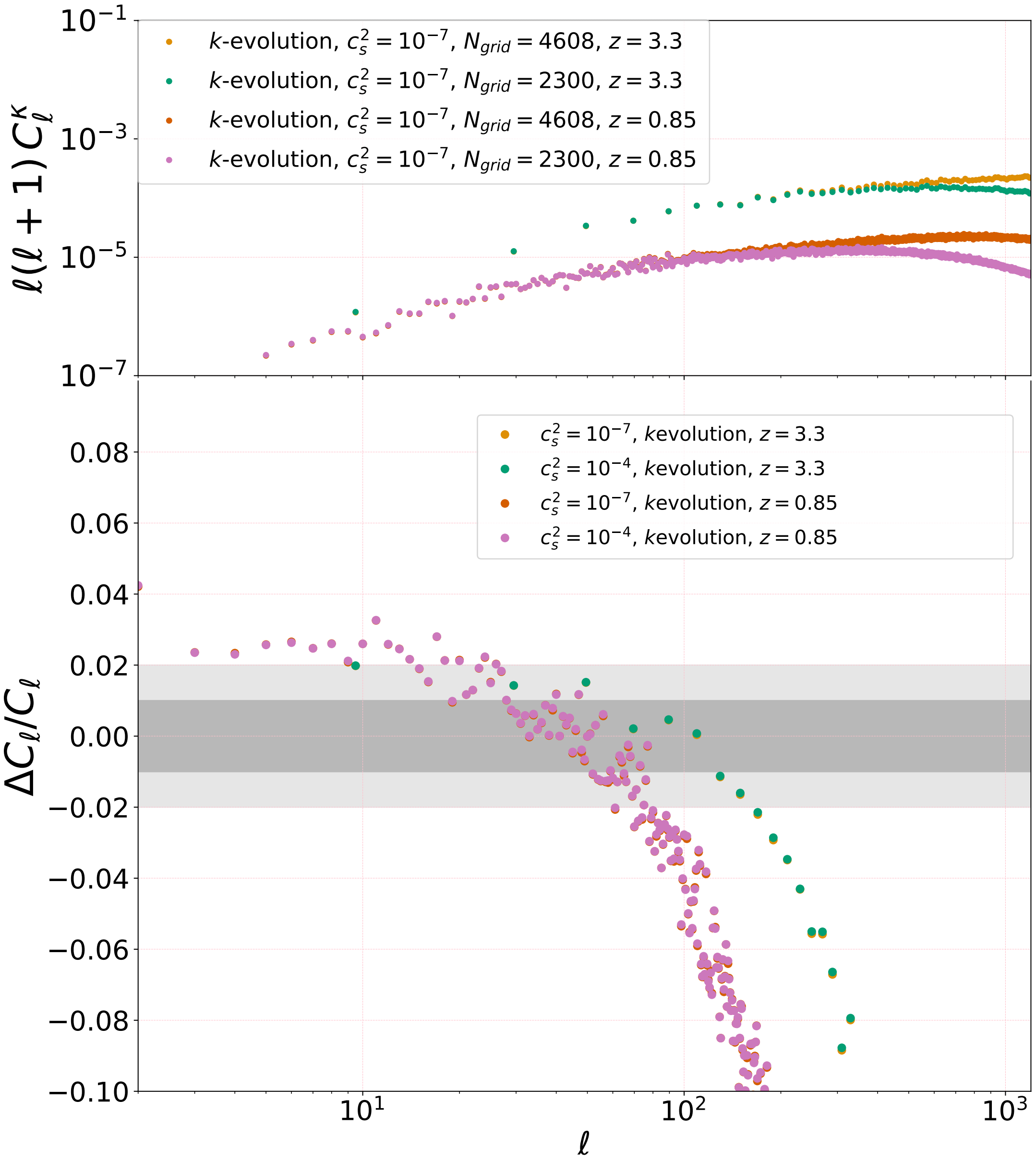

Figure 3.12: ***Top panel:*** We compare the convergence power spectra from two simulations with different resolutions, $N_{\text{grid}} = N_{\text{pcl}} = 4608^3$ and $N_{\text{grid}} = N_{\text{pcl}} = 2304^3$, at two source redshifts $z = 0.85$ and $z = 3.3$. ***Middle panel:*** The relative difference between the convergence power spectra of the same cosmology but different resolutions of the simulations are shown. This gives us an estimation of the finite resolution error on the convergence angular power spectra. The grey areas show 1% and 2% numerical agreement. ***Bottom panel:*** Comparing the relative change in the convergence power spectra between ΛCDM and k-essence cosmology with the speed of sound $c_s^2 = 10^{-7}$ from two simulations with different resolutions, $N_{\text{grid}} = N_{\text{pcl}} = 4608^3$ and $N_{\text{grid}} = N_{\text{pcl}} = 2304^3$, at source redshifts $z = 0.85$ and $z = 3.3$. The dashed lines show the linear theory prediction obtained from `CLASS`. The agreement across different resolutions shows that one can trust the relative change of power spectra at much higher multipoles than is the case for the individual power spectra themselves.

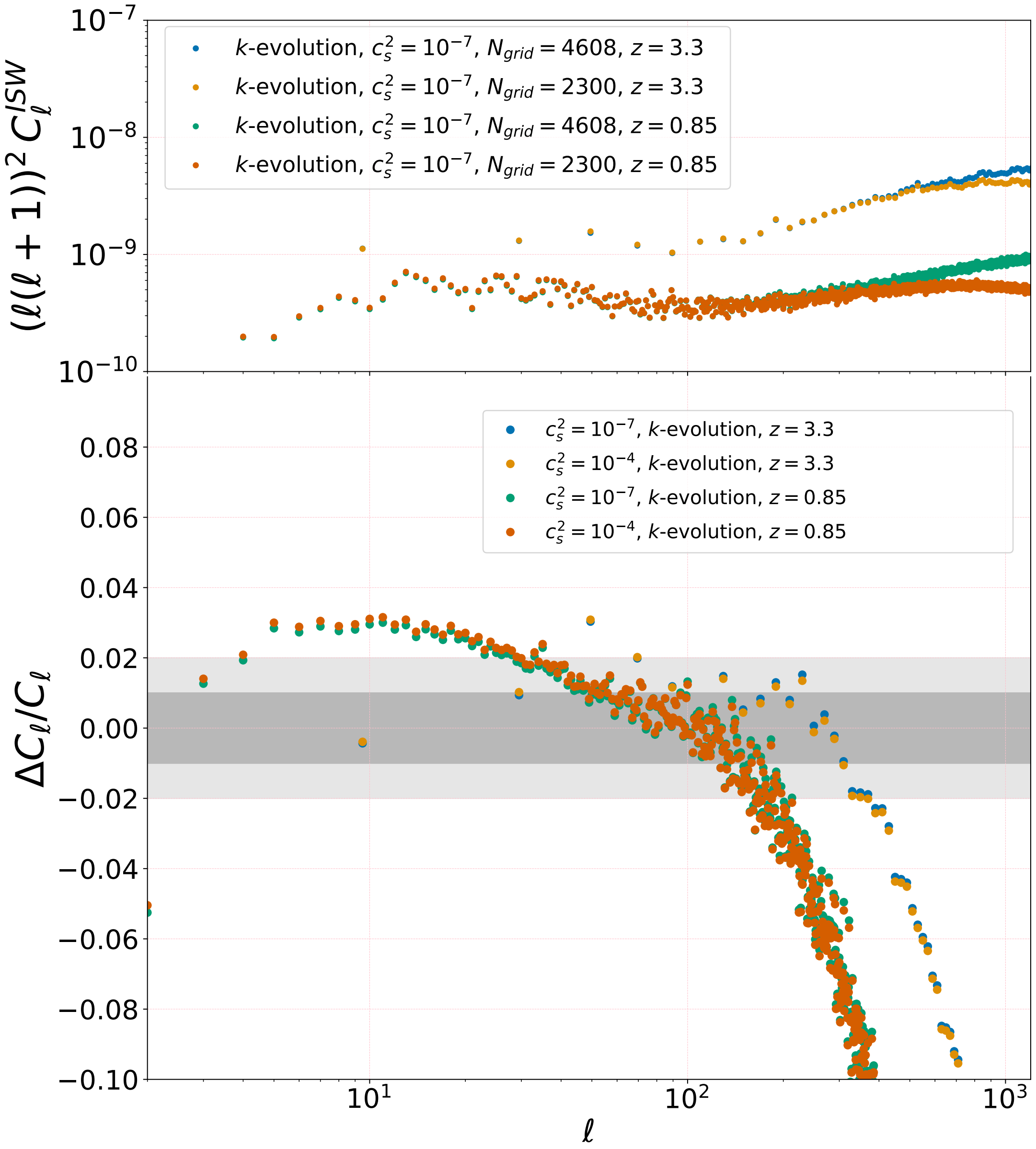

Figure 3.13: ***Top panel:*** We compare the ISW-RS angular power spectra from two simulations with different resolution, $N_{\rm grid} = N_{\rm pcl} = 4608^3$ and $N_{\rm grid} = N_{\rm pcl} = 2304^3$, at two source redshifts $z = 0.85$ and $z = 3.3$. ***Middle panel:*** The relative difference between the ISW-RS angular power spectra of the same cosmology but different resolutions of the simulations are shown. ***Bottom panel:*** The relative difference of ISW-RS angular power spectra between the k-essence cosmology with $c_s^2 = 10^{-7}$ and ΛCDM for two different spatial resolutions $N_{\rm grid} = N_{\rm pcl} = 4608^3$ and $N_{\rm grid} = N_{\rm pcl} = 2304^3$ at two source redshifts $z = 0.85$ and $z = 3.3$. The dashed lines show the linear theory prediction obtained from `CLASS`. Like Fig. 3.12, this figure shows that the finite resolution effect is cancelled significantly in the relative changes of the angular power spectra.

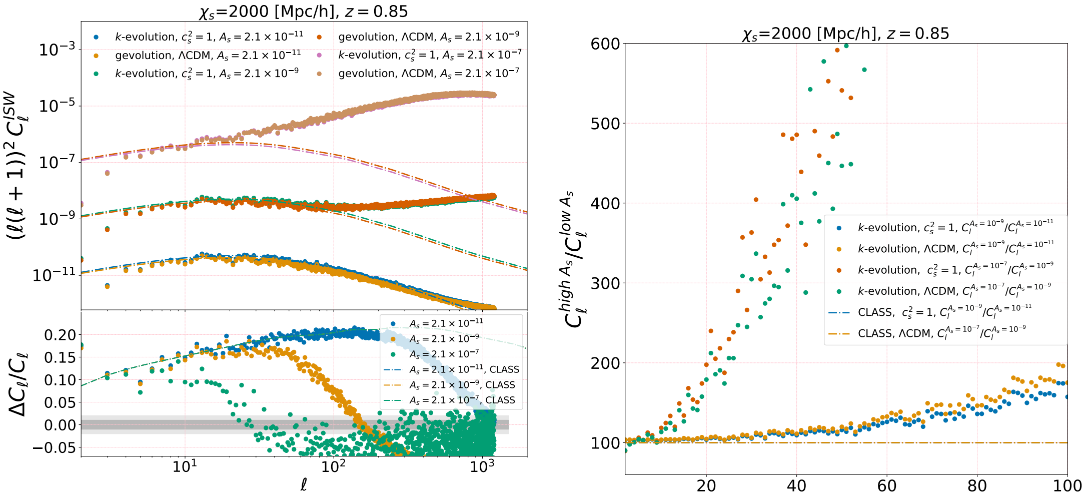

Figure 3.14: ***Left:*** The ISW-RS angular power spectra for two different cosmologies, ($w_0 = -0.9$, $c_s^2 = 1$) and ΛCDM with standard and low value of A_s, the amplitude of scalar perturbations. ***Right:*** The ratio of the ISW-RS signal from high value of A_s to low value of A_s are compared. The linear result is constant at all scales, and is simply the ratio of the two values of A_s. The fractional contribution of the Rees-Sciama effect depends on w_0 mainly because of suppressed growth and the corresponding shift of the non-linear scale with respect to ΛCDM.

two orders of magnitude. As a result, the evolution is almost linear up to much smaller scales, bringing the numerical result for the ISW-RS signal into very good agreement with the calculation of the linear ISW alone as performed by `CLASS`. This can be clearly seen in the left panel of Fig. 3.14 where the simulations with low A_s remain consistent with the prediction from `CLASS` well beyond $\ell \sim 100$. Taking the ratio of spectra from the simulations with the standard value of A_s to the ones with low A_s, we can therefore get a good estimate of the fractional contribution of the Rees-Sciama effect. The result of this analysis is shown in the right panel of Fig. 3.14, which suggests that the Rees-Sciama effect changes the signal by a few per cent at very low $\ell \lesssim 20$, and then gradually ramps up to reach a $\sim 100\%$ correction at around $\ell \sim 100$. Interestingly, the non-linear corrections are systematically larger in ΛCDM, which can be explained by the fact that the linear growth rate is slightly suppressed in our wCDM cosmology, see Fig. 3.1. This, in turn, is expected to lead to a corresponding relative suppression of second-order corrections like the Rees-Sciama effect.

Chapter 4

PARAMETRISING NON-LINEAR DARK ENERGY PERTURBATIONS

Based on:
Hassani et al. [2020d] Farbod Hassani(Geneva U., Dept. Theor. Phys.), Benjamin L'Huillier (Korea Astronomy & Space Science Institute, Department of Astronomy, Yonsei University), Arman Shafieloo (Korea Astronomy & Space Science Institute, Yuseong-gu, University of Science and Technology, Yuseong-gu), Martin Kunz (Geneva U., Dept. Theor. Phys.), Julian Adamek (Queen Mary, U. of London).
Parametrising non-linear dark energy perturbations, JCAP 04(2020) 039, [arXiv: 1910.01105]

Abstract: In this paper, we quantify the non-linear effects from k-essence dark energy through an effective parameter μ that encodes the additional contribution of a dark energy fluid or a modification of gravity to the Poisson equation. This is a first step toward quantifying non-linear effects of dark energy/modified gravity models in a more general approach. We compare our N-body simulation results from k-evolution with predictions from the linear Boltzmann code `CLASS`, and we show that for the k-essence model one can safely neglect the difference between the two potentials, $\Phi - \Psi$, and short wave corrections appearing as higher order terms in the Poisson equation, which allows us to use single parameter μ for characterizing this model. We also show that for a large k-essence speed of sound the `CLASS` results are sufficiently accurate, while for a low speed of sound non-linearities in matter and in the k-essence field are non-negligible. We propose a tanh-based parameterisation for μ, motivated by the results for two cases with low ($c_s^2 = 10^{-7}$) and high ($c_s^2 = 10^{-4}$) speed of sound, to include the non-linear effects based on the simulation results. This parametric form of μ can be used to improve Fisher forecasts or Newtonian N-body simulations for k-essence models.

4.1 Introduction

The accelerating expansion of the Universe is now well established based on observational results, for example from observations of the cosmic microwave background (CMB) anisotropies Planck Collaboration et al. [2016], type Ia supernovae Scolnic et al. [2018], and baryon acoustic oscillations Alam et al. [2017a]. Current data are in agreement with a cosmological constant as the driving force behind the acceleration. However, the cosmological constant suffers from severe fine-tuning issues that motivated the development of a plethora of modified gravity (MG) and dark energy (DE) models.

One of the simplest and most popular of these models is k-essence[1], featuring a single scalar field minimally coupled to gravity. The k-essence model was originally introduced to naturally explain why the universe has entered an accelerating phase without fine-tuning of the initial conditions and the parameters and also avoiding anthropic reasoning Armendariz-Picon et al. [2001].

Understanding the mysterious nature of DE/MG has become one of the most important unsolved problems in cosmology. Upcoming surveys Aghamousa et al. [2016b], Amendola et al. [2018], Santos et al. [2015a], Walcher et al. [2019] are planned with the aim of understanding this component by probing the expansion history of the Universe as well as structure formation with unprecedented precision. These surveys will put tight constraints on the cosmological parameters, including those that describe the physical properties of dark energy. While there have been many studies (for a review see e.g. Amendola et al. [2018]) on probing the DE/MG equation of state by observing the expansion history of the Universe, a consistent study of these theories including the non-linearities of DE/MG is not generally available. But to reach the full potential of constraining these theories, a modelling of the observables up to non-linear scales will be necessary. To this end, some of us have recently developed the N-body code "k-evolution" in which we consider dark energy, in this case a k-essence scalar field, as an independent component in the Universe. This code is described in more detail in the companion paper Hassani et al. [2019c], where we also study the effect of dark matter and gravitational non-linearities on the power spectrum of dark matter, of dark energy and of the gravitational potential, and compare k-evolution to Newtonian N-body simulations.

---

[1] It is worth mentioning that we use the term "k-essence" to refer to a general class of models featuring either a canonical (quintessence Peebles & Vilenkin [1999]) or a non-canonical kinetic term in the action.

Studying the non-linearities of such models in a consistent way enables us to predict the effects of DE/MG perturbations on the cosmological parameters. A full study of the k-essence model is particularly interesting as the dark energy perturbations become important at different scales with different amplitudes, depending on the equation of state w and speed of sound c_s. For example, in Hassani et al. [2019c] we show that k-essence structures for low speed of sound, e.g. $c_s^2 = 10^{-7}$, can become highly non-linear at small scales and that non-linearities have a large impact on quantities like the gravitational potential power spectrum.

Providing a sufficiently precise modelling of power spectra specifically for k-essence dark energy is the main goal of this article. We also discuss the different sources to the Hamiltonian constraint in the presence of k-essence dark energy to show that the impact of k-essence on power spectra can be captured by the modified gravity parameter μ on all scales of interest.

In Section 4.2 we review the theory of k-essence and describe the theoretical framework. In Section 4.3 we describe the numerical results, based on the k-evolution code Hassani et al. [2019c], a relativistic N-body code for clustering dark energy, and in Section 4.4 we provide basic recipes for how to use our results to improve Boltzmann and Newtonian N-body codes.

4.2 The k-essence model

k-essence theories are the most general local theories for a scalar field which is minimally coupled to Einstein gravity and involves at most two time derivatives in the equations of motion Armendariz-Picon et al. [2000], Gleyzes et al. [2015]. These theories are a good candidate for the late-time accelerated expansion as well as for the inflationary phase. As a viable and interesting candidate for dark energy to be probed by future cosmological surveys, these theories are implemented in several cosmological Boltzmann and N-body codes, including CAMB Lewis et al. [2000], CLASS Lesgourgues [2011], CONCEPT Dakin et al. [2019], *gevolution* Adamek et al. [2016c] and recently in k-evolution Hassani et al. [2019c]. In k-evolution, contrary to other codes that only consider linear dark energy perturbations, dark energy can cluster like the matter components which enables us to study the effect of dark energy non-linearities in a consistent way.

In k-essence theories the Lagrangian is written as a general function of the kinetic term and the scalar field, $P(X, \varphi)$. We consider the Friedman-Lemaître-Robertson-Walker (FLRW) metric in the conformal Poisson gauge to study the perturbations around the homogeneous universe.

$$ds^2 = a^2(\tau)\Big[- e^{2\Psi} d\tau^2 - 2B_i dx^i d\tau + \Big(e^{-2\Phi}\delta_{ij} + h_{ij}\Big) dx^i dx^j \Big] , \qquad (4.1)$$

where τ is conformal time, x^i are comoving Cartesian coordinates, Ψ and Φ are respectively the temporal and spatial scalar perturbations, and B_i and h_{ij} are the vector and tensor perturbations. Using the scalar-vector-tensor (SVT) decomposition we can recover the 4 scalar, 4 vector, and 2 tensor degrees of freedom in the metric (from which after fixing the gauge two scalar and two vector degrees of freedom are removed), which we are going to use to obtain the equations of motion for the perturbations. Our notation and the SVT decomposition are briefly discussed in Appendix 4.C.

The full action in the presence of a k-essence scalar field as a dark energy candidate reads

$$S = \frac{1}{16\pi G_N} \int \sqrt{-g} R d^4x + \int \sqrt{-g} \mathcal{L}_{\mathrm{DE}} d^4x + \int \sqrt{-g} \mathcal{L}_m d^4x , \qquad (4.2)$$

where G_N is Newton's gravitational constant, g is the determinant of the metric, R is the Ricci scalar, $\mathcal{L}_{\mathrm{DE}} = P(X, \varphi)$ is the general k-essence Lagrangian in which φ is the scalar field perturbation, $X = -\frac{1}{2} g^{\mu\nu} \partial_\mu \varphi \partial_\nu \varphi$ is the kinetic term, and $\mathcal{L}_m$ is matter Lagrangian.

Variation of the action with respect to scale factor $a(\tau)$ results in an equation for the evolution of the scale factor (Friedmann equation),

$$\frac{3}{2}\mathcal{H}^2 = -4\pi G_N a^2 \bar{T}^0_0, \qquad (4.3)$$

where $\mathcal{H} = a'/a$ and the prime here denotes the derivative with respect to conformal time. $\bar{T}^0_0$ is the background stress-energy tensor. The full stress-energy tensor including matter (cold dark matter, baryons and radiation) and k-essence is defined as

$$T^{\mu\nu} \equiv \frac{2}{\sqrt{-g}} \frac{\delta \mathcal{L}_{\mathrm{DE}}}{\delta g_{\mu\nu}} + \frac{2}{\sqrt{-g}} \frac{\delta \mathcal{L}_{\mathrm{m}}}{\delta g_{\mu\nu}} . \qquad (4.4)$$

We can parametrise the stress-energy tensor of a fluid with three parameters, namely the equation of state $w = \bar{p}/\bar{\rho}$, the squared speed of sound c_s^2, given in the fluid rest-frame through $\delta p = c_s^2 \delta\rho$, and the anisotropic stress σ. For k-essence both w and c_s^2 can vary as a function of time, while $\sigma = 0$ Hassani et al. [2019c]. However, in this work, we take w and c_s^2 to be constant. On the other hand the divergence of the k-essence stress-energy tensor gives the equation for k-essence density perturbations through the continuity[2] equation,

$$\delta'_{\mathrm{DE}} = -(1+w)\Big(\partial_i v^i_{\mathrm{DE}} - 3\Phi'\Big) - 3\mathcal{H}\left(\frac{\delta p_{\mathrm{DE}}}{\delta \rho_{\mathrm{DE}}} - w\right)\delta_{\mathrm{DE}} + 3\Phi'\left(1 + \frac{\delta p_{\mathrm{DE}}}{\delta \rho_{\mathrm{DE}}}\right)\delta_{\mathrm{DE}} + \frac{1+w}{\rho} v^i_{\mathrm{DE}}\partial_i\Big(3\Phi - \Psi\Big) \,, \tag{4.5}$$

where δ_{DE} is the k-essence density contrast and v^i_{DE} is the velocity perturbation of k-essence. In this form of the continuity equation we have included short wave corrections that are discussed in more detail later in this section.

We note that in Newtonian gauge we have the relation $\delta p = c_s^2 \delta\rho + 3\mathcal{H}(c_s^2 - c_a^2)\bar{\rho}(1+w)\theta/k^2$, where we have introduced the adiabatic speed of sound $c_a^2 = \bar{\rho}'/\bar{p}'$.

The variation of the action with respect to the lapse perturbation Ψ, in the weak field approximation, results in the Hamiltonian constraint Adamek et al. [2017b],

$$\nabla^2\Phi = 3\mathcal{H}\Phi' + 3\mathcal{H}^2\Psi + \frac{1}{2}\delta^{ij}\Phi_{,i}\Phi_{,j} + 4\pi G_N a^2 (1 - 2\Phi)\sum_X \bar{\rho}_X \delta_X \,, \tag{4.6}$$

where $\delta_X = \delta\rho_X/\bar{\rho}_X$ is the Poisson-gauge density contrast for each species. We usually split the total density perturbation $\bar{\rho}\delta$ into the contribution from the different species that cluster, in our case cold dark matter, baryon, radiation and the k-essence scalar field:

$$\bar{\rho}\delta = \rho_{\mathrm{cdm}}\delta_{\mathrm{cdm}} + \rho_{\mathrm{DE}}\delta_{\mathrm{DE}} + \rho_b\delta_b + \rho_r\delta_r \,, \tag{4.7}$$

where cdm, b, and DE respectively stand for cold dark matter (CDM), baryons, and k-essence. The last contribution is due to relativistic species (radiation and neutrinos) that we will neglect from now on as we are interested in late times. This does however have to be taken into account when going to high redshift, e.g. when considering the CMB. Moreover we define the short-wave corrections S and relativistic terms R in the Hamiltonian constraint equation as follows,

$$\mathrm{R}(\tilde{\mathrm{x}}, \tau) \equiv 3\mathcal{H}\Phi' + 3\mathcal{H}^2\Psi \,, \tag{4.8}$$

$$\mathrm{S}(\tilde{\mathrm{x}}, \tau) \equiv \frac{1}{2}\delta^{ij}\Phi_{,i}\Phi_{,j} - 8\pi G_N a^2 \Phi \sum_X \bar{\rho}_X \delta_X \,. \tag{4.9}$$

---

[2] In the companion paper Hassani et al. [2019c] we show that the Euler and continuity equations are equivalent to the scalar field equation in the weak field regime.

The relativistic terms $\mathrm{R}(\tilde{\mathrm{x}}, \tau)$ become important on large scales where $k \sim \mathcal{H}$. The short wave corrections $\mathrm{S}(\tilde{\mathrm{x}}, \tau)$, on the other hand, are due to the weak field scheme where we allow matter and k-essence densities to become fully non-linear i.e.

$$\delta_m \sim \delta_{\mathrm{DE}} \sim \mathcal{O}(1) \ , \tag{4.10}$$

while the metric perturbations remain small. As a result in this scheme we can have highly dense k-essence and matter structures while the metric is still FLRW with small perturbations. More detailed discussions on the weak field approximation are found in Adamek et al. [2016c], Hassani et al. [2019c]

4.3 Numerical results

4.3.1 The k-evolution code

k-evolution Hassani et al. [2019c] is a relativistic N-body code based on *gevolution* Adamek et al. [2016b,c]. The full sets of non-linear relativistic equations, six Einstein's equations $G_{\mu\nu} = 8\pi G T_{\mu\nu}$ as well as the scalar field equation (linearised in the k-essence field variables) are solved on a Cartesian grid with fixed resolution Adamek et al. [2017b], Hassani et al. [2019c] to update the particle positions and velocities. While in k-evolution the dark energy component is considered as an independent element whose equation of motion is fully coupled to the non-linear matter dynamics solved in the code, in *gevolution* it is not treated as an independent component and only the respective linear solution from the Boltzmann code `CLASS` is used to model dark energy perturbations. The effects of non-linear clustering of the k-essence scalar field on matter and gravitational potential power spectra are studied in Hassani et al. [2019c]. Also the effect of k-essence on the turn-around radius is studied using k-evolution in Hansen et al. [2020].

In order to probe the non-linearities of both matter and k-essence scalar field, we combined the data from two simulations with $N_{\mathrm{grid}} = 3840^3$ with two different resolutions: one with $L = 9000\, h^{-1}$Mpc and one with a physically smaller box with $L = 1280\, h^{-1}$Mpc, corresponding to respectively $2.3\, h^{-1}$Mpc and $0.33\, h^{-1}$Mpc length resolution. Furthermore, to study the relativistic terms which become important at large scales we also use a much lower spatial resolution simulation with $N_{\mathrm{grid}} = 3840^3$, $L = 90000\, h^{-1}$Mpc corresponding to $23.43\, h^{-1}$Mpc length resolution. In all of the figures, we remove the data with wavenumbers larger than 1/7 of the Nyquist frequency of the simulation to minimize any finite resolution effect. Moreover, by having different simulations with overlapping windows of wavenumbers we are able to test the convergence of the simulations and thus have control over the errors coming from finite resolution and finite box size (cosmic variance).

In our studies we consider $w = -0.9$ which gives accelerated expansion and is compatible with the current observational data Amendola et al. [2018] and two cases for the speed of sound, namely $c_s^2 = 10^{-4}$ and $c_s^2 = 10^{-7}$. These two cases are interesting as their respective sound horizons correspond to linear and non-linear scales. In fact, for the case with $c_s^2 = 10^{-4}$ the dark energy perturbations decay significantly at the quasi-linear and non-linear scales as the sound horizon wavenumber is about $k_s \approx 0.03\, h\text{Mpc}^{-1}$ and we do not expect to see large difference between the k-evolution scheme and when dark energy is treated linearly. In the case with $c_s^2 = 10^{-7}$ the sound horizon for dark energy is at a much higher wavenumber, $k_s \approx 1\, h\text{Mpc}^{-1}$, and we are able to see the dark energy perturbations impact on the other quantities. More details about the results of the two speeds of sound can be found in Hassani et al. [2019c].

4.3.2 Sources to the Hamiltonian constraint

In this subsection we discuss the different sources to the Hamiltonian constraint and according to the numerical results we argue that in the k-essence theories one can safely neglect short-wave corrections and also that the gravitational potential difference $\Phi - \Psi$ is negligible.

In Fig. 4.1 we compare all the terms to the Hamiltonian constraint (4.6); T_X in the figures refers to $\sqrt{\langle XX^* \rangle}$ in Fourier space. We also divide these terms by $\mathcal{H}^2$ to make them dimensionless. In the top-left plot the contribution from relativistic terms, from the k-evolution code which is introduced in Section 4.3.1 is shown in solid lines and from the linear Boltzmann code `CLASS` Blas et al. [2011b] in dash-dotted lines. These terms are the main contributions to the Hamiltonian constraint at large scales and high redshifts, as the other three terms decay at large scales. We note that the k-evolution and `CLASS` predictions for the relativistic terms start to differ already at relatively large scales, which comes from the difference between Φ' power spectra in these codes which is discussed in details in the companion paper Hassani et al. [2019c].

In the top-right figure the contribution from matter (baryons and cold dark matter) is shown. This term is the main contribution at small scales compared to the other terms, as matter perturbations dominate at those scales. The bottom-left figure shows the contribution from the short wave corrections to the Hamiltonian constraint, which is negligible. In the bottom-right figure the contribution from k-essence for $c_s^2 = 10^{-7}$ is shown. The contribution from this term peaks around the sound-horizon scale $k_s \approx 1h/\text{Mpc}$. These plots allow to compare the relative contribution of each term in the Hamiltonian constraint as a function of scale and redshift; we should however not forget that the power spectra also contain contributions from cross terms that we are not going to discuss in this paper.

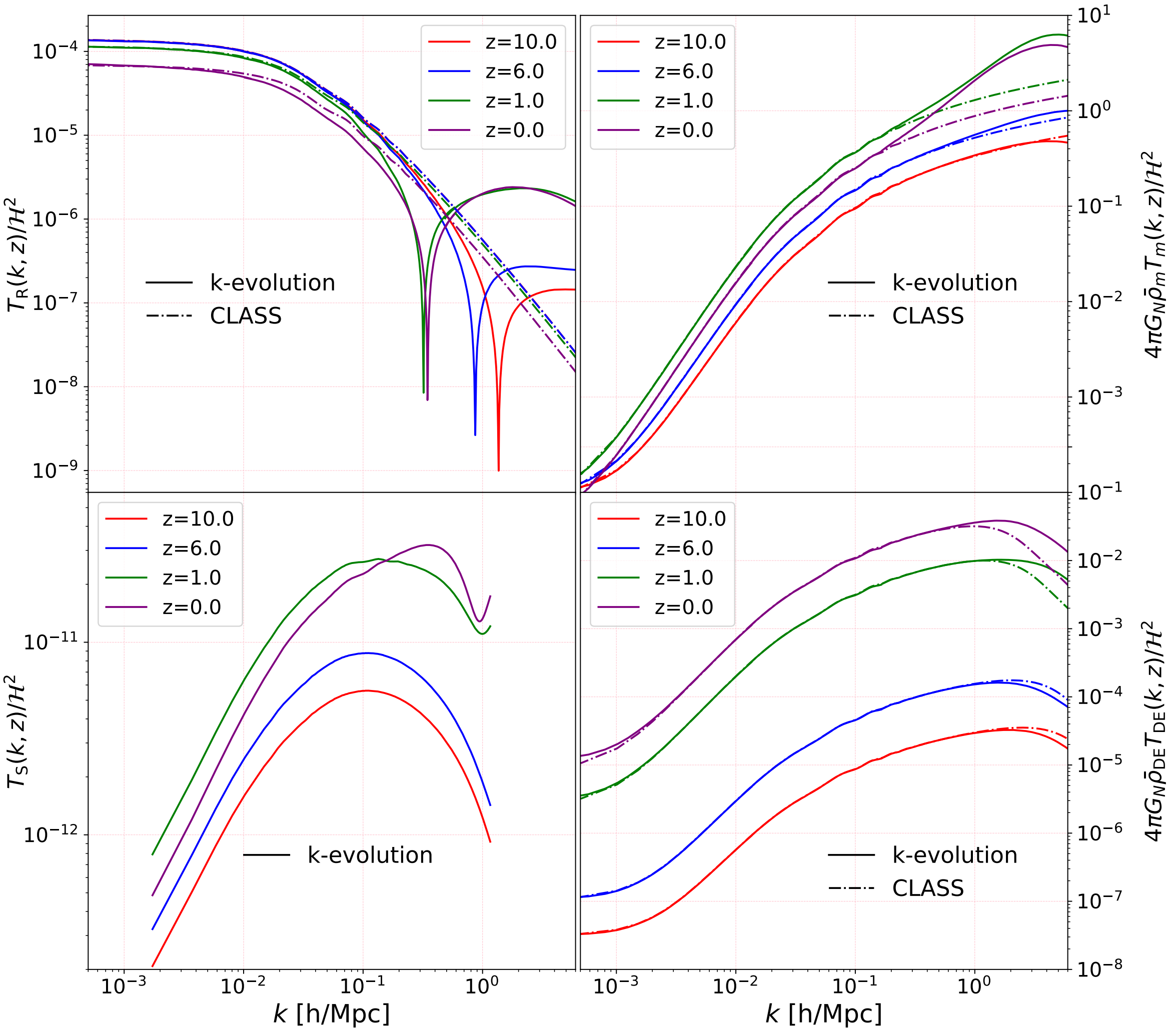

Figure 4.1: Sources to the Hamiltonian constraint, normalized to $\mathcal{H}^2$, in terms of wavenumber at different redshifts, from k-evolution in solid lines and from `CLASS` in dashed lines, for a k-essence speed of sound of $c_s^2 = 10^{-7}$. For the figures on the right, the y-axis is shown on the right. The x-axis is common between each column of figures. The figure on the left bottom, showing the short-wave corrections, is obtained using a simulation with $N_{\text{grid}} = 3840^3$ and box size $L = 9000\,h^{-1}$Mpc, while in the other three figures the results are obtained combining three simulations with $N_{\text{grid}} = 3840^3$ and box sizes $L = 90000\,h^{-1}$Mpc, $L = 9000\,h^{-1}$Mpc and $L = 1280\,h^{-1}$Mpc.

Variation of the action with respect to Φ_h (the scalar part of δg_{ij}) defined in

Eq. (4.18) leads to a constraint equation for $\Phi - \Psi$,

$$\nabla^4(\Phi-\Psi)-\left(3\delta^{ik}\delta^{jl}\frac{\partial^2}{\partial x^k \partial x^l} - \delta^{ij}\nabla^2\right)\Phi_{,i}\Phi_{,j} = 4\pi G_N a^2 \left(3\delta^{ik}\frac{\partial^2}{\partial x^j \partial x^k} - \delta^i_j \nabla^2\right) T^j_i \,, \tag{4.11}$$

where $\nabla^4 \doteq \delta^{ij}\delta^{lm}\partial_i\partial_j\partial_l\partial_m$. In this expression $\Phi-\Psi$ is sourced by the anisotropic part of the stress-energy tensor and a short-wave correction term. In first order perturbation theory, and neglecting radiation perturbations, we have $\Phi = \Psi$. Short-wave corrections and also anisotropic pressure generation in dark matter Ballesteros et al. [2012] and k-essence Hassani et al. [2019c] lead to a non-zero $\Phi - \Psi$. Contrary to the case of the Hamiltonian constraint, the contribution of short-wave corrections is of relative importance here, in particular at large scales. In absolute terms these higher-order effects are however expected to be small. To quantify the difference between the two potentials we measure $\sqrt{\mathcal{P}_{\Phi-\Psi}}/\sqrt{\mathcal{P}_{\Phi}}$ from our simulations (where $\mathcal{P}_{\Phi-\Psi}$ is the dimensionless power spectrum of $\Phi-\Psi$), shown as solid lines in Fig. 4.2. For comparison, the dashed lines show the same quantity generated from `CLASS` where it is solely due to radiation perturbations. On super-horizon scales, the contribution from radiation perturbations is larger than contribution from non-linearities, while in the quasi-linear regime the dominant contribution comes from the non-linearities. Both are however indeed very small and can be safely neglected at intermediate and small scales.

Variation of the action with respect to the shift perturbation results in the momentum constraint,

$$-\frac{1}{4}\nabla^2 B_i - \Phi'_{,i} - \mathcal{H}\Psi_{,i} = 4\pi G_N a^2 T^0_i \tag{4.12}$$

where in Poisson gauge (4.20), B_i is divergence-less or transverse i.e. $\delta^{ij}B_{i,j} = 0$. So the divergence of Eq. (4.12) reads,

$$-\nabla^2\Big(\Phi' + \mathcal{H}\Psi\Big) = 4\pi G_N a^2 \partial^i T^0_i \,. \tag{4.13}$$

If the stress-energy can be split into contributions from independent constituents, we can define the velocity divergence θ_X for each constituent such that

$$\partial^i T^0_i = \sum_X \bar{\rho}_X \Big(1 + w_X\Big)\theta_X = \theta_{\mathrm{tot}} \sum_X \bar{\rho}_X \Big(1 + w_X\Big) \,. \tag{4.14}$$

This definition of θ_X coincides with the linear velocity divergence in the case where the constituent can be described by a fluid, but it generalises to situations where this is no longer the case. We can now see that the relativistic terms in the Hamiltonian constraint Eq. (4.6) can be related to a different choice of density perturbation,

$$\nabla^2\Phi = \frac{1}{2}\delta^{ij}\Phi_{,i}\Phi_{,j} + 4\pi G_N a^2 (1 - 2\Phi)\sum_X \bar{\rho}_X \Delta_X \,, \tag{4.15}$$

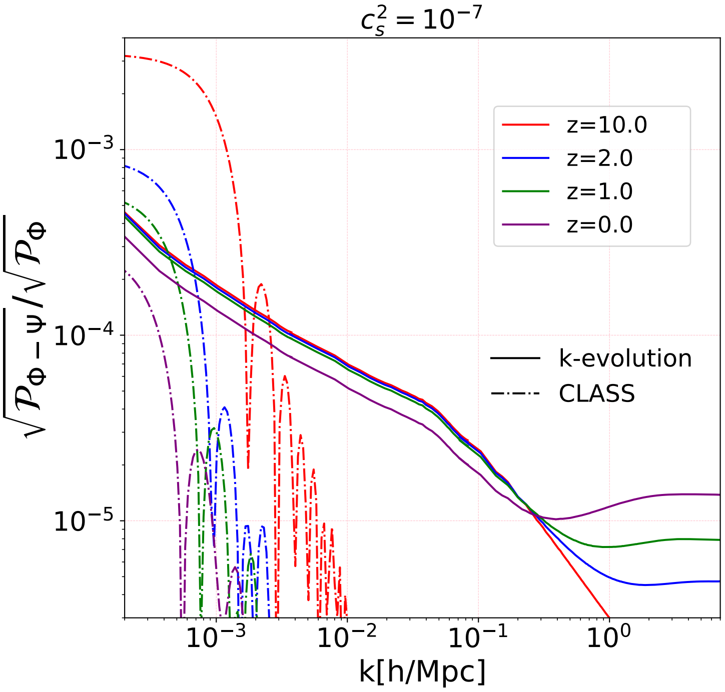

Figure 4.2: The quantity $\sqrt{\frac{\mathcal{P}_{\Phi-\Psi}}{\mathcal{P}_\Phi}}$ from k-evolution (solid lines) and from `CLASS` (dashed lines) at different redshifts as a function of wavenumber k. In k-evolution this quantity is non-zero due to the non-linearities in matter, k-essence and short-wave corrections, while in `CLASS` it is generated due to the radiation perturbations which oscillate and decay in k. The results are obtained combining three simulations with $N_{\text{grid}} = 3840^3$ and box sizes $L = 90000\,h^{-1}$Mpc, $L = 9000\,h^{-1}$Mpc and $L = 1280\,h^{-1}$Mpc.

where $\Delta_X = \delta_X - 3\mathcal{H}(1+w_X)\nabla^{-2}\theta_{\text{tot}}$ is the comoving density contrast. Eq. (4.15) is the Poisson equation dressed with short-wave corrections, which are the leading higher-order weak-field terms. Neglecting the (small) short-wave terms, the equation is linear even if the perturbations in the matter fields are large[3], and one can pass to Fourier space. Modifications of gravity where the gravitational coupling depends on time and scale can then be parametrised by introducing a function $\mu(k, z)$ such that

$$-k^2\Phi = 4\pi G_N a^2 \mu(k,z) \sum_X \bar{\rho}_X \Delta_X \,, \tag{4.16}$$

where the choice $\mu(k, z) = 1$ restores standard gravity. Furthermore, if one chooses to interpret the dark energy perturbations as a modification of gravity, the sum on the right-hand side would exclude $X = \mathrm{DE}$. Such an interpretation makes sense if the dark energy field is not coupled directly to other matter, so that it cannot be distinguished observationally from a modification of gravity (e.g. Kunz & Sapone [2007]).

---

[3] This also shows that in General Relativity the Poisson equation holds effectively on *all* scales, right down to milli-parsec scales where we may start to encounter effects from the strong-field regime of supermassive black holes.

Adopting this interpretation we can define an effective modification $\mu(k,z)$ as

$$\mu(k,z)^2 = \frac{k^4 \langle \Phi\Phi^* \rangle}{(4\pi G_N a^2 \bar{\rho}_m)^2 \langle \Delta_m \Delta_m^* \rangle}\,, \tag{4.17}$$

where $\bar{\rho}_m = \bar{\rho}_{\mathrm{cdm}} + \bar{\rho}_b$ and $\bar{\rho}_m \Delta_m = \bar{\rho}_{\mathrm{cdm}} \Delta_{\mathrm{cdm}} + \bar{\rho}_b \Delta_b$. Since our simulations are carried out in Poisson gauge they internally use δ_m and do not compute Δ_m directly. However, the difference between the two quantities is only appreciable at very large scales where θ_{tot} is given by its linear solution. For the purpose of computing $\mu(k,z)$ from simulations we therefore write,

$$\Delta_m \simeq \delta_m \left(1 + \frac{3\mathcal{H} T^{\theta}_{\mathrm{tot}}(k,z)}{k^2 T^{\delta}_m(k,z)}\right)\,, \tag{4.18}$$

where $T^{\theta}_{\mathrm{tot}}(k,z)$ and $T^{\delta}_m(k,z)$ are the linear transfer functions of θ_{tot} and δ_m, respectively. These can be computed with a linear Einstein-Boltzmann solver like `CLASS`.

4.3.3 Linear versus non-linear $\mu(k,z)$

In this subsection we show the $\mu(k,z)$ function obtained from k-evolution, which includes non-linearities in matter and k-essence as well as relativistic and short-wave corrections. We compare $\mu(k,z)$ from k-evolution with the results from the linear Boltzmann code `CLASS` Blas et al. [2011b], and with results from *gevolution* Hassani et al. [2019c] and `CLASS` with Halofit Takahashi et al. [2012].

In the two top panels of Fig. 4.3, the results from k-evolution and `CLASS` for two different speeds of sound are compared at different redshifts. In the two bottom panels $\mu(k,z)$ from k-evolution, *gevolution* and `CLASS` (linear and with Halofit) at $z = 0$ are shown.

In ΛCDM, where there are no dark energy perturbations, or modifications of gravity, we would have $\mu = 1$ on all scales and at all times. In Fig. 4.3 we see that due to the k-essence perturbations we have $\mu > 1$ at large scales, while we recover the ΛCDM limit on small scales or at early times. The maximum deviation from $\mu = 1$ is less than 5% for our choice of model, therefore the effect is small but not negligible. The reason why we expect to recover GR at high redshifts is that the DE/MG starts to dominate at low redshifts which is well supported by observations. In our model this is included by choosing a constant $w = -0.9$ close to -1, in which case the ratio of dark energy to dark matter density scales

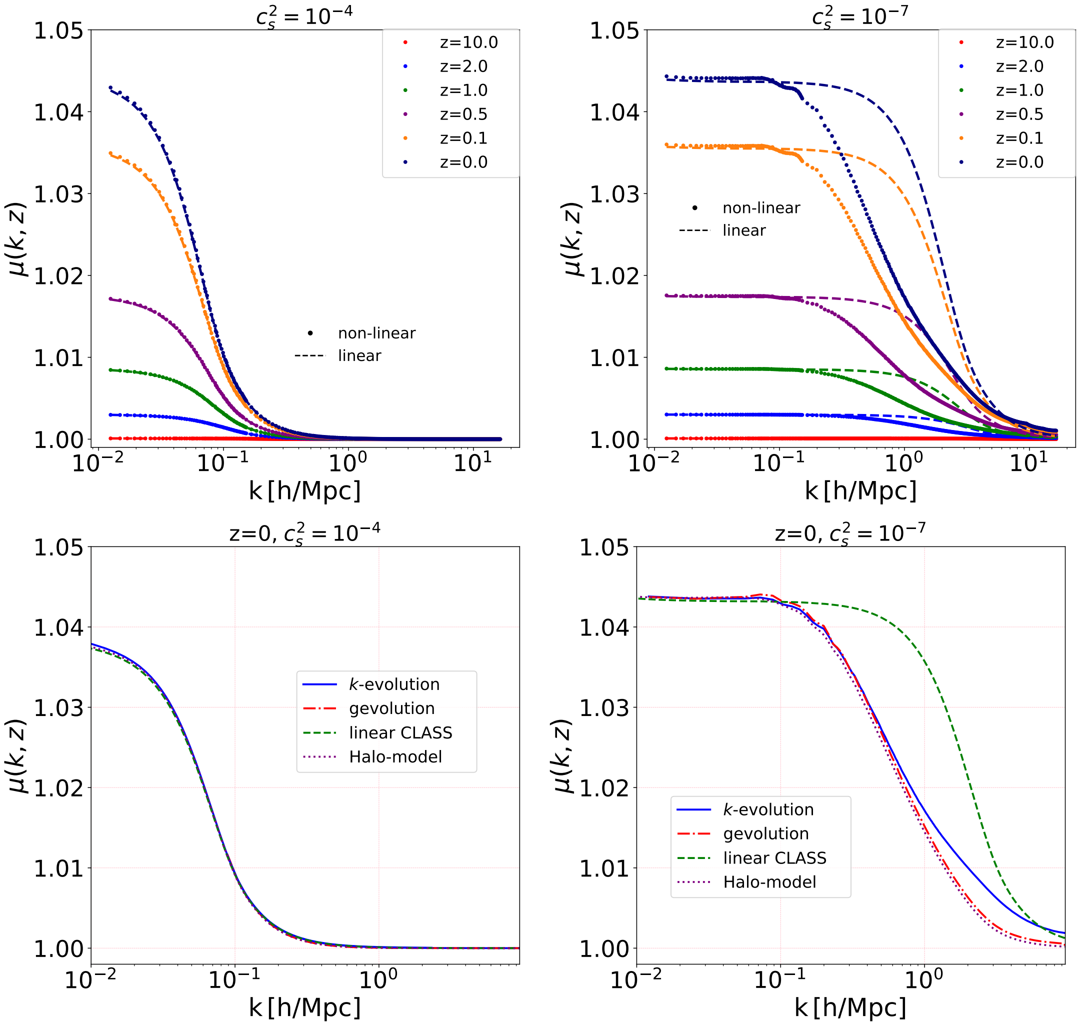

Figure 4.3: $\mu(k, z)$ from four different simulations and for two speeds of sound are compared. The left plots depict the case $c_s^2 = 10^{-4}$: all the curves agree well which shows that for high speeds of sound we can trust even linear codes. On the right we see the situation for k-essence with speed of sound $c_s^2 = 10^{-7}$, where differences are clearly visible. In the top panels k-evolution is compared with `CLASS` at different redshifts, while in the bottom figures we compare $\mu(k, z)$ from *gevolution*, k-evolution and `CLASS` with and without Halofit, at $z = 0$. The results are obtained using two simulations with two different box sizes $L = 9000\,h^{-1}$Mpc and $L = 1280\,h^{-1}$Mpc and $N_{\text{grid}} = 3840^3$.

like a^{-3w}, ensuring that the dark energy quickly becomes sub-dominant in the past.

At high wavenumbers, the k-essence perturbations are suppressed due to the existence of a sound-horizon, roughly at the comoving wavenumber $k = c_s\mathcal{H}$.

This is highly desirable as gravity is very well tested on small scales, so that models that lead to significant changes on solar system scales are ruled out by observations. The scaling of the sound horizon with c_s^2 also explains why the transition from $\mu > 1$ to $\mu = 1$ occurs on smaller scales for lower speeds of sound.

In addition, for the $c_s^2 = 10^{-4}$ case, the results from `CLASS` and k-evolution are indistinguishable at least until $z = 0.5$, and start to differ only slightly at $z = 0$ at large scales. For the $c_s^2 = 10^{-7}$ case, while the results from `CLASS` and k-evolution are consistent at both high- and low-k, there is a different transition from $\mu > 1$ to $\mu = 1$ in k-evolution compared to `CLASS`. This is because for the lower sound speed the sound-horizon lies within the scale of matter non-linearity. As dark matter clustering becomes non-linear, δ_m becomes much larger than in linear theory, which reduces Φ/δ_m and hence μ. This can be mimicked by turning on Halofit, and indeed using `CLASS` with Halofit to extract μ allows to match the result of k-evolution better at scales around $k \approx 0.1h/\mathrm{Mpc}$, as we can see in panel (d) of Fig. 4.3.

On even smaller scales, $k \gtrsim 1h/\mathrm{Mpc}$, the combination of `CLASS` with Halofit undershoots the k-evolution result. This is due to non-linear clustering of the k-essence field on small scales. This can only be correctly modeled by simulating the k-essence field itself. Also *gevolution* 1.2 with the `CLASS` interface, where k-essence is a realisation of the linear spectrum, is not able to simulate this region correctly.

4.3.4 A fitting function for μ in k-essence

To characterize the contribution of k-essence to the gravitational potential, and to simplify the inclusion of non-linear k-essence clustering in linear Boltzmann codes and in back-scaled Newtonian N-body simulations (see next section), we approximate the numerical $\mu(k, z)$ with a simple fitting formula. The fact that we recover GR/ΛCDM at small scales and that we have a constant modification to GR at large scales motivates us to choose a function that smoothly connects two different regimes, and we propose the following fitting function for $\mu(k, a)$:

$$f(k|\alpha, \beta, \gamma) = 1 + \alpha \Big(1 - \tanh\big(\beta(\log_{10} k - \gamma)\big)\Big) \, . \tag{4.19}$$

Here α controls the amplitude of μ on large scales, $\gamma = \log_{10} \kappa$ the location of the transition, and β the steepness of the transition. The variables α, β, and γ depend on time as well as on the cosmology. We can use the (α, β, γ) parameter space to distinguish between models / constrain cosmology. Additionally, the function (4.19) is C^∞ and its derivatives are easily computed, while numerical derivatives of simulation results are often noisy. In Appendix 4.B we discuss how these parameters control the shape of μ, and how well the fitting function

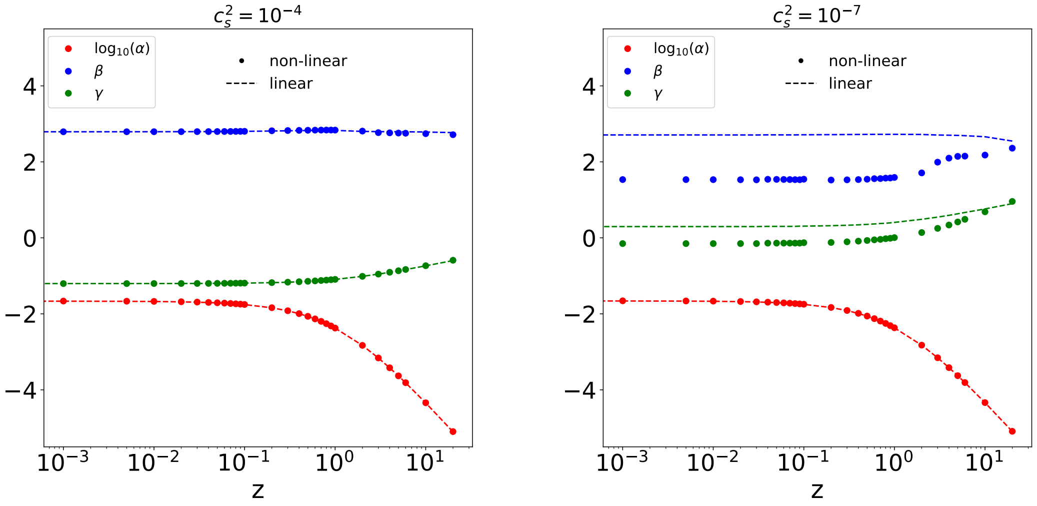

Figure 4.4: The fitted parameter values for the μ parametrization (4.19), for the two k-essence models with $c_s^2 = 10^{-4}$ (left) and $c_s^2 = 10^{-7}$ (right), as a function of redshift. Points and dashed lines are respectively the results of k-evolution and `CLASS`.

describes the simulation results. We find that for k-evolution and `CLASS`, the parametrisation (4.19) is able to describe $\mu(k, z)$ at the sub-percent level relative to μ.

The fit enables us to model $\mu(k, a)$ in a simple way and to describe its evolution by studying the time and scale evolution of the parameters. We perform the fit in the non-linear (k-evolution) and linear (`CLASS`) cases. Fig. 4.4 shows the evolution of three fitting parameters as a function of redshift for both the linear (solid lines) and non-linear (dots) cases. As expected from Fig. 4.3, for $c_s^2 = 10^{-4}$, there is little difference between the linear and non-linear cases. Also for the $c_s^2 = 10^{-7}$ case, the fitted amplitudes (α) are consistent between the linear and non-linear cases. Most of the difference arises in the steepness (β) and the location (γ) of the transition. In Appendix 4.B we provide an additional figure, Fig. 4.8 that shows in more details the evolution of the parameters. In that figure we can see that there are also detectable differences in β between the linear and k-evolution results for $c_s^2 = 10^{-4}$, but that they are relatively small. In Table. 4.1 we show the parameters (α, β, γ) fitted to the k-evolution data at redshifts $z = 0$ and $z = 1$ for both speeds of sound. The full redshift information for the fitting parameters are delivered as a text file in the arXiv submission.

		Parameters		
		α	β	γ
$c_s^2 = 10^{-4}$	$z = 0$	0.021	2.79	-1.20
	$z = 1$	0.00422	2.83	-1.10
$c_s^2 = 10^{-7}$	$z = 0$	0.020	1.46	-0.154
	$z = 1$	0.00429	1.53	0.0069

Table 4.1: Parameter values fitted to k-evolution results for both speeds of sound at two redshifts, $z = 0$ and $z = 1$.

4.4 Applications of $\mu(k, z)$

In this section we discuss how one can use the $\mu(k, z)$ parametrisation in combination with other codes, especially linear Boltzmann and Newtonian N-body codes. To answer this question, we first illustrate the differences between these codes in Fig. 4.5 when there is k-essence as a dark energy candidate. In k-evolution all the components including short-wave corrections, relativistic terms, matter and k-essence non-linearities are included. In Newtonian N-body codes, the equations are solved in N-body gauge, see Appendix 4.A for more details. In these codes one can capture the background evolution correctly, while short wave-corrections are absent and k-essence perturbations are at most taken into account through the initial conditions. In the linear Boltzmann codes, on the other hand, non-linearities in matter and k-essence as well as short wave corrections are absent.

4.4.1 Improving linear Boltzmann codes and Fisher forecasts with a parametrised μ

Recipes to predict the non-linear matter power spectrum are routinely implemented in Boltzmann codes in order to source weak lensing calculations, which are themselves linear but very sensitive to small-scale power. The $\mu(k, z)$ function presented in the previous section can then be used to correct for the non-linear effect of k-essence on the lensing. For example, $\mu(k, z)$ would appear as a simple factor in the line-of-sight integral for the lensing potential if the non-linear matter power spectrum is already calibrated for the correct background model. The

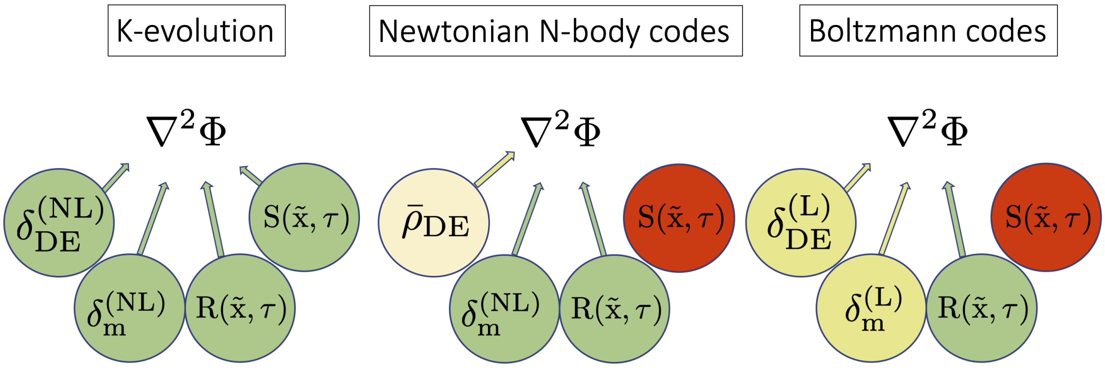
K-evolution
Newtonian N-body codes
Boltzmann codes
$\nabla^2\Phi$
$\nabla^2\Phi$
$\nabla^2\Phi$
$\delta_{\mathrm{DE}}^{(\mathrm{NL})}$
$\mathrm{S}(\tilde{\mathrm{x}},\tau)$
$\delta_{\mathrm{m}}^{(\mathrm{NL})}$
$\mathrm{R}(\tilde{\mathrm{x}},\tau)$
$\bar{\rho}_{\mathrm{DE}}$
$\mathrm{S}(\tilde{\mathrm{x}},\tau)$
$\delta_{\mathrm{m}}^{(\mathrm{NL})}$
$\mathrm{R}(\tilde{\mathrm{x}},\tau)$
$\delta_{\mathrm{DE}}^{(\mathrm{L})}$
$\mathrm{S}(\tilde{\mathrm{x}},\tau)$
$\delta_{\mathrm{m}}^{(\mathrm{L})}$
$\mathrm{R}(\tilde{\mathrm{x}},\tau)$

Figure 4.5: This picture compares the way that different codes solve the Poisson equation. On the left we have the relativistic N-body code k-evolution which uses the full Poisson equation including non-linear k-essence and matter densities, relativistic terms and short wave corrections (all in green). Standard Newtonian N-body codes (middle) solve the Poisson equation for the correct background expansion rate (term in light yellow), and include non-linear matter densities as well as relativistic terms in N-body gauge (terms in green), but do not take into account k-essence perturbations or shortwave (nonlinear GR) terms (in red). Linear Boltzmann codes like `CLASS` (on the right) are fully relativistic and include linear density perturbations for both matter and k-essence (in yellow), but no non-linear GR and matter contributions (in red).

same correction can also be applied in the context of Fisher forecasts.

4.4.2 Improving Newtonian simulations

In the companion paper Hassani et al. [2019c] we have shown that the so-called backscaling method to set initial conditions in Newtonian N-body codes is able to recover the correct non-linear matter power spectrum in k-essence models. As explained in detail in Hassani et al. [2019c], this is achieved by scaling back the linear power spectrum at the final redshift using the linear growth function in the given background model. While this works well for the matter power spectrum, it is impossible to simultaneously obtain an accurate power spectrum of the gravitational potential, as the latter is sourced additionally by k-essence perturbations. Our μ precisely parametrises the correction necessary to obtain the potential from the matter power spectrum, and additionally allows to reconstruct the power spectrum of k-essence perturbations. An immediate practical application would be to include this correction when calibrating emulators like Knabenhans et al. [2019].

4.5 Conclusions

In this paper we have studied metric perturbations in the weak-field regime of General Relativity, in the presence of a k-essence scalar field as dark energy. We showed that the short-wave corrections to the Hamiltonian constraint are negligible at all redshifts and all scales, while the relativistic terms are only relevant at large scales, leaving the terms with Poisson-gauge matter and k-essence density perturbations as the main source at quasi-linear and small scales. The relativistic terms and the density perturbations can be combined, in the usual way, to form a linear Poisson equation that then holds on all scales of interest in cosmology.

We study the contribution of the k-essence scalar field to the metric perturbations through the μ parametrisation that encodes the additional contribution of a dark energy fluid or a modification of gravity to the Poisson equation. As the Poisson equation is valid on all scales, this description works even at non-linear scales if μ is understood as an average effect. We show that for k-essence fields with a high speed of sound, the linear theory agrees with simulation results, while for models with a small speed of sound we see large deviations from linear theory. Our results are thus important for tests of low speed of sound k-essence models with future surveys.

We encode our k-essence simulation results for $\mu(k, z)$ in an easy-to-use tanh-based fitting function, together with recipes on how to include the function in linear Boltzmann codes or Newtonian N-body simulations with different expansion rate but without additional k-essence field. While in this paper we only consider two k-essence models with different speeds of sound, we plan to provide fits to $\mu(k, z)$ for a wider range of models in a follow-up publication.

Acknowledgements

FH would like to thank Jean-Pierre Eckmann for helpful comments about manuscript and useful discussions. FH and MK acknowledge financial support from the Swiss National Science Foundation. This work was supported by a grant from the Swiss National Supercomputing Centre (CSCS) under project ID s710. BL would like to acknowledge the support of the National Research Foundation of Korea (NRF-2019R1I1A1A01063740). AS would like to acknowledge the support of the Korea Institute for Advanced Study (KIAS) grant funded by the Korean government. JA acknowledges funding by STFC Consolidated Grant ST/P000592/1.

APPENDIX

4.A Discussion about N-body gauge

The correspondence between Newtonian N-body simulations and GR can be established through a particular gauge, called the N-body gauge Fidler et al. [2016], in which, generally speaking, one requires

$$\nabla^2 \Phi_N = 4\pi G_N \bar{\rho}_m \delta_m^{\text{count}} \,, \tag{4.1}$$

and

$$\frac{dv^i}{d\tau} + \mathcal{H} v^i = -\nabla \Psi \,, \tag{4.2}$$

where in the first equation Φ_N is the contribution of non relativistic matter to Φ, and δ_m^{count} is a counting density (rest mass per coordinate volume). With two scalar gauge generators L and T at one's disposal, where $\tau \to \tau + T$ and $x^i \to x^i + \nabla^i L$ are the coordinate transformations, it turns out that under quite generic conditions there is a family of gauge transformations that satisfy the above two conditions at the linear level.

To illustrate this, let us start from the Poisson gauge and find T, L such that above equations hold. The first thing to note is that Ψ corresponds to a gauge-invariant variable (we are working at linear order), so the second equation already holds in Poisson gauge. Since velocities transform as $v^i \to v^i + \nabla^i L'$ maintaining the form of the second equation readily requires $L' \simeq 0$.

Before turning to the first equation, let us define the scalar metric perturbations of the N-body gauge as follows:

$$\begin{aligned} ds^2 =& a^2 \Big[-\left(1 + 2A^{\text{Nb}}\right) d\tau^2 - 2\nabla_i B^{\text{Nb}} dx^i d\tau + \left(1 + 2H_L^{\text{Nb}}\right) \delta_{ij} dx^i dx^j \\ & - 2\left(\nabla_i \nabla_j - \frac{\delta_{ij}}{3}\nabla^2\right) H_T^{\text{Nb}} dx^i dx^j \Big] \end{aligned} \tag{4.3}$$

Noting how the various scalar perturbations transform, for a T and L connecting the N-body gauge to Poisson gauge we have

$$\Phi = -H_L^{\text{Nb}} - \mathcal{H}T - \frac{1}{3}\nabla^2 L \,, \tag{4.4}$$

$$\Psi = A^{\text{Nb}} + \mathcal{H}T + T' \,, \tag{4.5}$$

$$0 = B^{\text{Nb}} + T - L' \Rightarrow B^{\text{Nb}} \simeq -T \,, \tag{4.6}$$

$$0 = H_T^{\text{Nb}} - L \Rightarrow H_T^{\text{Nb}} = L \,, \tag{4.7}$$

and

$$\delta_X = \delta_X^{\rm Nb} - 3\left(1 + w_X\right)\mathcal{H}T\,. \tag{4.8}$$

We can insert these expressions into the Hamiltonian constraint (keeping the term $\nabla^2\Phi$ in place) to obtain

$$\nabla^2\Phi+3\mathcal{H}\left(H_L^{\rm Nb\prime} + \mathcal{H}T' + \mathcal{H}'T\right)-3\mathcal{H}^2\left(A^{\rm Nb} + \mathcal{H}T + T'\right) = 4\pi G_N a^2 \sum_X \bar{\rho}_X\left[\delta_X^{\rm Nb} - 3\left(1 + w_X\right)\mathcal{H}T\right]\,, \tag{4.9}$$

where we already used the condition $L' \simeq 0$. Noting that

$$\mathcal{H}^2 - \mathcal{H}' = 4\pi G_N a^2 \sum_X \bar{\rho}_X\left(1 + w_X\right) \tag{4.10}$$

we immediately get

$$\nabla^2\Phi+3\mathcal{H}H_L^{\rm Nb\prime}-3\mathcal{H}^2A^{\rm Nb} = 4\pi G_N a^2\sum_X \bar{\rho}_X\delta_X^{\rm Nb} = 4\pi G_N a^2\bar{\rho}_m\left(\delta_m^{\rm count} - 3H_L^{\rm Nb}\right)+4\pi G_N a^2\sum_{X\neq m}\bar{\rho}_X\delta_X^{\rm Nb} \tag{4.11}$$

The requirement that this equation is compatible with eq. (4.1) does not yet fix the gauge completely. One may try to require that $H_L^{\rm Nb} \simeq 0$ which means that $\delta_m^{\rm Nb} = \delta_m^{\rm count}$. This means that not only are the Newtonian equations satisfied, but also the counting density *is* the physical density in that gauge.

One can easily see from the last equation that $H_L^{\rm Nb} \simeq 0$ also suggests $A^{\rm Nb} \simeq 0$, and one can verify that, as long as pressure perturbations are small, this condition can be met Fidler et al. [2016]. We can then infer T and L as follows.

$$\Psi = \mathcal{H}T + T'\,, \qquad \Phi = -\mathcal{H}T - \frac{1}{3}\nabla^2 L\,, \tag{4.12}$$

hence

$$\mathcal{H}\Psi + \Phi' = \left(\mathcal{H}^2 - \mathcal{H}'\right)T\,, \tag{4.13}$$

where $L' \simeq 0$ was assumed. We can now see that the momentum constraint implies $T = -\nabla^{-2}\theta_{\rm tot}$ and hence $\delta_m^{\rm Nb} = \Delta_m$. Inserting T back into its relation with Φ above, we also get

$$\nabla^2 L = 3\mathcal{H}\nabla^{-2}\theta_{\rm tot} - 3\Phi\,. \tag{4.14}$$

The right-hand side is the comoving curvature perturbation which is indeed conserved at late times in standard cosmology. Hence our assumption $L' \simeq 0$ was consistent.

4.B Details of the fitting function for $\mu(k, z)$

In this Appendix we discuss the properties of tanh fitting function, we also compare the fitted values to the underlying simulation results and show that the tanh fitting function works quite well. As explained in more detail in the main text, we need a function to smoothly connect two different regimes, namely, between $\mu \simeq$ constant on large scales to $\mu = 1$ on small scales. To do this, we propose the following form, at a fixed redshift:

$$f(k|\alpha, \beta, \gamma) = 1 + \alpha \Big(1 - \tanh\Big(\beta(\log_{10} k - \gamma)\Big)\Big) . \tag{4.15}$$

The parameter $\gamma = \log_{10} \kappa$ determines the location of the transition, β the steepness of the transition, while $1 + 2\alpha$ is the value of μ for $k \to 0$. All of these parameters are functions of redshift (or scale factor). The fit enables us to describe the scale dependence of $\mu(k, a)$ in a simple way, while the time dependence can be studied through the evolution of fit parameters with redshift.

In Fig. 4.6 we show the validity of the fitting tanh function for $\mu(k, a)$ as measured from k-evolution. For both speeds of sound at some redshifts and all scales, the accuracy of the fit is of the sub-percent level. In Fig. 4.7 the relative difference between fit and data from `CLASS` is shown. For both speeds of sound at all redshifts and all scales, tanh is a good fit. In Fig. 4.8 the evolution of fit parameters for k-evolution and `CLASS` data is shown.

4.C Scalar-vector-tensor decomposition and notation

In this appendix we briefly discuss the scalar-vector-tensor decomposition and we introduce our notation for the metric perturbations after the decomposition. Using the SVT decomposition Lifshitz [1946] we can decompose B_i into the curl-free (longitudinal) and divergence-free (transverse) components,

$$B_i = B_i^{\perp} + B_i^{\parallel} \text{ where } \vec{\nabla} \cdot B^{\perp} = \vec{\nabla} \times B^{\parallel} = 0 \tag{4.16}$$

Also we can decompose the tensor perturbations analogously,

$$h_{ij} = h_{ij}^{\parallel} + h_{ij}^{\perp} + h_{ij}^{(S)} \ , \tag{4.17}$$

Here

$$h_{ij}^{\parallel} = \Big(\nabla_i \nabla_j - \frac{1}{2}\delta_{ij}\nabla^2\Big)\Phi_h \ . \tag{4.18}$$

where Φ_h Bertschinger [2001] is a scalar and we have assumed that h_{ij} is traceless, and

$$h_{ij}^{\perp} = \nabla_i h_j^{\perp} + \nabla_j h_i^{\perp} \ . \tag{4.19}$$

where $h_i^{\perp}$ is a divergenceless vector. The two degrees of freedom left in the tensor modes $h_{ij}^{(S)}$ correspond to the two polarisations of gravitational waves.

Fixing the gauge to Poisson gauge will remove two vector and two scalar degrees of freedom as we have the following constraints,

$$\delta^{ij} B_{i,j} = \delta^{ij} h_{ij} = \delta^{jk} h_{ij,k} = 0 \ . \tag{4.20}$$

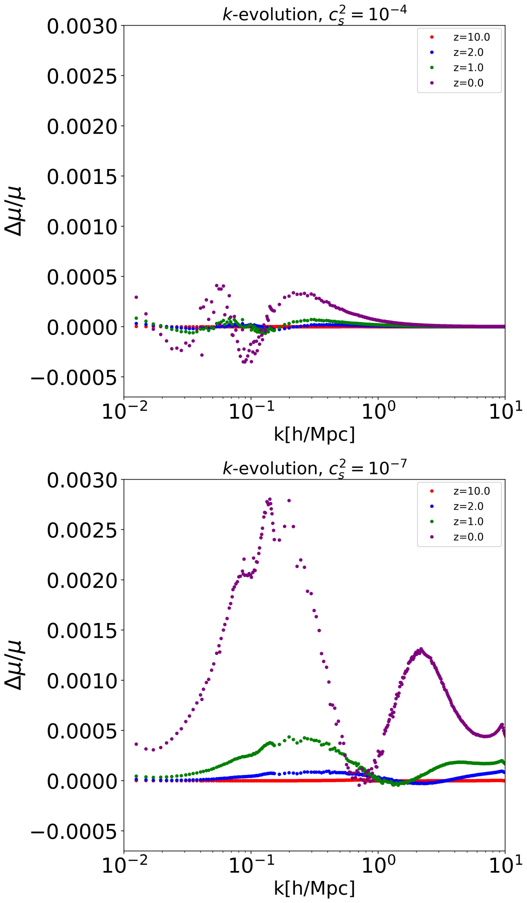

Figure 4.6: The relative error for the fits compared to the actual μ obtained from k-evolution, for two different speeds of sound, $c_s^2 = 10^{-7}$ (right) and $c_s^2 = 10^{-4}$ (left). The accuracy of the fit is of the sub-percent level for both speeds of sound at all redshifts and all scales.

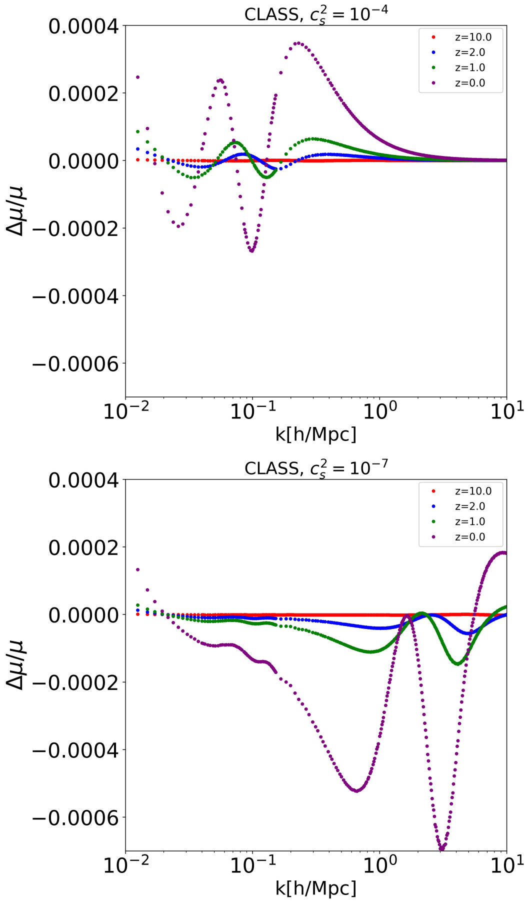

Figure 4.7: The relative error of the fits compared to `CLASS` results for two speeds of sound, $c_s^2 = 10^{-7}$ (right) and $c_s^2 = 10^{-4}$ (left). The results show that the accuracy of the fit is of the sub-percent level for both speeds of sound at all redshifts and all scales.

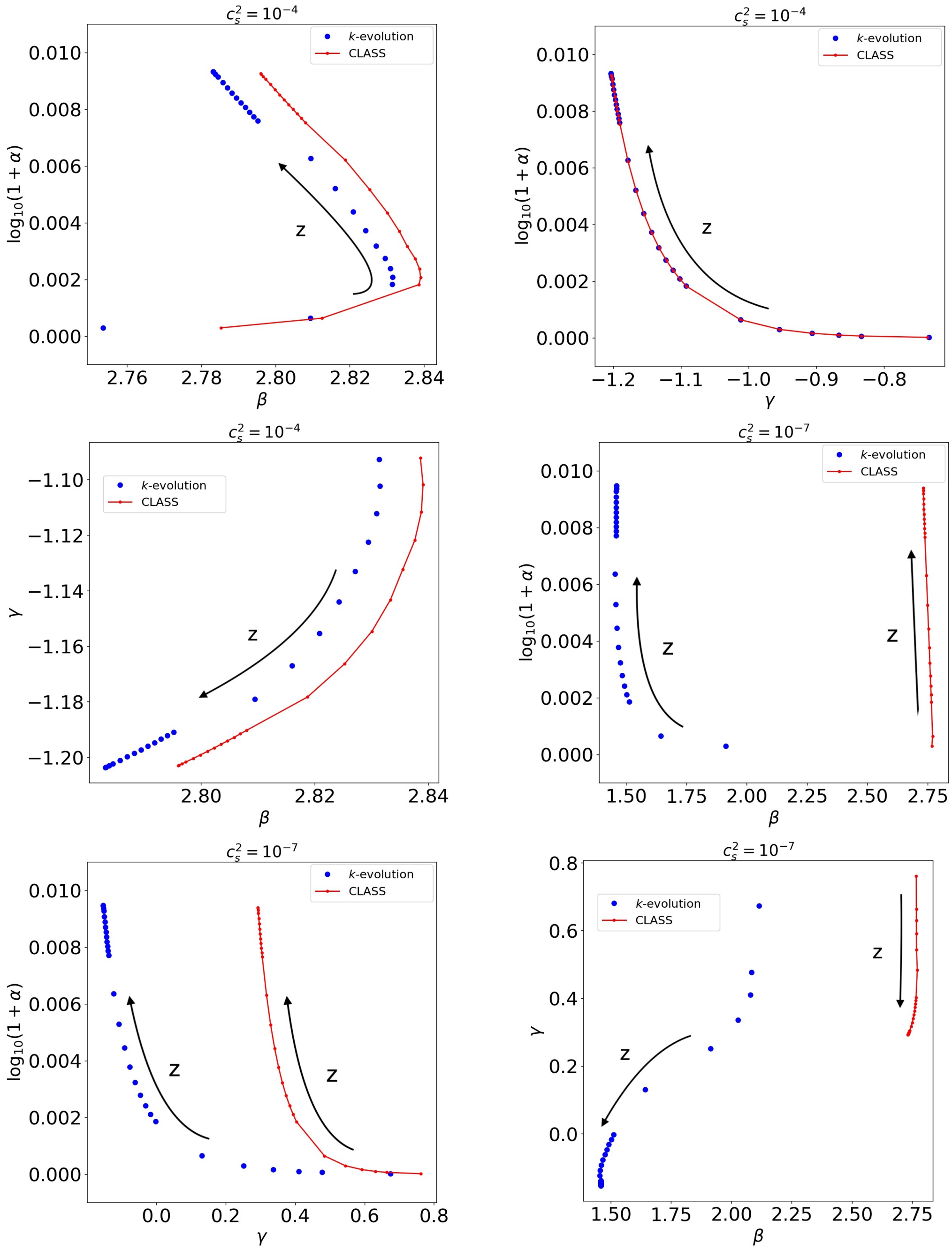

Figure 4.8: Evolution of the fit parameters $\log_{10}(1+\alpha)$, β, and γ for k-evolution and `CLASS` data for two speeds of sound $c_s^2 = 10^{-4}$ (top) and 10^{-7} (bottom) is shown. The arrows show the direction of decreasing redshift (increasing time). For the case of low speed of sound (bottom panel) the parameter values obtained from k-evolution and from the linear code `CLASS` differ, while for large speed of sound (top panel) the parameters almost match, suggesting that one could simply use linear Boltzmann codes for treating high speed of sound k-essence models.

Chapter 5

A NEW INSTABILITY IN CLUSTERING DARK ENERGY

Based on:
Farbod Hassani, Pan Shi, Julian Adamek, Martin Kunz and Peter Wittwer *A new instability in clustering dark energy*, **in preparation**

Abstract: In this paper we discuss non-linear terms in the Effective Field Theory of Dark Energy (EFT of DE) for the k-essence model. Such terms open a new window to cosmological models for dark energy. We studied such models in 3+1 dimensions using cosmological N-body simulation k-evolution [Hassani et al., 2019a]. We discovered that in the case of low speed of sound (high Mach number in the fluid description) where some linear terms vanish from the dynamics of dark energy, the non-linear partial differential equation for dark energy suffers from the non-linear instability and blows up in finite time. This might seem an artifact of the simulation procedure. However, we show analytically, for the 1+1 dimensional case, that the divergence is real: This is proven and studied mathematically in Shi, Pan et. al. [c,a,b]. We also argue how this phenomenon transfers to 3+1 dimensions.

The important conclusion is that dark energy as a fluid with high Mach number (low speed of sound) cannot be used as a viable candidate for explaining the accelerated expansion of the universe, because the evolution will diverge before one reaches the current epoch. We illustrate the dependence on the speed of sound in several simulations.

5.1 Introduction

In the near future we will benefit from numerous high precision observations Aghamousa et al. [2016b], Amendola et al. [2016], Walcher et al. [2019], **?**, probing the Universe at different epochs, from the very early times when cosmic microwave background radiation (CMB) photons started to propagate and the Universe was around 400,000 years old to today, where the Universe is 13.82 billion years old. One of the central focuses of the future surveys will be aimed at understanding the nature of dark energy, which is the reason behind the late time accelerated expansion of the universe. The accelerated expansion has already been approved by several independent observations Ade et al. [2015b], Alam et al. [2017a], Scolnic et al. [2018].

Over the past years, a wide range of theories has been developed by cosmologists and particle physicists with the aim to address question of the accelerated expansion of the universe, either by modifying the theory of gravity or by considering dark energy as a fluid component with a negative pressure Clifton et al. [2012c], Ishak [2019]. Among these theories, effective field theory (EFT) of dark energy Gleyzes et al. [2015], Gubitosi et al. [2013b], like any other effective theory, has become very popular since it allows to describe dark energy occurring at a chosen energy scale with an appropriate number of free parameters in a model independent way. The free parameters in the effective theory could correspond to a fundamental theory at high energy and respect the low-energy symmetries Cheung et al. [2008].

The main advantage of using effective theories is that one can study the physical phenomena without being specific about the fundamental theory. Instead one writes a general low-energy effective theory using the symmetries and theoretical constraints in order to compare a generic theory against observations.

In this paper we focus on the EFT of dark energy, keeping only two free parameter, α_K at the perturbation level and w_0 at the background level which is equivalent to the well known theory of k-essence, which has been first proposed in 2000 Armendariz-Picon et al. [2000, 2001] to naturally, and without any fine tuning explain the accelerated expansion of the universe. At linear level k-essence theory has been explored well and is considered a viable theory for the late time accelerated expansion of the universe. This theory has been successful in explaining all cosmological observations to date. However, by increasing the precision of the observations in the near future, we hopefully will be able to probe the non-linear scales to a great degree, which it will give us the chance to falsify the k-essence model or constrain its parameters.

Here, we use the equations derived in Hassani et al. [2019a] for the non-linear evolution of k-essence as an effective field theory, parametrised with the equation of state w and the speed of sound c_s. The free parameters appearing in the field picture e.g., α_K can be interpreted when writing the theory in the fluid picture. In the Appendix A of Hassani et al. [2019a] we showed that the fluid description and the field picture are equivalent and by the well-defined transformation given in the reference, one can simply change the picture.

In this paper, we show that the effective field theory of dark energy for k-essence, in the limit of low speed of sound suffers from a new instability. We study the instability in 3+1 dimensions numerically in the cosmological context, and comment on the equation in 1+1 dimensions.

In Sec. 5.2 we present the numerical results for 3+1 D in the cosmological context where we solve the full 3+1 D partial differential equation for the k-essence scalar field numerically, using the effective field theory framework. In Sec. 5.3 we show that for low speed of sound the solution to this partial differential equation (PDE) blows up at some time before the current age of the universe. In Sec. 5.4 we study the relevant partial differential equation in 1+1 D in matter domination analytically and we show that the term that we have recognized as the reason behind the instability shares similar properties with the 3+1 D version that has been identified in cosmological simulations. We also comment on the way that system blows up, as well as on the time when the solution ceases to exist. At the end we show how increasing the speed of sound could stabilize the system.

5.2 Field equations

In this section we write down the equations for k-essence dark energy scalar field parametrised with the equation of state w and the speed of sound c_s^2 expanded around the background solution to second order of the weak field expansion. The equation as well as the stress energy tensor for clustering dark energy are obtained and discussed in detail in Hassani et al. [2019a]. In Hassani et al. [2019a] we showed the results for clustering dark energy where we only keep linear terms in the dark energy scalar field equations.

The full partial differential equation (PDE) in 3+1 dimensions including the non-linear correction in the weak field regime reads [Hassani et al., 2019a],

$$
\begin{aligned}
\partial_\tau \pi &= \zeta - \mathcal{H}\pi + \Psi \,, \qquad (5.1)\\
\partial_\tau \zeta &= 3w\mathcal{H}\zeta - 3c_s^2\left(\mathcal{H}^2\pi - \mathcal{H}\Psi - \partial_\tau\mathcal{H}\pi - \partial_\tau\Phi\right) + c_s^2\vec{\nabla}^2\pi \\
&\quad - \left(\vec{\nabla}\left[2(c_s^2-1)\zeta + c_s^2\Phi - \Psi\right]\right)\cdot\vec{\nabla}\pi - \left[(c_s^2-1)\zeta + c_s^2\Phi - c_s^2\Psi\right]\vec{\nabla}^2\pi \\
&\quad - \frac{\mathcal{H}}{2}\left[(2+3w+c_s^2)(\vec{\nabla}\pi)^2 + 6c_s^2(1+w)\pi\vec{\nabla}^2\pi\right] + \frac{c_s^2-1}{2}\partial_i\left(\partial_i\pi(\vec{\nabla}\pi)^2\right) \,, \qquad (5.2)
\end{aligned}
$$

In the former equation π is the dark energy scalar field and ζ is an auxiliary field written in terms of the scalar field π, its time derivative $\partial_\tau\pi$ with respect to conformal time and the gravitational potential Ψ. Moreover, $(\vec{\nabla}\pi)^2 \equiv \vec{\nabla}\pi\cdot\vec{\nabla}\pi$, in $\partial_i\left(\partial_i\pi(\vec{\nabla}\pi)^2\right)$ we sum over the index i and $\partial_i \equiv \vec{\nabla}_i = \frac{\partial}{\partial x_i}$. The Eq. 5.2 is equivalent to the continuity and the Euler equations as discussed in the Appendix A in [Hassani et al., 2019a],

$$
\partial_\tau\delta = -(1+w)\left(\theta - 3\partial_\tau\Phi\right) - 3\mathcal{H}\left(\frac{\delta p}{\delta\rho} - w\right)\delta + 3\partial_\tau\Phi\left(1 + \frac{\delta p}{\delta\rho}\right)\delta + \frac{1+w}{\rho}v^i\partial_i\left(3\Phi - \Psi\right) . \qquad (5.3)
$$

$$
\partial_\tau\theta + (3w-1)\mathcal{H}\,\theta + \nabla^2(\Psi+\sigma) + \frac{\nabla^2\delta P}{\rho(1+w)} - (5\partial_\tau\Phi + \partial_\tau\Psi)\theta + \frac{\nabla^2\Psi}{1+w}\left(1 + \frac{\delta P}{\delta\rho}\right)\delta - \frac{\partial_i\Sigma_i^j}{\rho(1+w)}\partial_j(3\Phi - \Psi) = 0 \,. \qquad (5.4)
$$

Where we have used the following notation,

$$
\delta \doteq \frac{\delta\rho}{\rho}\,, \qquad \theta \doteq e^{-2(\Phi+\Psi)}\partial_i v^i\,, \qquad \sigma \doteq \frac{\vec{\nabla}^{-2}\delta^{ik}\partial_k\partial_j\Sigma_i^j}{\rho+p}\,. \qquad (5.5)
$$

Where $\vec{\nabla}^{-2}$ is the inverse Laplacian operator. The fluid picture properties read as follows in terms of the field properties,

$$\begin{aligned}
\delta\rho &= -\frac{\rho+p}{c_s^2}\left[3c_s^2\mathcal{H}\pi - \zeta - \frac{2c_s^2-1}{2}(\vec{\nabla}\pi)^2\right] , \\
\delta p &= -(\rho+p)\left[3w\mathcal{H}\pi - \zeta + \frac{1}{6}(\vec{\nabla}\pi)^2\right] , \\
v^i &= -e^{2(\Phi+\Psi)}\left[1 - \frac{1}{c_s^2}\left(3c_s^2(1+w)\mathcal{H}\pi - \zeta + c_s^2\Psi\right) + \frac{c_s^2-1}{2c_s^2}(\vec{\nabla}\pi)^2\right]\partial_i\pi , \\
\Sigma_{ij} &= (\rho+p)\left[\partial_i\pi\partial_j\pi - \frac{1}{3}(\partial_k\pi)^2\delta_{ij}\right] .
\end{aligned} \tag{5.6}$$

However in the k-evolution approach, we solve the equations written in the field language and we solve a second order PDE to update the scalar field π and its time derivative $\partial_\tau\pi$. Numerical results from the k-evolution for the full non-linear PDE show that there exists a speed of sound c_{s_0}, such that, for speed of sound c_s smaller than c_{s_0}, the PDE blows up in finite time. In the following section we show the numerical results for the small and large speeds of sound, where the PDE is, respectively, unstable and stable, and afterwards we justify the numerical results by solving the equations in lower dimension.

5.3 Simulations

In this section we show the results from k-evolution for the conservative initial conditions where we set the values of the fields π and ζ to zero everywhere on the lattice at the initial redshift $z = 100$. The reason for choosing zero initial conditions for π and ζ is mainly that the initial conditions based on the linear theory lead to a singularity in the density of the scalar field. As there is a c_s^2 term in the denominator in the Eq. 5.6, the initial conditions have to be such that $\left(3c_s^2\mathcal{H}\pi - \zeta - \frac{2c_s^2-1}{2}(\vec{\nabla}\pi)^2\right) \sim c_s^2$, and taking $\pi_{ini} = 0$ and $\zeta_{ini} = 0$ will respect this condition. In addition, having no scalar field at large enough redshift and let it being produced by the dynamics due to the gravitational potential is more physical than assuming other initial conditions for this system.

Starting the simulation at some initial time and solving the full equations of motion in the weak field approximation using the N-body code k-evolution for low speed of sound, one sees numerically that the scalar field π diverges and as a result the simulation breaks down in finite time. In Fig. 5.1 we show the results for the simulation for the scalar field on a 2D snapshot at surfaces which go through the point with the maximum second derivative. In these snapshots which are made for a short period of time in the simulation, one can see how suddenly an instability is formed in the scalar field dynamics and that the system blows up at a certain time. Since other cosmological quantities are coupled to the scalar field, the other components will also diverge, the dark matter particles speed up and the simulation breaks down.

If one looks at other points than the point we chose, one sees that the instability does not appear in all snapshots at the same times. The reason why the instability is first formed around the point with highest curvature will become clear when we study the system in 1+1 D analytically.

In Fig. 5.2 we show the evolution of the scalar field mapped in a direction (1D) in order to have a closer look at what happens when the instability is generated and the system blows up. According to the 1D cross-sections, the blowup first happens at a minimum point with the highest curvature. In the simulation the curvature of this point increases to finally become infinity as the minimum becomes sharper and sharper in time.

According to our numerical results using k-evolution code for the full implementation of clustering dark energy (5.1) and (5.2), one sees that the equations are unstable and diverge in finite time for low speed of sound only. Indeed, for a fixed cosmological parameters and $w_0 = -0.9$ the system only blows up when $c_s^2 \leq 10^{-4.7}$. In Fig. 5.3 and Fig. 5.4 the blow up time and also the average of the ζ field for different speeds of sound are shown. As the two figures suggest when decreasing c_s^2, there is a value for c_s^2 where the system becomes unstable. Moreover, it is interesting to point out that we know that the limit of low speed of sound is the limit where the most important linear terms in the dynamics of scalar field vanish and we end up with a highly non-linear evolution of the field. The number $c_s^2 = 10^{-4.7}$ for the speed of sound squared can be understood by comparing the two important terms in the dynamics of the scalar field. As we are going to show the stability of this system is ensured when the term $c_s^2\nabla^2\pi$ dominates over the non-linear term $-\frac{\mathcal{H}}{2}\Big(5c_s^2 + 3w - 2\Big)\,(\nabla\pi)^2$. As these are the two important contributions to the dynamics, using the approximative scaling relation, for these two terms i.e. assuming that $\nabla^2\pi \sim L^{-2}\pi$ and $(\nabla\pi)^2 \sim L^{-2}\pi^2$. Here, we are assuming that each spatial derivative contributes as a factor of $1/L$. Also assuming the matter domination i.e., $\mathcal{H} = 2/\tau$, and the first order perturbative solution for $\pi \approx \frac{\Psi}{3}\tau$ calculated in Eq. D.6 in Hassani et al. [2019a] we roughly have,

$$c_s^2 \approx \frac{-\mathcal{H}}{2}\Big(5c_s^2 + 3w - 2\Big)\pi = \Big(\frac{2}{3} - w\Big)\Psi\,. \tag{5.7}$$

with the values of $w = -0.9$ and $\Psi = 10^{-5}$ this gives $c_s^2 = 10^{-4.8}$ which is close to $c_s^2 = 10^{-4.7}$ as obtained from the numerical results in Fig. 5.4.

The study of the full coupled non-linear system of equations including Einstein's equations and the non-linear second order equation for the dark energy sector seems challenging. However, our numerical results show that we do not need to worry about whether dark energy sources the gravity part or other components. Even if we solve the equation for the scalar field independently whether it sources other components or not we get an instability at almost the same time,

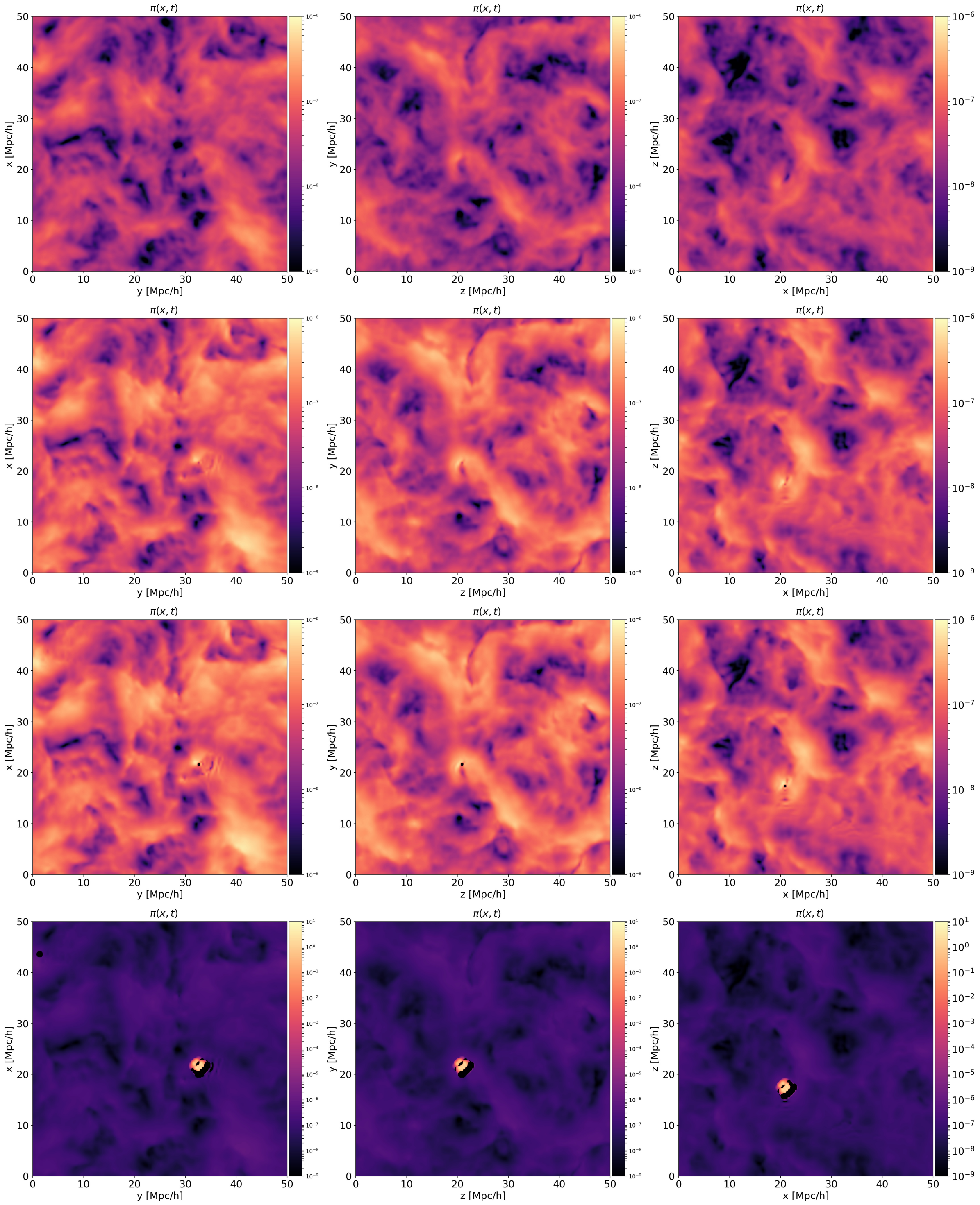

Figure 5.1: From top to bottom: The evolution in time of the scalar field π evolution in a 2D cross section in $x-y$, $x-z$ and $y-z$ surfaces in a short interval of time around blowup time at the point with the maximum curvature. The instability is formed locally in a point with the maximum curvature which physically corresponds to the center of the dark matter halos.

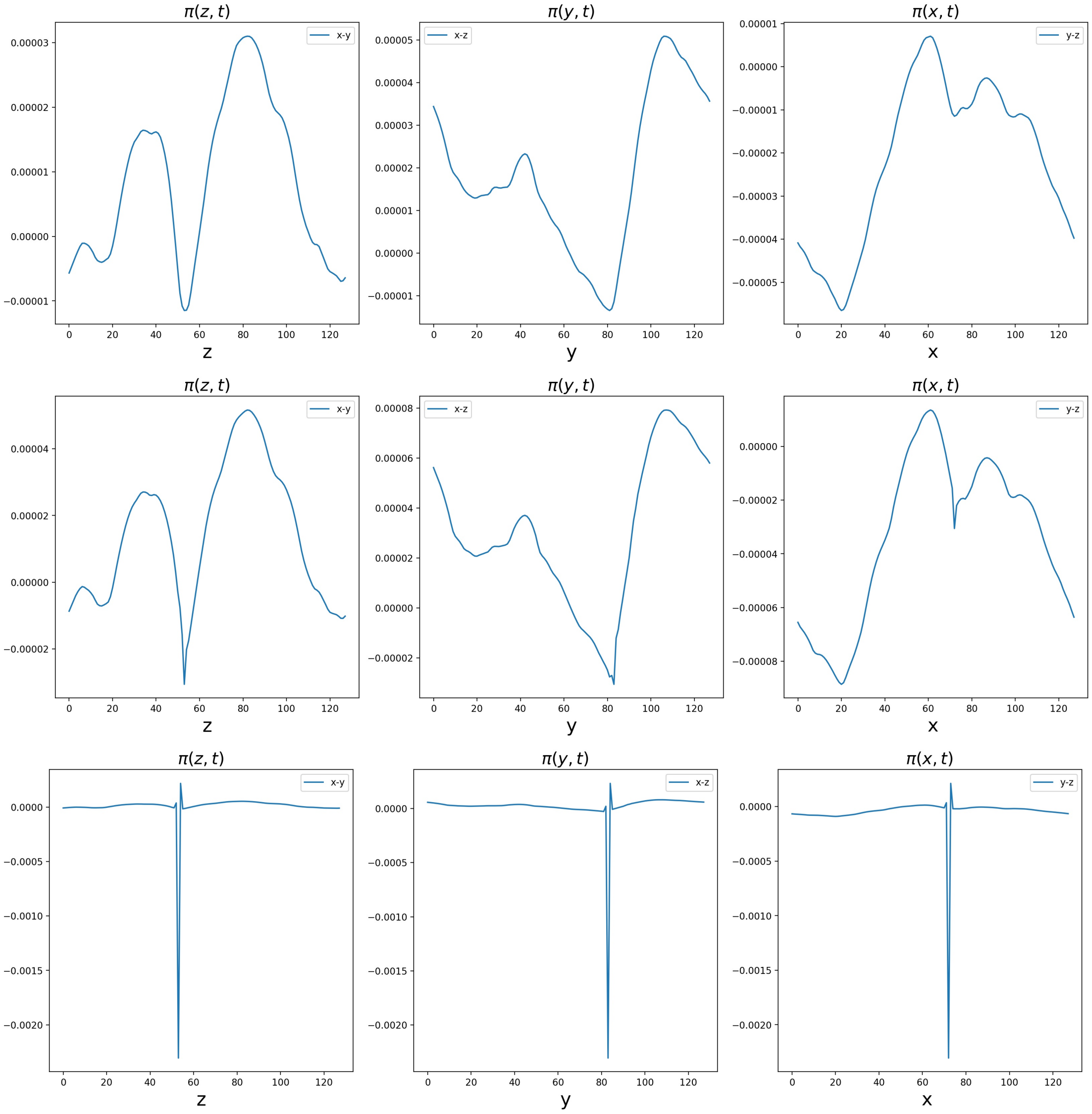

Figure 5.2: 1D cross section of the scalar field evolution on a line passing through the point with the maximum curvature. These figures show how the instability is formed in the local minima with highest curvature.

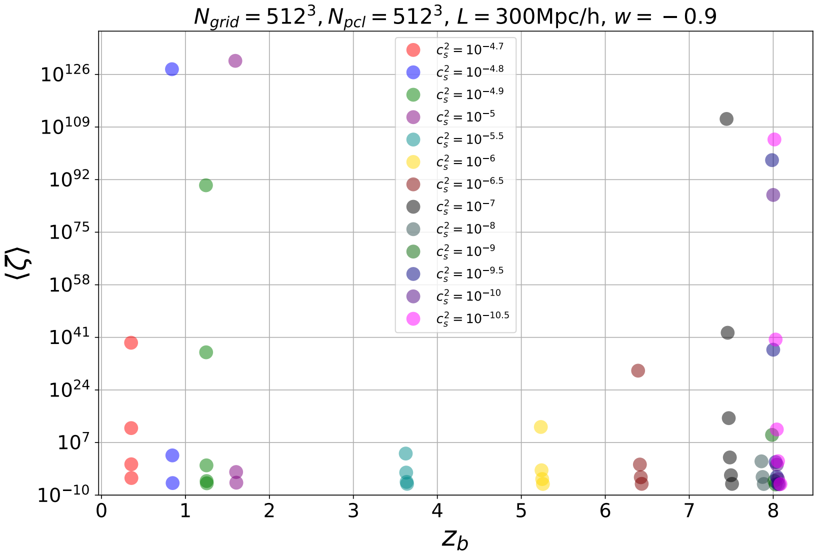

Figure 5.3: The average of ζ as a function of blow-up redshift for different speeds of sound are plotted. As it is clear from the figure, the blow up happens very fast and the average value of the fields go from a very small value to a very large value. This is a simulation for the case when k-essence does not source other components and also the initial condition is set to 0 at $z = 100$. When ζ blows up, the scalar field π and other components, if they are coupled, blow up immediately. Here we only showed the results for the speeds of sound for which the scalar field blows up, so in fact according to our numerical result $c_s^2 \leq 10^{-4.7}$. The PDE blows up in the age of the Universe ($z = 0$).

especially when the time precision of the simulation is high enough. In Fig. 5.5 we show the blow up time (redshift) for different precisions of time in the code for the situation when dark energy sources other components (in circle) and when dark energy does not source other components (in star). According to the figure the blow up time does not depend on whether the dark energy sources other components or not.

Another interesting and important result is that by increasing the resolution of the simulation, the system blows up earlier in time. In Fig. 5.6 the blow up time for different spatial resolutions is shown. We will justify this result when we study the system in 1+1 D, but roughly this behavior is due to the fact that by increasing the resolution of the simulation, we sample the initial condition from higher wavenumbers in the gravitational potential power spectrum so that the curvature of the potential wells increases compared to the lower resolution simulation. As we will show in the 1+1 D and spherically symmetric 3+1 D

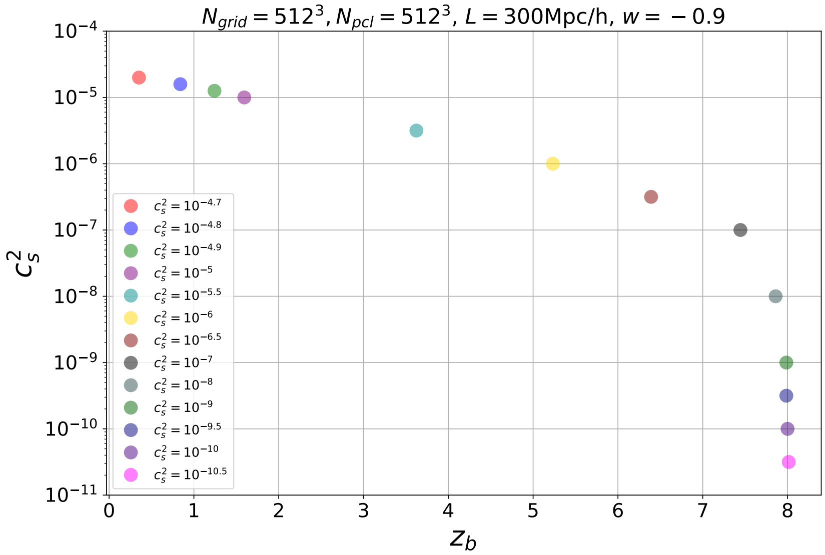

Figure 5.4: The speed of sound squared as a function of blow up redshift is shown. There are two limits, namely high speed of sound for which the system does not blow up anymore and very low speed of sound for which the system blows up at the redshift near to the blow up redshift for $c_s^2 \to 0$. This figure is calculated for the case when the scalar field does not source matter and potentials and also, when the initial condition is chosen equal to zero.

results, the instability is forming around the minima of the gravitational potential wells and the blowup time depends on the curvature of these potential wells. In the 3+1 D case, by increasing the spatial resolution of the simulation in the cosmological context, we also increase the curvature of the potential wells.

In Fig. 5.7 we verify that changing the initial redshift would not change the blow up time significantly as the blowup redshift converges to a number. In the figure the initial conditions for the position and speed of the particles are made using the solution of the linear theory at that redshift, while the scalar field is set to zero at the initial time.

Motivated by the numerical results in 3+1 D in the cosmological context, we study the simplified version of the full equation in the mathematical context in 1+1 D in the next section.

5.4 1+1 dimensions

In this section we discuss the main terms in the PDE governing the scalar field dynamics. In particular we discuss the non-linear dynamics in 1+1 dimensions.

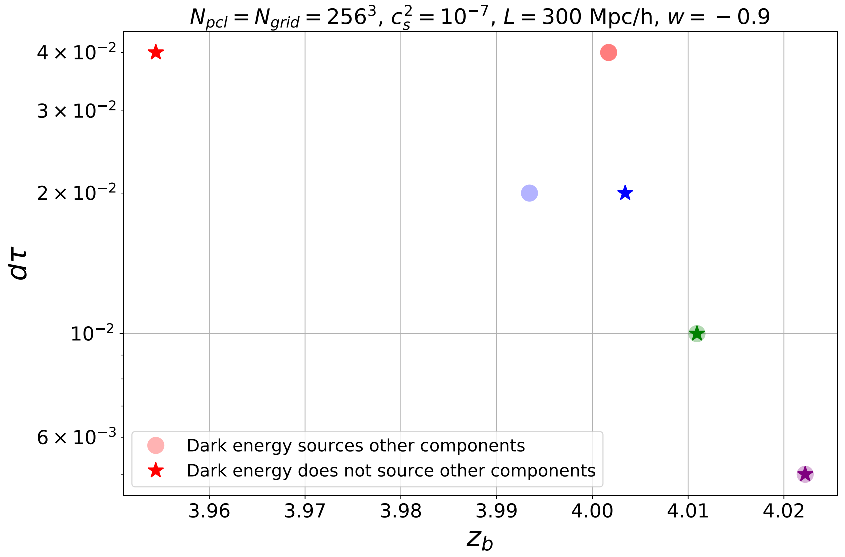

Figure 5.5: Time resolution of the simulation as a function of the blow up time for the case dark energy component, respectively, sources and does not source other components (circles and stars respectively). As we increase the time resolution, i.e. decrease $d\tau$ in the simulation the blow-up time converges.

We show that the non-linear PDE is suffering from the non-linear instability with similar behavior of what we found in the 3+1 D case. We would like to emphasize that the full study of the dynamics in 3+1 D and also in 1+1 D is a difficult task and needs a detailed study which is beyond the scope of this paper. However, the specific term (that is $(\nabla\pi)^2$), which we have recognized as of the main reason behind the instability of the system, is studied it thoroughly in Shi, Pan et. al. [c,a,b] in a mathematical context. Here, we study this term with a more physical approach.

5.4.1 Full non-linear PDE in 1+1 D

We rewrite the Eq. 5.2 as a second order PDE form in 1+1 D which is more appropriate for analytical studies,

$$\begin{aligned}&\partial_\tau^2\pi + \mathcal{H}(1-3w)\partial_\tau\pi + \Big(\partial_\tau\mathcal{H} - 3w\mathcal{H}^2 + 3c_s^2(\mathcal{H}^2 - \partial_\tau\mathcal{H})\Big)\pi \\ &- \partial_\tau\Psi(x) + 3\mathcal{H}(w - c_s^2)\Psi(x) - 3c_s^2\partial_\tau\Phi(x) - c_s^2\partial_x^2\pi = \mathcal{N}(\pi, \partial_\tau\pi, \partial_x\pi, \partial_x\partial_\tau\pi, \partial_x^2\pi)\end{aligned} \tag{5.8}$$

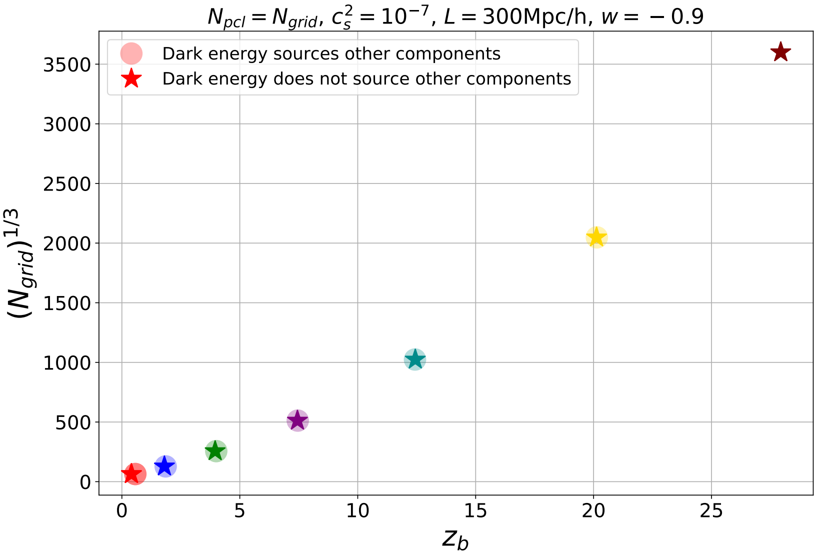

Figure 5.6: Number of grids, equal to number of particles, as a function of the blowup redshift for the clustering dark energy with $c_s^2 = 10^{-7}$ and $w = -0.9$, for the two cases where dark energy sources, respectively, does not source other components. The case when dark energy PDE is solved without sourcing dark matter and potentials is shown by stars in the figure and the case when the full equations are solved is shown with circles. As we increase the spatial resolution, the system blows up at higher redshifts or earlier time.

where $\mathcal{N}(\pi, \partial_\tau\pi, \partial_x\pi, \partial_x^2\pi)$ includes all the non-linear terms which reads as follows,

$$\begin{aligned}
&\mathcal{N}(\pi, \partial_\tau\pi, \partial_x\pi, \partial_x\partial_\tau\pi, \partial_x^2\pi) = -\frac{\mathcal{H}}{2}\Big(5c_s^2 + 3w - 2\Big)\,(\partial_x\pi)^2 + 2(1-c_s^2)\partial_x\pi\partial_x\partial_\tau\pi \\
&-\Big[(c_s^2-1)\Big(\partial_\tau\pi + \mathcal{H}\pi - \Psi\Big) + c_s^2(\Phi - \Psi) + 3\mathcal{H}c_s^2(1+w)\pi\Big]\partial_x^2\pi + (2c_s^2-1)\partial_x\Psi\partial_x\pi \\
&-c_s^2\partial_x\Phi\partial_x\pi + \frac{3(c_s^2-1)}{2}(\partial_x\pi)^2\partial_x^2\pi
\end{aligned} \tag{5.9}$$

The previous equation is called "non-linear damped wave equation" Gallay & Raugel [1998] in the literature. It has been studied by mathematicians for some cases of non-linearities mainly in the form $\mathcal{N}(\pi, \partial_\tau\pi)$ [**??**] but not in the general form appearing in the effective field theory of dark energy which is $\mathcal{N}(\pi, \partial_\tau\pi, \partial_x\pi, \partial_x^2\pi)$. In fact the important remark is that for large speeds of sound and using the fact that π, $\partial_\tau\pi$ and $\partial_x\pi$ are small, the dominant term in the dynamics would be the linear part of the PDE, whereas in the limit $c_s^2 \to 0$ the term $c_s^2\partial_x^2\pi$ is removed and we end up with a non-linear PDE.

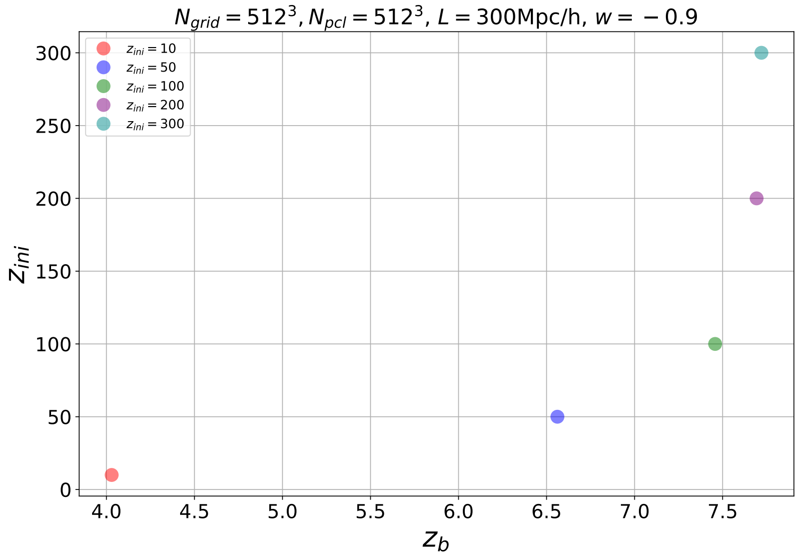

Figure 5.7: The initial redshift of the simulation versus the blow up redshift is plotted. If we start the simulation at higher redshifts the blowup redshift converges.

5.4.2 Simplified PDE

The numerical results in Fig. 5.4 show that the system in 3+1 D blows up for the cases with low speed of sound. To study the system analytically, in order to show that the instability is not a result of numerical imprecisions, we make some assumptions: first, we limit ourself to 1+1 D; second, we study the small sound speed limit and we set $c_s^2 = 0$, which is the case for which we see the instability in higher dimensions. The full equation for the scalar field then reads,

$$\begin{aligned}
&\partial_\tau^2\pi + \mathcal{H}(1-3w)\partial_\tau\pi + (\partial_\tau\mathcal{H} - 3w\mathcal{H}^2)\pi - \partial_\tau\Psi + 3w\mathcal{H}\Psi \\
&- 2\partial_x\partial_\tau\pi\partial_x\pi - (\mathcal{H} - \frac{3w\mathcal{H}}{2})\partial_x\pi\partial_x\pi + \partial_x\Psi\partial_x\pi - (\partial_\tau\pi + \mathcal{H}\pi - \Psi)\partial_x^2\pi \qquad (5.10) \\
&+ \frac{3}{2}\partial_x\pi\partial_x\pi\partial_x^2\pi = 0
\end{aligned}$$

where the fields are in general functions of the time and position i.e. $\pi \equiv \pi(\tau, x)$. We assume $\pi(\tau, x) = 0$ and $\zeta(\tau, x) = 0$ at the initial time τ_i similar to the 3+1 D case. According to the Eq. 5.1 this implies that $d\pi(\tau_i, x)/d\tau = \Psi(x)$ where $\Psi(x)$ is the gravitational potential at initial time τ_i. We further simplify the equation by considering it for the case matter domination, where the scale factor scales as $a \sim \tau^{\frac{-1}{3}}$, the Hubble function is $\mathcal{H} = 2/\tau$ and $\partial_\tau\Psi = 0$.

The Eq. 5.8 is still mathematically difficult to solve as there are different non-linear contributions to the equation. However, our numerical results for the 3+1 D case in the cosmological context show that the most important non-linear term in this PDE is $(\nabla\pi)^2$ or $\partial_x\pi\partial_x\pi$ in 1+1 D. Thus, in our analytic approach we focus on only one non-linear term in the PDE, which gives the equation,

$$\partial_\tau^2\pi + \mathcal{H}(1-3w)\partial_\tau\pi + (\partial_\tau\mathcal{H} - 3w\mathcal{H}^2)\pi + 3w\mathcal{H}\Psi - (\mathcal{H} - \frac{3w\mathcal{H}}{2})\partial_x\pi\partial_x\pi = 0 \tag{5.11}$$

The linear part of the previous equation is in fact a second order ODE which is easily solvable. In the next subsection, employing the solution of the second order ODE, we are going to use some coordinate and field transformations to further simplify the equation.

5.4.3 Simplification

Here we simplify the Eq. 5.11, mainly we aim to remove $\partial_\tau\pi$, π and constants from the equation. From now on, for the sake of simplicity, we denote the time derivatives with a dot and the spatial derivatives with a prime i.e.,

$$\dot{f} \equiv \partial_\tau f = \frac{df}{d\tau}, \qquad f' \equiv \partial_x f = \frac{df}{dx}. \tag{5.12}$$

First we write down the Eq. 5.11 in the following form,

$$\ddot{\pi} + \alpha(\tau)\dot{\tau}\pi + \beta(\tau)\pi + \lambda(\tau) = \gamma(\tau)(\pi')^2 \tag{5.13}$$

where we have used the following definitions,

$$\alpha(\tau) \equiv \mathcal{H}(1-3w),\ \beta \equiv (\dot{\mathcal{H}} - 3w\mathcal{H}^2),\ \lambda(\tau) \equiv 3w\mathcal{H}\Psi,\ \gamma(\tau) \equiv -(\mathcal{H} - \frac{3w\mathcal{H}}{2}). \tag{5.14}$$

Let $f(\tau) \neq 0$ solve the following 2nd order ODE:

$$\ddot{f} + \alpha(\tau)\dot{f} + \beta(\tau)f = 0 \tag{5.15}$$

then define

$$\pi(x,\tau) =: f(\tau)u(x,\tau)\,, \tag{5.16}$$

and substitute back into the Eq. 5.13 we obtain

$$\ddot{f}u + 2\dot{f}\partial_\tau u + f\partial_\tau^2 u \quad + \quad \alpha(\tau)(\dot{f}u + f\partial_\tau u) \quad + \quad \beta(\tau)fu + \lambda(\tau) = \gamma(\tau)f^2\,(u')^2 \tag{5.17}$$

Reordering the terms gives

$$f\ddot{u} + (2\dot{f} + \alpha(\tau)f)\dot{u} + (\ddot{f} + \alpha(\tau)\dot{f} + \beta(\tau)f)u + \lambda(\tau) = \gamma(\tau)f^2\,(u')^2 \tag{5.18}$$

the third term on the left is 0 according to Eq. 5.15, so we have,

$$\ddot{u}+\frac{2\dot{f}+\alpha(\tau)f}{f}\dot{u}+\lambda(\tau)=\gamma(\tau)f\left(u'\right)^2 \tag{5.19}$$

For simplicity, we define

$$\frac{2\dot{f}+\alpha(\tau)f}{f}=:p(\tau),\quad \gamma(\tau)f:=q(\tau) \tag{5.20}$$

and the equation reads,

$$\ddot{u}+p(\tau)\dot{u}+\lambda(\tau)=q(\tau)\left(u'\right)^2 \tag{5.21}$$

Changing the time variable and redefining the field as $u(\tau,x)=:v(x,s(\tau))$, and substituting in the previous equation gives,

$$\ddot{v}\dot{s}^2+\dot{v}\ddot{s}+p(\tau)\dot{v}\dot{s}+\lambda(\tau)=q(\tau)\left(v'\right)^2 \tag{5.22}$$

where $s(\tau)$ is determined by solving the following equation,

$$\ddot{s}(\tau)+p(\tau)\dot{s}(\tau)=0 \tag{5.23}$$

and we obtain

$$\dot{s}(\tau)=\exp\left(-\int_{\tau_{ini}}^{\tau}p(\sigma)d\sigma\right) \tag{5.24}$$

Substituting back the solution to the Eq. 5.22 we obtain

$$\ddot{v}(x,s)+\lambda(s(\tau))=q(\tau)\exp\left(2\int_{\tau_{ini}}^{\tau}p(\sigma)d\sigma\right)\left(v'\right)^2(x,s) \tag{5.25}$$

Solving τ from the equation $\dot{s}(\tau)=\exp\left(-\int_{\tau_{ini}}^{\tau}p(\sigma)d\tau\right)$, we get $\tau:=\tilde{\tau}(s)$ and therefore the right hand side of the above equation can be expressed in terms of s,

$$\begin{gathered}\ddot{v}(x,s)+\lambda(s(\tau))=\tilde{\gamma}(s)\left(v'\right)^2(x,s)\\ \text{where } \tilde{\gamma}(s):=q(\tilde{t}(s))\exp\left(2\int_{\tau_{ini}}^{\tilde{\tau}(s)}p(\sigma)d\sigma\right)\end{gathered} \tag{5.26}$$

For simplicity we use t instead of s as a time variable and we have the following simplified equation,

$$\ddot{v}(\tau,x)+\lambda(t)=\tilde{\gamma}(t)\left(v'\right)^2(\tau,x) \tag{5.27}$$

To get rid of $\lambda(t)$ term we will perform one more transformation as follows

$$\tilde{v}(\tau,x):=v(\tau,x)+r(t) \tag{5.28}$$

Substituting in to the equation gives,

$$\ddot{\tilde{v}}(\tau, x) + \ddot{r} + \lambda(t) = \tilde{\gamma}(t) \left(\tilde{v}'\right)^2 (\tau, x) \tag{5.29}$$

Solving $\ddot{r} + \lambda(t) = 0$ we obtain,

$$r(t) = c_1 + c_2 t - \int_{t_{ini}}^{t} \int_{t_{ini}}^{\sigma} \lambda(s)\, ds\, d\sigma \tag{5.30}$$

with $r(t)$ of this form and substituting in Eq. 5.27 results in,

$$\ddot{\tilde{v}}(\tau, x) = \tilde{\gamma}(t) \left(\tilde{v}'\right)^2 (\tau, x) \tag{5.31}$$

To this end we redefine $x \to \sqrt{\tilde{\gamma}}\, x$ to remove the $\tilde{\gamma}$ term, too. In the new time coordinate we will have the simplified equation,

$$\ddot{\tilde{v}}(\tau, x) = \left(\tilde{v}'\right)^2 (\tau, x) \tag{5.32}$$

From now on, instead of considering the full PDE Eq. 5.11, we focus on the following PDE with the initial conditions mentioned above. We remind the reader that the time and the scalar field in this equation are different from what we had in Eq. 5.11. However, the result presented in the following sections can be translated to solutions for the equations for $\pi(x, \tau)$.

We will solve the following PDE analytically in the next chapter,

$$\begin{aligned} &\partial_\tau^2 \pi(\tau, x) = \Big(\partial_x \pi(\tau, x)\Big)^2 \\ &\pi(0, x) = 0 \\ &\partial_\tau \pi(0, x) = \Phi(x) \end{aligned} \tag{5.33}$$

5.4.4 Solution to the simplified PDE

From now on we omit the arguments and we simply write π in the equation Eq. (5.33).

First of all, the most interesting property of Eq. 5.33 is that the minima and maxima of π do not move in space and stay at the same point in time which will be validated in the numerical results in 1+1 D in Sec. 5.4.7. To prove this we use the fact that an extremum at time t_*, means by definition that $\frac{d\pi}{dx}(\tau_*, x_s) = 0$, where x_s is the position of the extremum and τ_* is the time at which we have an extremum at x_s. Now we show that using the partial differential equation and the initial conditions, the extremum stays at the same position at all times τ, i.e. $\frac{d\pi}{dx}(\tau, x_s) = 0$.

We define $D(\tau, x) \equiv \frac{d\pi}{dx}(\tau, x)$ where according to the initial condition we know $\pi(0, x) = 0$ so $D(0, x) = 0$. Taking the spatial derivative of the PDE (Eq. 5.33), we obtain,

$$\begin{aligned} &\partial_\tau^2 \pi(\tau, x) = D(\tau, x)^2 \\ &\frac{d}{d\tau^2}\frac{d\pi}{dx}(\tau, x) = 2D(\tau, x)\frac{dD}{dx}(\tau, x), \\ &\frac{d^2 D}{d\tau^2}(\tau, x) = 2D(\tau, x)\frac{dD}{dx}(\tau, x), \end{aligned} \tag{5.34}$$

since $D(0, x) = 0$ it also implies that $\frac{dD(\tau,x)}{d\tau^2}(0, x) = 0$. On the other hand we have

$$\frac{dD(\tau, x)}{d\tau}(0, x) = \frac{d}{dx}\frac{d\pi}{d\tau}(0, x) = \frac{d\Phi}{dx}(x) \tag{5.35}$$

Let's take x_s such that $\frac{d\Phi}{dx}(x_s) = 0$ meaning that x_s is a stationary point of the initial function D. We write the Eq. 5.34 for the point x_s as follows,

$$\frac{d^2 D}{d\tau^2}(\tau, x_s) = 2D(\tau, x_s)\frac{dD}{dx}(\tau, x_s) \tag{5.36}$$

The previous equation is an ODE for the evolution of the spatial derivative of π in time. Defining $a(t) = D(\tau, x_s)$ and $b(t) = \frac{dD}{dx}(\tau, x_s)$, we can rewrite the ODE as following

$$\ddot{a}(t) = 2\, a(t) b(t). \tag{5.37}$$

The initial conditions are,

$$\begin{aligned} a(0) &= D(0, x_s) = 0 \qquad (5.38) \\ \dot{a}(0) &= \frac{dD}{d\tau}(0, x_s) = 0 \\ \ddot{a}(0) &= 0. \end{aligned}$$

The initial conditions imply that $a(t) = D(t, x_s) = 0$, i.e., at all times the spatial derivative of the point remains 0. So the extrema remain at the same position in time.

Paying attention to the extrema in the Φ function one can approximately expand the scalar field π around the minima and maxima as a quadratic function,

$$\pi(\tau, x) = \kappa(\tau)(x - x_s)^2 \tag{5.39}$$

where κ can have either signs. It is interesting to see that first of all the quadratic function is a solution of the PDE and the quadratic shape is preserved during the evolution. We can use this property to obtain an ODE out of the PDE for the evolution of the curvature of the minima and maxima. Using the ansatz (5.39) in the equation (5.33) we obtain,

$$\kappa''(\tau) = 4\kappa(\tau)^2 \tag{5.40}$$

where 2κ is the second derivative at minima and maxima and the previous equation gives us the evolution for the curvature. The initial condition for the equation is obtained using the initial condition for the PDE.

$$\begin{aligned} &\pi(0,x) = 0 \longrightarrow a(0) = 0 \qquad (5.41)\\ &\frac{d}{d\tau}\frac{d^2\pi}{dx^2}(0,x_s) = \frac{d^2\Phi}{dx^2}(x_s) \longrightarrow \dot{a}(0) = \frac{1}{2}\frac{d^2\Phi}{dx^2}(x_s) \end{aligned}$$

To solve Eq. 5.40 we first multiply both sides by $\kappa'(\tau)$,

$$\frac{1}{2}\frac{d(\kappa'(\tau)^2)}{d\tau} = \frac{4}{3}\frac{d(\kappa(\tau)^3)}{d\tau} \tag{5.42}$$

Integrating results in,

$$\kappa'(\tau)^2 = \kappa'(0)^2 + \frac{8}{3}\kappa(\tau)^3 - \frac{8}{3}\kappa(0)^3 \tag{5.43}$$

On the other hand, for the minima, i.e., $\kappa_{ini} > 0$ the integral reads,

$$\int_{\kappa(0)=\kappa_{ini}}^{-\infty} \frac{d\kappa}{\sqrt{\kappa'(0)^2 + \frac{8}{3}\kappa(\tau)^3}} = \int_0^{\tau_b} d\tau \tag{5.44}$$

To compute the integral we define $s = \frac{8}{3\kappa'(0)^2}\kappa$ so we have,

$$\tau_b = \frac{1}{\sqrt{\kappa'(0)^2}}.\left(\frac{3}{8}\kappa'(0)^2\right)^{\frac{1}{3}} \int_{\kappa(0)=\kappa_{ini}}^{\infty} \frac{ds}{\sqrt{1+s^3}} \tag{5.45}$$

For the case where $\kappa_{ini} = \epsilon$ where ϵ is very small, the curvature of the minimum point increases and blows up with the time given by,

$$\tau_b = \frac{1}{|\kappa'(0)^2|}.\left(\frac{3}{8}\kappa'(0)^2\right)^{\frac{1}{3}} 2.8043. \tag{5.46}$$

where we have used $\int_{\kappa(0)=0}^{\infty} \frac{ds}{\sqrt{1+s^3}} \approx 2.8043$ and $\kappa'(0) = \frac{1}{2}\frac{d^2\Phi}{dx^2}$. So the minima according to the PDE blow up at a finite time given by the Eq. 5.45 which depends on the initial curvature of the point.

5.4.5 An example

We consider the Cauchy problem for $x \in \mathbb{R}$ and $t \geq 0$ given by

$$\begin{aligned} \ddot{\pi}(\tau, x) &= (\pi'(\tau, x))^2 \\ \pi(\tau_0, x) &= 0 \\ \dot{\pi}(\tau_0, x) &= 1 - \cos(\pi x) = \tfrac{1}{2}\pi^2 x^2 - \tfrac{1}{24}\pi^4 x^4 + \dots \end{aligned} \tag{5.47}$$

where we have taken a cos function as the initial condition. The first term in the Taylor expansion of the cos function is a quadratic term which we discussed it in the previous subsection, now we want to comment about the higher order contributions. We first discuss the behavior of the solution near $x = 0$. Taking derivatives of the Eq. 5.47 results in the following equations,

$$\begin{aligned} \ddot{\pi}'(\tau, x) &= 2\pi'(\tau, x)\pi''(\tau, x), \\ \ddot{\pi}''(\tau, x) &= 2\pi'(\tau, x)\pi'''(\tau, x) + 2\pi''(\tau, x)\pi''(\tau, x), \\ \ddot{\pi}'''(\tau, x) &= 2\pi'(\tau, x)\pi^{(4)}(\tau, x) + 6\pi''(\tau, x)\pi'''(\tau, x), \\ \ddot{\pi}^{(4)}(\tau, x) &= 2\pi'(\tau, x)\pi^{(5)}(\tau, x) + 8\pi''(\tau, x)\pi^{(4)}(\tau, x) + 6\pi'''(\tau, x)^2. \end{aligned} \tag{5.48}$$

Now let $a(\tau) = \pi'(0, \tau), b(\tau) = \pi''(0, \tau), c(\tau) = \pi'''(0, \tau), d(\tau) = \pi^{(4)}(0, \tau)$. Then we have

$$\begin{aligned} \ddot{a} &= 2ab \\ \ddot{b} &= 2ac + 2b^2 \\ \ddot{c} &= 2ad + 6bc \\ \ddot{d} &= 2a\pi^{(5)}(0, \tau) + 8bd + 6c^2 \end{aligned} \tag{5.49}$$

since $a(0) = \dot{a}(0) = 0$ for our initial data the solution of Eq. 5.49 is $a(\tau) = 0$ as long as b is well defined. This means in particular that $x = 0$ remains a critical point at all times. The equations therefore reduce to;

$$\begin{aligned} \ddot{b} &= 2b^2, \\ \ddot{c} &= 6bc, \\ \ddot{d} &= 8bd + 6c^2, \end{aligned} \tag{5.50}$$

since $c(0) = \dot{c}(0) = 0$ therefore we have $c(\tau) = 0$, so that the equations reduce to

$$\ddot{b} = 2b^2, \tag{5.51}$$

$$\ddot{d} = 8bd \tag{5.52}$$

and the expansion of π at $x = 0$ reduces to

$$\pi(\tau, x) = b(\tau)\frac{x^2}{2} + d(\tau)\frac{x^4}{4!} + \dots \tag{5.53}$$

in particular since $b(0) = 0, \dot{b}(0) = \pi^2$ we see from Eq. 5.50 that $b(\tau)$ is always positive so that $x = 0$ remains a minimum.

To analyze the behavior of $b(t)$ in more details we note that the equation for b is the Newton equation for a mass-point of mass one in the potential $V(b) = -\frac{2}{3}b^3$. The total energy defined as below is invariant under the time evolution.

$$E = \frac{1}{2}\dot{b}^2 - \frac{2}{3}b^3. \tag{5.54}$$

Based on our initial condition we have $E = \frac{1}{2}\dot{b}(0)^2 - \frac{2}{3}b(0)^3 = \frac{1}{2}\phi''(0)^2 - \frac{2}{3}\psi''(0)^3 = \frac{1}{2}\pi^4$. From Eq. 5.54 we obtain

$$\begin{aligned}\tau &= \int_{b(0)}^{b(\tau)} \frac{d\beta}{\sqrt{\frac{4}{3}\beta^3 + 2E}} \leq \int_0^{\infty} \frac{d\beta}{\sqrt{\frac{4}{3}\beta^3 + 2E}} \\ &= \frac{1}{2^{\frac{5}{6}}3^{\frac{2}{3}}} B\left(\frac{1}{6}, \frac{1}{3}\right)\frac{1}{E^{\frac{1}{6}}} = 1.187831729448194321\dots =: \tau_b\end{aligned} \tag{5.55}$$

This means that the mass-point disappears in finite time at infinity, i.e., $b(\tau)$ blows up as t approaches τ_b. More precisely, as τ approaches τ_b

$$\tau_b - \tau = \int_{b(\tau)}^{\infty} \frac{d\beta}{\sqrt{\frac{4}{3}\beta^3 + 2E}} = \int_{b(\tau)}^{\infty} \frac{1}{\sqrt{\frac{4}{3}\beta^3}}\left(1 + \frac{2E}{\frac{4}{3}\beta^3}\right)^{-\frac{1}{2}} d\beta = \frac{\sqrt{3}}{\sqrt{b(\tau)}} + E\mathcal{O}\left(\frac{1}{b(\tau)^{\frac{7}{2}}}\right) \tag{5.56}$$

from which one gets, as τ approaches τ_b

$$\frac{3}{(\tau_b - \tau)^2} = b(\tau) + E\ \mathcal{O}\left(\frac{1}{b(\tau)^2}\right) \tag{5.57}$$

and therefore as τ approaches τ_b

$$b(\tau) = \frac{3}{(\tau_b - \tau)^2} + E\ \mathcal{O}\left((\tau_b - \tau)^4\right) \tag{5.58}$$

We now discuss the solution of the Eq. 5.52, since $b(\tau)$ blows up at $\tau = \tau_b$, $d(\tau)$ blows up as well, and substituting Eq. 5.58 to the Eq. 5.52 and solving the new ODE, one gets asymptotically as τ approaches τ_b

$$d(\tau) = \frac{\text{const.}}{(\tau_b - \tau)^{2\beta+2}} + \dots E\ \mathcal{O}\left((\tau_b - \tau)^9\right) \tag{5.59}$$

for some constants depending on the initial condition. The constant is negative if $d(0) \leq 0$ and $\dot{d}(0) < 0$ which are the cases we considered and is positive if $d(0) \geq 0$ and $d(0) \geq 0$. The index β is given by,

$$\beta = \frac{-5 + \sqrt{97}}{4} = 1.212214450449\ldots \tag{5.60}$$

Similar blowup rates can be computed for higher order space derivatives which leads to the conjecture that as τ approaches τ_b

$$\pi(\tau, x) = (\tau_b - \tau)^{2\beta-2} f\left(\frac{x}{(\tau_b - \tau)^{\beta}}\right) + u_0(\tau, x)) \tag{5.61}$$

5.4.6 Spherically symmetric case

It's also interesting to note that the equation in 3+1 dimension with spherical symmetry is the same as the equation in 1+1D as

$$\vec{\nabla}\pi.\vec{\nabla}\pi \to \left(\frac{\partial\pi}{\partial r}\right)^2 \tag{5.62}$$

and the PDE reads,

$$\partial_\tau^2\pi(\tau, r) = \left(\frac{\partial\pi}{\partial r}\right)^2 \tag{5.63}$$

So similar to the 1+1 D case the minima blow up at finite time given by Eq. 5.46 and $\kappa'(0) = \frac{1}{4}\frac{\partial^2\Phi}{\partial r^2}(r_{min})$.

If we consider non-zero c_s^2 the wave term also appears in the equation and according to the ∇^2 in the Spherical coordinate we obtain the following equation,

$$\ddot{\pi}(\tau, r) = \left(\frac{\partial\pi(\tau, r)}{\partial r}\right)^2 + c_s^2\frac{1}{r}\frac{\partial^2}{\partial r^2}(r\pi(\tau, r)) \tag{5.64}$$

$$\ddot{\pi}(\tau, r) = \left(\frac{\partial\pi(\tau, r)}{\partial r}\right)^2 + c_s^2\left(\frac{\partial^2\pi(\tau, r)}{\partial r^2}\right) + \frac{2c_s^2}{r}\left(\frac{\partial\pi(\tau, r)}{\partial r}\right) \tag{5.65}$$

5.4.7 Numerical studies in 1+1 D

In this subsection we aim to solve the PDEs numerically on the lattice in 1+1 D and to compare with the analytical results we have obtained in the previous sections and the results in 3+1 D in the cosmological contexts. Here we also comment on the terms that could prevent the system from blowing up for large speeds of sound.

The first equation that we solve numerically is the following equation, which we have shown to blow up at the local minima and local maxima,

$$\begin{aligned}&\partial_\tau^2\pi(\tau,x)=\Big(\partial_x\pi(\tau,x)\Big)^2\\&\pi(0,x)=0\\&\frac{d\pi}{d\tau}(0,x)=\Phi(x)\end{aligned}\tag{5.66}$$

We take $\Phi(x)=\cos(\frac{4\pi x}{L})$ where $N_{grid}=2048$ is the number of points and $dx=1$ is distance between the points on the 1D lattice. First of all the curvature at the minimum point is given by $\frac{16\pi^2}{L^2}=0.000037$, by solving the following integral we obtain the blowup time according to our analytical expression in Eq. 5.45,

$$\tau_b=\frac{1}{\sqrt{\kappa'(0)^2}}.\left(\frac{3}{8}\kappa'(0)^2\right)^{\frac{1}{3}}\int_{0.000037}^{\infty}\frac{ds}{\sqrt{1+s^3}}=\frac{1}{\sqrt{\kappa'(0)^2}}.\left(\frac{3}{8}\kappa'(0)^2\right)^{\frac{1}{3}}.2.80433\tag{5.67}$$

Substituting $\kappa'(0)=\frac{1}{2}\frac{\partial^2\Phi}{\partial x^2}=1.88\times10^{-5}$, the blowup time reads,

$$\tau_b=76.0202\tag{5.68}$$

In Fig. 5.8 we show the numerical results for the scalar field π and it's first and second time derivative in the top panel and it's spatial derivative in the bottom panel. This figure verifies our claims of the previous subsections; i.e. the extrema do not move in time and are fixed at a position, the curvature of the maxima and minima increases and the maxima become flatter while the minima become sharper and blow up at some point. Moreover paying attention to the $\partial_x\pi$ in the middle part of the bottom panel of the figure one realizes that this function shares similar behavior with caustic singularities Arkani-Hamed et al. [2007], Babichev [2016] which comes from the fact that to leading order according to the Eq. 5.6 the velocity v_x is $\partial_x\pi$ in 1+1 D and the maxima and minima travel toward each other to form a caustic in a finite time. To verify our analytical results, we compare the blowup time obtained from the solution of the ODE with the numerical solution from the PDE at the minimum point in Fig. 5.9. According to the figure our theoretical solution and the numerical results agree very well.

For the sake of completeness, we also simulate the full PDE written in 5.10 for the case when $c_s^2=1$, to show that the linear term $c_s^2\nabla^2\pi$ can change the behavior of the system from a divergent to the stable one. In fig. 5.10 we show the numerical results for the scalar field and its time and spatial derivative in, respectively, the top and bottom panels. According to these figures the system for large speeds of sound in 1+1 D is similar to the 3+1 D case which is stable. In Fig. 5.11 we show the evolution of the curvature at the minimum. According to this figure the curvature eventually, after a period of increase, decays and there are no signs of the instability.

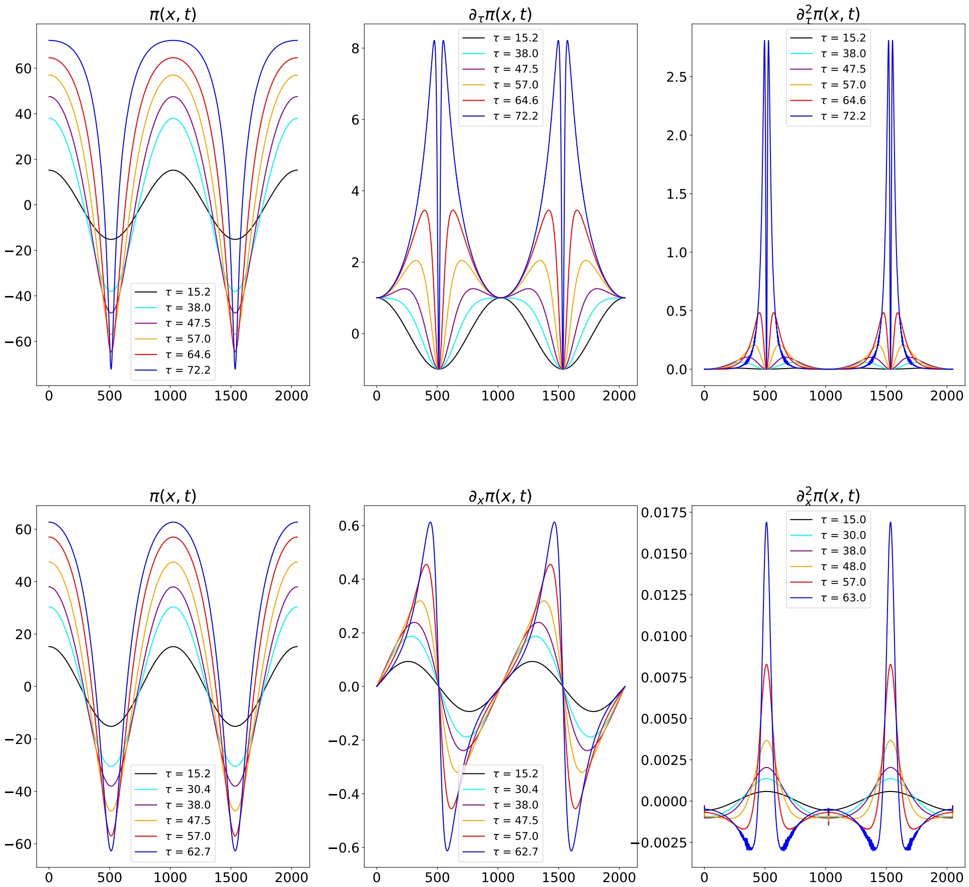

Figure 5.8: ***Top***: The scalar field and its time derivatives on the 1+1 D lattice at different times for a cos function as an initial condition are shown. Analytically the curvature of the scalar field at the minimum blows up at time $\tau_b \approx 76$.
Bottom: The scalar field and its spatial derivative on the lattice for different times are shown. Due to the numerical noises appearing in the second order spatial derivative we only show the results up to $\tau = 62.7$. It is also interesting to see that $\partial_x \pi$ behaves similar to a gradient catastrophe that one would see in some situations in the fluid dynamics.

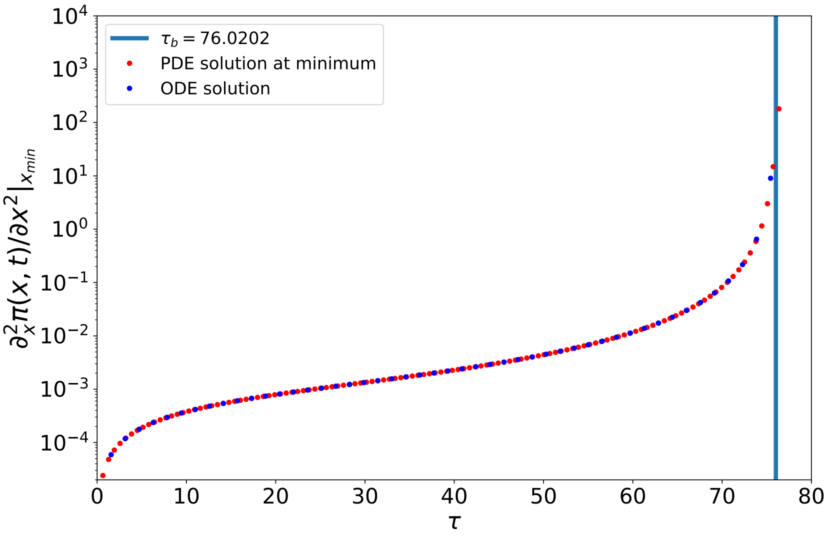

Figure 5.9: The evolution of the curvature of the minimum in time according to the Eq. 5.33. According to the figure the solution of the ODE, the analytical solution in (5.46) and the curvature evolution obtained from the solution of the PDE are consistent.

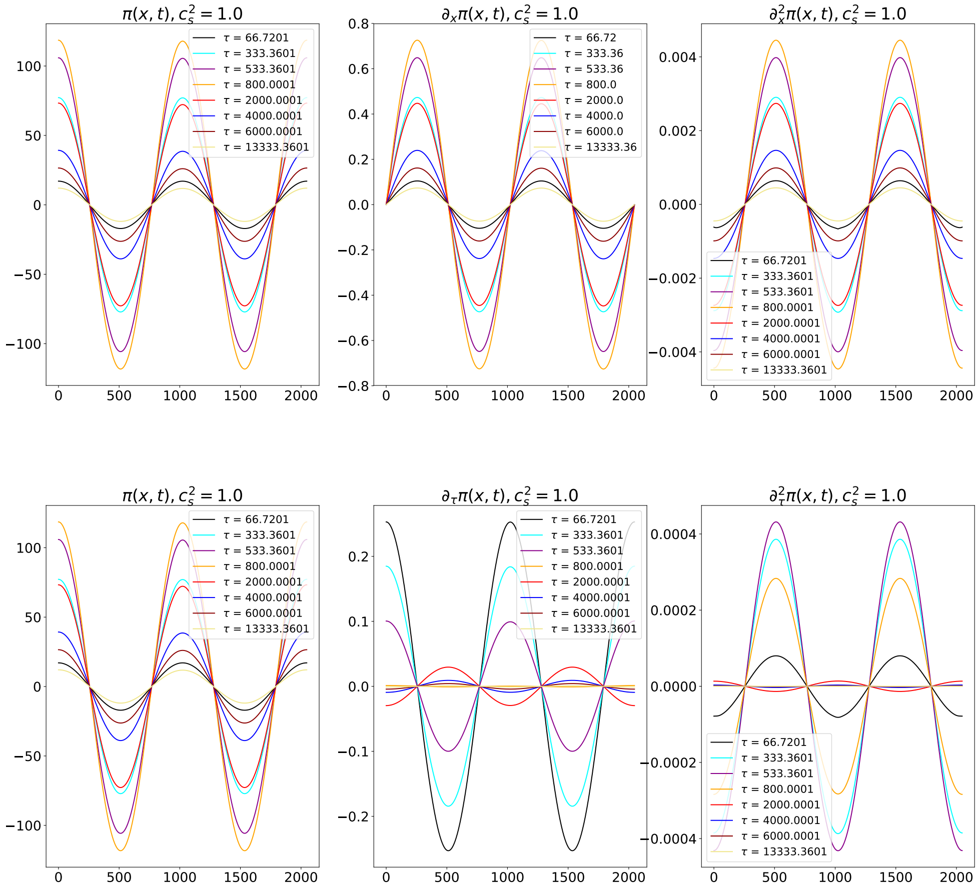

Figure 5.10: Similar to the Fig. 5.9 but for when the full PDE in 1+1 D for $c_s^2 = 1$ is solved. According to this figure for the large value of c_s^2 the system is stabilized.

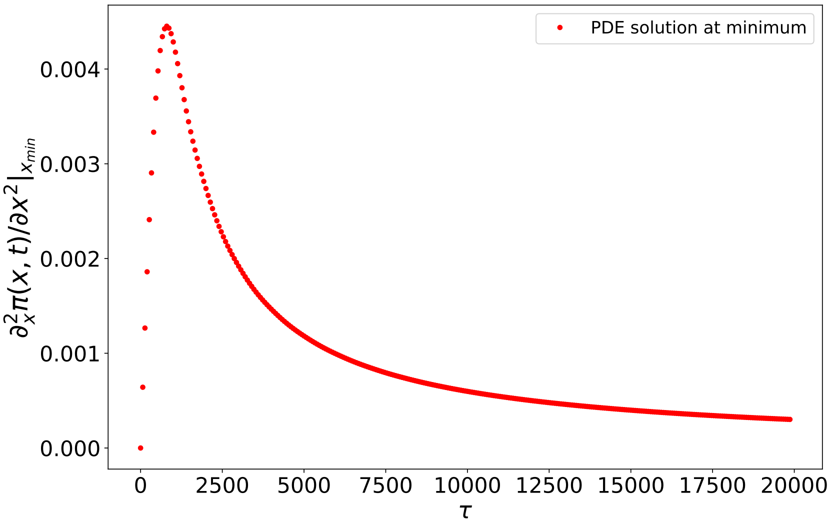

Figure 5.11: The evolution of the curvature at the minimum point according to the numerical solution to the full PDE. The curvature at the minima reach a maximum and then decreases.

APPENDIX

5.A Linear equation

Neglecting the non-linear terms, the differential equation for the low speed of sound is stable. In the following, we find the linear analytic solution in 1+1 D in matter domination. For this we assume $w = -1$, and the solution for a general w can also be obtained in a simple way. Taking $w = -1$, we can write the linear part as,

$$\partial_\tau^2 \pi(\tau, x) + \frac{8}{\tau} \partial_\tau \pi(\tau, x) + \frac{10}{\tau^2} \pi(\tau, x) = \frac{6}{\tau} \Psi(x). \tag{5.69}$$

According to the existence and uniqueness theorem for second order differential equations, we have a unique solution for the ODE for $\tau > 0$.
The two fundamental solutions of the equation are $\pi_1 = \frac{A}{\tau}$ and $\pi_2 = \frac{B}{\tau^2}$ and the Wronskian reads $W(\pi_1, \pi_2) = \pi_1 \partial_\tau \pi_2 - \pi_2 \partial_\tau \pi_1 = -\frac{AB}{\tau^4}$. The particular solution of the equation is obtained,

$$\pi_p(\tau) = -\pi_1(\tau) \int \frac{\pi_2(\tau) f(\tau)}{W(\pi_1, \pi_2)} d\tau + \pi_2(\tau) \int \frac{\pi_1(\tau) f(\tau)}{W(\pi_1, \pi_2)} d\tau \tag{5.70}$$

where $f(\tau) = \frac{3}{\tau} \Psi(x)$. Computing the integral results in the following particular solution $\pi_p(\tau)$,

$$\pi_p(\tau) = \frac{\Psi \tau}{2} \tag{5.71}$$

As a result, the full solution to the equation reads,

$$\pi(x, \tau) = \frac{A}{\tau} + \frac{B}{\tau^2} + \frac{\Psi(x)\tau}{2}. \tag{5.72}$$

Here A and B are defined from the initial condition at τ_{ini}. However, the linear part of the equation does not change the shape of the scalar field and rescales the initial function as it is only time dependent.

Chapter 6

THE DETECTION OF RELATIVISTIC CORRECTIONS IN COSMOLOGICAL N-BODY SIMULATIONS

Based on:
Eckmann & Hassani [2019] Jean-Pierre Eckmann, Farbod Hassani *The detection of relativistic corrections in cosmological N-body simulations*, Celestial Mechanics and Dynamical Astronomy volume 132, Article number: 2 (2020), [arXiv: 1909.04652]

Abstract: Cosmological N-body simulations are done on massively parallel computers. This necessitates the use of simple time integrators, and, additionally, of mesh-grid approximations of the potentials. Recently, Adamek et al. [2016b], Barrera-Hinojosa & Li [2020] have developed general relativistic N-body simulations to capture relativistic effects mainly for cosmological purposes. We therefore ask whether, with the available technology, relativistic effects like perihelion advance can be detected numerically to a relevant precision. We first study the spurious perihelion shift in the Kepler problem, as a function of the integration method used, and then as a function of an additional interpolation of forces on a 2-dimensional lattice. This is done for several choices of eccentricities and semi-major axes. Using these results, we can predict which precisions and lattice constants allow for a detection of the relativistic perihelion advancein N-body simulation. We find that there are only small windows of parameters—such as eccentricity, distance from the central object and the Schwarzschild radius—for which the corrections can be detected in the numerics.

6.1 Introduction

We consider here so-called (cosmological) N-body simulations such as [Adamek et al., 2016a, Springel, 2005, Teyssier, 2002a]. In these numerical studies, potentials between the (many) particles are computed on a lattice (mesh-grid) because of the way such calculations are implemented on supercomputers. Additionally, some of these projects (such as Adamek et al. [2016b], Barrera-Hinojosa & Li [2020]) add relativistic corrections to the forces and therefore to the trajectories of particles. The aim of our study is to give bounds on the detectability of these effects, given the computational restrictions of these large-scale projects. We will see that in many current simulations, the necessary precision to detect relativistic effects on the orbits of particles can simply not be achieved.

It is of course not difficult to devise codes which will compute the perihelion advance under relativistic corrections to arbitrary high precision. It is not the aim of our paper to study such algorithms, but rather, to see how well the integration algorithms work in the N-body simulations. In these simulations, because one considers essentially a gas of many particles, the user is restricted to rather standard integration methods, which just use the differential equations, but necessarily can not make use of the many invariants known for the (non-relativistic) Kepler problem, see *e.g.*, [Preto & Saha, 2009]. Therefore, we need to first study the performance of standard integration schemes, such as Euler, Runge-Kutta, and Leap-Frog, because these are the methods which are widely used. We will see that only with very high precision one is able to detect the (usually quite small) relativistic corrections. Once this has been done, we can turn our attention to the effects of the discretizations (of space), which give then bounds on the necessary grid constants for which relativistic effects could be detected. We will determine parameter regions where the relativistic effects can be detected, and show that, most often, these regions are quite small.

By starting with the simple Kepler problem, in [2], we can concentrate on the different numerical effects in a systematic and clean way. Even so, the reader should realize that there are several quantities to be considered. The first is the numerical precision of the time integrator. We study it here in the context of the subroutines in ODEX [Hairer et al., 1993], and we also compare it to other methods, such as Euler, leapfrog (Verlet-Störmer) [Hairer et al., 2003] or Runge-Kutta with fixed time step.

To do this, we quantify the numerical errors on trajectories of particles revolving around a central object. This will allow us to give conditions which ascertain which orbits in a specific N-body simulation are precise enough to be able to measure the general relativistic perihelion[1] shift.

After this, we consider the particle-mesh N-body scheme, as is widely used, see *e.g.*, [Adamek et al., 2016a, Springel, 2005]. In it, forces (coming from fields and potentials) are discretized and represented on a lattice. Such elements [Arnold, 2002] are then used to compute the values of the fields at the particles' positions.

The force interpolation approximations are usually piecewise differentiable, and, depending on the implementations mentioned above, use different elements. It is clear that if the mesh size of the approximation (of the force) goes to 0, so will the error. But the relevant question here is to quantify what kind of phenomena can be captured, given the numerous hardware and modeling constraints.

Particle-mesh N-body simulations are used to study the evolution of particles under gravity. These codes can be used to study systems at different scales, from cosmological scales to the size of the solar system, as the methods and forces are appropriate for all scales. In the particle-mesh N-body scheme [Adamek et al., 2016a, Springel, 2005], space-discretizations are performed to take care of the large number of particles. We analyze two common force interpolations which are used for N-body simulations purposes, namely the so-called linear and bilinear methods, which respectively correspond to first and second order interpolation. We will see that, under conditions to be specified, the effect of spatial discretization can be quite large and sometimes depends on the angle θ between the direction of the perihelion and the axes of the discrete lattice. This happens when the discretization produces discontinuous forces, *i.e.,* for the first order force interpolation. In this case the maximal errors are proportional to the lattice constant dx. On the other hand, in the second order force interpolation, when one varies θ, there is a small perihelion shift, fluctuating around 0. These fluctuations are seen to be of order $dx^{1.3}$. Due to the highly nonlinear step size of ODEX, we are not able to derive analytically this size of the fluctuations.

---

[1] We use "perihelion" even if the central mass is not the sun.

Our numerical tests show that, unless the discretization is extremely fine, the system will show an uncertainty of the perihelion, for the Kepler problem, for both force interpolation methods. Our calculations give limits on the detectability of relativistic effects, as a function of method, lattice spacing, as well as eccentricity and the relativistic parameter $\Upsilon \equiv r_{\mathrm{sch}}/r_{\mathrm{per}}$, the ratio of perihelion distance of the orbit r_{per} and the Schwarzschild radius of the central mass r_{sch}.

6.2 Using standard time integrators

Our main interest is the detectability of general relativistic effects in N-body simulations, and in particular the study of discretization effects. But we first need to be sure that the time integration which is used in these projects does not already destroy the precision of the result more than the effect of the space discretization. This is the subject of this section.

A Hamiltonian problem can be integrated either as a motion in Euclidean space, or one can exploit the underlying symplectic structure of the problem. Of course, there are very good symplectic integrators, [Hairer et al., 2010], but we decided not to use them, for two reasons.

The first is that in the particle-mesh N-body codes, the Euclidean approach is used to solve the system including particles and the fields on the lattice coordinates and expressing the system in symplectic coordinates is difficult. Second, as noted in [Hairer et al., 2003] even the symplectic methods do not preserve the Runge-Lenz-Pauli vector (the orientation of the semi-major axis). This means that because of our focus on the relativistic perihelion advance, the symplectic integrators present no particular advantage. So we will stick with the classical high-order Runge-Kutta integrators ODEX [Hairer et al., 1993]. Because it allows for “continuous output” we can use it to determine easily the advance of the perihelion with high precision.

We summarize those properties of ODEX which are relevant for our study. As we will be working with elements to interpolate forces, we need to explain how the algorithm deals with discontinuities. This is illustrated in [Hairer et al., 1993, Chapter II.9 and in particular, Fig. 9.6]. In the interior of a plaquette, the algorithm chooses a high enough order to reach the required tolerance with a large time step h. On approaching the singularity, the algorithm lowers the order (to 4) but decreases h. In fact, the jump is approximated by a polynomial of degree 4, and this defines something like a new initial condition across the discontinuity. In the case of Runge-Kutta with fixed time step, the paper [Back, 2005] shows that there is a mean systematic error across the jump, which can be viewed as a weighted combination of evaluations of the vector field across the singularity.

6.3 Perihelion variation for time integrators with fixed time step

Here, we study the precision of perihelion calculations when working with *exact* forces. In later sections, we will then see how the grid discretization further affects this precision. Certainly, if we want to discriminate between non-relativistic and relativistic effects, already the integration with exact forces needs to be precise enough. This will force us to choose a small enough time step h.

We analyze the perihelion shift for several standard time integrators with fixed time step, namely Euler, Newton-Störmer-Verlet-leapfrog, 2nd order and 4th order Runge-Kutta.

We call the time step h and we solve the Kepler problem in the form[2]

$$\ddot{x}(t) = F(t, x)/m \ , \tag{6.1}$$

with x, v, and F in ^{2} and m the mass of the object. For the convenience of the reader, we spell out these well-known methods.

Euler method In this case, we solve (6.1) in the form

$$\begin{aligned} v_{n+1} &= v_n + a_n h \ , \\ x_{\mathrm{n+1}} &= x_n + v_{n+1} h \ , \end{aligned}$$

where v_n is the velocity vector at time step (n) which is defined as $v_n \equiv (x_n - x_{n-1})/h$ and a_n is the acceleration and is defined as the ratio of the force and mass $a_n \equiv a(t_n, x_n) = F(t_n, x_n)/m$. It is well-known that this implicit/backward Euler method is more stable than the explicit/forward Euler method. But it is somewhat more difficult to implement for non-linear differential equations.

Newton-Störmer-Verlet-leapfrog method For this widely used method (sometimes called "kick-drift-kick" form of leap-frog) [Hairer et al., 2003][Eq. 1.5], the updates are

$$\begin{aligned} v_{n+1/2} &= v_n + a_n \frac{h}{2} \ , \\ x_{n+1} &= x_n + v_{n+\frac{1}{2}} h \ , \\ v_{n+1} &= v_{n+\frac{1}{2}} + a_{n+1} \frac{h}{2} \ . \end{aligned}$$

This method is used more often as it is a symplectic method and stable and is shown to work very well for various stiff ODEs [Hairer et al., 2003].

---

[2] All positions, velocities, and the like are in ^{2}.

Second order Runge-Kutta method Finally, we will comment on the perihelion advance for the 2nd and 4th order Runge-Kutta methods (with fixed time step h). The Kepler problem using 2nd order Runge-Kutta algorithm—also known as midpoint method—reads,

$$\begin{aligned} k_x^{(1)} &= v_n \ , \\ k_v^{(1)} &= a_n \ , \\ k_x^{(2)} &= v_{n+\frac{1}{2}} \ , \\ k_v^{(2)} &= a_{n+\frac{1}{2}} \ , \\ x_{n+1} &= x_n + k_x^{(2)} h \ , \\ v_{n+1} &= v_n + k_v^{(2)} h \ , \end{aligned}$$

where $k_x^{(1)}$ is the estimate of velocity (derivative of x) in time step n, $k_v^{(1)}$ is the estimate of acceleration (derivative of v) in time step n and the same for $k_x^{(2)}$ and $k_v^{(2)}$. The acceleration at time $n+\frac{1}{2}$ is obtained by

$$a_{n+\frac{1}{2}} \equiv \frac{F(t_{n+\frac{1}{2}}, x_{n+\frac{1}{2}})}{m} = \frac{F\Big(t_{n+\frac{1}{2}}, x_n + k_x^{(1)} h/2\Big)}{m} \ .$$

Also, to obtain the velocity at time $n+\frac{1}{2}$ we need to use $k_v^{(1)}$. The corresponding tableau for the second order Runge-Kutta method for each first order differential equation is

$$\begin{array}{c|cc} 0 & & \\ 1/2 & 1/2 & \\ \hline & 0 & 1 \end{array} \ .$$

Fourth order Runge-Kutta method The Kepler problem using forth order Runge-Kutta method is basically the same as second order Runge-Kutta, but with three points instead of one point in between to solve the position and velocity. The tableau we use for this method is [Butcher, 1963]

$$\begin{array}{c|cccc} 0 & & & & \\ 1/2 & 1/2 & & & \\ 1/2 & 0 & 1/2 & & \\ 1 & 0 & 0 & 1 & \\ \hline & 1/6 & 1/3 & 1/3 & 1/6 \end{array} .$$

6.3.1 Results for various integration schemes

We solve the Kepler problem with the methods described above and find the perihelion variation for different time steps h. To determine the perihelion point of the orbit we choose several points near the minimum distance to the central object after each revolution. Then we fit a parabola (for Runge-Kutta, we take a 4th order polynomial to find the point closest to the central mass) and the minimum of the parabola is taken as the perihelion point. Fig. 6.1 illustrates how this is done, for the particular example of Mercury. The red point is the perihelion. The spurious shift of the perihelion of Mercury using 2nd order Runge-Kutta method with $h = 0.00625$, which is the case considered in Fig. 6.1, is $\sim 7.8 \times 10^{-5}$ radians. We measure the positions in units Giga meters (Gm $\equiv 10^9$ m) , time in Mega seconds (Ms $= 10^6$ sec) and masses in $M_{\text{earth}} = 5.972 \times 10^{24}$ Kg. In these units, the initial position (at the perihelion), is $46.001272(\cos(\theta), \sin(\theta))$ where θ is the angle between x-axis and semi-major axis. The initial velocity is perpendicular to the line connecting Mercury and the Sun, with magnitude 58.98. The potential is $-GM/r$ with $GM = 132733$ measured in the code's units [3]. When we will study the problem on the lattice, the angle θ will be important. In Fig. 6.2 the magnitude of perihelion variation for the different time integrators and the step size h is shown. The horizontal line shows the value of relativistic perihelion advance, the green/red regions respectively show where the time integrator precision is/is not good enough to observe relativistic perihelion advance. Because time integrators over- or underestimate the perihelion, we plot its absolute deviation (which for Newton's law should be zero). This absolute value sets a limit of how small one has to take a time step h to be able to detect general relativistic corrections to the orbits.

The relativistic parameter $\Upsilon = r_{\text{sch}}/r_{\text{per}}$ for the Mercury-Sun case with $r_{\text{per}} = 46 \times 10^6$ km and $r_{\text{sch}} = 2.95$ km is $\Upsilon \approx 6.4 \times 10^{-8}$. The eccentricity of Mercury is

---

[3] In units $\text{Gm}^3 \cdot M_{\text{earth}}^{-1} \cdot \text{Ms}^{-2}$.

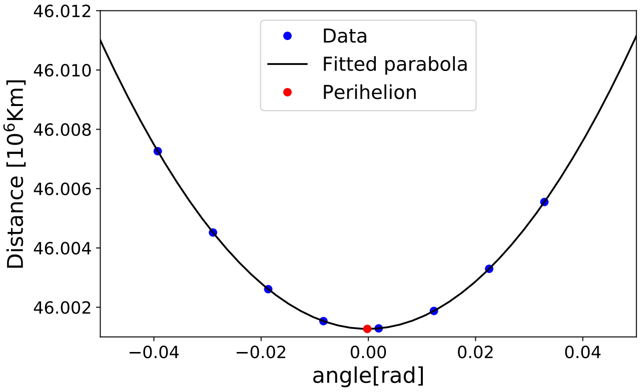

Figure 6.1: Detecting the spurious perihelion change for the Kepler problem for the Mercury-Sun system. For each time step of integration we determine the angle and the distance from the central body (the blue points), using the 2nd order Runge-Kutta method. We then fit a parabola through these points, and the minimum of the distance to the Sun is the red point (perihelion point). Note that the red point is very slightly to the left of 0 and shows the spurious perihelion shift due to the time integration imprecisions. We use this method to find the perihelion shift and to decrease the errors we take average over three revolutions.

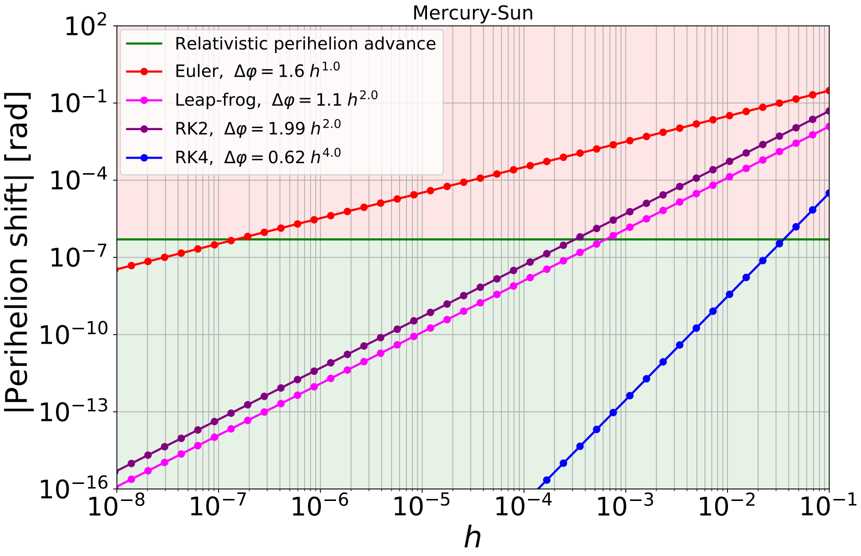

Figure 6.2: Achievable precision for different integrators, as a function of step size h. Shown is the absolute value of the perihelion shift for the Mercury-Sun problem. To make relativistic corrections distinguishable, only points in the green region are good enough. The data points correspond to 1/3 of the advance after 3 rotations.

≈ 0.205630. Both parameters are considered small as the distance of Mercury to the Sun is much larger than the Schwarzschild radius of the Sun. We therefore consider also a more extreme case, where the relativistic effects are larger, such as the stars in the Galactic center known as the S-stars [Parsa et al., 2017] which are revolving around the central super massive black hole. For one of them, S2, the relativistic parameter at perihelion point is estimated from measurements to be $\Upsilon \approx 8.8 \times 10^{-5}$, and the eccentricity is 0.884. The details about the relativistic parameter and eccentricity can be found in Appendix 6.B.

In our numerical study, we cover therefore a large range of these parameters. Our results are summarized for the four integration methods in Fig. 6.2 as a function of the time step h. In Fig. 6.3 the comparison is done as a function of Υ/Υ_0, where Υ_0 is the relativistic parameter at perihelion point for the Mercury-Sun system. We also show the dependence on eccentricity.

6.4 Force interpolation

Having considered the numerics of the classical methods, we now study the effect of discretizing space. We again restrict attention to two dimensions and set, throughout, the lattice spacing equal to dx.[4] In particular, we study the two force interpolations (linear and bilinear) which are mainly used in N-body simulations, see *e.g.*, [Springel, 2005] and [Adamek et al., 2016a], and for which we will present numerical results. A very useful systematic derivation of finite elements for derivatives and differential complexes can be found in [Arnold, 2002]. The setup is as follows: We are given a potential Φ, in our case the Newtonian potential $\Phi(x_1, x_2) = -GM/\sqrt{x_1^2 + x_2^2} = -GM/r$, from which we want to derive the forces on the particles. In the bilinear (quadratic) method the mesh is given by integer coordinates (in $\mathbb{Z}^2$), and we assume that Φ is known in all points (i, j), with $i, j \in \mathbb{Z}$.[5] The force at lattice point i, j is then approximated by a vector with components

$$\begin{aligned} f_{i,j}^{(x)} &= \frac{\Phi_{i+1,j} - \Phi_{i-1,j}}{2} \ , \\ f_{i,j}^{(y)} &= \frac{\Phi_{i,j+1} - \Phi_{i,j-1}}{2} \ . \end{aligned}$$

---

[4] Due to the discretization, the angular momentum vector might not be conserved and we might have 3D motion, here we assume that the force perpendicular to the plane of motion vanishes.

[5] Finite elements are of course obtained more easily on triangular lattices, but, because of requirements of large parallel computations, we study the lattice $\mathbb{Z}^2$.

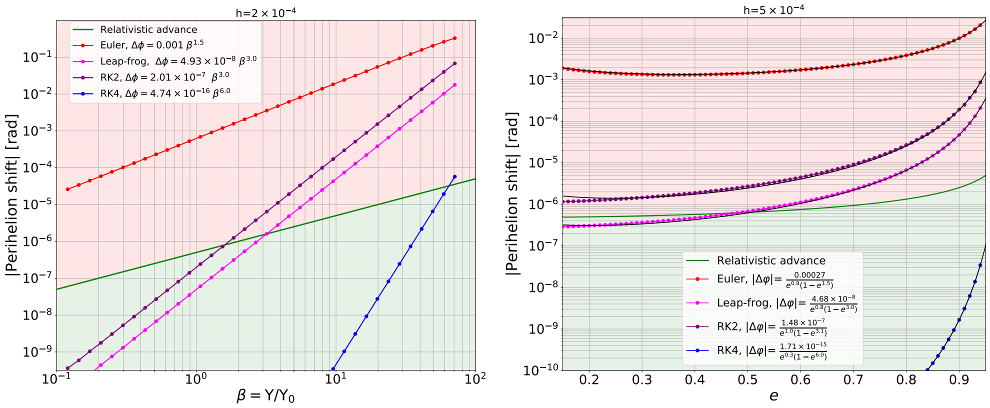

Figure 6.3: **Left**: The absolute value of the perihelion shift as a function of the normalized relativistic parameter $\beta = \Upsilon/\Upsilon_0$, where Υ_0 is the relativistic parameter for Mercury-Sun. The red region shows where the method will fail to discriminate the relativistic perihelion advance from the integration errors (for the chosen step size of $h = 0.0002$). In the green region one can safely use the method, for that specific orbit. When increasing β, the numerical perihelion shift increases, as according to (6.6) the velocity of the object in the perihelion point scales like $\sqrt{\Upsilon}$, while the perihelion distance scales like $\frac{1}{\Upsilon}$. In all the methods the slope of the curve is higher than the slope of the relativistic advance curve $\Delta\varphi \sim \Upsilon$, which shows that for the orbits with large relativistic parameters, one has to choose the method and the time step very carefully. **Right**: The same representation as a function of eccentricity e. In all the methods, by increasing the eccentricity the numerical perihelion variation increases, as according to the (6.7) the velocity of the object and perihelion distance rescales respectively by $\sqrt{\frac{1+e}{1+e_0}}$ and $\frac{1-e}{1-e_0}$. In order to be able to measure the relativistic perihelion advance at each eccentricity we need to use the method with the appropriate step size, for example Euler and second order Runge-Kutta do not work for any eccentricity, while leapfrog is good for $e \lesssim 0.5$ and fourth order Runge-Kutta works perfectly for all eccentricities. All data points correspond to 1/3 of the advance after 3 rotations

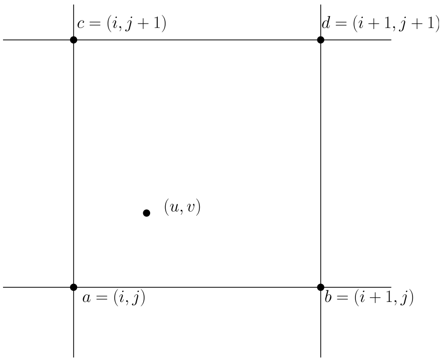

Figure 6.4: Notation for a plaquette on the unit mesh in ^{2}.

Note that the difference is taken over 2 mesh points around the point of interest. Assume that the point $x = (u, v) \in^2$ lies in the square with corners

$$a = (i, j) \ , \quad b = (i+1, j) \ , \quad c = (i, j+1) \ , \quad d = (i+1, j+1) \ ,$$

cf. Fig. 6.4. We let $f_a^{(x)} = f_{i,j}^{(x)}$, and similarly for the other corners and the direction (y).

Let i be the integer part of u and let j be the integer part of v, and set $\xi = u - i$, $\eta = v - j$. The interpolated forces are then given by

$$\begin{aligned} F^{(x)}(u,v) &= \left(f_a^{(x)}(1-\xi) + f_b^{(x)}\xi\right) \cdot (1-\eta) + \left(f_c^{(x)}(1-\xi) + f_d^{(x)}\xi\right) \cdot \eta \ , \\ F^{(y)}(u,v) &= \left(f_a^{(y)}(1-\eta) + f_c^{(y)}\eta\right) \cdot (1-\xi) + \left(f_b^{(y)}(1-\eta) + f_d^{(y)}\eta\right) \cdot \xi \ . \end{aligned} \tag{6.2}$$

Note that "c" and "b" change position between the x and y components.This interpolation method is called **bilinear method** as it is combination of two linear interpolations along the square, so it is a quadratic interpolation [Arnold, 2002]. This interpolation is continuous across the boundaries in both directions and for both components of the vector field. To verify this, one can for example restrict to the line connecting a and b. Then $\eta = 0$, and therefore one gets

$$\begin{aligned} F^{(x)}(u,v) =& f_a^{(x)}(1-\xi) + f_b^{(x)}\xi \ , \\ F^{(y)}(u,v) =& f_a^{(y)}(1-\xi) + f_b^{(y)}\xi \ . \end{aligned}$$

The important thing is that the values only depend on a and b, but not on c and d and so continuity is guaranteed. The 3 other edges are similar.

In this scheme, as is well known, one needs 8 evaluations of Φ per plaquette. When the mesh size is dx instead of 1, all the calculations scale accordingly.

The other method, **linear method** which is also widely used in cosmological N-body simulations *e.g.*, [Adamek et al., 2016a] is given, with similar notation—using g and G instead of f and F—by

$$\begin{aligned} g^{(x)}_{i,j} &= \Phi_{i+1,j} - \Phi_{i,j} \ , \\ g^{(y)}_{i,j} &= \Phi_{i,j+1} - \Phi_{i,j} \ , \\ G^{(x)}(u,v) &= g^{(x)}_a(1-\eta) + g^{(x)}_c\eta \ , \\ G^{(y)}(u,v) &= g^{(y)}_b(1-\xi) + g^{(y)}_d\xi \ , \end{aligned}$$

with $a, \dots, d$ as before. This method is of lower order than the previous one, and needs fewer evaluations. The advantage is that they need less memory, but of course, it is only 1^{st} order.

Note that if (u,v) crosses the line connecting a and b, then $G^{(x)}$ is continuous, but $G^{(y)}$ has a jump discontinuity (of order about $\mathcal{O}(\Phi_{i,j} - \Phi_{i+1,j})$ when i and j are not too close to 0). Similar considerations hold on the other boundaries of the unit plaquette.

This scheme only needs 4 evaluations of Φ per 2-dimensional plaquette, but the interpolation is not continuous. The Kepler problem can still be integrated numerically, but there will appear a spurious phase shift which is caused by the discontinuity. But the numerical errors again scale with the mesh size, albeit on a larger scale than in the first method.

We will now present the numerical results for these cases, and then discuss the limitations they imply on trajectories in N-body simulations. Of course, often calculations are done in ^{3}, resp. $\mathbb{Z}^3$, but for the study of numerical issues, 2 dimensions are enough. Restriction to 1 dimension is too easy, since the two methods coincide in that case.

6.5 Discretization vs relativistic perihelion advance

We have seen that high precision is needed to discriminate relativistic effects in the planar two-body problem. As several N-body codes use—in addition to the standard numerical integration schemes, a *discretization* of space—we now study the effects of these discretizations. To concentrate on them, we use a numerical integration of very high precision (ODEX, tolerance $8 \cdot 10^{-11}$) so that the effects described earlier are minimal, and the effect of discretization becomes visible.

As we want to measure the perihelion advance due to the discretization we stick to the general equations in which we do not use the symmetries of the Kepler problem. We just assume that the motion is on a plane and we solve the equations for the relative distance between two masses assuming that $m \ll M$,

$$\begin{aligned}(\dot{x}, \dot{y}) &= (v_x, v_y) \ , \\ (\dot{v}_x, \dot{v}_y) &= (H^{(x)}(u,v), H^{(y)}(u,v)) \ ,\end{aligned}$$

where $H^{(x)}(u,v)$ is $F^{(x)}(u,v)$ or $G^{(x)}(u,v)$ as defined in Section 6.4 .

We have, so far, analyzed in detail how much numerical precision is needed to detect general relativistic effects, as a function of eccentricity and the relativistic parameter Υ.

We start by presenting results for the bilinear interpolation (6.2). The simulations are done as follows: We take the parameters for Mercury, with initial position at $46.001 \cdot (\cos(\theta), \sin(\theta))$ and a velocity perpendicular to the Mercury-Sun line, of magnitude 58.98, in the counterclockwise direction. We require a tolerance of 8×10^{-11}, which is attainable with quadruple precision, using ODEX. For each value of θ, we determine the time for 1, 2, and 3 returns to the perihelion. The perihelion is found by looking for that angle where the distance from the sun is minimal. This angle is found by linear and quadratic bisection, up to machine precision, using the “continuous output” from ODEX.[6] We repeat this for 180 initial angles covering 360 degrees in steps of 2 degrees, and this gives us 3×180 data points.[7] In Fig. 6.5 and Fig. 6.6 we show the results for several values of dx, for linear and bilinear approximation. Further inspection shows that these distributions are close to Gaussian, but the variance is somewhat smaller than dx, actually $dx^{1.3}$ is a reasonable approximation. As we mentioned before, an analytic estimate of this variance is difficult, because ODEX works with variable step size and order, with quite dramatic changes near the edges of the plaquettes.

In the case of the linear interpolation, the discontinuity leads to an effective advance of the perihelion, which furthermore depends strongly on the initial angle θ. Qualitatively, this can be understood by the angles at which the orbit crosses the discontinuities. Using otherwise the same parameters as above, the results are summarized in Fig. 6.7. The advance A of the perihelion follows closely a cosine (with a phase-shift) $A/dx \sim 0.145 \cos(\theta + 2.34) \sim 0.145 \cos(\theta + 3\pi/4)$. We also checked that the advance of the perihelion changes sign if the initial velocity changes sign. Also note that the average of the advance of the perihelion is close to zero. To generalize the results to include different orbits in N-body simulations especially the ones with high eccentricity and high relativistic parameter, we studied how the perihelion shift depends on eccentricity and relativistic parameter. These are shown in Fig. 6.7. Given the number of particles considered in current N-body simulations (*e.g.*, 7000^3 in [Yu et al., 2017]) and the restrictions of current hardware, (same number of lattice points), we see that relativistic corrections of the orbits can not be detected.

---

[6] We use the standard algorithm “zeroin” of Dekker.

[7] For example, after 3 turns, we divide the total angle by 3, we do not take the difference between the angle for 3 and 2 turns. Of course, errors on these points will average out somewhat.

An interesting effect of the discretization for fixed dx is the dependence on eccentricity e. We observed that the deviations scale about as $\frac{1}{e(1-e^2)}$ for the linear interpolation. This means that the effect is largest at extreme values of e. The deviation is also proportional to Υ, while the relativistic correction is proportional to $\frac{\Upsilon}{1-e^2}$.

The code for such tests and for other parameters can be obtained from the authors.

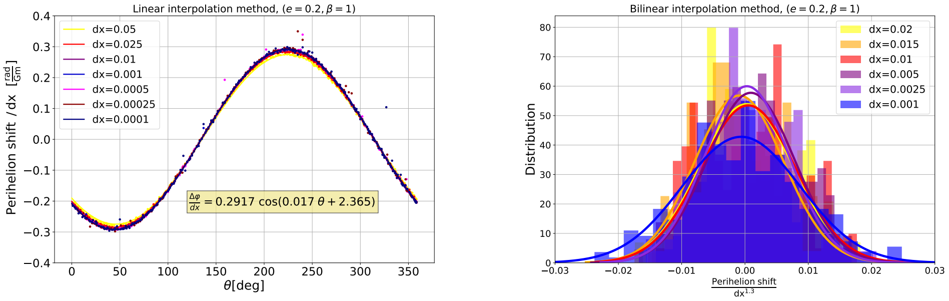

Figure 6.5: **Left**: Linear interpolation: The advance of the perihelion due to the discretization effect depends on the initial angle of the perihelion. For each value of dx, we show the deviation in radians, divided by dx. The curves clearly coincide. This shows that the deviations scale linearly with dx.
Right: Bilinear interpolation: We consider the perihelion shifts, divided by $dx^{1.3}$, for 180 equally spaced initial angles of the orbit. The bar graphs show the distribution of these quantities, for various choices of dx. We see that they obey a Gaussian fit (the solid lines). This shows that the shifts are random.

6.6 Conclusions

We see that the numerical study of relativistic effects can have two problems. First, the integration method must choose a small enough time step to reach a precision which is better than the size of the relativistic correction. Second, if, additionally, the forces are discretized, the grid size must be quite fine, so that the relativistic corrections are not washed out by the approximation.

In particular, our results allow one to estimate for which choices of Υ, e, and θ, the relativistic effects are larger than the numerical and discretization effects generated by h and dx.

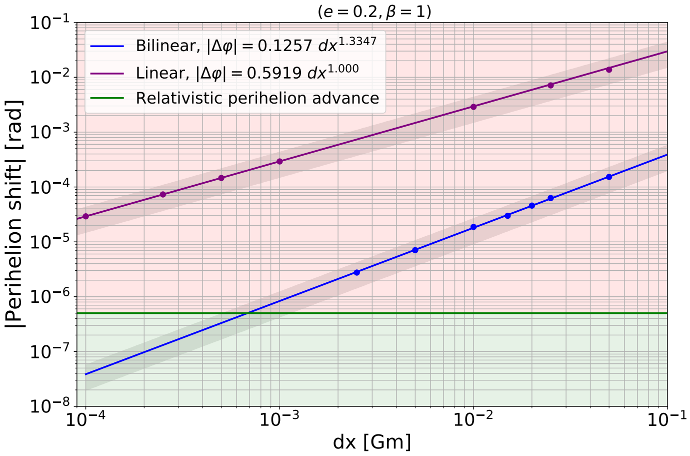

Figure 6.6: Dependence of the standard deviation of the perihelion shift for the two methods, as a function of dx. For the bilinear method, numerical fluctuations are too large to get reliable results for $dx \lesssim 10^{-3}$. The grey regions around the fitted blue and magenta lines show the 50% deviation from the central fit value.

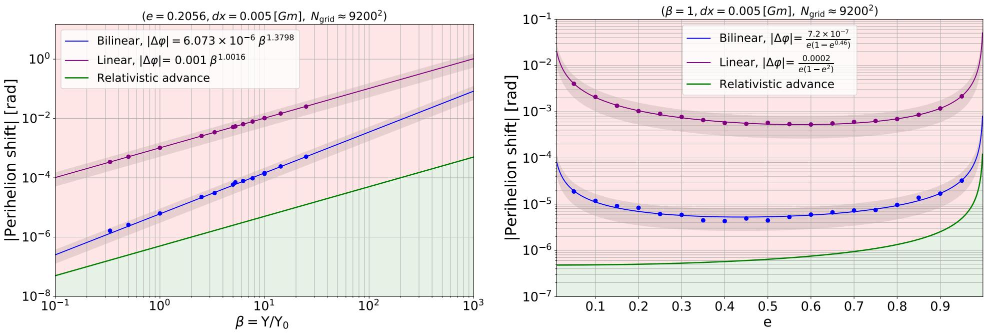

Figure 6.7: Comparison of linear vs. bilinear interpolation. **Left**: Behavior as a function of the theoretical relativistic parameter β. The green line shows the relativistic perihelion advance and therefore the green/magenta area determines the regions for β where one can/cannot detect the perihelion advance. Note that for the parameters e, dx, and N_{grid} used in the figure, no method is able to detect relativistic corrections.
Right: The same study, now as a function of eccentricity e. According to the green/magenta regions the relativistic effects can not be detected for the choice of β, dx, and N_{grid}.

Acknowledgements

We thank Martin Kunz for asking questions leading to this paper, and for helpful discussions. We thank Ruth Durrer and Jacques Rougemont for helpful comments about our manuscript. JPE acknowledges partial support by an ERC advanced grant "Bridges" and FH acknowledges financial support from the Swiss National Science Foundation.

APPENDIX

6.A Newtonian and relativistic orbits

Here first we review the equations of motion and properties of the orbits in the mechanics of Newtonian particles, then we derive the equations for general relativistic motion. In 2-dimension polar coordinates (r, ϕ) the Newton equations take the form

$$\ddot{r} - r\dot{\phi}^2 = -\frac{GM}{r^2}$$

Writing the angular momentum per mass l in polar coordinates results in

$$l = r^2\dot{\phi} \ .$$

Changing the variable to $u(\phi) = 1/r(\phi)$ gives

$$\frac{d^2}{d\phi^2}u + u = \frac{GM}{l^2} \ . \tag{6.3}$$

To obtain the relativistic perihelion advance we repeat, for the convenience of the reader, some parts of [Stephani, 2004, p. 193]. The Schwarzschild metric as a spherically symmetric vacuum solution reads,

$$ds^2 = -\Big(1 - \frac{r_{\mathrm{sch}}}{r}\Big)c^2dt^2 + \Big(1 - \frac{r_{\mathrm{sch}}}{r}\Big)^{-1}dr^2 + r^2\Big(d\theta^2 + \sin^2\theta \, d\phi^2\Big) \ ,$$

where r_{sch} is the Schwarzschild radius, defined by $r_{\mathrm{sch}} = \frac{2GM}{c^2}$, t and r, θ, ϕ are respectively time and spatial spherical coordinates.[8] To obtain geodesic equations one starts from the classical action of massive test particle,

$$\mathcal{A} = -m_o \int \sqrt{-g_{\mu\nu}\frac{\underset{\cdot}{\mathrm{x}}^{\mu}}{d\tau}\frac{\underset{\cdot}{\mathrm{x}}^{\nu}}{d\tau}}d\tau \ ,$$

where m_o is the mass of the object. Applying Euler-Lagrange equation to the Lagrangian of the test particle gives four equations, in which one sees that the angular momentum is conserved. Therefore, the motion is in a plane. By simple algebra on the equations one finds the equation of motion as

$$\frac{d^2}{d\phi^2}u + u = \frac{GM}{l^2} + \frac{3}{2}r_{\mathrm{sch}}u^2 \ , \tag{6.4}$$

---

[8] In this section, θ is not the angle of the major axis, but just one of the 3 Euler coordinates.

which is like Newton's equation (6.3) plus a term which is coming from relativistic correction. We solve (6.4) to obtain the relativistic perihelion advance per period, which is well approximated by

$$\Delta\phi_p \approx \frac{3\pi r_{\rm sch}}{a\left(1-e^2\right)} \ , \tag{6.5}$$

where a is semi-major axis and e is the eccentricity of the orbit.

For Mercury, this leads to the well-known advance of 42.98 arc sec perihelion advance per century, or ~ 0.103 arc sec per period.

6.B The parameterization of orbits

To see the effect of discretization on different orbits in N-body simulations, we parameterize a general orbit with three parameters (Υ, θ, e), where e is the eccentricity, Υ is the relativistic parameter at perihelion and θ is the angle of semi-major axis with the lattice squares. It is important to note that, these parameters are enough to explain any closed orbits in N-body simulations. Moreover having the three parameters one could uniquely construct the mass of central object as well as the initial position and velocity of the particle.

Relativistic parameter The relativistic parameter $\Upsilon = \frac{r_{\rm sch}}{r_{\rm per}}$, for a fixed mass of central object it shows the scale of the orbits and for a fixed size of the orbit it is an indicator of the mass of central object. If we assume that the mass of central object is fixed, by changing the relativistic parameter, different quantities of the orbit would scale as following,

$$\begin{aligned} M &\to M \ , & r_{\rm per} &\to \frac{r_{\rm per}}{\Upsilon} \ , \\ T &\to \Upsilon^{3/2} T \ , & v_{\rm per} &\to \sqrt{\Upsilon} v_{\rm per} \ . \end{aligned} \tag{6.6}$$

$r_{\rm per}$ is the perihelion radius, T is the period of the orbit and $v_{\rm per}$ is the velocity of the object in the perihelion point. To rescale the orbit for the fixed central body mass and fixed eccentricity one has to change the initial conditions as following to obtain the new orbit,

$$\begin{aligned} x_0 &= \frac{r_{\rm per}}{\Upsilon} \ , & y_0 &= 0 \ , \\ v_x &= 0 \ , & v_y &= \sqrt{\Upsilon} v_{\rm per} \ . \end{aligned}$$

We could of course change the central object mass instead of changing the size of the orbit while having the same relativistic parameter.

Eccentricity Another parameter which is important in characterizing an orbit is the eccentricity, to change the eccentricity we keep the semi-major axis length fixed and we change the positions and velocities in the perihelion point to recover the desired eccentricity for the orbits

$$r_{\rm per} \to r_{\rm per}\,\frac{1-e}{1-e_0}\ , \qquad v_{\rm per}\!\to v_{\rm per}\sqrt{\frac{1+e}{1+e_0}}\ , \tag{6.7}$$

where e is the new eccentricity and e_0 is the reference eccentricity (in our case mercury). Note that changing eccentricity also results in changing the perihelion distance and relativistic parameter.

Rotation It appears that the angle between the semi-major axis and the lattice squares, is an important parameter specially in the linear force interpolation. To rotate the orbit by angle θ we can follow the coordinate transformations and start from the following initial condition to obtain the correct orbit,

$$\begin{aligned} x_0 =&\ \ r_{\rm per}\cos(\theta)\ , \qquad & y_0 =& r_{\rm per}\sin(\theta)\ , \\ v_x =& -v_{\rm per}\sin(\theta)\ , \qquad & v_y =& v_{\rm per}\cos(\theta)\ . \end{aligned}$$

In Fig. 6.8 we have illustrated the orbits with different ellipticity, relativistic parameter and angle obtained from numerical results.

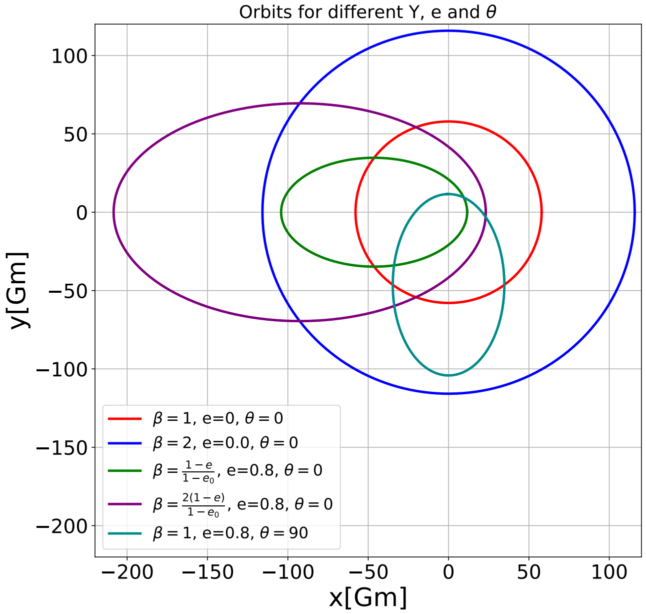

Figure 6.8: Some examples of the parameterization of elliptic orbits, which show the role of $\beta = \Upsilon/\Upsilon_0$, e, and θ. The orbits are obtained by solving the differential equations.

Chapter 7

N-BODY SIMULATIONS FOR PARAMETRISED MODIFIED GRAVITY

Based on:
Hassani & Lombriser [2020] Farbod Hassani(Geneva U., Dept. Theor. Phys.), Lucas Lombriser (Geneva U., Dept. Theor. Phys.)
N-body simulations for parametrised modified gravity, Monthly Notices of the Royal Astronomical Society 2020 497 (2): 1885-1894, [arXiv: 2003.05927]

Abstract: We present `MG-evolution`, an N-body code simulating the cosmological structure formation for parametrised modifications of gravity. It is built from the combination of parametrised linear theory with a parametrisation of the deeply nonlinear cosmological regime extrapolated from modified spherical collapse computations that cover the range of known screening mechanisms. We test `MG-evolution`, which runs at the speed of conventional ΛCDM simulations, against a suit of existing exact model-specific codes, encompassing linearised and chameleon $f(R)$ gravity as well as the normal branch of the Dvali-Gabadadz-Porrati braneworld model, hence covering both large-field value and large-derivative screening effects. We compare the nonlinear power spectra produced by the parametrised and model-specific approaches over the full range of scales set by the box size and resolution of our simulations, $k = (0.05 - 2.5)$ h/Mpc, and for two redshift slices, $z = 0$ and $z = 1$. We find sub-percent to one-percent level recovery of all the power spectra generated with the model-specific codes for the full range of scales. `MG-evolution` can be used for generalised and accurate tests of gravity and dark energy with the increasing wealth of high-precision cosmological survey data becoming available over the next decade.

7.1 Introduction

A wealth of high-precision measurements in the Solar System, of astrophysical objects, of gravitational wave emissions, and in the laboratory have put Einstein's Theory of General Relativity (GR) under intense scrutiny [Abbott et al., 2016, Baker et al., 2019, Hulse & Taylor, 1975, Kapner et al., 2007, Will, 2014]. In these regimes GR has successfully passed all tests so far. Its application to cosmology, however, involves vastly different length scales, which in orders of magnitude compare to the extent of the Solar System as the scale of everyday human experience to the scale of an atomic nucleus. It is therefore important to conduct independent tests of GR in the cosmological regime. The necessity of a dominating dark sector to explain the cosmic large-scale observations [Abbott et al., 2018, Hildebrandt et al., 2016, Perlmutter et al., 1999, Planck Collaboration et al., 2018, Riess et al., 1998b] provides additional motivation for this endeavour. Traditionally the late-time accelerated expansion of our Universe has been a particularly important driver for the development of modifications of GR. As direct cause of the acceleration this motivation is, however, challenged by the confirmation of a luminal speed of gravity [Abbott et al., 2017, Lombriser & Lima, 2017]. But cosmic acceleration could nonetheless be attributed to a dark energy component that may couple nonminimally to matter, modifying gravity and leaving an observable impact on cosmological scales.

The past two decades have seen a steep growth in cosmological tests of gravity and dark energy [Ishak, 2019, Joyce et al., 2016a, Koyama, 2016], and in the upcoming years, we will benefit from numerous high-precision experiments [Aghamousa et al., 2016b, LSST Dark Energy Science Collaboration, 2012, Laureijs et al., 2011, Walcher et al., 2019, Weltman et al., 2020] that will enable us to put tight cosmological constraints on the properties of dark energy and modified gravity theories. Specifically, we will see an increase in the wealth of high-quality data in the nonlinear regime of cosmic structure formation. This is a regime of particular interest for tests of gravity since viable modifications of GR must employ screening mechanisms [Babichev et al., 2009, Hinterbichler & Khoury, 2010, Khoury & Weltman, 2004, Vainshtein, 1972] to recover GR in high-density regions to comply with the stringent bounds from Solar-System, astrophysical, gravitational wave, and laboratory experiments. These are inherently nonlinear effects and naturally in the nonlinear cosmological small-scale structure is where modified gravity transitions to GR and thus also where unique signatures of screening are to be expected. The forthcoming nonlinear cosmological survey data therefore make cosmological tests of gravity a very timely enterprise.

To predict the complex nonlinear structure formation due to gravity, we typically rely on N-body simulations. N-body codes have been developed for a range of alternative gravity models [Baldi, 2012, Barreira et al., 2013, Brax et al., 2012b, Li et al., 2012a, Li et al., 2013, Llinares et al., 2014, Mead et al., 2015, Oyaizu et al., 2008, Puchwein et al., 2013, Schmidt et al., 2009a, Valogiannis & Bean, 2017, Wyman et al., 2013, Zhao et al., 2011] (for an introductory text see Li [2018]). Importantly, these simulations model the cosmic structure of specific modified gravity theories. However, a plethora of modified gravity models are conceivable based on the prospects of novel interactions of matter with new fields. A systematic approach is therefore required to more comprehensively explore the manifold cosmological implications from the possible modifications of gravity. But this is not feasible with a model-by-model implementation in N-body codes. Hence, much effort has gone into developing parametrisation frameworks (see Lombriser [2018] for a review). While parametrisations of the linear and quasilinear modifications are well understood, it is less clear how to develop parametrisations of modified gravity in the deeply nonlinear cosmological regime. In general, spherical collapse computations have proven very useful in capturing the modified gravity effects at deeply nonlinear scales. Motivated by the variety of screening mechanisms that can operate in scalar-tensor theories, a parametrisation of the modified gravitational forces acting on the spherical top-hat overdensities has been developed in Lombriser [2016]. Together with linear and quasilinear parametrisations the spherical collapse parametrisation can be used in an adapted halo model framework to model the nonlinear matter power spectra of arbitrary modified gravity theories [Cataneo et al., 2019]. An N-body implementation of such a parametrisation framework, covering the linear to deeply nonlinear regime, has so far not been developed. N-body codes for parametrised modified gravity exist in the context of large-field value screening [Brax et al., 2012a], which however does not encompass models with large-derivative screening, or for purely phenomenological parametrisations [Thomas & Contaldi, 2011], which however do not accurately represent the effect of screening mechanisms in the cosmic structure formation. A physically motivated but general parametrisation of modified gravity effects for the implementation in N-body codes would both allow to simulate specific models with one code as well as to broadly parametrise and explore the modified gravity effects in simulations for the multitude of conceivable models and test these against the future survey data.

In this paper, we develop and present the first N-body code, dubbed `MG-evolution`, for parametrised modifications of gravity that encompass all known screening effects. We derive the parametrisation from generalised linear theory and the parametrised spherical collapse model of Lombriser [2016]. We describe our parametrised simulations and test the performance for three types of modifications for which exact N-body simulation data are available. These are the linearised and chameleon $f(R)$ gravity models [Hu & Sawicki, 2007] and the normal branch Dvali-Gabadadze-Porrati (nDGP) model [Dvali et al., 2000]. For a comparison of the simulation outputs we present the nonlinear matter power spectra produced by these models within the parametrised and exact approaches.

The paper is organised as follows. In Sec. 7.2, we review the linear and nonlinear parametrisations of modified gravity in Fourier and real space, respectively. We then introduce a Fourier-space parametrisation that covers all scales and discuss its implementation in N-body codes. We develop and test our `MG-evolution` N-body implementation in Sec. 7.3. We test the performance of the parametrised code in reproducing the exact N-body results of existing codes for linearised and chameleon $f(R)$ gravity as well as the nDGP model. We conclude with a discussion of our results in Sec. 7.4. Finally, we discuss details of moving beyond the quasistatic approximation and differences between simulations of parametrised modified gravity in Fourier and real space in the appendix.

7.2 Parametrising modified gravity for N-body simulations

The cosmic structure formation in a given gravitational theory is most accurately modelled with N-body simulations, where the particles in the simulation are incrementally displaced from their initial positions according to the Poisson equation. This computation is conveniently performed in Fourier space, where the effective Poisson equation is given by

$$\left(\frac{k}{a}\right)^2 \Phi(a,k) = 4\pi G_{\rm eff}(a,k,\ldots)\delta\rho_{\rm m}(a,k)\,. \tag{7.1}$$

$G_{\rm eff}(a,k,\ldots)$ denotes the effective gravitational coupling, in general a function of time and wavenumber k, which parametrises the effects of alternative gravity theories on structure formation. The gravitational potential Ψ is cast in the Poisson gauge with the line element

$$ds^2 = a^2(\tau)\Big[-e^{2\Psi}d\tau^2 + e^{-2\Phi}\delta_{ij}dx^i dx^j\Big] \tag{7.2}$$

and $\delta\rho_{\rm m}$ denotes the matter density perturbation.

In addition to the modification of the Poisson equation, modified gravity models typically also introduce a gravitational slip between the spatial and temporal gravitational potentials, quantifying an effective anisotropic stress. In general, modifications of gravity can also change the cosmological background expansion, but our focus here is on the parametrisation of linear (Sec. 7.2.1) and nonlinear (Sec. 7.2.2) effects on structure formation. For simplicity, for the practical examples in Sec. 7.3 we shall therefore specify to models with a ΛCDM expansion history, but we stress that the formalism introduced here is not dependent on this choice. For a review of general parametrisations of modified gravity, we refer the reader to Lombriser [2018].

7.2.1 Linear parametrisation

At the level of linear perturbations and in the quasistatic regime, where we neglect time derivatives with respect to spatial derivatives, the effective modification of the Poisson equation of local four-dimensional metric theories of gravity that lead to at most second spatial derivatives in the equations of motion takes the form [Silvestri et al., 2013]

$$G_{\rm eff,L}(a,k) = \frac{1+p_1(a)k^2}{p_2(a)+p_3(a)k^2}\,, \tag{7.3}$$

where $p_i(a)$ are generally three independently free functions of time. Note that more accurately one may adopt a semi-dynamical approximation [Lombriser & Taylor, 2015b], as discussed in App. 7.A, which includes the evaluation of the time derivatives at a pivot scale that can be absorbed into Eq. (7.3). This correction typically only contributes at near-horizon scales, but it becomes particularly important for scalar-tensor theories with higher-order derivatives, where it contributes to leading order at all linear scales.

7.2.2 Nonlinear parametrisation

A parametrisation of modified gravity effects on the nonlinear cosmic structure formation that captures all known screening mechanisms has been proposed in Lombriser [2016] through the parametrisation of the spherical collapse equations in real space. The effective gravitational coupling in this approach can be written as

$$\frac{G_{\text{eff}}(a,r)}{G} = A + \sum_{i}^{N_0} B_i \prod_{j}^{N_i} \mathcal{F}_{ij}\,, \tag{7.4}$$

where A corresponds to the effective coupling in the fully screened limit, typically unity, B_i is the coupling in the fully unscreened limit, e.g., Eq. (7.3) that can be computed using the linear theory, N_0 and N_i characterise the respective number of transitions, and i, j are positive integers. The $\mathcal{F}_{ij}$ are some transition functions parametrising screening or other suppression effects. To parametrise these transitions Lombriser [2016] adopted a generalised form of the Vainshtein screening effect in nDGP (Sec. 7.3.3) with

$$\mathcal{F} \sim b\left(\frac{r}{r_0}\right)^{a_f}\left\{\left[1+\left(\frac{r_0}{r}\right)^{a_f}\right]^{1/b} - 1\right\}, \tag{7.5}$$

where r_0 denotes the screening scale, which in general can be time, mass, and environment dependent. The parameter a_f (should not be confused with the scale factor a) determines the radial dependence of the coupling in the screening limit along with b that characterises an interpolation rate between the screened and unscreened limits. Screening effects such as the chameleon [Khoury & Weltman, 2004, Li & Efstathiou, 2012, Lombriser et al., 2014] symmmetron [Hinterbichler & Khoury, 2010, Taddei et al., 2014], k-mouflage [Babichev et al., 2009, Brax & Valageas, 2014], and Vainshtein [Dvali et al., 2000, Schmidt et al., 2010, Vainshtein, 1972] effects as well as other suppression effects such as the linear shielding mechanism [Lombriser & Taylor, 2015a] or Yukawa suppression approximatively but analytically and sufficiently accurately map onto this transition function by specifying the expressions that the corresponding couplings assume in the limits of large and small r and $r \to r_0$. Furthermore, it was argued that in principle the parameter values can directly be determined from the action of a given gravitational theory after adopting the scaling method of McManus et al. [2016] and counting the powers of second and first spatial derivatives and the scalar field potential.

Note that one may also adopt other transition functions to interpolate between the two different regimes than Eq. (7.5) such as a tanh or sigmoid [Hassani et al., 2019b] function and perform the analogous matching of the limits.

Finally, for our practical examples in Sec. 7.3, we will only consider models that recover GR in the fully screened limit, thus, $A = 1$ in Eq. (7.4), and for which there is only one screening effect operating ($N_0 = N_i = 1$). Hence, $B_i = B$ is given by the linear effective coupling in Eq. (7.3), and $\mathcal{F}_{ij} = \mathcal{F}$ shall be specified by Eq. (7.5).

7.2.3 Full parametrisation in Fourier space

To model the effective modification of the gravitational coupling on all scales, the linear and nonlinear limits, Eqs. (7.3) and (7.4), may be combined into one expression, for instance, by adopting Eq. (7.3) for B_i in Eq. (7.4). But this simple combination can only be performed for models where Eq. (7.3) is scale independent such as in nDGP gravity (Sec. 7.3.3). More generally, one must perform a Fourier transform of either Eq. (7.3) or Eq. (7.4) to unify the effective modifications in either real or Fourier space. We discuss the advantages and disadvantages of the two different approaches in App. 7.B. Due to the simplicity in solving Eq. (7.1), we adopt the Fourier space approach as our main method, and in the following we discuss the procedure we adopt to convert Eq. (7.4) into a nonlinear effective gravitational coupling in Fourier space.

For this purpose, instead of the real space description in Eq. (7.4), we wish to write the parametrised gravitational coupling as

$$\frac{\tilde{G}_{\mathrm{eff}}(a,k)}{G} = A + \sum_i^{N_0} B_i \prod_j^{N_i} \tilde{\mathcal{F}}_{ij} \,, \tag{7.6}$$

where $\tilde{\mathcal{F}}_{ij}$ are now transition functions in Fourier space that parametrise screening or other suppression effects,

$$\tilde{\mathcal{F}} \sim b \left(\frac{k_0}{k}\right)^{a_f} \left\{ \left[1 + \left(\frac{k}{k_0}\right)^{a_f} \right]^{1/b} - 1 \right\} \tag{7.7}$$

with k_0 characterising an effective screening Fourier wavenumber. Note that Eq. (7.6) is not simply a recasting of Eq. (7.4) into Fourier space, which instead involves complicated convolutions (see App. 7.B).

An immediate advantage of working in Fourier space is that we can now directly adopt Eq. (7.3) for the linear limit B_i. We stress, however, that the phenomenological parametrisation (7.7) can also be configured to match the scale dependence of the linear (or linearised) effective coupling given by Eq. (7.3). This is due to the applicability of the transition function to the Yukawa suppression [Lombriser, 2016]. We test the performance of this description in Sec. 7.3.1.

The crucial aspect of converting Eq. (7.4) into Eq. (7.6) is how the screening scale r_0 in Eq. (7.5) must be reinterpreted for Eq. (7.7) in terms of k_0. We adopt the following procedure for this conversion. As in Lombriser [2016] for the computation of the modified spherical collapse, we first replace $r \to a\, r_{\mathrm{th}} y_{\mathrm{h}}$, where $r_{\rm th}$ is the comoving radius of a top-hat density $\rho_{\rm m}$ characterising a halo in our simulation and $y_{\rm h} = (\rho_{\rm m}/\bar{\rho}_{\rm m})^{-1/3}$ denotes the dimensionless top-hat radius with the cosmological background density $\bar{\rho}_{\rm m}$. We then perform the replacement $y_{\rm h}/y_0 \to k_0/k$ motivated from the scaling relation $y \sim r \sim 1/k$ in which take a single wavenumber in Fourier space, k corresponding to a radius, r in real space. This approximation relies on the fact that we assume an oscillatory behavior with a wavenumber r for the densities and potentials of the structures in real space. The dimensionless screening scale typically evolves in time and can also be dependent on mass and environment $y_{\rm env}$. We thus perform the additional replacement $y_{\rm h}/y_{\rm env} \to k_{\rm env}/k$. Note that hereby the screening scale k_0 can hence become effectively k dependent due to dependencies on mass and environment.

For our simulations of parametrised modified gravity, we will focus on models with one screening transition with and without the addition of a linear Yukawa suppression. In this case, the effective parametrised gravitational coupling of the nonlinear Poisson equation simplifies to

$$\frac{\tilde{G}_{\rm eff}(a,k)}{G} = 1 + \frac{\Delta G_{\rm eff,L}}{G} b \left(\frac{k_0}{k}\right)^{a_f} \left\{ \left[1 + \left(\frac{k}{k_0}\right)^{a_f} \right]^{1/b} - 1 \right\} , \tag{7.8}$$

where $\Delta G_{\rm eff} \equiv G_{\rm eff} - G$.

As with the linear modification there are two options of using a parametrisation of $G_{\rm eff}$. One can either compute the functions $p_i(a)$ along with k_0, b and a_f for a specified modified gravity model, or one can phenomenologically parametrise these components and perform a simulation for a given set of parameter values. Cosmological observations may then be used to generally constrain the available parameter space. Here, we will follow the first approach and test the performance of the parametrised simulation framework with specific models against the simulation output of correspondent model-specific N-body codes. We will, however, allow for a calibration of the model parameters in the expressions derived for k_0 or of the interpolation parameter b against the model-specific simulations when not predicted analytically. While the parameter values could be computed numerically by other means [Lombriser, 2016], the motivation behind this approach is that in a parametrised approach it is primarily important that a set of parameter values can be chosen to reproduce a model. If observations favour a nonstandard set of parameter values, the exact model these parameters correspond to may still be determined in retrospect. It is however generally feasible to replace the calibration with analytic predictions or simple numerical computations, and we expect future work to improve upon this point. But this is beyond the scope of this first exploratory work.

7.2.4 Implementation in N-body code

For our simulations of parametrised modified gravity, we use a Newtonian version of the *gevolution* N-body code [Adamek et al., 2016b], where we implement the parametrised gravitational coupling in Fourier space, Eq. (7.8). We shall refer to this implementation as the `MG-evolution` code. Note that *gevolution* is a particle-mesh N-body code, in which in the Newtonian version the Poisson equation is solved in Fourier space to update particle positions and momenta. In contrast, in `MG-evolution` the modified Poisson equation is used to move the particles in the N-body code. It is worth mentioning that *gevolution*, as a relativistic N-body code, is mainly developed to study the relativistic effects in the cosmic large-scale structure. Although we currently use the Newtonian version of *gevolution*, it paves the way for an implementation of a modified gravity parametrisation that includes relativistic effects.

Due to the simplicity in our implementation, the run-time for a parametrised modified gravity simulation is almost the same as for ΛCDM runs. This is a great advantage of the parametrised N-body code over exact model-specific simulations, which can slow down simulations tenfold [Li et al., 2012b].

To test the accuracy of our parametrised approach, in Sec. 7.3 we compare our simulation output against that of other simulations for a range of well studied specific modified gravity models.

7.3 Testing the N-body code

In order to test our framework for the parametrised modified gravity N-body simulations introduced in Sec. 7.2 and its `MG-evolution` implementation in *gevolution* (Sec. 7.2.4), we shall consider three toy scenarios: linearised $f(R)$ (Sec. 7.3.1), chameleon $f(R)$ (Sec. 7.3.2), and nDGP gravity (Sec. 7.3.3). These are representative for the different types of suppression effects one can encounter in modified gravity models: linear effects (Yukawa) as well as screening by large potential wells (chameleon) and large derivatives (Vainshtein) [Joyce et al., 2016a].

For the `MG-evolution` simulations we use $N_{\rm pcl} = 256^3$ for the number of particles, a boxsize of $L = 200$ Mpc/h, and $N_{\rm grid} = 256^3$ for the number of grids. These are relatively small simulations but suffice for our purpose. The $f(R)$ and nDGP simulations used in this work for the comparison are taken from Cataneo et al. [2019], which were run using `ECOSMOG` [Li et al., 2012b], an extension of the `RAMSES` code [Teyssier, 2002b] that has been developed to simulate different classes of non-standard gravity models. The cosmological parameters adopted in all of the simulations are $\Omega_{\rm b}h^2 = 0.02225$, $\Omega_{\rm c}h^2 = 0.1198$, $H_0 = 100h = 68$ km s^{-1}Mpc^{-1}, $A_{\rm s} = 2.085 \times 10^{-9}$ and $n_s = 0.9645$. Our test quantity for the comparison of the output of the parametrised against the exact modified gravity model N-body simulations will be the matter power spectrum, for which we shall consider the range of scales where the upper bound in k, 2.5 h/Mpc, is set according to the Nyquist frequency[1] of our `MG-evolution` simulations and the lower bound, 0.05 h/Mpc, is set by their boxsize. It is worth mentioning that as the data from the low-resolution simulations are very noisy, so for the sake of better illustration, the data in all the figures in this paper are smoothed with a Gaussian filter to remove the noises. The standard deviation for Gaussian kernel is taken $\sigma = 2.5$ in all simulations. We use gaussian_filter function in SciPy 1.0 [Virtanen et al., 2020] to do the smoothing.

Like in *gevolution* in `MG-evolution` the initial conditions are configured using a linear Boltzmann code, here `CLASS` [Lesgourgues, 2011], at high redshifts, where perturbation theory is still valid. We refer to App. A of Adamek et al. [2016a] for more details on producing the high-redshift initial conditions with linear Boltzmann codes. For the numerical results presented in this paper we use $z = 100$ as the initial redshift. Since the modifications of gravity of interest here reduce to GR at early times, we choose the same initial conditions for our modified gravity runs as for the ΛCDM simulation. Note that we do not use the same seeds as used in Cataneo et al. [2019], but since we compare the relative difference between the modified gravity and ΛCDM matter power spectra, i.e. $\frac{P_{\rm MG}-P_{\Lambda\rm CDM}}{P_{\Lambda\rm CDM}}$, the error introduced due to the cosmic variance is almost cancelled out.

7.3.1 Linearised $f(R)$ gravity

At linear scales of $f(R)$ gravity in the quasistatic limit, the modified Poisson equation (7.1) in Fourier space takes the form

$$k^2\Phi_k = -4\pi G\Big(\frac{4}{3} - \frac{1}{3}\frac{\mu^2 a^2}{k^2+\mu^2 a^2}\Big) a\, \delta\rho_k\,, \tag{7.9}$$

where Φ_k denotes the Fourier transform of the gravitational potential. The Compton wavelength λ of the scalaron field and its mass μ are specified by

$$\mu^{-2} = \lambda^2 = \frac{-6\bar{f}_{R0}}{3H_0^2(\Omega_m + 4\Omega_\Lambda)}\left(\frac{1+\frac{\Omega_\Lambda}{\Omega_m}}{a^{-3}+\frac{4\Omega_\Lambda}{\Omega_m}}\right)\,, \tag{7.10}$$

where we have assumed a Hu & Sawicki [2007] model with exponent $\tilde{n} = 1$. The model parameter $\bar{f}_{R0} \equiv df(\bar{R})/d\bar{R}(z=0)$ parametrises the strength of the gravitational modification and together with the usual cosmological parameters fully specifies the $f(R)$ modification. Eq. (7.9) can be cast into Eq. (7.3) and can also be adopted at nonlinear scales, which corresponds to a linearisation of the effective gravitational coupling $G_{\rm eff}$ [Oyaizu et al., 2008].

---

[1] We remove part of the data because of the error introduced by finite resolution effects.

Hence, while the mapping of linearised $f(R)$ gravity into our parametrised framework described by Eq. (7.8) can be done exactly, we shall test here the performance of the parametrisation (7.7) for the Yukawa suppression described by Eq. (7.9). Thus, we want to express Eq. (7.9) as

$$\frac{\Delta G_{\rm eff}}{G}|_{\rm Yukawa} = \frac{b}{3}p\left[\left(1+\frac{1}{p}\right)^{\frac{1}{b}}-1\right] \tag{7.11}$$

where $p = \left(\frac{kb^n}{a\mu}\right)^{-a_f}$, $a_f = \frac{-2b}{b-1}$, and $n = \frac{b}{a_f(b-1)}$ can be inferred from the limits of Eq. (7.9) following the procedure laid out in Lombriser [2016].

We compare the matter power spectra produced in the parametrised framework against those from the simulations of the exact modification, both implemented in `MG-evolution`, in Fig. 7.1. We consider two strengths of the modification, $\bar{f}_{R0} = -10^{-5}$ and $\bar{f}_{R0} = -10^{-6}$, and two redshift slices at $z = 0$ and $z = 1$. The parametrisation (7.11) produces an accurate match to the exact simulations with Eq. (7.9) for all of these outputs and for the full range of scales up to $k = 2.5$ h/Mpc. The interpolation parameter seems to assume the universal value $b = 3$ independent of redshift and strength of the modification.

While the parametrised transition function accurately reproduces the Yukawa suppression, as discussed in Sec. 7.2.1, the adoption of Fourier space for the description of the effective gravitational coupling $G_{\rm eff}(a, k)$ in the Poisson equation allows us to directly make use of the simple linear expression (7.3) instead. We shall thus adopt Eq. (7.3) for the Yukawa regime in the following.

7.3.2 Chameleon $f(R)$ gravity

Next we shall consider parametrised simulations for the full $f(R)$ model, without the linearisation performed in Sec. 7.3.1. We parametrise the effective gravitational coupling of the model with Eq. (7.8). For the Yukawa regime, we can simply adopt Eq. (7.3) and hence we are left with a parametrisation of the chameleon screening mechanism by Eq. (7.7). More specifically, we write the parametrisation as

$$\frac{\Delta G_{\rm eff}}{G}|_{\rm tot} = \frac{\Delta G_{\rm eff}}{G}|_{\rm Yukawa} \times \frac{\Delta G_{\rm eff}}{G}|_{\rm Chameleon}\,, \tag{7.12}$$

where $\frac{\Delta G}{G}|_{\rm Yukawa}$ is given by Eq. (7.9). The chameleon screening regime $\frac{\Delta G}{G}|_{\rm Chameleon}$ in contrast is parametrised as

$$\frac{\Delta G}{G}|_{\rm Chameleon} = b\left(\frac{k_0}{k}\right)^{a_f}\left\{\left[1+\left(\frac{k}{k_0}\right)^{a_f}\right]^{\frac{1}{b}}-1\right\}. \tag{7.13}$$

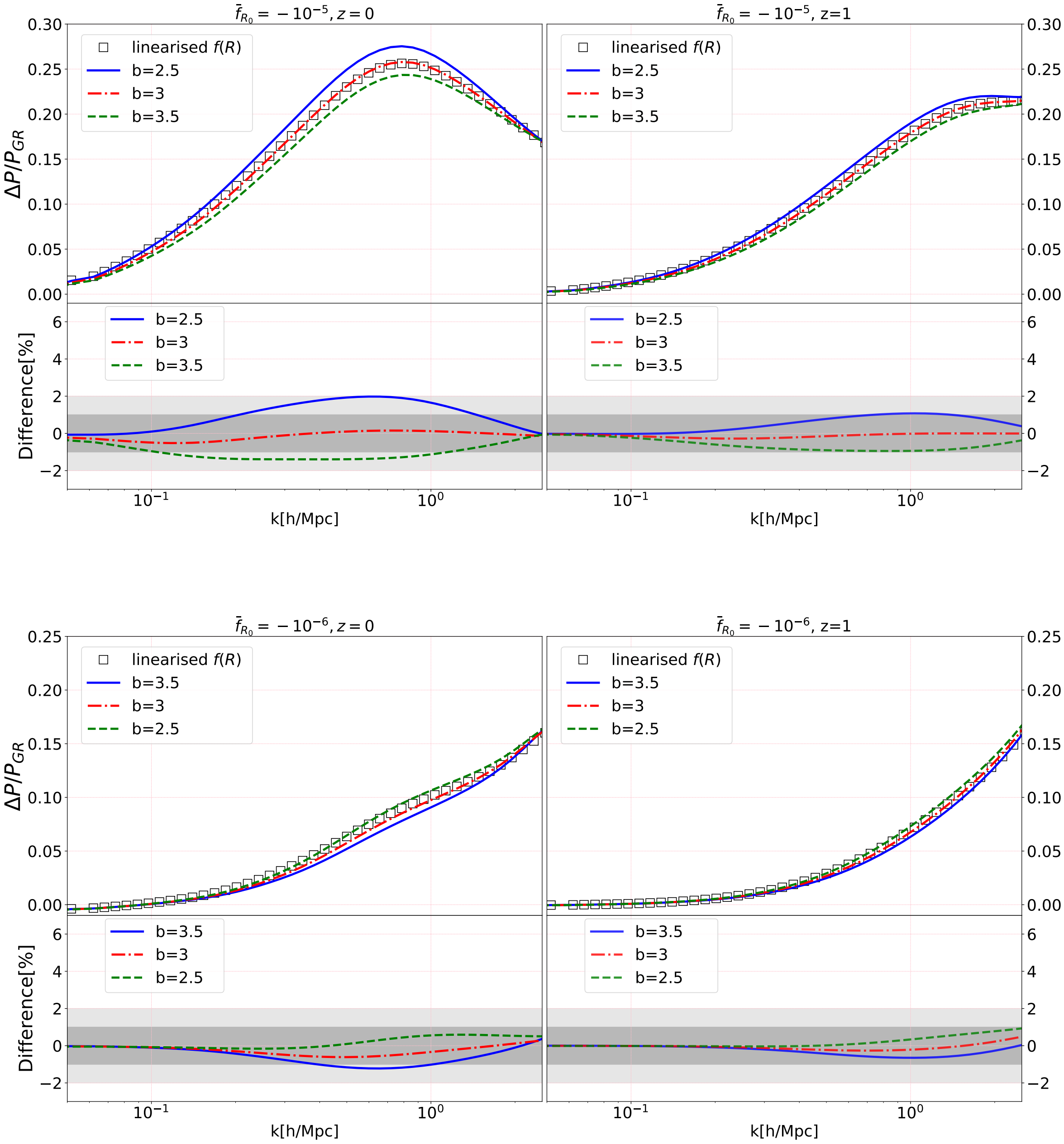

Figure 7.1: Relative difference between the matter power spectra produced by the parametrised (Eq. (7.11)), and exact (Eq. (7.9)) `MG-evolution` implementations of the Yukawa suppression in linearised $f(R)$ gravity for redshifts $z = 0$ (*left panels*) and $z = 1$ (*right panels*) and three different values of the interpolation parameter b. The simulations are run for $\bar{f}_{R0} = -10^{-5}$ (*top panels*) and $\bar{f}_{R0} = -10^{-6}$ (*bottom panels*). The value $b = 3$ provides a good match of the parametrised simulations to the exact implementation.

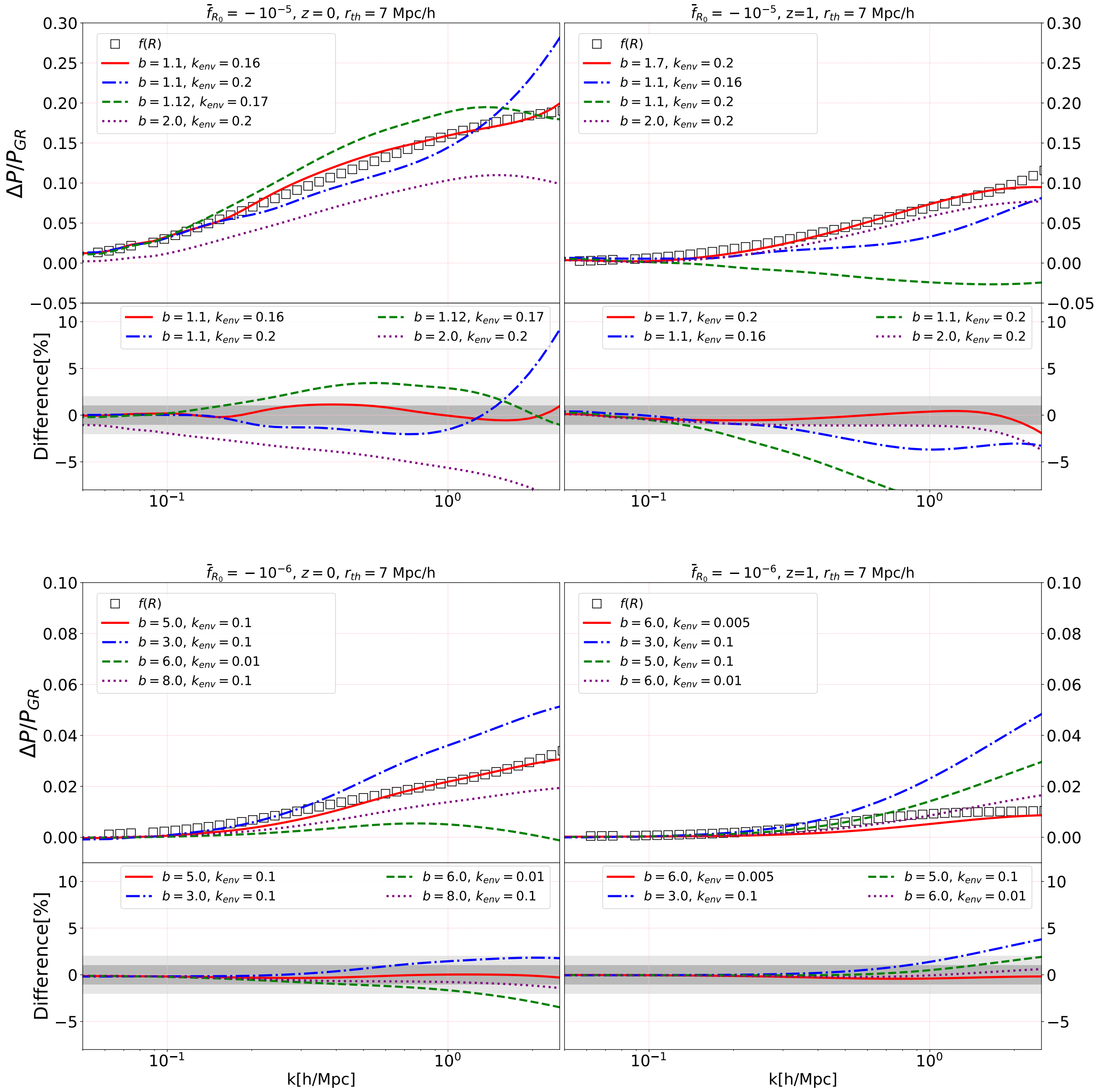

Figure 7.2: Same as Fig. 7.1 but for chameleon $f(R)$ gravity with comparison of the parametrised `MG-evolution` simulations against the exact model simulations [Cataneo et al., 2019]. The parametrised simulations were run for four different values each of the interpolation parameter b and the environmental suppression scale $k_{\rm env}$, where the corresponding comoving top-hat radius was fixed to $r_{\rm th} = 7$ Mpc/h. *Top panel*: For the values ($b = 1.1$, $k_{\rm env} = 0.16$ h/Mpc) at $z = 0$ and ($b = 1.7$, $k_{\rm env} = 0.2$ h/Mpc) at $z = 1$ we find a $\sim 1\%$ match over all scales to $k = 2.5$ h/Mpc. *Bottom panel*: A match of $\sim 1\%$ is found for ($b = 5.0$, $k_{\rm env} = 0.1$ h/Mpc) at $z = 0$ and ($b = 6.0$, $k_{\rm env} = 0.005$ h/Mpc) at $z = 1$.

To find $\frac{k}{k_0}$ we will first inspect the real space parametrisation in Eq. (7.5), described by Lombriser [2016]. Here, the screening scale r_0 is determined by the relation between thin-shell thickness x of the chameleon mechanism and the physical top-hat radius $r_{\rm th}$. More specifically,

$$\frac{\Delta G_{\rm eff}}{G} = \frac{1}{3}\Big\{1 + \min\Big[(x-1)^3, 0\Big]\Big\} \tag{7.14}$$

with thin-shell thickness

$$x = -C_1 r^7 \Big(C_2^{-2} - C_3^{-2}\Big)\,, \tag{7.15}$$

where the coefficients are given by

$$C_1 = \frac{-\bar{f}_{R0}}{\Omega_m H_0^2 r_{\rm th}^3}\left(\frac{\Omega_m + 4\Omega_\Lambda}{4\Omega_\Lambda}\right)^2, \tag{7.16}$$

$$C_2 = \frac{\Omega_m}{4\Omega_\Lambda} r_{\rm th}^3\,, \tag{7.17}$$

$$C_3^2 = C_2^2\left(\frac{y_{\rm h}}{y_{\rm env}}\right)^6 \tag{7.18}$$

and $y_{\rm h} = \frac{r}{a r_{\rm th}}$ is the dimensionless top-hat radius with $y_{\rm env}$ correspondingly characterising a dimensionless environmental radius. We also have $y_0 = \frac{r_0}{a r_{\rm th}}$ for the dimensionless screening scale. Note that r is a physical radius whereas $r_{\rm th}$ is the comoving top-hat radius.

In the screened limit, we have $\Delta G_{\rm eff}/G \approx x$ ($x \ll 1$) and $\Delta G_{\rm eff}/G \approx b(r/r_0)^7/3$ ($r \ll r_0$) in Eq. (7.5). Performing the approximation $y \propto r \propto k^{-1}$, we obtain

$$\frac{r_0}{r} \to \frac{k}{k_0} = \left\{\frac{3C_1}{bC_2^2}\max\left[\left(\frac{\rm k}{\rm k_{env}}\right)^6 - 1, 0\right]\right\}^{-1/7}\frac{\rm k}{\rm a}\,, \tag{7.19}$$

where a is the scalar factor and we have used the maximum function to prevent negative screening scales when $k < k_{\rm env}$ with $k_{\rm env}$ denoting the effective environmental wavenumber. There are three parameters in this expression, namely the interpolation rate b, the comoving top-hat radius $r_{\rm th}$ and the environmental Fourier wavenumber $k_{\rm env}$. The top-hat radius and environmental wavenumber need to be understood here as effective, or average, quantities. While $r_{\rm th}$ and b are degenerate in k/k_0, b also appears in $\frac{\Delta G}{G}|_{\rm Chameleon}$. In principle, these parameters could be determined from theory [Lombriser, 2016], but for the reasons discussed in Sec. 7.2.3 we shall treat them as free parameters. For simplicity, however, we set the comoving top-hat radius to $r_{\rm th} = 7$ Mpc/h, motivated by a typical galaxy cluster mass.

In Fig. 7.2 we compare the matter power spectra produced with our parametrised N-body simulations for the gravitational modifications in Eqs. (7.11), (7.12) and

(7.13) against the simulations of the exact $f(R)$ modification from Cataneo et al. [2019] for $\bar{f}_{R0} = -10^{-5}$ and $\bar{f}_{R0} = -10^{-6}$ at redshifts $z = 0$ and $z = 1$. We also vary b and k_{env}. For $\bar{f}_{R0} = -10^{-5}$, we find that our parametrisation with values ($b = 1.1$, $k_{\text{env}} = 0.16$ h/Mpc) at $z = 0$ and ($b = 1.7$, $k_{\text{env}} = 0.2$ h/Mpc) at $z = 1$ provides a $\sim 1\%$ level match to the simulated power spectra of the exact model over all scales to $k = 2.5$ h/Mpc. For $\bar{f}_{R0} = -10^{-6}$, we find a sub-percent level match for the parameters ($b = 5.0$, $k_{\text{env}} = 0.1$ h/Mpc) at $z = 0$ and ($b = 6.0$, $k_{\text{env}} = 0.005$ h/Mpc) at $z = 1$ over all scales to $k = 2.5$ h/Mpc. It is worth noting that the match to the exact simulations could be improved by allowing for the additional variation of r_{th} or by a finer grid in the parameter space. At this level of accuracy, however, one would also need to run higher-resolution simulations.

7.3.3 Normal branch DGP gravity

Finally, we consider another widely studied modified gravity theory: the Dvali-Gabadadze-Porrati (DGP) braneworld model [Deffayet, 2001, Dvali et al., 2000]. For theoretical and observational consistency [Koyama, 2005, Lombriser et al., 2009], we specify to the normal branch of the model (nDGP). The new free parameter introduced here is the crossover scale r_c that controls the leakage of gravity from the 4D brane to the 5D bulk spacetime.

In the linear limit of the nDGP model, or the weak-brane phase, the effective gravitational coupling G_{eff} in the quasistatic modified Poisson equation (7.1) is scale independent and reads

$$\frac{G_{\text{eff}}}{G} = 1 + \frac{1}{3\beta(a)}\,, \tag{7.20}$$

where the function $\beta(a)$ is defined as

$$\beta(a) = 1 + \frac{4}{3a}\frac{\mathcal{H}}{\mathcal{H}_0}\mathcal{H}_0 r_c\left(1 + \frac{\mathcal{H}'}{2\mathcal{H}^2}\right) \tag{7.21}$$

with primes denoting derivatives with respect to the conformal time and $\mathcal{H}$ indicating the Hubble expansion in conformal time. More generally, due to the Vainshtein mechanism, caused by derivative self-interactions, this linear modification is suppressed in high-denity regions, where the model recovers GR. More specifically [Koyama & Silva, 2007, Schmidt, 2009], for a spherically symmetric matter density perturbation $\delta\rho$ we have

$$\frac{G_{\text{eff}}}{G} = 1 + \frac{2}{3\beta(a)}\frac{\sqrt{1 + x^{-3}} - 1}{x^{-3}} \tag{7.22}$$

where $x \equiv \frac{r}{r_*}$ and r_* is the Vainshtein radius,

$$r_* = \left(\frac{16G\delta M r_c^2}{9\beta^2}\right) \tag{7.23}$$

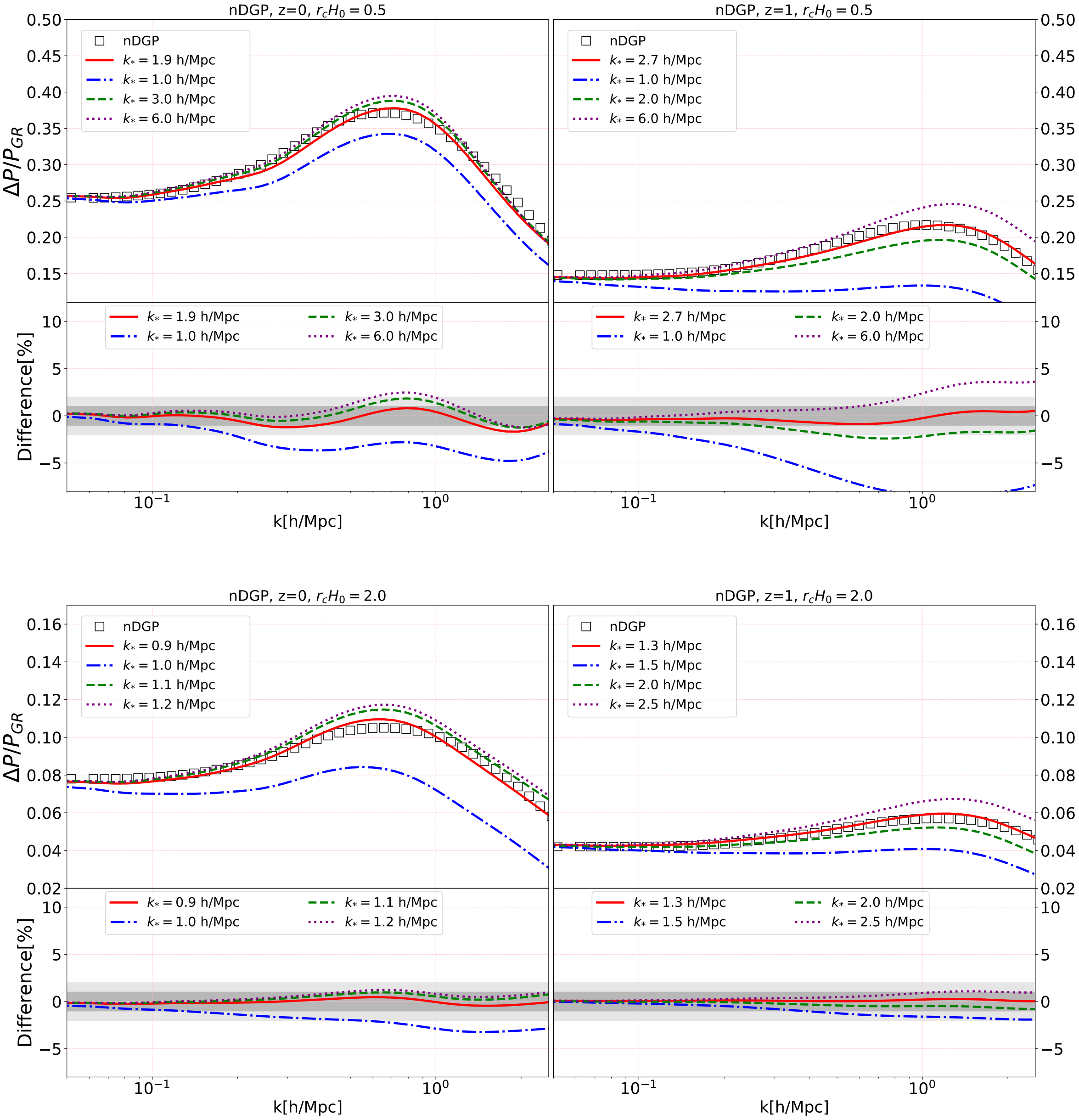

Figure 7.3: Same as Fig. 7.2 but for nDGP gravity. *Top panels*: Comparison for the model parameter $H_0 r_c = 0.5$ for four different values of the effective Vainshtein wavenumber k_* at $z = 0$ (*left panel*) and $z = 1$ (*right panel*). The value $k_* = 1.6$ h/Mpc at $z = 0$ and $k_* = 2.7$ h/Mpc at $z = 1$ recovers the exact simulations at percent level across all scales to $k = 2.5$ h/Mpc. *Bottom panels*: Comparison for $H_0 r_c = 2.0$ for four different values of k_* at $z = 0$ (*left panel*) and $z = 1$ (*right panel*). The values $k_* = 1.1$ h/Mpc at $z = 0$ and $k_* = 2.0$ h/Mpc at $z = 1$ provide sub-percent level matches.

with mass fluctuation

$$\delta M = 4\pi\delta\rho r^3/3\,. \tag{7.24}$$

This can be rewritten as

$$\frac{\Delta G_{\text{eff}}}{G} = \frac{2}{3\beta}\frac{\sqrt{1+\epsilon}-1}{\epsilon} \tag{7.25}$$

with

$$\epsilon \equiv x^{-3} = \left(\frac{r_*}{r}\right)^3 = \frac{8\mathcal{H}_0^2 r_c^2}{9\beta^2}\Omega_m(a)\delta = \frac{8\mathcal{H}_0^2 r_c^2}{9\beta^2}\Omega_{m,0}a^{-3}\delta\,. \tag{7.26}$$

Given that the form of the real-space transition in Eq. (7.5) is motivated by nDGP it is trivial to cast Eq. (7.25) into Eq. (7.5):

$$B \to \frac{1}{3\beta},\;\; a_f \to 3,\;\; b \to 2,\;\; r_0 \to r_*\,. \tag{7.27}$$

We now wish to translate this into a parametrisation of the gravitational modification in Fourier space, Eq. (7.7). Note, however, that we have also performed parametrised N-body simulations with this real-space expression and compared against the outputs of Cataneo et al. [2019], finding good agreement with those when applying a smoothing radius for δ (see App. 7.B).

To obtain the parametrised modification in Fourier space, we perform the approximation

$$\epsilon = \left(\frac{r_*}{r}\right)^3 \to \left(\frac{k}{k_0}\right)^3, \tag{7.28}$$

where $k_0 = k_*$ is the wavenumber corresponding approximately to the Vainshtein radius r_*, and we find

$$\frac{\Delta G}{G}\Big|_{\text{nDGP}} = \frac{1}{3\beta}\left(\frac{k_*}{k}\right)^3\left\{\left[1+\left(\frac{k}{k_*}\right)^3\right]^{\frac{1}{2}} - 1\right\}. \tag{7.29}$$

While the effective screening wavenumber k_* can in principle be modelled [Lombriser, 2016], we shall treat it here as a free parameter following the discussion in Sec. 7.2.3.

As in the exact model simulations of Cataneo et al. [2019], we adopt a cosmological background that matches that of ΛCDM, or equivalently we consider an artificial dark energy fluid that cancels out the effect of modified gravity in the background and as a result we obtain the same expansion history [Schmidt, 2009]. We choose two different strengths of the modification, $H_0 r_c = 0.5$ and $H_0 r_c = 2.0$, for comparing with the exact simulations. Fig. 7.3 shows the matter power spectra produced in the N-body simulations of the parametrised and exact models for the two choices of $H_0 r_c$ at two redshifts, $z = 0$ and $z = 1$. The parametrised simulations cover different values of the effective screening wavenumber k_*. For $H_0 r_c = 0.5$, percent matches are achieved for $k_* = 1.9$ h/Mpc at $z = 0$ and $k_* = 2.7$ h/Mpc at $z = 1$ up to $k = 2.5$ h/Mpc. For $H_0 r_c = 2.0$ sub-percent level matches are found for $k_* = 0.9$ h/Mpc at $z = 0$ and $k_* = 1.3$ h/Mpc at $z = 1$.

7.4 Conclusions

Einstein's Theory of General Relativity has been validated by an ever increasing amount of high-precision measurements ranging from the Solar System to micron scales. However, its validation over cosmological distances at a comparable precision level remains an important endeavour. Additional motivation for cosmological tests of gravity is drawn from the requirement of a currently dominating dark energy contribution to explain the accelerated expansion of the Universe. Over the next decade we will benefit from new cosmological surveys of unprecedented precision with which we will be able to put tight constraints on the cosmological properties of dark energy and modified gravity theories. Of special interest will be the nonlinear regime of cosmic structure formation, where unique signatures are expected from the screening mechanisms that viable modified gravity theories must employ to recover GR in the well-tested Solar-System region. For robust predictions of the complex nonlinear structure, matching the observational precision with corresponding computational accuracy, we need to perform N-body simulations of the modified large-scale structure. To date, an excessive amount of viable modified gravity theories can be formulated based on the prospects of novel interactions of matter with new fields. A systematic testing of the manifold cosmological implications from the possible modifications of gravity based on a model-by-model implementation in N-body codes is infeasible.

To overcome this limitation, in this paper we have proposed a parametrisation of the modified gravity effects on the linear and nonlinear cosmological structure formation adequate for N-body codes. It is constructed from a parametrisation framework for linear theory and a parametrisation formalism for the deeply nonlinear scales, which is based on modified spherical collapse computations that incorporate the effects from the variety of available screening mechanisms. Employing this framework, we have developed `MG-evolution`, a Fourier-space implementation of this approach that is built on the Newtonian version of the *gevolution* N-body code. We have tested our parametrised code with a number of widely studied modified gravity models, including $f(R)$ and nDGP gravity, which encompass both large-field value and derivative screening effects with the employment of the chameleon and Vainshtein mechanisms, and for which exact N-body implementations are available. We have shown that the parametrised approach is capable of recovering the nolinear matter power spectra produced by the exact code implementations of these models to sub-percent accuracy up to the highly nonlinear scales of $k = 2.5$ h/Mpc covered by our simulations.

In future work we plan to explore our nonlinear parametrised gravity framework employing higher resolution simulations that extend the results to larger wavenumbers. We moreover wish to apply and test our parametrised code with further modified gravity models. Finally, we envisage the employment of the code for observational applications, offering an accurate generalised modelling tool for the exploitation of nonlinear data from forthcoming cosmological surveys in large-scale tests of gravity.

Acknowledgements

We thank Matteo Cataneo and Baojiu Li for providing $f(R)$ and nDGP simulation outputs. FH would like to thank Mona Jalilvand for assistance with the numerical simulations. FH acknowledges support by Project Funding of the Swiss National Science Foundation (SNSF) (No. 182231). LL was supported by a SNSF Professorship grant (No. 170547). Numerical computations were performed on the Baobab cluster of the University of Geneva.

APPENDIX

7.A Semi-dynamical perturbations

In Sec. 7.2.1 we have adopted the quasistatic limit, neglecting time derivatives over spatial deriviatives, for our description of the effective gravitational coupling $G_{\rm eff}$ in the modified Poisson equation. While this approximation is accurate in linear theory of Horndeski scalar-tensor modifications of gravity at scales well below the sound horizon [Lombriser & Taylor, 2015b], it can break down at near horizon scales and beyond. More accurately, one may therefore describe the modification of the Poisson equation within a semi-dynamical approximation, where time derivatives are evaluated and included at a pivot scale.

Following Lombriser & Taylor [2015b] we obtain for $G_{\rm eff} = \mu(a,k)$ the k-dependent expression

$$G_{\rm eff}(a,k) = \frac{1}{8\pi M^2}\frac{\mu_{+2}k_H^2 + \mu_{+4}k_H^4 + \mu_{+6}k_H^6}{\mu_{-0} + \mu_{-2}k_H^2 + \mu_{-4}k_H^4 + \mu_{-6}k_H^6}\,, \tag{7.30}$$

where $\mu_{\pm i}$ and M^2 are functions of time only, specified in Lombriser & Taylor [2015b], and $k_H \equiv k/(aH)$. Note that in the small-scale limit, formally where $k \to \infty$, this simplifies to

$$G_{{\rm eff},\infty}(a) = \frac{\mu_{+6}}{\mu_{-6}} = \frac{1}{8\pi M^2}\frac{\mu_\infty^+ + \alpha_{\rm H}\left(f_\Psi \mu_{\Psi,\infty}^+ + f_\zeta \mu_{\zeta,\infty}^+\right)}{\mu_\infty^- + \alpha_{\rm H}\left(f_\Psi \mu_{\Psi,\infty}^- + f_\zeta \mu_{\zeta,\infty}^-\right)}\,, \tag{7.31}$$

where $f_\Psi \equiv d\ln\Psi/d\ln a$ and $f_\zeta \equiv d\ln\zeta/d\ln a$ encapsulate time derivatives of the perturbations with ζ denoting the comoving curvature. The functions $\mu_\infty^\pm$ and $\mu_{\Psi\wedge\zeta,\infty}^\pm$ are time dependent but independent of f_Ψ and f_ζ such that velocity fields and time derivatives of the spatial metric potential only contribute for beyond-Horndeski models ($\alpha_{\rm H} \neq 0$) at leading order in the small-scale limit [Lombriser & Taylor, 2015b]. Hence, for Horndeski theories, at leading order one can set $f_\zeta = f_\Psi = 0$, in which case $G_{\rm eff}(a,k)$ can directly be expressed by the time-dependent EFT functions $\{\alpha_i\}$, $\{\Omega, \Gamma, \Lambda, \ldots\}$, or the inherently stable basis [Kennedy et al., 2018, Lombriser et al., 2019].

Finally, alternatively to adopting the expression (7.30), one may simply compute the linear perturbations and evaluate $G_{\rm eff}$ from the modified Poisson equation (7.1).

7.B Fourier versus real space simulations

As discussed in Sec. 7.2.2, while the linear modification B in Eq. (7.4) is specified in Fourier space, the nonlinear expression for $\mathcal{F}$ is generally given in real space. It is in general computationally not feasible to find the nonlinear modification to gravity in Fourier space from the modification in real space (e.g., nDGP) as one has to deal with convolutions. The Fourier transformation $\mathcal{F}_{\mathcal{T}}$ of the real-space Poisson equation,

$$\mathcal{F}_{\mathcal{T}}\Big\{\nabla^2\Phi_N\Big\} = \mathcal{F}_{\mathcal{T}}\Big\{(1+\frac{\Delta G_{\rm eff}}{G})\delta\rho\Big\}\,, \tag{7.32}$$

using the convolution theorem, gives

$$-k^2\Phi_N = \mathcal{F}_{\mathcal{T}}\Big\{1+\frac{\Delta G_{eff}}{G}\Big\} * \mathcal{F}_{\mathcal{T}}\Big\{\delta\rho\Big\}\,, \tag{7.33}$$

where $*$ refers to the convolution. Calculating this expression analytically is not practical since we do not have access to the full $\delta\rho$ analytically and moreover, computing it numerically is also not feasible because we need to integrate over all the lattice points in Fourier space which is contradictory to the nature of N-body simulations as the equations are solved in parallel and each part of the lattice only has access to its neighbourhood. Due to these complications we have therefore resorted to the effective parametrised Poisson equation (7.8).

It is however worth mentioning that we nevertheless performed real-space simulations for the parametrisations of the $f(R)$ and nDGP cases. In these simulations, while we found satisfactory results for the small scale behaviours, i.e., the chameleon and Vainshtein screening limits, for the large-scale behaviours we initially did not. To overcome the issues at large scales we used a smoothed density field instead of the local one in the real-space parametrised modified Poisson equation. We performed the smoothing with a Gaussian window function $W_G(\vec{x};R)$ defined as

$$W_G(\vec{x};R) = \frac{3}{4\pi R^3}e^{-|x|^2/2R^2}\,, \tag{7.34}$$

where R is the smoothing radius and we can construct the smoothed density field $\delta(\vec{x};R)$ from the local value $\delta(\vec{x})$ through

$$\delta(\vec{x};R) = \int \delta(\vec{x}')W_G(\vec{x};R)d\vec{x}'\,. \tag{7.35}$$

We employed the convolution theorem to simplify this expression to

$$\hat{\delta}(\vec{k};R) = \delta(\vec{k})W_G(\vec{k};R) \tag{7.36}$$

such that finally, the density smoothed over the radius R with a Gaussian window function reads

$$\delta(\vec{x}, R) = \mathcal{F}_{\mathcal{T}}{}^{-1}\left[\hat{\delta}(\vec{k}, R)e^{-(kR)^2/2}\right]. \tag{7.37}$$

This procedure produces relatively consistent results for the parametrised real-space nDGP simulations on all scales. The results for the large-scale behaviour in the parametrised real-space $f(R)$ simulations, however, does not improve. This can be attributed to the scale dependence in the Yukawa suppressed regime of $f(R)$ gravity, which is not present for the nDGP modification. Having found good agreement of the parametrised Fourier-space simulations with the exact simulations in Sec. 7.3, we leave an improvement of the parametrisation of the Yukawa regime in real space to future work.

Chapter 8

DISTINGUISHING COSMOLOGIES USING THE TURN-AROUND RADIUS NEAR GALAXY CLUSTERS

Based on:
Hansen et al. [2020] Steen H. Hansen, Farbod Hassani, Lucas Lombriser, Martin Kunz *Distinguishing cosmologies using the turn-around radius near galaxy clusters* , **JCAP 01** (2020) 048, [arXiv: 1906.04748]

In Section 8, we introduce .

Abstract: Outside galaxy clusters the competition between the inwards gravitational attraction and the outwards expansion of the Universe leads to a special radius of velocity cancellation, which is called the turn-around radius. Measurements of the turn-around radius hold promises of constraining cosmological parameters, and possibly even properties of gravity. Such a measurement is, however, complicated by the fact that the surroundings of galaxy clusters are not spherical, but instead are a complicated collection of filaments, sheets and voids. In this paper we use the results of numerically simulated universes to quantify realistic error-bars of the measurement of the turn-around radius. We find that for a ΛCDM cosmology these error-bars are typically of the order of 20%. We numerically simulate three different implementations of dark energy models and of a scalar dark sector interaction to address whether the turn-around radius can be used to constrain non-trivial cosmologies, and we find that only rather extreme models can be distinguished from a ΛCDM universe due to the large error-bars arising from the non-trivial cluster environments.

8.1 Introduction

The turn-around radius is the unique distance where the gravitational pull of large cosmological structures exactly cancels the expansion of the Universe. It therefore provides a special place to constrain the properties of the expanding universe, for instance the amount of dark energy [Pavlidou & Tomaras, 2014, Pavlidou et al., 2014], or the force of gravity from the gravitational structures [Cataneo & Rapetti, 2018, Faraoni, 2016]. The main observational difficulty with a measurement of the turn-around radius is that the 3-dimensional position of galaxies is very difficult to obtain, since only the 2-dimensional position on the sky is readily observable. For very nearby objects it may be possible to measure the turn-around radius directly [Hoffman et al., 2018]. This complication at cosmological distances may be overcome if one could measure a coherent motion of some of the galaxies. One such possibility was suggested in [Falco et al., 2014], where it was demonstrated that galaxies in large 2-dimensional sheets in their early phase of gravitational collapse indeed have properties allowing one to determine the full 3-dimensional spatial distribution. From numerical simulations it is known that these large structures are Zeldovich pancakes (also called sheets), which are over-densities that have only collapsed along the one dimension [Brinckmann et al., 2016, Wadekar & Hansen, 2015]. In reference [Lee et al., 2015b] it was proposed that it is possible to use a detection of such a sheet to actually measure the turn-around radius. This method has subsequently been investigated in a series of papers, in order to measure properties either of the clusters or of the expanding universe Lee [2016, 2017, 2018], Lee & Li [2017], Lee & Yepes [2016], Lee et al. [2015a], Rong et al. [2016]. It was recently suggested that ΛCDM model and an f(R) model of modified gravity could fairly easily be distinguished in the future, by measuring the turn-around radius and the virial mass [Lopes et al., 2019] (see also [Capozziello et al., 2018, Lopes et al., 2018]). Most of the analyses mentioned above assume that the gravitational potential of the large cosmological structures are approximately spherical, and that the measured turn-around radius in a given direction therefore provides a fair representation of the turn-around radius of the galaxy cluster. The departure from sphericity around a galaxy cluster does, however, induce a large scatter in the measured turn-around radius. This is because the coherently moving galaxies (Zeldovich pancakes) which are used to measure the turn-around radius, are quite localized in space, and hence highly directional. In this paper we will first of all check to which degree this is an accurate approach, and at the same time we will quantify the magnitude of the error-bar of the measured turn-around radius. It turns out that the corresponding error-bars are significant, and must be included in future analyses. We then use this result to evaluate to which degree one can actually use measurements of turn-around radii to constrain alternative cosmologies. As concrete examples we consider the numerical implementations of three dark energy models and of a scalar dark sector interaction, which can be compared with the standard ΛCDM cosmology. We demonstrate that a correct inclusion of the systematic error-bars is very important, and makes it rather difficult to distinguish between different cosmologies.

8.2 Turn-around radius

Figure 8.1 exemplifies the non-triviality of uniquely defining the turn-around radius for realistic cosmological structures. The green dots show particles within 10 virial radii of the cluster. The larger, red triangles show particles which have the property that they have zero radial velocity with respect to the central cluster (plus/minus 100 km/sec), and should thus represent particles at the turn-around radius. The red particles shown in the left panel are selected from a thin slice of width half a virial radius, and we only select particles outside of two virial radii, since the particles inside the virial radius on average are all at rest with respect to the centre. The filled, central circle represents 1 virial radius. The red circle is a guide-the-eye line at 5 times the virial radii.

The problem is clearly seen on the left panel of figure 8.1, namely that it is very difficult to define a unique turn-around radius. First of all, in directions in space with significant substructure, the turn-around radius may appear significantly closer to the cluster, because the gravitational potential of the large substructures affects the flow.

The second issue is, that it is not easy to observationally select a spatial slice, because it is virtually impossible to measure the line-of-sight distance to a

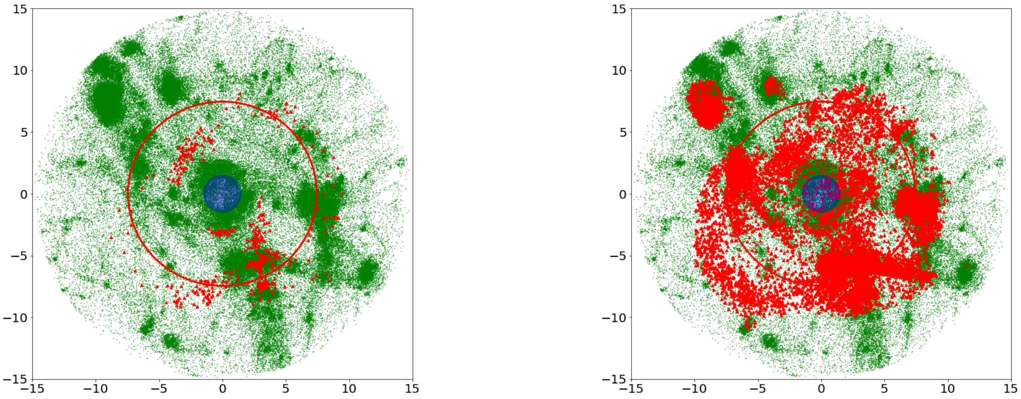

Figure 8.1: This figure exemplifies that the turn-around radius is hard to identify uniquely. The green dots represent all particles out to 10 virial radii around a large galaxy cluster. The central blue region is one virial radius, and the red circle is a guide-the-eye line. The red, triangular symbols represent galaxies which happen to have zero radial velocity with respect to the central galaxy cluster. The corresponding radius is the turn-around radius. Along directions with massive substructures the potential is highly non-trivial (and non-spherical) and hence the turn-around radius depends on the direction in which it is measured. Left panel: The zero radial velocity galaxies (colour-coded red) are selected from a thin slice perpendicular to the line-of-sight. Right panel: All the (almost spherically distributed) galaxies with zero radial velocity are colour-coded red.

given galaxy. Therefore a more realistic representation would be the right panel in figure 8.1. This figure demonstrates the necessity of first identifying some coherence between some of the galaxies, for instance by first finding a sheet, as proposed in [Falco et al., 2014].

The large substructures on the r.h.s. of Figure 1 appear to have zero radial velocity. That is mainly an effect of the use of "large" symbols, and the fact that we here colour-code all particles with zero velocity plus/minus 100 km/sec. This velocity range was chosen to make the infall galaxies visible on the l.h.s. of Figure. 1. The substructures each have a significant internal velocity dispersion, and only a fraction of their particles happen to have zero radial velocity with respect to the direction towards the nearby galaxy cluster at this specific moment in time.

Some of the zero-radial-velocity particles may happen to be splashback particles (returning towards the cluster after a recent merger). Such particles are not likely to end up as coherently moving galaxies (like in a Zeldovich pancake) so we have not studied this further.

8.3 Finding the turn-around radius

Measuring the turn-around radius requires a few steps Lee et al. [2015b]. The first is to find a collection of galaxies whose motion is somehow correlated. The simplest choice is probably to select galaxies which form part of a Zeldovich pancake [Falco et al., 2014]. These are identified as lines in observational phase-space, which is the directly observationally space spanned by projected radial distance and line-of-sight velocity. Some of the disadvantages of using the Zeldovich pancakes are that they are almost invisible on the sky (their projected spatial over-density is quite low), and secondly that they must be viewed at an angle between 20 and 70 degrees with respect to the line-of-sight [Brinckmann et al., 2016]. The advantage is, that once found, the infall velocities of the galaxies belonging to the pancake is coherent. This allows one to determine the viewing angle of the pancakes, and thereby the actual radial distance to the nearby galaxy cluster can be determined Falco et al. [2014].

The next step is to use that the radial velocities of galaxies near a galaxy cluster are the sum of two terms, namely the expansion rate of the Universe, $v_H = r\,H$, and the peculiar velocity, v_p, which is negative due to the attractive force of gravity directed towards the large nearby galaxy cluster. One thus has

$$v_r = v_H + v_p \,. \tag{8.1}$$

It happens that the peculiar velocity typically follows the simple form

$$v_p = -a \left(\frac{r_v}{r} \right)^b \,, \tag{8.2}$$

where the coefficient b is of the order 0.42 for massive galaxy clusters Falco et al. [2014]. This shape of the peculiar velocity profile is often valid in the range between 3 and 10 virial radii. The virial radius, r_v, is here defined as r_{200}, namely the radius within which the average density is 200 times the average density of the universe. The constant a is a normalization to be determined. The detailed coefficients of equation (8.2) are, however, both dependent on the cluster mass and redshift Falco et al. [2014], Lee [2016]. In the analysis of this paper we will only use the fact that the shape is given by equation (8.2), and we will even allow the coefficients to be different for different directions around a given galaxy cluster.

The last step is now to solve eq. (8.1) for $v_r = 0$, which directly gives us the turn-around radius Lee et al. [2015b]. In a future actual measurement one would also have to propagate the error-bars on the Hubble parameter and on the measured galaxy positions. For the present analysis we do not need to consider these.

In this paper we wish to measure the general scatter in the turn-around radius near galaxy clusters, and we therefore use all 49 directions in space. This means that in this paper we do not need to identify Zeldovich pancakes. Instead, we take the full region near galaxy clusters directly from a numerical simulation, and solve eqs. (3.1) and (3.2) to find $v_r = 0$ in 49 directions in space.

8.4 Spatial cones

For each numerically simulated galaxy cluster we wish to investigate the effect of non-sphericity on the determined turn-around radius. In order to quantify the variations along different directions in space, we separate the sphere into 49 cones of equal size. This fraction is chosen to resemble the fraction on the sky covered by a Zeldovich pancake [Brinckmann et al., 2016, Falco et al., 2014]. The peculiar velocity of the particles in each cone are now averaged in spherical bins, and the result is shown in figure 8.2. The solid, red curve is the spherical average of the full sphere. This figure shows a particularly well-behaved and relaxed cluster, and therefore the infall profiles are similar in all directions. In the innermost region (inside 1 or 2 virial radii) we see that the peculiar velocity equals minus the Hubble expansion, in such a way that the average radial velocity is zero in eq. (8.1). At large radii (from about 4 to 10 virial radii) the peculiar velocity is seen to slowly go to zero. The spherical average is seen to represent a fair average of the 49 cones.

A much more typical infall velocity picture is shown in figure 8.3. First of all we see a larger spread amongst the velocity profiles of the 49 directions, and a few of the directions are even seen to have *positive* peculiar velocities (crossing zero around 8 virial radii for this specific cluster). A few of these directions are here color-coded red. The cause of these positive peculiar velocities are large nearby structures, whose potentials significantly perturb the velocities of the particles in those directions. This is clearly seen in figure 8.4, where those regions are again color-coded red (triangles, at 4 o'clock). Another problematic peculiar velocity curve is seen in figure 8.3 to depart from the average trend around 6 virial radii, and becoming *larger* (more negative) at increasing radii. A few of these directions are color-coded blue. This is another feature of large, nearby substructures, as clearly seen on figure 8.4 (squares, at 1 o'clock).

When we identify Zeldovich pancakes on the sky, it is straightforward to avoid directions in space which have large overdensities of galaxies. We therefore assume that these directions have been identified, and we will remove them from the following analysis. Concretely, for this paper we use a simplified approach, and perform the following two tests. First, if the velocity profile along a specific direction happens to have positive peculiar velocity, then we remove that direction from the analysis (corresponding to the red lines in figure 8.3). Secondly, for any given direction in space, we will fit a power-law to the peculiar velocity both between 3-5 and 5-7 virial radii, and if any of the power-law coefficients

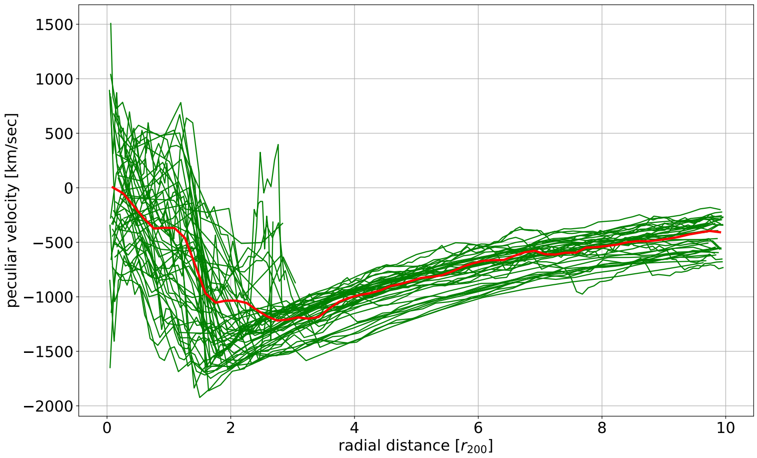

Figure 8.2: Peculiar velocity as a function of radial distance. The 49 green lines each represent particles in a cone on the sky. The solid red curve is the spherical average. This cluster is particularly well behaved and equilibrated. Within approximately 1 virial radius the average radial velocity is zero, and therefore eq. (3.1) tells us that the peculiar velocity on average exactly cancels the Hubble expansion. Between approximately 1 and 3 virial radii there is infall towards the galaxy cluster (the total radial velocity is negative), and toward larger radii the peculiar velocity transitions slowly to zero.

are negative, then we remove that direction (corresponding to the blue lines in figure 8.3).

All the remaining directions will have slightly different infall profiles, and in order to measure a realistic error-bar for the determined turn-around radius, we will compare the variation amongst all these directions.

For each direction we now fit a power-law to the peculiar velocity in the radial range $3 - 7$ virial radii

$$v_p(r) = -a \left(\frac{r_v}{r} \right)^b . \tag{8.3}$$

Including slightly smaller/larger radii has very small effect on our conclusions. Since we know the full radial velocity is given by

$$v_r(r) = r\,H - a \left(\frac{r_v}{r} \right)^b , \tag{8.4}$$

we can find the turn-around radius by solving $v_r(r) = 0$ for the radius Lee et al. [2015b]. For each cluster we now have up to 49 values for the turn-around radius. As a measure of central value and error-bars we use the 50, 16.8 and

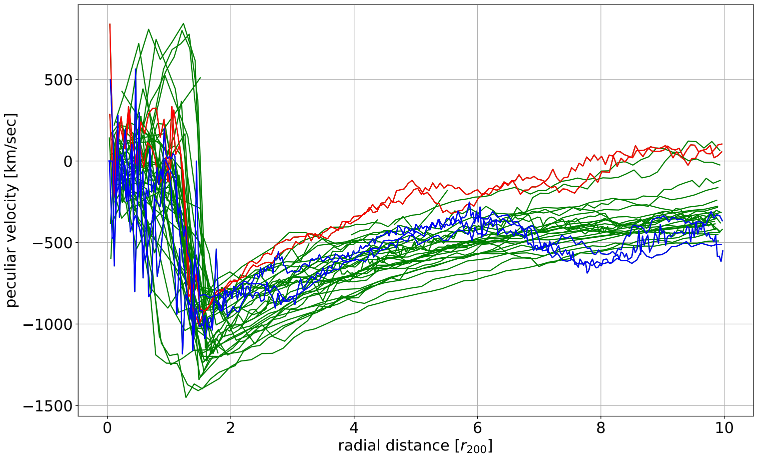

Figure 8.3: Peculiar velocity as a function of radial distance. The 49 lines each represent particles in a cone on the sky. Many of the directions are seen to behave similarly at large distances, however, a few directions stand out: A few directions (red) even have positive peculiar velocities, and a few have a clear transition (blue, here transitioning between 6 and 8 virial radii). These non-trivial peculiar velocity profiles arise because of massive sub-structures perturbing the overall potential.

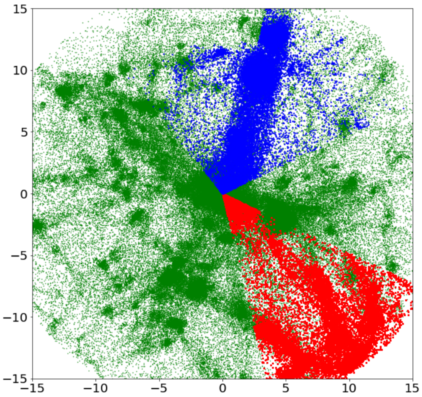

Figure 8.4: The spatial distribution of the particles belonging to the peculiar velocity profiles of figure 8.3. Some of the particles at 4 o'clock even have positive peculiar velocities.

83.2 percentiles. Since the distribution of the turn-around radii is unknown, we also compare with error-bars estimated by fitting a Gauss (as well as an inverse-gamma distribution) to the distributions of turn-around radii, and we find no statistically significant change in any conclusions.

We select 100 massive clusters in the mass-range $10^{14.2} - 10^{15.4} M_\odot$ in a given numerical cosmological simulation. Considering first a standard ΛCDM cosmological simulation, we plot the central turn-around radius with error-bars as a function of virial mass in figure 8.5. From this figure we see two things, first of all that the error-bars are rather significant for any given cluster, typically of the order 20%. For equilibrated and fairly isolated clusters this may be as low as 10%, and for less equilibrated clusters as high as 40%. And second, that there are large variations from cluster to cluster, even for similar mass clusters. The relative error-bars are shown in figure 8.6 for 100 clusters from a ΛCDM simulation.

The trend of the mass-dependence of the turn-around radius can be approximated with a line of the shape

$$r_{\rm ta} = r_{15} + \alpha_{\rm r} \times \log\left(\frac{M}{10^{15} M_\odot}\right) . \tag{8.5}$$

Today less than 10 Zeldovich pancakes have been identified, and yet we are considering using 100 as a future goal. In principle one could generalize the statistical analysis in the present paper by varying the number of clusters. We leave that for a future analysis.

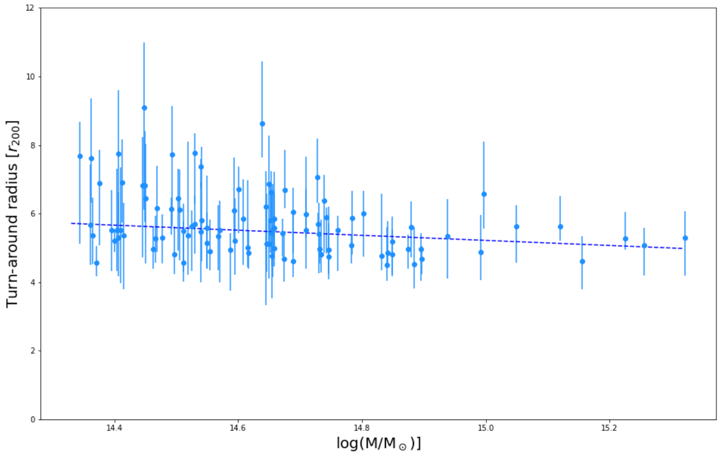

Figure 8.5: The measured turn-around radius as a function of virial mass for 100 massive galaxy clusters from a ΛCDM simulation. The data can be approximated with a line of the shape in equation (8.5) using $r_{15} = 5.2 \pm 0.1$ and $\alpha_r = -0.74 \pm 0.4$.

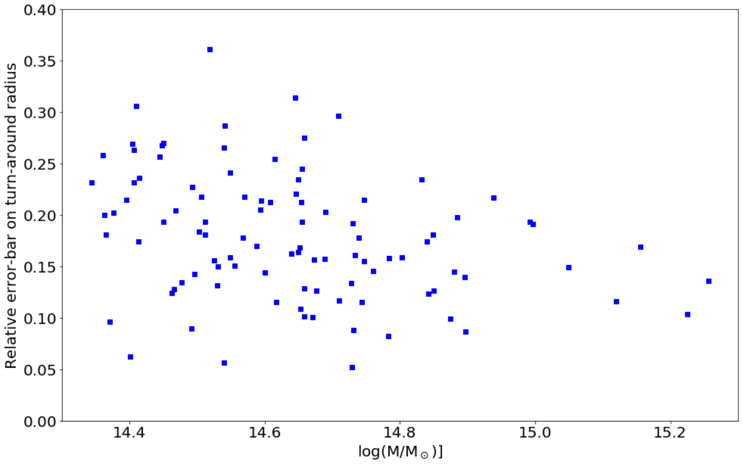

Figure 8.6: The relative error-bars on the turn-around radius as a function of mass for a ΛCDM simulation. The figure shows the symmetrized error-bars divided by the central value of $r_{\rm ta}$.

8.5 Various cosmologies

In order to quantify the capability of the turn-around radius to constrain non-standard cosmologies, we shall consider three different classes of scalar field theories embedded in the action

$$S = \int d^4x\sqrt{-g}\left[\frac{R}{2\kappa^2} + K(\phi, X)\right] + S_c[\psi_c; A_c^2(\phi)g_{\mu\nu}] + S_b[\psi_c; A_b^2(\phi)g_{\mu\nu}] \,, \quad (8.6)$$

where $K(\phi, X)$ is a free function of the scalar field ϕ and $X \equiv -\frac{1}{2}\partial^\mu\phi\partial_\mu\phi$. $A_c^2(\phi)$ and $A_b^2(\phi)$ describe couplings of the cold dark matter and baryonic matter fields, ψ_c and ψ_b, to the metric field $g_{\mu\nu}$ defining the Ricci scalar R. Furthermore, $\kappa^2 \equiv 8\pi G$ with bare gravitational coupling G.

In the following, we shall briefly introduce the three specific models of interest: quintessence (Sec. 8.5.1) and k-essence (Sec. 8.5.2) dark energy and a scalar field interaction between cold dark matter particles (Sec. 8.5.3). In Sec. 8.6, we will then describe the numerical implementations and simulations.

8.5.1 Quintessence

Quintessence Ratra & Peebles [1988], Wetterich [1988] theories are the archetypal dark energy models and are described by Eq. (8.6) with the choice of $K(\phi, X) = X - V(\phi)$ with a canonical kinetic contribution, linear in X, and the scalar field potential $V(\phi)$. The models are minimally coupled to the matter sector with $A_b = A_c = 1$. The freedom in choosing $V(\phi)$ can be represented by the freedom in choosing the time dependent dark energy equation of state $-1 < w(t) \leq 1$, where

$$w = \frac{\dot{\phi}^2 - 2V}{\dot{\phi}^2 + 2V} \quad (8.7)$$

and dots indicate derivatives with respect to cosmological time t.

8.5.2 *k*-essence

The k-essence Armendariz-Picon et al. [1999] models describe a class of more exotic dark energy models with noncanonical kinetic contributions in $K(\phi, X)$, nonlinear in X, that are minimally coupled to the matter fields ($A_b = A_c = 1$). The freedom in the choice of function $K(\phi, X)$ introduces an additional freedom over the quintessence models with the squared nonluminal sound speed of scalar field fluctuations

$$c_s^2 = \frac{K_X}{2X\, K_{XX} + K_X} \quad (8.8)$$

in addition to

$$w = \frac{K}{2X\, K_X - K} \,, \quad (8.9)$$

where subscripts of X denote derivatives with respect to X.

8.5.3 Scalar dark sector interactions

As a third example, we study the interaction of cold dark matter with the scalar field ϕ, specified by the choices $K(\phi, X) = X - V(\phi)$, a minimal coupling to baryons $A_b = 1$, and nonminimally coupled dark matter particles $A_c = A(\phi)$. We choose an interaction

$$A^2(\phi) = 1 + \sqrt{\frac{2}{3}}\kappa\phi \tag{8.10}$$

and a potential of the form

$$V(\phi) = V_0 + V_1\sqrt{\kappa\phi} \tag{8.11}$$

with

$$V_0 = \frac{\Lambda}{\kappa^2}\,, \quad V_1 = -\frac{\bar{R}_0}{\kappa^2}\left(\sqrt{\frac{2}{3}}\chi_0\right)^{1/2}\,, \tag{8.12}$$

where $\bar{R}_0$ is the Ricci scalar evaluated at the current cosmological background and χ_0 is the model parameter with $\chi \equiv \sqrt{2/3}\kappa\phi$. For $\chi_0 \ll 1$ the background matches that of ΛCDM, and for our analysis we shall adopt the parameter value $\chi_0 = 10^{-4}$.

Note that we have chosen the model such that the dark sector interaction reduces to the Hu-Sawicki ($n = 1$) $f(R)$ gravity model Hu & Sawicki [2007] in the absence of baryons ($S_b = 0$). In this case, $\chi_0 = -\left.(df/dR)\right|_{R=\bar{R}(z=0)} \equiv -\left.f_R\right|_{R=\bar{R}(z=0)} \equiv -f_{R0}$. The correspondence follows from applying the conformal transformation of the metric $\tilde{g}_{\mu\nu} = A^2(\phi)g_{\mu\nu}$ in the limit of $\chi \ll 1$ ($\phi \ll 1$). The resulting coupling to the Ricci scalar can be cast as $f_R R$ such that the Lagrangian density of the gravitational sector becomes $\mathcal{L}_g = R + f(R)$ with $f(R) = -2\Lambda - f_{R0}\bar{R}_0^2/R$. For simplicity, we will assume here that all matter is in the form of cold dark matter such that the models become equivalent. Stringent Solar-System constraints on $f(R)$ gravity, relying on a baryonic coupling, however, no longer apply. Cosmological constraints Lombriser [2014] such as from the abundance of clusters that are largely independent of the baryonic coupling require $\chi_0 \lesssim (10^{-5} - 10^{-4})$ Cataneo et al. [2016], Lombriser et al. [2012a], Schmidt et al. [2009b].

The choice of interaction (8.10) and potential (8.11) induces a chameleon screening mechanism for deep gravitational potentials $|\Psi_{\rm N}| \gg 3\,|\delta\chi|\,/2 \equiv 3\,|\chi - \chi_0|\,/2$. The potential wells for the structures considered in this work are, however, significantly weaker ($\chi_0 = 10^{-4}$). Screening effects can therefore be neglected, and we can adopt a linearisation of the interaction. More specifically, we linearise the quasistatic scalar field equation around the cosmological background such that Lombriser et al. [2012b], Schmidt et al. [2009a]

$$\nabla^2 \delta\chi - m^2 \delta\chi = \frac{\kappa^2}{3} \delta\rho_m \,, \tag{8.13}$$

where the scalar field mass of the Yukawa interaction is given by

$$m^2 = \frac{1}{6\chi_0} \frac{\bar{R}^3}{\bar{R}_0^2} \,. \tag{8.14}$$

For the Poisson equation

$$\nabla^2 \Psi_{\mathrm{N}} = \frac{\kappa^2}{2} \delta\rho_m + \frac{1}{2} \nabla^2 \delta\chi \,, \tag{8.15}$$

this implies an enhanced effective gravitational coupling for the cold dark matter particles constituting $\delta\rho_m$, which in Fourier space is given by

$$\frac{k^2}{a^2} \Psi_{\mathrm{N}} = -\left(1 + \frac{1}{3} \frac{k^2}{k^2 + m^2 a^2}\right) \frac{\kappa^2}{2} \delta\rho_m \,. \tag{8.16}$$

8.6 Numerical simulations

To investigate the power of using the turn-around radius in distinguishing different cosmologies, we run simulations for k-essence dark energy (Sec. 8.5.2) models and a scalar field interaction in the dark sector that reduces to linearised $f(R)$ gravity in the absence of baryons. These can then be compared with a standard ΛCDM simulation. The initial conditions for the simulations are set using the linear transfer functions from the linear Boltzmann code CLASS Blas et al. [2011a] at high redshift (z=100). All simulations use the same seeds as initial conditions. Our ΛCDM simulations are performed using the gevolution code, which is a relativistic particle-mesh N-body code with a fixed resolution Adamek et al. [2016a]. For the k-essence and quintessence simulations we have used the k-evolution code, which is a relativistic N-body code based on gevolution, in which the k-essence scalar field and Einstein's equations are solved to update the particles' positions and momenta. Detailed tests of this code will be presented in [Hassani et al., 2019c, 2020b].

The simulation of the scalar dark sector interaction is performed through an implementation of the modified Poisson equation (8.16) in a Newtonian N-body code based on gevolution Hassani & Lombriser [2020], which has been validated against the results of Ref. Schmidt et al. [2009a].

We have thus four different simulations (in addition to ΛCDM) to quantify the effects of a different background, clustering of a k-essence scalar field and the effect on the clustering coming from the scalar dark sector interactions on the turn-around radius. All simulations have a comoving boxsize of $L = 300$ Mpc/h, and discretize the fields on a grid of linear size $\mathrm{N_{grids}}$=512, giving a length resolution of 0.58 Mpc/h. The dark matter phase space is sampled by $\mathrm{N_{pcl}} = 512^3$ particles, corresponding to a mass resolution of 1.74×10^{10} $\mathrm{M_\odot}$/h. The detailed parameters of each simulation are shown in table 8.1.

	ΛCDM	SDSI	quintessence	quintessence	k-essence
k_{pivot} $[\frac{1}{\mathrm{Mpc}}]$	0.05	0.05	0.05	0.05	0.05
A_s	2.215×10^{-9}	2.215×10^{-9}	2.215×10^{-9}	2.215×10^{-9}	2.215×10^{-9}
$\Omega_b h^2$	0.022032	0.022032	0.022032	0.022032	0.022032
$\Omega_{cdm} h^2$	0.12038	0.12038	0.12038	0.12038	0.12038
$T_{cmb}[K]$	2.7255	2.7255	2.7255	2.7255	2.7255
N_{ur}	3.046	3.046	3.046	3.046	3.046
c_s^2	–	–	1	1	-10^{-7}
Ω_Λ	0.687862	0.687862	–	–	–
Ω_{de}	–	–	0.687862	0.687862	0.687862
w_{de}	–	–	-0.9	-0.8	-0.9
χ_0	–	10^{-4}	–	–	–
Initial redshift	100	100	100	100	100

Table 8.1: The table shows the full information of the simulations, the red color shows where the parameters are changed in different simulations. In the absence of baryons the scalar dark sector interaction (SDSI) model matches a linearised Hu-Sawicki ($n = 1$) $f(\mathrm{R})$ gravity model with $\chi_0 = |f_{R0}|$. Note that the imaginary sound speed for k-essence is simply chosen to maximise phenomenological modifications in the simulations.

8.6.1 Results

We compare two of the non-trivial cosmologies with a ΛCDM simulation in figures 8.7 and 8.8. The first impression is that it will be very difficult to distinguish between different cosmologies, because of the large error-bars for each cluster,

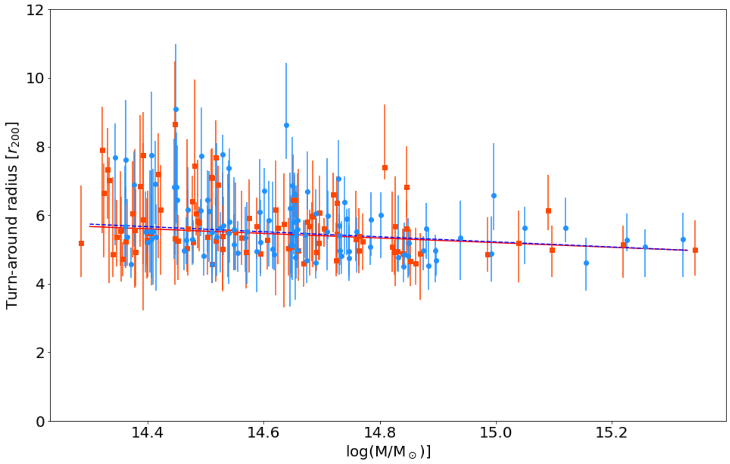

Figure 8.7: ΛCDM v.s. k-essence with $w = -0.9$ and $c_s^2 = 1$ (corresponding to a quintessence model). The turn-around radius for the quintessence model with $w = -0.9$ (red symbols, red solid line) is seen to have essentially the same dependence on mass as ΛCDM (blue symbols, blue dashed line). These two models cannot be distinguished when measuring the turn-around radius for 100 galaxy clusters.

and the large cluster to cluster variation. To that end a careful statistical analysis is needed.

One might wonder if it would be advantageous to consider galaxy groups (or galaxies [Pavlidou & Tomaras, 2014]) to perform this analysis. That is, however, still not possible, because the turn-around radius is still only measurable using the Zeldovich pancake method, which only works near galaxy clusters. The reason is, that the Zeldovich pancake method relies on the gravitational perturbation exerted by the cluster on the nearby galaxy flow.

In order to address the problem of cosmic variance, we ran 3 extra numerical simulations of standard ΛCDM universes, with different random seeds for the initial conditions. By comparing the analysis of each of these universes against the prediction from our first simulation we can estimate the magnitude of variance between different representations of the same cosmology. To that end we fit the first ΛCDM simulation result by a fit of the shape given in eq. (8.5), $r_{\rm ta}^{\rm fit}$. This is then used in a chi-squared comparison where we use a sum over the clusters

$$\chi^2 = \sum_{\rm i} \frac{\left(r_{\rm ta}^i - r_{\rm ta}^{\rm fit}\right)^2}{\sigma_i^2}\,. \tag{8.17}$$

Here we use symmetrized error-bars for σ_i (average of upper and lower error-

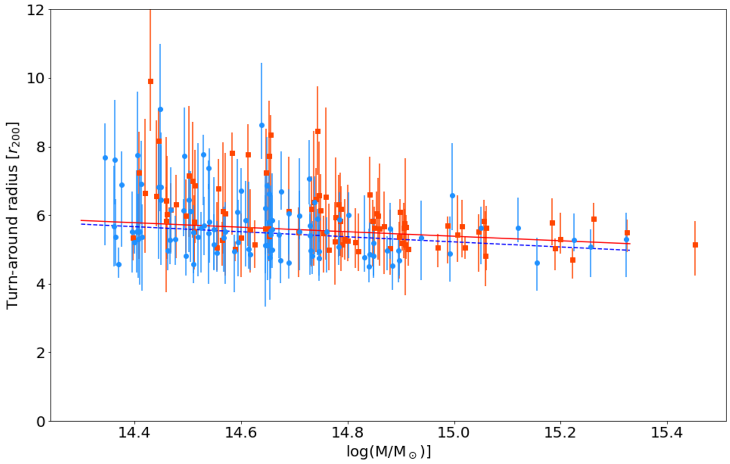

Figure 8.8: ΛCDM v.s. scalar dark sector interaction (SDSI). The turn-around radius for the SDSI model (red symbols, red solid line) is seen to have moved to slightly higher turn-around radius for the same mass, when compared to ΛCDM (blue symbols, blue dashed line). The SDSI mass-dependence of the virial mass may be approximated with a straight line of the form in equation (8.5), using $r_{15} = 5.4 \pm 0.08$ and $\alpha_\mathrm{r} = -0.7 \pm 0.3$. Measuring the turnaround radius for approximately 100 clusters will allow one to distinguish the two cosmologies.

bars). Our first simulation has χ^2 per degree of freedom of 0.8, indicating that the error-bars are reasonable.

Comparing with each of the other ΛCDM simulations leads to $\Delta\chi^2$ between 1 and 6. This implies that when any given cosmology is contrasted with the ΛCDM, then any $\Delta\chi^2$ less than approximately 6 will not allow us to distinguish the two.

When we perform the same statistical estimator for the simulations of quintessence or k-essence (see the cosmological parameters in table 8.1) we get $\Delta\chi^2$ less than 6 for all the cosmologies. This implies that none of the cosmologies will be distinguishable from ΛCDM.

The same statistical estimator for the simulations of SDSI cosmology gives $\Delta\chi^2 = 9.2$, and thus indicates that it will (as the only one amongst the ones considered here) be distinguishable from ΛCDM. Formally one might think that $\Delta\chi^2 = 9.2$ implies that for the two free parameters used in the fit, the two cosmologies are distinguishable at 99% CL, however, that estimate does not include the cosmic variance, and the real CL is therefore smaller. A careful analysis of the statistics would require a larger number of simulations and is beyond the scope of this paper.

The entire analysis presented above has been based on observations at redshift zero. It is clear that different cosmologies have different evolution and structure formation, and it is therefore likely that an analysis including the redshift dependence will lead to somewhat stronger constraints than what we have obtained here.

8.7 Conclusions

The environments of galaxy clusters are complex distributions of sub-structures, filaments, sheets and voids. This implies that the turn-around radius, where the radial velocity of galaxies is zero, varies when different directions in space are considered. This implies that one must include a systematic error-bar when measuring the turn-around radius in the future. We use ΛCDM numerical simulations to quantify the magnitude of this error-bar, and we find that it is about 20% of the measured turn-around radius for typical clusters, going down to about 10% for the most equilibrated and spherical structures. Furthermore, we show that one must carefully avoid measuring the turn-around radius along directions with large sub-structures.

We use a range of non-trivial cosmological simulations to gauge to which extent the inclusion of this realistic error-bar allows one to measure a departure from a ΛCDM universe, and we find that it becomes possible only for the most extreme cosmologies we considered, such as scalar dark sector interaction with fairly large interactions.

Acknowledgements

It is a pleasure to thank Mona Jalilvand and Julian Adamek for support with the numerical simulations. SHH is grateful to the Swiss National Science Foundation and Carlsberg Foundation for supporting his visit to University of Geneva. This project is partially funded by the Danish council for independent research, DFF 6108-00470. L.L. acknowledges support by a Swiss National Science Foundation Professorship grant (No. 170547). FH and MK acknowledge funding by the Swiss National Science Foundation. This work was supported by a grant from the Swiss National Supercomputing Centre (CSCS) under project ID s710.

Chapter 9

SUMMARY AND CONCLUSION

9.1 Summary

To understand the reason behind the observed accelerating expansion of the Universe is one of the most notable enigmas in modern cosmology, and conceivably in fundamental physics. In the upcoming years, near future surveys will probe structure formation with unprecedented precision and will put firm constraints on the cosmological parameters, including those that describe properties of the dark energy. In light of this, this thesis focuses on precision cosmology by characterizing the non-linear evolution of cosmological components using N-body simulations. We consistently study the dark matter and dark energy/modified gravity theories up to non-linear scales and pinpoint viable models by comparing our results to observational data.

In Chapter 2 we obtained the general effective field theory parameterisation for k-essence model employing the weak field approximation. Making use of the obtained k-essence equations in the effective form, we have developed k-evolution, a relativistic N-body code based on gevolution, to study clustering dark energy precisely. In this setup, we compared the results from k-evolution with those of the linear Boltzmann code CLASS and gevolution to quantify the effect of non-linearities on the dark matter, dark energy and gravitational potential power spectra. In addition, we commented on the Newtonian N-body simulations with back-scaled initial conditions using k-evolution code.

In Chapter 3, with our purpose-built N-body code, k-evolution, that solves the coupled evolution of dark energy field and the dark matter particles, we studied the cosmological observables extracted from the gravitational potential, specifically the integrated Sachs-Wolfe and non-linear Rees-Sciama effect (ISW-RS) weak gravitational lensing, Shapiro time delay and gravitational redshift computed on the past light cone of an observer at $z = 0$. The observables discussed in this paper are calculated via a raytracing method integrating to the source redshifts $z \approx 0.85$ and $z \approx 3.3$, covering respectively a full sky map and a pencil beam in our simulations. Comparing results from the two N-body codes, gevolution, and k-evolution with the linear Boltzmann code CLASS we were able to evaluate the different effects coming from dark energy, specifically the effect from a different background evolution, from linear dark energy perturbations and from the non-linear evolution of dark energy itself. In this chapter we showed that among all observable the ISW-RS signal is the strongest probe of the clustering of dark energy.

In Chapter 4 we studied metric perturbations in the weak-field regime of General Relativity, in the presence of a k-essence scalar field as dark energy. We showed that the short-wave corrections to the Hamiltonian constraint are negligible at all redshifts and all scales, while the relativistic terms are only relevant at large scales, leaving the terms with the matter and k-essence density perturbations as the main source at quasi-linear and small scales. The relativistic terms and the density perturbations can be combined, in the usual way, to form a linear Poisson equation that then holds on all scales of interest in cosmology. We studied the contribution of the k-essence scalar field to the metric perturbations through the μ parametrisation that encodes the additional contribution of a dark energy fluid or a modification of gravity to the Poisson equation. We encoded our k-essence simulation results for $\mu(k, z)$ in an easy-to-use tanh-based fitting function, together with recipes on how to include the function in linear Boltzmann codes or Newtonian N-body simulations with different expansion rate but without the additional k-essence field.

In Chapter 5 we discussed non-linear terms in the EFT of DE for k-essence model. Such terms open a new window in cosmological models for dark energy. We studied such models in 3+1 dimensions using k-evolution code. We discovered that in the case of low speed of sound (high Mach number in the fluid description) where some linear terms vanish from the dynamics of dark energy, the non-linear partial differential equation for dark energy suffers from a non-linear instability and the Universe, as a result, ceases to exist in a finite time. We showed analytically, for the 1+1 dimensional case, that the divergence is real and is not an artifact in the numerical simulations. The important conclusion in this chapter is that k-essence dark energy as a fluid with high Mach number (low speed of sound) cannot be used as a viable candidate for explaining the accelerated expansion of the universe, because the evolution will diverge before one reaches the current epoch.

In Chapter 6 we showed that a numerical study of relativistic effects can have two problems. First, the integration method must have a small enough time step to reach a precision which is better than the size of the relativistic correction. Second, if, additionally, the forces are discretized, the grid size must be quite fine, so that the relativistic corrections are not washed out by the approximation. In particular, our results allow one to estimate for which choices of Υ, e, and θ, the relativistic effects are larger than the numerical and discretization effects generated by h and dx.

In Chapter 7 we have proposed a parametrisation of the modified gravity effects on the linear and nonlinear cosmological structure formation adequate for N-body codes. We have tested our parametrised code, `MG-evolution`, with a number of widely studied modified gravity models, including $f(R)$ and nDGP gravity, which encompass both large-field value and derivative screening effects with the employment of the chameleon and Vainshtein mechanisms, and for which exact N-body implementations are available. We showed that the parameterised approach is capable of recovering the nolinear matter power spectra produced by the exact code implementations of these models to sub-percent accuracy up to the highly nonlinear scales of $k = 2.5$ h/Mpc covered by our simulations.

In Chapter 8 we used ΛCDM numerical simulations to quantify the magnitude of a systematic error-bar when measuring the turn-around radius, and we found that it is about 20% of the measured turn-around radius for typical clusters, going down to about 10% for the most equilibrated and spherical structures. Furthermore, we showed that one must carefully avoid measuring the turn-around radius along directions with large sub-structures. We used a range of non-trivial cosmological simulations to gauge to which extent the inclusion of this realistic error-bar allows one to measure a departure from a ΛCDM universe, and we found that it becomes possible only for the most extreme cosmologies we considered, such as scalar dark sector interaction with fairly large interactions.

9.2 Outlook

The works that we discussed in this thesis can be expanded in different directions. Possible directions regarding Chapter 2 are:

- Going beyond k-evolution code and developing N-body simulations of a wide class of dark energy and modified gravity (DE/MG) models. This requires us to obtain the relevant equations of motion for EFT of dark energy and modified gravity theories written in the weak field approximation.

- Quantifying the degeneracy between the effect of massive neutrinos and clustering dark energy.
- Developing N-body simulations to explore the effect of non-standard dark matter scenarios on the structure formation
- Systematic study of primordial gravitational waves using relativistic N-body simulations.

Concerning Chapter 4 the interesting ideas are:

- Providing fits to $\mu(k, z)$ for a wider range of parameters. We are going to encode our DE/MG simulation results for $\mu(k, z)$ in an easy-to-use tanh-based fitting function, together with recipes on how to include the function in linear Boltzmann codes or Newtonian N-body simulations with different expansion rate but without additional DE/MG field.
- Providing tanh/sigmoid function fits to $\mu(k, z)$ for some MG theories to improve the EuclidEmulator.

Possible projects concerning Chapter 5:

- In an ongoing project with Pan Shi and Peter Wittwer in Shi, Pan et. al. [c,a,b], we are studying the instability in 1+1 D mathematically. We have already found the universal solution and blowup time for some class of initial conditions. We also have proved the existence and uniqueness of the solution.
- Using the results of the math paper in 1+1 D, we plan to put new constraints on the properties of clustering dark energy and possibly some DE/MG scenarios.

Future plans regarding Chapter 7:

- In future work we plan to explore our nonlinear parametrised gravity framework employing higher resolution simulations that extend the results to larger wavenumbers.
- We plan to apply and test our parametrised code with further modified gravity models.

Possible projects regarding Chapter 8:

- Looking at the time evolution of the turn around radius to see its sensitivity to cosmology and possibly put new constraints on the background evolution and the properties of dark energy component.
- Constraining dark matter properties by considering the dynamics in and near galaxy clusters using state of the art simulations.

BIBLIOGRAPHY

Aarseth S. J., 1963, MNRAS, 126, 223

Abate A., et al., 2012, preprint (`arXiv:1211.0310`)

Abbott B. P., et al., 2016, Phys. Rev. Lett., 116, 221101

Abbott B. P., et al., 2017, Astrophys. J., 848, L13

Abbott T. M. C., et al., 2018, Phys. Rev., D98, 043526

Adamek J., Daverio D., Durrer R., Kunz M., 2016a, JCAP, 07, 053

Adamek J., Daverio D., Durrer R., Kunz M., 2016b, Nature Physics, 12, 346

Adamek J., Daverio D., Durrer R., Kunz M., 2016c, Journal of Cosmology and Astro-Particle Physics, 2016, 053

Adamek J., Brandbyge J., Fidler C., Hannestad S., Rampf C., Tram T., 2017a, Mon. Not. Roy. Astron. Soc., 470, 303

Adamek J., Durrer R., Kunz M., 2017b, Journal of Cosmology and Astro-Particle Physics, 1711, 004

Adamek J., Clarkson C., Coates L., Durrer R., Kunz M., 2019, Phys. Rev., D100, 021301

Adamek J., Barrera-Hinojosa C., Bruni M., Li B., Macpherson H. J., Mertens J. B., 2020a, Class. Quant. Grav., 37, 154001

Adamek J., Rasera Y., Corasaniti P. S., Alimi J.-M., 2020b, Phys. Rev., D101, 023512

Ade P. A. R., et al., 2014a, Astron. Astrophys., 571, A17

Ade P. A. R., et al., 2014b, Astronomy & Astrophysics, 571, A19

Ade P. A. R., et al., 2015b

Ade P., et al., 2015a

Ade P. A. R., et al., 2016, Astronomy & Astrophysics, 594, A21

Aghamousa A., et al., 2016a, preprint (`arXiv:1611.00036`)

Aghamousa A., et al., 2016b

Alam S., et al., 2017a, Mon. Not. Roy. Astron. Soc., 470, 2617

Alam S., Zhu H., Croft R. A. C., Ho S., Giusarma E., Schneider D. P., 2017b, Monthly Notices of the Royal Astronomical Society, 470, 2822?2833

Alsing J., Kirk D., Heavens A., Jaffe A., 2015, Mon. Not. Roy. Astron. Soc., 452, 1202

Amendola L., Tsujikawa S., 2010, Dark Energy: Theory and Observations. Cambridge University Press, doi:10.1017/CBO9780511750823

Amendola L., Kunz M., Sapone D., 2008, Journal of Cosmology and Astroparticle Physics, 2008, 013

Amendola L., et al., 2016

Amendola L., et al., 2018, Living Reviews in Relativity, 21, 2

Arkani-Hamed N., Cheng H.-C., Luty M. A., Mukohyama S., 2004, Journal of High Energy Physics, 05, 074

Arkani-Hamed N., Cheng H.-C., Luty M. A., Mukohyama S., Wiseman T., 2007, JHEP, 01, 036

Armendariz-Picon C., Damour T., Mukhanov V. F., 1999, Phys. Lett. B, 458, 209

Armendariz-Picon C., Mukhanov V. F., Steinhardt P. J., 2000, Phys.Rev.Lett., 85, 4438

Armendariz-Picon C., Mukhanov V. F., Steinhardt P. J., 2001, Phys. Rev., D63, 103510

Arnold D. N., 2002, arXiv Mathematics e-prints, p. math/0212391

Arnowitt R., Deser S., Misner C. W., 1959, Physical Review, 116, 1322

Aubourg É., et al., 2015, Phys. Rev. D, 92, 123516

Babichev E., 2016, JHEP, 04, 129

Babichev E., Deffayet C., Ziour R., 2009, Int. J. Mod. Phys., D18, 2147

Back A., 2005, Runge Kutta behavior in the presence of a jump discontinuity

Bacon D. J., Refregier A. R., Ellis R. S., 2000, MNRAS, 318, 625

Bagla J. S., 2005, Curr. Sci., 88, 1088

Bagla J. S., Padmanabhan T., 1997, Pramana, 49, 161

Baker T., Ferreira P. G., Skordis C., Zuntz J., 2011, Phys. Rev., D84, 124018

Baker T., Ferreira P. G., Skordis C., 2013, Phys. Rev., D87, 024015

Baker T., et al., 2019, arXiv e-prints, p. arXiv:1908.03430

Baldi M., 2012, Physics of the Dark Universe, 1, 162

Ballesteros G., Hollenstein L., Jain R. K., Kunz M., 2012, Journal of Cosmology and Astro-Particle Physics, 1205, 038

Barnes J., Hut P., 1986, Nature, 324, 446

Barreira A., Li B., Hellwing W. A., Baugh C. M., Pascoli S., 2013, J. Cosmology Astropart. Phys., 1310, 027

Barrera-Hinojosa C., Li B., 2020, J. Cosmology Astropart. Phys., 2020, 007

Bartelmann M., Schneider P., 2001, Phys. Rept., 340, 291

Battye R. A., Pearson J. A., 2012, JCAP, 1207, 019

Beck R., Csabai I., Racz G., Szapudi I., 2018, Monthly Notices of the Royal Astronomical Society, 479, 3582?3591

Becker M. R., 2013, Monthly Notices of the Royal Astronomical Society, 435, 115

Behroozi P. S., Wechsler R. H., Wu H.-Y., 2013, Astrophys. J., 762, 109

Bellini E., Sawicki I., 2014, JCAP, 07, 050

Bertschinger E., 1998, Annual Review of Astronomy and Astrophysics, 36, 599

Bertschinger E., 2001, in Cosmology 2000: Proceedings, Conference, Lisbon, Portugal, 12-15 Jul 2000. pp 1–25 (`arXiv:astro-ph/0101009`)

Blanchard A., et al., 2019, preprint (`arXiv:1910.09273`)

Blas D., Lesgourgues J., Tram T., 2011a, JCAP, 07, 034

Blas D., Lesgourgues J., Tram T., 2011b, Journal of Cosmology and Astro-Particle Physics, 2011, 034

Blas D., Lesgourgues J., Tram T., 2011c, Journal of Cosmology and Astroparticle Physics, 2011, 034?034

Bloomfield J., 2013, JCAP, 1312, 044

Bloomfield J. K., Flanagan É. É., Park M., Watson S., 2013, JCAP, 1308, 010

Bonvin C., Durrer R., 2011, Phys. Rev. D, 84, 063505

Bonvin C., Caprini C., Durrer R., 2006, Phys. Rev. Lett., 97, 081303

Bouchet F. R., Hernquist L., 1988, ApJS, 68, 521

Bouchet F. R., Kandrup H. E., 1985, ApJ, 299, 1

Bouchet F. R., Adam J. C., Pellat R., 1985, A&A, 144, 413

Brandbyge J., Hannestad S., 2009, JCAP, 05, 002

Brandbyge J., Rampf C., Tram T., Leclercq F., Fidler C., Hannestad S., 2017, Mon. Not. Roy. Astron. Soc., 466, L68

Brandenberger R. H., 2004, Lect. Notes Phys., 646, 127

Brax P., Valageas P., 2014, Phys. Rev., D90, 023508

Brax P., Davis A.-C., Li B., Winther H. A., 2012a, Phys. Rev., D86, 044015

Brax P., Davis A.-C., Li B., Winther H. A., Zhao G.-B., 2012b, J. Cosmology Astropart. Phys., 2012, 002

Breton M.-A., Rasera Y., Taruya A., Lacombe O., Saga S., 2019, Mon. Not. Roy. Astron. Soc., 483, 2671

Brinckmann T., Lindholmer M., Hansen S., Falco M., 2016, J. Cosmology Astropart. Phys., 2016, 007

Broadhurst T., Scannapieco E., 2000, The Astrophysical Journal, 533, L93

Bullock J. S., Boylan-Kolchin M., 2017, Ann. Rev. Astron. Astrophys., 55, 343

Burgess C., 2004, Living Rev. Rel., 7, 5

Butcher J. C., 1963, Journal of the Australian Mathematical Society, 3, 185?201

Cabass G., Gerbino M., Giusarma E., Melchiorri A., Pagano L., Salvati L., 2015, Physical Review D, 92

Cai Y.-C., Cole S., Jenkins A., Frenk C., 2009a, Mon. Not. Roy. Astron. Soc., 396, 772

Cai Y.-C., Cole S., Jenkins A., Frenk C., 2009b, Monthly Notices of the Royal Astronomical Society, 396, 772?778

Cai Y.-C., Cole S., Jenkins A., Frenk C. S., 2010, MNRAS, 407, 201

Cai Y.-C., Li B., Cole S., Frenk C. S., Neyrinck M., 2014, Monthly Notices of the Royal Astronomical Society, 439, 2978?2989

Cai Y., Neyrinck M., Mao Q., Peacock J., Szapudi I., Berlind A., 2017, Monthly Notices of the Royal Astronomical Society, 466, 3364

Caldwell R., 2004. `https://physicsworld.com/a/dark-energy/`

Capozziello S., Dialektopoulos K. F., Luongo O., 2018, Int. J. Mod. Phys. D, 28, 1950058

Cappi A., 1995, A&A, 301, 6

Carbone C., Petkova M., Dolag K., 2016, JCAP, 1607, 034

Cataneo M., Rapetti D., 2018, International Journal of Modern Physics D, 27, 1848006

Cataneo M., Rapetti D., Lombriser L., Li B., 2016, JCAP, 12, 024

Cataneo M., Lombriser L., Heymans C., Mead A., Barreira A., Bose S., Li B., 2019, Mon. Not. Roy. Astron. Soc., 488, 2121

Challinor A., Lewis A., 2011, Phys. Rev. D, 84, 043516

Cheung C., Creminelli P., Fitzpatrick A., Kaplan J., Senatore L., 2008, JHEP, 03, 014

Clifton T., Ferreira P. G., Padilla A., Skordis C., 2012a, Phys. Rept., 513, 1

Clifton T., Ferreira P. G., Padilla A., Skordis C., 2012b, Phys. Rept., 513, 1

Clifton T., Ferreira P. G., Padilla A., Skordis C., 2012c, Physics Reports, 513, 1?189

Creminelli P., Luty M. A., Nicolis A., Senatore L., 2006, JHEP, 0612, 080

Creminelli P., D'Amico G., Norena J., Vernizzi F., 2009, JCAP, 02, 018

Cusin G., Lewandowski M., Vernizzi F., 2018a, JCAP, 1804, 005

Cusin G., Lewandowski M., Vernizzi F., 2018b, JCAP, 1804, 061

Dakin J., Hannestad S., Tram T., Knabenhans M., Stadel J., 2019, JCAP, 1908, 013

Deffayet C., 2001, Phys. Lett., B502, 199

Del Popolo A., Le Delliou M., 2017, Galaxies, 5, 17

Dodelson S., 2003, Modern Cosmology. Academic Press, Amsterdam, doi:https://doi.org/10.1016/B978-012219141-1/50019-X

Dossett J., Ishak M., 2013, Phys. Rev. D, 88, 103008

Durrer R., 2001, J. Phys. Stud., 5, 177

Durrer R., 2008, The Cosmic Microwave Background. Cambridge University Press, doi:10.1017/CBO9780511817205

Durrer R., 2015, Class. Quant. Grav., 32, 124007

Dvali G. R., Gabadadze G., Porrati M., 2000, Phys. Lett., B485, 208

Eckmann J.-P., Hassani F., 2019, Celestial Mechanics and Dynamical Astronomy, 132, 2

Efstathiou G., Davis M., White S. D. M., Frenk C. S., 1985, ApJS, 57, 241

Endlich S., Nicolis A., Porto R. A., Wang J., 2013, Phys. Rev. D, 88, 105001

Ernst Hairer Christian Lubich G. W., 2003/5, Acta numerica, 12, 399

Falco M., Hansen S. H., Wojtak R., Brinckmann T., Lindholmer M., Pandolfi S., 2014, MNRAS, 442, 1887

Faraoni V., 2016, Physics of the Dark Universe, 11, 11

Fidler C., Tram T., Rampf C., Crittenden R., Koyama K., Wands D., 2016, Journal of Cosmology and Astro-Particle Physics, 1609, 031

Fidler C., Tram T., Rampf C., Crittenden R., Koyama K., Wands D., 2017, JCAP, 12, 022

Francis C. L., Peacock J. A., 2010, Monthly Notices of the Royal Astronomical Society, 406, 2?13

Frusciante N., Papadomanolakis G., 2017, JCAP, 1712, 014

Frusciante N., Perenon L., 2020, Phys. Rept., 857, 1

Gallay T., Raugel G., 1998, Journal of Differential Equations, 150, 42

Gleyzes J., 2015, PhD thesis, U. Paris-Sud 11, Dept. Phys., Orsay, Cham, doi:10.1007/978-3-319-41210-8

Gleyzes J., Langlois D., Piazza F., Vernizzi F., 2013, Journal of Cosmology and Astro-Particle Physics, 1308, 025

Gleyzes J., Langlois D., Vernizzi F., 2015, Int. J. Mod. Phys., D23, 1443010

Gorski K. M., Hivon E., Banday A. J., Wandelt B. D., Hansen F. K., Reinecke M., Bartelmann M., 2005, The Astrophysical Journal, 622, 759

Granett B. R., Neyrinck M. C., Szapudi I., 2008, The Astrophysical Journal, 683, L99?L102

Gubitosi G., Piazza F., Vernizzi F., 2013a, Journal of Cosmology and Astro-Particle Physics, 1302, 032

Gubitosi G., Piazza F., Vernizzi F., 2013b, Journal of Cosmology and Astroparticle Physics, 2013, 032?032

Hairer E., Nørsett S. P., Wanner G., 1993, Solving Ordinary Differential Equations I (2nd Revised. Ed.): Nonstiff Problems. Springer-Verlag, Berlin, Heidelberg

Hairer E., Lubich C., Wanner G., 2003, Geometric numerical integration illustrated by the Störmer-Verlet method. Cambridge University Press, p. 399?450, doi:10.1017/CBO9780511550157.006

Hairer E., Lubich C., Wanner G., 2010, Geometric Numerical Integration. Springer Series in Computational Mathematics, Dordrecht, doi:10.1007/3-540-30666-8, `https://cds.cern.ch/record/1250576`

Handley W., Lemos P., 2019, Phys. Rev. D, 100, 043504

Hannestad S., Tu H., Wong Y. Y. Y., 2006, Journal of Cosmology and Astroparticle Physics, 2006, 025?025

Hansen S. H., Hassani F., Lombriser L., Kunz M., 2020, JCAP, 01, 048

Hartmann S., 2001, Studies in History and Philosophy of Science Part B: Studies in History and Philosophy of Modern Physics, 32, 267

Hassani F., Lombriser L., 2020, Monthly Notices of the Royal Astronomical Society, 497, 1885

Hassani F., Baghram S., Firouzjahi H., 2016, JCAP, 1605, 044

Hassani F., Adamek J., Kunz M., Vernizzi F., 2019a

Hassani F., L'Huillier B., Shafieloo A., Kunz M., Adamek J., 2019b, arXiv e-prints, p. arXiv:1910.01105

Hassani F., Adamek J., Kunz M., Vernizzi F., 2019c, JCAP, 12, 011

Hassani F., Adamek J., Kunz M., 2020a

Hassani F., L'Huillier B., Shafieloo A., Kunz M., Adamek J., 2020b, JCAP, 04, 039

Hassani F., L'Huillier B., Shafieloo A., Kunz M., Adamek J., 2020c, JCAP, 04, 039

Hassani F., L'Huillier B., Shafieloo A., Kunz M., Adamek J., 2020d, J. Cosmology Astropart. Phys., 2020, 039

Hikage C., et al., 2019, Publ. Astron. Soc. Jap., 71, Publications of the Astronomical Society of Japan, Volume 71, Issue 2, April 2019, 43, https://doi.org/10.1093/pasj/psz010

Hildebrandt H., et al., 2016

Hinterbichler K., Khoury J., 2010, Phys. Rev. Lett., 104, 231301

Hockney R. W., Eastwood J. W., 1988, Computer simulation using particles

Hoffman Y., et al., 2018, Nature Astronomy, 2, 680

Holmberg E., 1941, ApJ, 94, 385

Hu W., Cooray A., 2001, Phys. Rev., D63, 023504

Hu W., Sawicki I., 2007, Phys. Rev. D, 76, 064004

Hulse R. A., Taylor J. H., 1975, ApJ, 195, L51

Ishak M., 2019, Living Rev. Rel., 22, 1

Jain B., Taylor A., 2003, Phys. Rev. Lett., 91, 141302

Jalilvand M., Ghosh B., Majerotto E., Bose B., Durrer R., Kunz M., 2020, Phys. Rev. D, 101, 043530

Jennings E., Baugh C. M., Angulo R. E., Pascoli S., 2010, Mon. Not. Roy. Astron. Soc., 401, 2181

Jimeno P., Broadhurst T., Coupon J., Umetsu K., Lazkoz R., 2015, Mon. Not. Roy. Astron. Soc., 448, 1999

Jones B. J. T., 1997, in Valls-Gabaud D., Hendry M. A., Molaro P., Chamcham K., eds, Astronomical Society of the Pacific Conference Series Vol. 126, From Quantum Fluctuations to Cosmological Structures. p. 1, `https://ui.adsabs.harvard.edu/abs/1997ASPC..126....1J`

Joyce A., Jain B., Khoury J., Trodden M., 2015, Phys. Rept., 568, 1

Joyce A., Lombriser L., Schmidt F., 2016a, Ann. Rev. Nucl. Part. Sci., 66, 95

Joyce A., Lombriser L., Schmidt F., 2016b, Ann. Rev. Nucl. Part. Sci., 66, 95

Kapner D. J., Cook T. S., Adelberger E. G., Gundlach J. H., Heckel B. R., Hoyle C. D., Swanson H. E., 2007, Phys. Rev. Lett., 98, 021101

Kennedy J., Lombriser L., Taylor A., 2018, Phys. Rev., D98, 044051

Khosravi S., Mollazadeh A., Baghram S., 2016, JCAP, 09, 003

Khoury J., Weltman A., 2004, Phys.Rev.Lett., 93, 171104

Kim Y., Croft R. A. C., 2004, The Astrophysical Journal, 607, 164?174

Knabenhans M., et al., 2019, Mon. Not. Roy. Astron. Soc., 484, 5509

Kohlinger F., et al., 2017, Mon. Not. Roy. Astron. Soc., 471, 4412

Koyama K., 2005, Physical Review D, 72

Koyama K., 2016, Rept. Prog. Phys., 79, 046902

Koyama K., 2018, Int. J. Mod. Phys. D, 27, 1848001

Koyama K., Silva F. P., 2007, Phys. Rev., D75, 084040

Kunz M., Sapone D., 2007, Phys. Rev. Lett., 98, 121301

LSST Dark Energy Science Collaboration 2012, arXiv e-prints, p. arXiv:1211.0310

Lagos M., Baker T., Ferreira P. G., Noller J., 2016, Journal of Cosmology and Astro-Particle Physics, 1608, 007

Laureijs R., et al., 2011, p. arXiv:1110.3193

Lee J., 2016, ApJ, 832, 123

Lee J., 2017, ApJ, 839, 29

Lee J., 2018, ApJ, 856, 57

Lee J., Li B., 2017, ApJ, 842, 2

Lee J., Yepes G., 2016, ApJ, 832, 185

Lee J., Kim S., Rey S.-C., 2015a, ApJ, 807, 122

Lee J., Kim S., Rey S.-C., 2015b, ApJ, 815, 43

Lepori F., Adamek J., Durrer R., Clarkson C., Coates L., 2020

Lesgourgues J., 2011

Lewis A., Challinor A., 2006, Phys. Rept., 429, 1

Lewis A., Challinor A., Lasenby A., 2000, The Astrophysical Journal, 538, 473–476

Li B., 2018, Simulating Large-Scale Structure for Models of Cosmic Acceleration. 2514-3433, IOP Publishing, doi:10.1088/978-0-7503-1587-6, `http://dx.doi.org/10.1088/978-0-7503-1587-6`

Li B., Efstathiou G., 2012, Mon.Not.Roy.Astron.Soc., 421, 1431

Li M., Li X.-D., Wang S., Wang Y., 2011, Commun. Theor. Phys., 56, 525

Li B., Zhao G.-B., Teyssier R., Koyama K., 2012a, J. Cosmology Astropart. Phys., 2012, 051

Li B., Zhao G.-B., Teyssier R., Koyama K., 2012b, J. Cosmology Astropart. Phys., 2012, 051

Li B., Barreira A., Baugh C. M., Hellwing W. A., Koyama K., Pascoli S., Zhao G.-B., 2013, J. Cosmology Astropart. Phys., 1311, 012

Li P., Dodelson S., Hu W., 2019, Phys. Rev. D, 100, 043502

Lifshitz E., 1946, J. Phys.(USSR), 10, 116

Llinares C., Mota D. F., Winther H. A., 2014, Astron. Astrophys., 562, A78

Lombriser L., 2014, Annalen Phys., 526, 259

Lombriser L., 2016, J. Cosmology Astropart. Phys., 2016, 039

Lombriser L., 2018, Int. J. Mod. Phys., D27, 1848002

Lombriser L., Lima N. A., 2017, Phys. Lett., B765, 382

Lombriser L., Taylor A., 2015a, Phys. Rev. Lett., 114, 031101

Lombriser L., Taylor A., 2015b, JCAP, 1511, 040

Lombriser L., Hu W., Fang W., Seljak U., 2009, Phys. Rev., D80, 063536

Lombriser L., Slosar A., Seljak U., Hu W., 2012a, Phys. Rev. D, 85, 124038

Lombriser L., Koyama K., Zhao G.-B., Li B., 2012b, Phys. Rev. D, 85, 124054

Lombriser L., Koyama K., Li B., 2014, J. Cosmology Astropart. Phys., 03, 021

Lombriser L., Dalang C., Kennedy J., Taylor A., 2019, J. Cosmology Astropart. Phys., 1901, 041

Lopes R. C., Voivodic R., Abramo L. R., Sodre Laerte J., 2018, JCAP, 09, 010

Lopes R. C., Voivodic R., Abramo L. R., Sodre L., 2019, JCAP, 07, 026

Ma C.-P., Bertschinger E., 1995a, ApJ, 455, 7

Ma C.-P., Bertschinger E., 1995b, Astrophys.J., 455, 7

Mandelbaum R., 2018, Ann. Rev. Astron. Astrophys., 56, 393

Martin J., 2012a, Comptes Rendus Physique, 13, 566

Martin J., 2012b, Comptes Rendus Physique, 13, 566

McManus R., Lombriser L., Penarrubia J., 2016, J. Cosmology Astropart. Phys., 1611, 006

Mead A., Peacock J., Heymans C., Joudaki S., Heavens A., 2015, Mon. Not. Roy. Astron. Soc., 454, 1958

Nusser A., 2016, The Astrophysical Journal, 821, L2

Oyaizu H., Lima M., Hu W., 2008, Phys. Rev., D78, 123524

Padmanabhan T., 1996, Cosmology and Astrophysics through Problems. `https://ui.adsabs.harvard.edu/abs/1996cap..book.....P`

Padmanabhan T., 2000, Theoretical Astrophysics. Vol. 1, Cambridge University Press, doi:10.1017/CBO9781139171083

Padmanabhan T., 2002, Theoretical Astrophysics - Volume 3, Galaxies and Cosmology. Vol. 3, doi:10.2277/0521562422,

Padmanabhan T., 2010, Gravitation: Foundations and Frontiers. `https://ui.adsabs.harvard.edu/abs/2010grav.book.....P`

Parsa M., Eckart A., Shahzamanian B., Karas V., Zajacek M., Zensus J. A., Straubmeier C., 2017, The Astrophysical Journal, 845, 22

Pavlidou V., Tomaras T. N., 2014, J. Cosmology Astropart. Phys., 2014, 020

Pavlidou V., Tetradis N., Tomaras T. N., 2014, J. Cosmology Astropart. Phys., 2014, 017

Peebles P. J. E., Vilenkin A., 1999, Phys. Rev., D59, 063505

Peiris H. V., Spergel D. N., 2000, The Astrophysical Journal, 540, 605?613

Percival W. J., Cole S., Eisenstein D. J., Nichol R. C., Peacock J. A., Pope A. C., Szalay A. S., 2007, Mon. Not. Roy. Astron. Soc., 381, 1053

Perlmutter S., et al., 1999, ApJ, 517, 565

Piazza F., Vernizzi F., 2013, Class.Quant.Grav., 30, 214007

Pich A., 1998, in Les Houches Summer School in Theoretical Physics, Session 68: Probing the Standard Model of Particle Interactions. pp 949–1049 (`arXiv:hep-ph/9806303`)

Planck Collaboration et al., 2016, A&A, 594, A13

Planck Collaboration et al., 2018, arXiv e-prints, p. arXiv:1807.06209

Potter D., Stadel J., Teyssier R., 2016

Pratten G., Lewis A., 2016, JCAP, 08, 047

Preto M., Saha P., 2009, Astrophys. J., 703, 1743

Puchwein E., Baldi M., Springel V., 2013, Mon. Not. Roy. Astron. Soc., 436, 348

Ratra B., Peebles P., 1988, Phys. Rev. D, 37, 3406

Rees M. J., Sciama D. W., 1968, Nature, 217, 511

Refregier A., 2003, Ann. Rev. Astron. Astrophys., 41, 645

Reverberi L., Daverio D., 2019, JCAP, 07, 035

Riess A. G., et al., 1998a, Astron. J., 116, 1009

Riess A. G., et al., 1998b, AJ, 116, 1009

Rong Y., Liu Y., Zhang S.-N., 2016, MNRAS, 455, 2267

Sachs R., Wolfe A., 1967, Astrophys. J., 147, 73

Sadeh I., Feng L. L., Lahav O., 2015, Phys. Rev. Lett., 114, 071103

Santos M., et al., 2015a, in Advancing Astrophysics with the Square Kilometre Array (AASKA14). p. 19 (`arXiv:1501.03989`)

Santos M., et al., 2015b, PoS, AASKA14, 019

Sapone D., Kunz M., 2009, Phys. Rev., D80, 083519

Schmidt F., 2009, Phys. Rev., D80, 043001

Schmidt F., Lima M. V., Oyaizu H., Hu W., 2009a, Phys. Rev. D, 79, 083518

Schmidt F., Vikhlinin A., Hu W., 2009b, Phys. Rev. D, 80, 083505

Schmidt F., Hu W., Lima M., 2010, Phys. Rev., D81, 063005

Schmidt F., Leauthaud A., Massey R., Rhodes J., George M. R., Koekemoer A. M., Finoguenov A., Tanaka M., 2011, The Astrophysical Journal, 744, L22

Scolnic D. M., et al., 2018, Astrophys. J., 859, 101

Scranton R., et al., 2003

Seljak U., 1996, The Astrophysical Journal, 460, 549

Shapiro I. I., 1964, Phys. Rev. Lett., 13, 789

Shi, Pan et. al., On a second order in time Hamilton-Jacobi type equation issued from cosmology, in prep.

Shi, Pan et. al., Scale-invariant solutions to a Hamilton-Jacobi type equation issued from cosmology, in prep.

Shi, Pan et. al., Stability of a blow-up solution for a second order in time Hamilton-Jacobi type equation, in prep.

Silvestri A., Pogosian L., Buniy R. V., 2013, Physical Review D, 87

Spergel D., et al., 2003, Astrophys. J. Suppl., 148, 175

Springel V., 2005, MNRAS, 364, 1105

Spurio Mancini A., Reischke R., Pettorino V., Schäfer B. M., Zumalacárregui M., 2018, MNRAS, 480, 3725

Stadel J. G., 2001, PhD thesis, UNIVERSITY OF WASHINGTON

Stephani H., 2004, Relativity: An Introduction to Special and General Relativity, 3 edn. Cambridge University Press, doi:10.1017/CBO9780511616532

Straumann N., 2002, in 18th IAP Colloquium on the Nature of Dark Energy: Observational and Theoretical Results on the Accelerating Universe. (`arXiv:gr-qc/0208027`)

Stueckelberg E., 1938, Die Wechselwirkungskräfte in der Elektrodynamik und in der Feldtheorie der Kernkräfte (Teil II und III). Vol. 1, doi:10.1007/978-3-7643-8878-2_17,

Szapudi I., Prunet S., Pogosyan D., Szalay A. S., Bond J., 2000

Taddei L., Catena R., Pietroni M., 2014, Phys. Rev., D89, 023523

Takahashi R., Sato M., Nishimichi T., Taruya A., Oguri M., 2012, Astrophys. J., 761, 152

Takahashi R., Hamana T., Shirasaki M., Namikawa T., Nishimichi T., Osato K., Shiroyama K., 2017, The Astrophysical Journal, 850, 24

Tegmark M., et al., 2004, Phys. Rev. D, 69, 103501

Tegmark M., et al., 2006, Phys. Rev. D, 74, 123507

Teyssier R., 2002a, A&A, 385, 337

Teyssier R., 2002b, Astronomy & Astrophysics, 385, 337

Thomas D. B., Contaldi C. R., 2011, arXiv e-prints, p. arXiv:1112.6378

Trenti M., Hut P., 2008, Scholarpedia, 3, 3930

Tsujikawa S., 2015, Lect.Notes Phys., 892, 97

Vainshtein A. I., 1972, Phys. Lett., 39B, 393

Valogiannis G., Bean R., 2017, Phys. Rev., D95, 103515

Van Waerbeke L., et al., 2000, A&A, 358, 30

Verde L., Treu T., Riess A. G., 2019, Nature Astronomy, 3, 891

Virtanen P., et al., 2020, Nature Methods, 17, 261

Vuarnoz D., Jusselme T., 2018, Energy, 161, 573

Wadekar D., Hansen S. H., 2015, MNRAS, 447, 1333

Walcher C. J., et al., 2019, The Messenger, 175, 12

Wandelt B. D., Hivon E., Gorski K. M., 2001, Physical Review D, 64

Watts P., Coles P., 2003, Mon. Not. Roy. Astron. Soc., 338, 806

Weinberg S., 1989, Rev. Mod. Phys., 61, 1

Weinberg S., 2008, Cosmology. Cosmology, OUP Oxford, doi:10.1007/s10714-008-0728-z

Weller J., Lewis A. M., 2003, Mon. Not. Roy. Astron. Soc., 346, 987

Weltman A., et al., 2020, Publ. Astron. Soc. Austral., 37, e002

Wetterich C., 1988, Nucl. Phys. B, 302, 668

Wikipedia contributors 2020a, Cosmic Calendar — Wikipedia, The Free Encyclopedia, `https://en.wikipedia.org/w/index.php?title=Cosmic_Calendar&oldid=960793844`

Wikipedia contributors 2020b, Effective field theory — Wikipedia, The Free Encyclopedia, `https://en.wikipedia.org/w/index.php?title=Effective_field_theory&oldid=968379505`

Will C. M., 2014, Living Rev. Rel., 17, 4

Wojtak R., Hansen S. H., Hjorth J., 2011, Nature, 477, 567

Wyman M., Jennings E., Lima M., 2013, Phys. Rev., D88, 084029

Yoo J., Fitzpatrick A. L., Zaldarriaga M., 2009, Phys. Rev. D, 80, 083514

Yu H.-R., et al., 2017, Nature Astronomy, 1, 0143

Zhao G.-B., Li B., Koyama K., 2011, Phys. Rev., D83, 044007

Zhu H., Alam S., Croft R. A. C., Ho S., Giusarma E., Leauthaud A., Merrifield M., 2019, Gravitational redshift profiles of MaNGA BCGs (`arXiv:1901.05616`)

von Hoerner S., 1960, ZAp, 50, 184